Searching for Dark Sectors with Proton Bremsstrahlung

by

Saeid Foroughi-Abari
B.Sc., Isfahan University of Technology, 2015
M.Sc., Sharif University of Technology, 2017

A Dissertation Submitted in Partial Fulfillment of the
Requirements for the Degree of

DOCTOR OF PHILOSOPHY

in the Department of Physics and Astronomy

University of Victoria

Searching for Dark Sectors with Proton Bremsstrahlung

by

Saeid Foroughi-Abari
B.Sc., Isfahan University of Technology, 2015
M.Sc., Sharif University of Technology, 2017

Supervisory Committee

Dr. Adam Ritz, Supervisor
(Department of Physics and Astronomy)

Dr. Robert Kowalewski, Departmental Member
(Department of Physics and Astronomy)

Dr. Stan Dosso, Outside Member
(School of Earth and Ocean Sciences)

Abstract

This dissertation explores the sensitivity of high-luminosity colliders and fixed target facilities to low mass new physics in so-called dark sectors that are coupled to the Standard Model of particle physics. These new physics scenarios are motivated by the need to explain empirical puzzles, including the nature of the dark matter in the universe and the origin of neutrino mass. Avoiding over-production and reproducing the observed relic abundance of thermal dark matter candidates requires that low mass (sub-GeV) dark sector degrees of freedom are coupled to the Standard Model via new light force mediators. In this context, we revisit the minimal case of a scalar singlet S coupled to the Standard Model through the Higgs portal and impose new constraints by interpreting the dataset from the LSND experiment. Motivated by proposals for new searches at Fermilab and the Large Hadron Collider (LHC), the rate of proton bremsstrahlung of light dark vectors and scalars is revisited. The proton bremsstrahlung, which involves mixing with meson resonances, is a primary production mode in the forward direction near the resonance region. We derive an approximate method of evaluating the proton bremsstrahlung and compare the resulting distributions and rates with those obtained via variants of the Fermi-Weizsacker-Williams approximation.

Additionally, the newly proposed LHC Forward Physics Facility (FPF) emerged as a highly promising site for searching for long-lived particles, millicharged particles, and especially for studying high-energy colliding neutrinos. Within this context, the FORMOSA experiment, located in the LHC forward region, is proposed to provide exceptional sensitivity in the search for millicharged particles by exploiting their scintillation signature. Furthermore, the thesis explores the FPF's potential to probe the neutrino electromagnetic properties, including neutrino millicharge, magnetic moment, and charge radius, as well as the weak mixing angle, using an intense beam of highly energetic neutrinos of all three flavors. The study of new interactions within the neutrino sector can enhance our understanding of neutrinos and establish the connection between the dark sector and neutrino physics on a broader scale.

Table of Contents

List of Tables

List of Figures

Acknowledgements

I would like to extend my heartfelt gratitude to my supervisor, **Prof. Adam Ritz**, for his exceptional support, kindness, and steady professionalism throughout my PhD journey. His guidance, encouragement, direction, and invaluable advice have been instrumental in shaping my research and academic development.

I am deeply grateful to my collaborators, **Dr. Felix Kling** and **Dr. Yu-Dai Tsai**, for our remarkable collaboration on studying millicharged dark sectors, and neutrino electromagnetic properties. Their expertise, enthusiasm, and collaborative spirit have enhanced the depth and quality of my research. I would also like to thank **Dr. Nikita Blinov** for all the great discussions, guidance, and kind support he provided. I am grateful for his patience in answering my many questions and for the opportunity to learn from him.

I am also grateful to the **Forward Physics Facility Collaboration** for inviting me to join their Beyond Standard Model (BSM) working group. Being part of this collaboration has offered me a unique and enriching graduate experience, providing valuable opportunities for collaboration, learning, and professional growth.

I would like to extend my thanks to my beloved wife, **Hanieh**, for her love, encouragement, and unwavering support. Your presence and understanding during the challenges of this journey have been immeasurable.

I would like to express my profound appreciation to my **parents** for nurturing my curiosity and providing unwavering support. Their love and encouragement have been constant sources of strength throughout my academic pursuits.

I express my sincere gratitude for the financial support I have received through the Natural Sciences and Engineering Research Council of Canada's (**NSERC**) scholarship.

O’ day, arise! Shine your light, the particles are dancing

Thanks to Him the Universe is dancing,

The souls are dancing, overcome with ecstasy, free from body and mind

I’ll whisper in your ear where their dance is leading them

All the particles in the sky and in the desert are dancing

puzzled and bemused to the ray of light, they seem insane

All these particles are not so different than we are, happy or miserable, perplexed and bewildered

We are all beings in the ray of Light from The Beloved, nothing can be said.

Rumi *(Jalal ad-Din Muhammad)*
13th-century Persian poet, theologian and Sufi Saint

Chapter 1

Introduction

The Standard Model of particle physics has been remarkably well-tested experimentally, and its predictions align consistently with a wide range of measurements. Despite the success of the SM, particle physics faces several challenges in understanding fundamental aspects such as explaining the nature of dark matter, the origin of observed matter-antimatter asymmetry, the origin of neutrino mass, and many more aspects of fundamental physics. These outstanding questions continue to inspire the exploration of physics beyond the Standard Model.

A wealth of astrophysical and cosmological evidence substantiates the existence of dark matter, an undiscovered form of matter that eludes direct observation and accounts for approximately five times more mass than ordinary matter in the present Universe. Dark matter is distinct from baryons or the known neutrinos but is crucial for explaining various observations across different length scales and evolutionary time periods in the Universe. The dark matter case is one of the biggest unsolved problems of modern physics and cosmology.

If dark matter is made out of particles [1], its mass and nature are still unknown. An effort is therefore underway to probe viable scenarios across a broad range of parameters, including mass. Despite using various approaches to observe the non-gravitational interactions of dark matter, such as direct searches employing underground detectors to investigate dark matter scattering with ordinary matter, indirect searches utilizing ground-based and satellite telescopes to detect potential decay or annihilation signatures of dark matter within the galaxy, and collider searches using high-energy particle collisions to produce dark matter particles, no conclusive evidence of its particle nature has yet been discovered. Nevertheless, these null searches have imposed stringent constraints on the parameter space of dark matter, providing valuable insights for the construction of theoretical models.

Among the vast expanse of our uncertainty regarding dark matter particle mass and plausible scenarios, Weakly Interacting Massive Particle (WIMP) with mass ranging from GeV to TeV represents a simple and effective model for formulating dark matter scenarios produced thermally in the early Universe. The sensitivity of conventional direct detection experiments diminishes considerably as the WIMP mass decreases below a GeV scale, rendering the nuclear recoil energy too small to be detected by current-generation experiments. Motivated by null searches from direct detection experiments targeting WIMPs [2], significant attention has shifted towards light dark matter with sub-GeV masses. However, the annihilation cross-section of low mass dark matter through the Standard Model states would be too small to generate a consistent dark matter energy density in the early Universe in comparison with what is observed [3]. To account for the observed relic abundance today, dark matter with a mass below a few GeV must annihilate into the visible matter via new light force mediators [4, 5].

The strongest empirical evidence for new physics beyond the Standard Model, in particular for dark matter and neutrino mass, may hint at the presence of a more complex hidden/dark sector [6, 7, 8, 9, 10, 11, 12, 13, 14, 15, 16, 17, 18, 19, 20, 21, 22]. The dark sectors framework, which requires new light weakly-coupled particles to act as portals to the Standard Model, has enriched the phenomenology of light dark matter models. These portal interactions are among the most interesting and promising benchmark models and have been studied in great detail in recent years (see e.g. [23, 24, 25]).

The elusive nature of dark matter necessitates high-intensity accelerator beams or astrophysical sources to produce detectable signals. Proton and electron fixed target experiments at the luminosity frontier offer a promising avenue to probe relatively light weakly coupled degrees of freedom in hidden sector scenarios [26, 27, 28, 29, 30, 31, 32, 33, 34, 35, 36, 37, 38, 39, 40, 41, 42, 43, 44, 45, 46, 47, 48, 49, 50, 51]. The accelerator signals of light dark matter at the GeV scale are complementary to non-relativistic signals such as scattering in direct detection. These dark sector particles, as new force carriers, can help resolve anomalies in particle physics and/or explain the observed excesses from astrophysical observations.

This dissertation's research program focuses on estimating the potential sensitivity to light dark sectors coupled to the Standard Model via various portals, including the Higgs portal, kinetically-mixed vector portal, and higher-dimensional operators. Both analytic and numerical analysis techniques are employed to evaluate production rates and explore the parameter space of long-lived particles and millicharged dark sectors in fixed targets and colliders. As another research direction, interactions of neutrinos are studied, in particular, their electromagnetic (EM) properties. Testing of new interactions in the neutrino sector, in existing and future experiments, is crucial to determine the nature of neutrinos (Dirac or Majorana) or to probe new physics beyond the Standard Model [52]. These neutrino properties could also be connected to intriguing experimental anomalies, including the NuTeV anomaly [53].

1.1 Contents

This dissertation consists of seven chapters, starting with this introduction as the first chapter. A summary of the topics covered in each chapter is provided below as an overview of the thesis structure.

Chapter 2 contains an overview of various aspects of dark matter, including astrophysical and cosmological evidence, known properties, production mechanisms in the early universe, and experimental searches for its non-gravitational interactions. In addition, motivations for studying light hidden sectors are introduced, along with a theoretical framework for constructing such scenarios and an outline of experimental strategies that can be employed to effectively probe them. The subsequent chapters of this dissertation are based on four publications.

Chapter 3 revisits the minimal case of a scalar singlet S coupled to the Standard Model through the Higgs portal, that decays visibly to leptons for scalar masses below the di-pion threshold. The dataset from the LSND experiment is found to impose the leading constraints within two mass windows between $m_S \sim 100$ and 350 MeV. In the process, we analyze some scalar production channels in the target, finding that proton bremsstrahlung provides the dominant channel at LSND beam energies. The results and analyses from this chapter were published as "LSND Constraints on the Higgs Portal" in Phys. Rev. D 102 (2020) 3, 035015 [arXiv:2004.14515 [hep-ph]].

Chapter 4 revisits the production of dark vectors and scalars via proton bremsstrahlung, making use of a model that describes the underlying nucleon scattering cross-section in the forward direction due to pomeron exchange. We compare the resulting distributions and rates with those obtained via variants of the Fermi-Weizsacker-Williams approximation and provide production rate distributions for a range of beam energies, including those relevant to the proposed Forward Physics Facility at the High Luminosity-LHC. The research presented in this chapter was published as ”Dark Sector Production via Proton Bremsstrahlung” in Phys. Rev. D 105 (2022) 9, 095045 [arXiv:2108.05900 [hep-ph]].

Chapter 5 investigates the sensitivity of a scintillation-based detection to millicharged dark sectors in the LHC forward region. The proposed FORMOSA experiment is capable to provide the best sensitivity to search for milliCharged Particles (mCPs) in the 10 MeV to 100 GeV mass window by exploiting their scintillation signature. mCPs can arise in the dark sector framework with massless dark photons, and interestingly, could account for a fraction of the dark matter abundance motivated by the EDGES anomaly [54]. We show that a large region of parameter space for milliCharged dark matter models can be constrained by FORMOSA during HL-LHC operation. The findings and analyses presented in this chapter were published in Phys. Rev. D 104 (2021) 3, 035014 [arXiv:2010.07941 [hep-ph]]. As part of this project, my contributions included performing analysis and calculations to determine the sensitivity reach of FORMOSA, as well as examining the mCP scintillation signature and making estimates of potential background sources.

Chapter 6 investigates the potential of the Forward Physics Facility [55] to probe the neutrino electromagnetic properties [52], including neutrino millicharge, magnetic moment, and charge radius. The study reveals that the proposed detectors at the LHC forward region, benefiting from the large flux of tau neutrinos, offer the strongest laboratory-based sensitivity to the tau neutrino magnetic moment and millicharge by searching for excess in low recoil energy electron scattering events. Furthermore, by precisely measuring the rate of neutral current deep inelastic scattering events, the proposed detectors at the Forward Physics Facility have the potential to obtain the strongest experimental bounds on the neutrino charge radius for the electron neutrino, and one of the leading bounds for the muon neutrino flavor. The same signature could also be used to measure the weak mixing angle with high precision. The work presented in this chapter entitled ”Neutrino Electromagnetic Properties and the Weak Mixing Angle at the LHC Forward Physics Facility” is submitted to Phys. Rev. D and [arXiv:2301.10254 [hep-ph]]. In this project, my contributions involved investigating elastic and deep-inelastic neutrino scattering signatures, developing approaches utilizing scintillator-type and neutrino detectors for low recoil energy exploration, calculating neutrino electromagnetic interaction rates, comparing findings with experimental bounds, and performing analysis to obtain the expected sensitivity to the weak mixing angle.

Chapter 7 concludes the dissertation with a concise summary of the accomplished research and highlights future possibilities for exploration.

Chapter 2

Dark Matter and New Physics Beyond the Standard Model

2.1 Introduction

The Standard Model (SM), as a consistent theoretical framework, describes almost all known particles (and anti-particles) and interactions among them (ignoring gravity) up to very high energy scales (*e.g.* the Planck scale), with the exception of neutrino mass. The SM consists of three successive generations of fermions as matter (leptons and quarks), four gauge bosons as force carriers (photon, gluon, W, and Z mediators), and the recently discovered elementary particle, the Higgs Boson [56]. The SM provides an excellent description of the weak, strong, and electromagnetic forces, which are the only channels through which particles can interact with each other. Various particle physics experiments precisely measure the agreement between data and the predictions of the SM in search of any hint of new physics.

The SM does not explain several pieces of evidence for new physics such as the existence of dark matter (DM). Astrophysical and cosmological observations, spanning various sources and distance scales [1], have provided compelling evidence that SM matter can only account for nearly 5% of the mass and energy density content of the observable universe and that there is an additional 25% of our current universe made of non-baryonic dark matter [57].

From a particle phenomenology point of view, the evidence for DM and also neutrino mass may point to the presence of hidden (dark) sectors with degrees of freedom weakly coupled to the SM [6, 7, 8, 9, 10, 11, 12, 13, 14, 15, 16, 17, 18, 19, 20, 21, 22]. One of the directions toward the hunt for physics beyond the SM is the search for a dark sector. The indirect interactions of a dark sector with visible matter result in evading detection in particle-physics experiments. Therefore, high-intensity accelerator beams or astrophysical sources would be necessary to produce them at a detectable rate [26]. In particular, relatively light degrees of freedom in hidden sector scenarios could be efficiently probed at the luminosity frontier including a variety of proton [26, 27, 28, 29, 58, 31, 32, 33, 34, 35, 36, 38, 39] and electron [43, 44, 45, 46, 47, 48, 49, 50] fixed target experiments.

This Chapter explores various aspects of DM, including its astrophysical and cosmological evidence, known properties, production mechanisms in the early universe, experimental searches for its non-gravitational interactions, and motivations for hidden sectors. In Section 2.2, we discuss the astrophysical and cosmological evidence supporting the existence of DM and its known properties. An overview of DM production mechanism in the early Universe is provided in Section 2.3. Furthermore, Section 2.4 provides an overview of the current status of experimental endeavours aimed at detecting the non-gravitational interaction of DM. Section 2.5 discusses motivations for a hidden sector. We provide an overview of the constituent particles and interactions within the SM in Section 2.6, followed by a theoretical framework for how dark sector portals to SM can be formulated, presented in Section 2.7. Finally, in Section 2.8 we will discuss how benchmark dark sector models can be explored experimentally using accelerator-based probes.

2.2 Dark Matter Properties and Candidates

The empirical evidence for DM is overwhelming and comes from cosmological and astrophysical measurements including the pattern of the cosmic microwave background (CMB) power spectrum [59], the linear matter power spectrum of density perturbations [60], cluster and galactic rotation curves [61] and gravitational lensing [62, 63, 64, 65].

The evolution of our Universe and the structures within it provide valuable clues about the existence and properties of DM and before discussing the evidence for DM, it is crucial to have a comprehensive understanding of the history of the Universe. In the framework of standard cosmology [66, 67], initially, the primordial Universe is dense and hot, and all of the visible matter (quarks, leptons, photons) are in thermal equilibrium. The relic abundance of stable species such as photons, neutrinos, electrons, protons, and light elements began to form during or after a period known as Big Bang Nucleosynthesis (BBN), which started when the temperature of the photon bath dropped below $\lesssim 1\,\mathrm{MeV}$ after the neutrino-photon decoupling. BBN is considered the earliest observable epoch from which we can trace the abundance of light elements, including Helium, and deuterium. Following BBN, the next significant observable event in the timeline of the universe was the production of cosmic microwave background (CMB) radiation. This radiation originated when the temperature of the universe dropped to approximately eV levels, causing electrons and protons to cool and combine to form neutral atoms (recombination). At this point, the universe became transparent to photons, and we observe the relic radiation today as the CMB. Finally, the large-scale structure of the universe, characterized by the distribution of galaxies and cosmic structures, became observable at later stages.

In particle physics, it is convenient to use natural units by setting $\hbar = c = 1$, which gives all quantities dimensions of energy to some power, *e.g.* mass, and temperature have units of energy, while length and time have units of $(\text{energy})^{-1}$. The cross-section with the dimension of $(\text{energy})^{-2}$ might be measured in barn units, where $1\,\text{pb} = 10^{-36}\,\text{cm}^2$. A useful conversion factor is $1\ \text{GeV}^{-2} = 3.89 \times 10^8\,\text{pb}$.

2.2.1 Cosmological Scale

Cosmological observations of the early universe provide us with solid evidence for the existence of DM, as obtained through the analysis of the cosmic microwave background (CMB). The CMB is an isotropic radiation observed today at a temperature of about $\sim 2.7\,K$ and comprises a nearly perfect thermal distribution of photons emitted during the recombination epoch, which occurred around $\sim 300,000$ years after the Big Bang. Precise measurements of the CMB [68] allow us to detect deviations from the isotropic CMB on the order of $\mathcal{O}(10^{-5})$. These anisotropies in the temperature fluctuations of the CMB can be expanded into a series of spherical harmonics to obtain the CMB power spectrum as illustrated in Fig. 2.1. The relative height of the CMB power spectrum sensitively depends on the presence of DM in the Universe [69].

A similar density fluctuation pattern is evident in the matter power spectrum obtained from the mapping of the distribution of large-scale structures [70], as well as measuring of hydrogen atom absorption lines in the spectra of distant galaxies, known as the Lyman-alpha [71, 72]. The observed inhomogeneities in the power spectrum of matter, which are related to the density of the baryon-photon fluid at the time of recombination, can be described by acoustic oscillations created by the radiation pressure of photons that counteract the gravitational pull of matter. Unlike baryons, DM only contributes to gravitational effects, which differentiates its influence on these fluctuations from baryons.

By examining the pattern of CMB temperature fluctuations, and in combination with complementary measurements from Type Ia Supernova surveys [73, 74] and baryon-acoustic oscillations (BAO) measurements [60, 75], the energy content of the present-day Universe in the form of dark energy, total (non-relativistic) matter, and baryonic matter can be accurately determined. Considering the cold DM paradigm in the standard ΛCDM cosmology model, the average density of DM and baryons in the Universe obtained from the *Planck* collaboration analysis of the CMB observations is [76]

$$\Omega_{\mathrm{DM}} h^2 = 0.11933 \pm 0.00091, \tag{2.1}$$

$$\Omega_{\mathrm{b}} h^2 = 0.02242 \pm 0.00014, \tag{2.2}$$

where $\Omega_i = \rho_i / \rho_{c,0}$ is the present-time fraction of the energy density divided by the critical density of the Universe, defined as $\rho_{c,0} = 3H_0^2/8\pi G$. The reduced Hubble parameter $h = 0.6766 \pm 0.0042$ corresponds to $H_0 = 100\,h\,\mathrm{km/s/Mpc}$, which represents the present-day expansion rate of the Universe.

2.2.2 Large-Scale Structures

The large-scale structure epoch of the Universe represents the phase where primordial density fluctuations grow under the influence of gravity, leading to the formation of galaxies, clusters, and cosmic filaments. Modelling of large-scale structure formation with non-interacting DM matches with the observation of the matter distribution very well down to the scale of the inner regions of galaxy halos. The evolution of cosmic structures is supported by cosmological simulations of structure formation [78, 79] and in order to form structures as small as galaxies and dwarf galaxies, DM must be sufficiently cold, which means non-relativistic, at the time of structure formation.

However, there are a number of small-scale challenges of the cold DM paradigm such as the cusp–core problem, the missing satellite problem and the too-big-to-fail problem. A component of DM could be classified as warm to potentially address some of these challenges on small scales, although there are some strong limits on warm DM models [80]. DM can also have some amount of self-scattering to address the aforementioned small-scale structure anomalies. Self-interaction [81] of order $\sigma/m \sim 1\ \mathrm{cm}^2/\mathrm{g}$ on the scale of galaxies can significantly heat the DM in the halo,

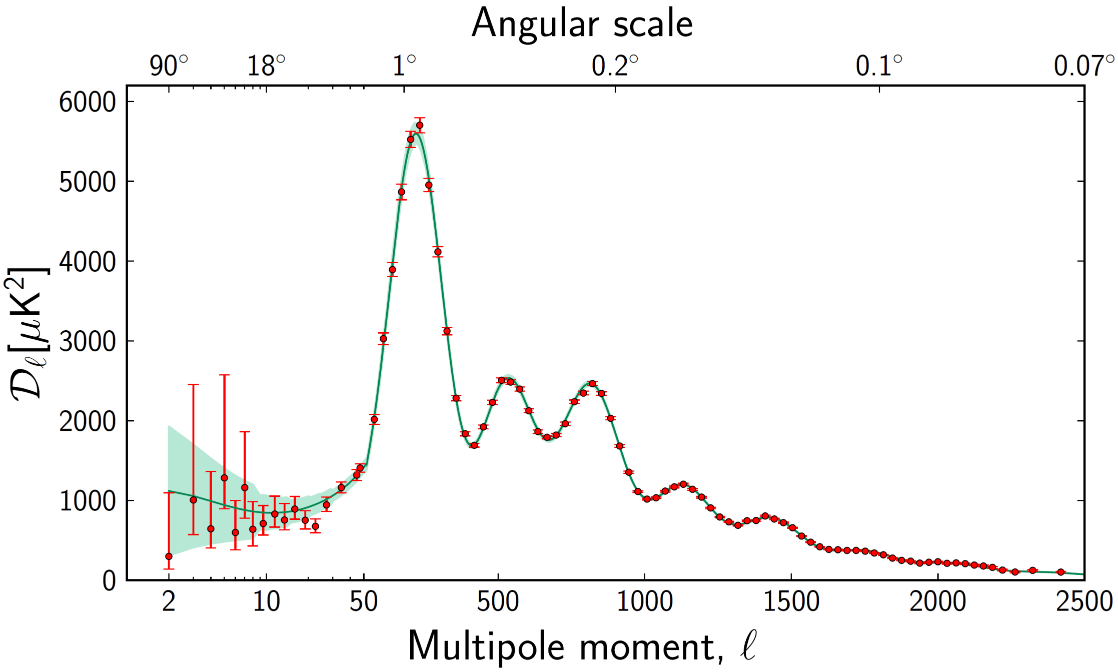

Figure 2.1: A plot showing the pattern of CMB temperature fluctuations from Planck Collaboration [77] and the best fit of the ΛCDM cosmological model. The vertical axis is the angular power spectrum. The relative height of the 2nd and 3rd peaks provides information about DM and baryon contributions [69] to the matter density. Copyright Ade et al., Astronomy & Astrophysics, vol 571, pages 48, 2014, reproduced with permission © ESO.

thus suppressing sub-halo structures and affecting the central density of galaxies.

2.2.3 Galactic Scale

Another widely accepted observational piece of evidence for the presence of DM, which is historically important, comes from the measurements of rotation curves for a large number of galaxies [61, 82, 83]. The rotation velocity of stars concentrated in a disk around the center of galaxies can be measured using the Doppler shift of light from baryonic matter. Observations of 21 cm atomic hydrogen lines show that the rotation curve flattens out at large distances r from the galactic center, instead of falling off as $r^{-1/2}$ as predicted by Newtonian gravity.

The unexpected flattening in the galactic rotation curves, which occurs well beyond the visible matter distribution, allows us to infer that the mass distribution of DM in galaxies is described by a nearly spherically symmetric halo around the galactic center. The DM halo dominates the total mass of most galaxies and provides a

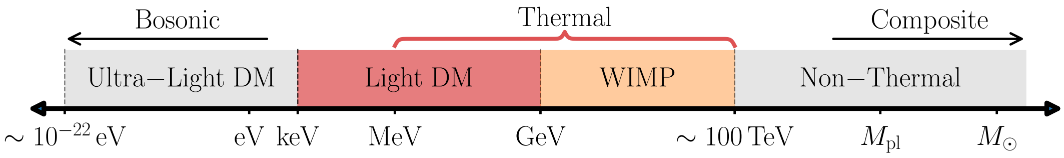

Figure 2.2: A sketch adapted from [90], showing the mass scale of possible DM candidates spanning 80 orders of magnitude. This plot is not to scale.

potential to stabilize the spiral galaxy disks [84]. Unlike baryons, DM does not have strong non-gravitational self-interactions and does not lose energy through dissipative forms. Numerical cosmological simulations (with collision-less DM) confirm the common picture of large spherically symmetric DM halos surrounding galaxies [85]. The numerical simulations also suggest a universal radial density profile, often referred to as the Navarro-Frenk-White (NFW) profile [86].

Combining X-ray observations of hot gas emissions and weak gravitational lensing in the analysis of colliding galaxy clusters provides further evidence for the existence of DM. A striking example that is often cited to illustrate this phenomenon is the merging Bullet Cluster [87]. X-ray observations show that the visible gas slows down and merges in cluster collisions due to interactions, while gravitational lensing shows that most of the mass distribution remains within each halo and is separated from the baryonic gas. Often from these observations, DM is inferred to be weakly self-interacting.

2.2.4 Candidates

The preceding discussion has focused on the cosmological and astrophysical evidence for DM, primarily based on large-scale observations. Our current understanding of DM relies primarily on macroscopic observations because no DM particles have yet been identified by any experiments (see Section 2.4). Nevertheless, these observations provide preliminary indications about the essential particle properties of DM (for a recent review, see *e.g.* [88, 89]). Any successful DM candidate must have general properties consistent with these observations from cosmic to galactic scales, which suggest that the DM must consist of stable non-baryonic matter, nearly cold (non-relativistic), non-luminous in galaxies or clusters, have weak non-gravitational interactions, and the correct relic density of $\Omega h^2 \simeq 0.12$.

However, even though we know very well the overall properties of DM on large scales, due to the gravitational essence of these observations, little is known about the particle nature of DM. In particular, the mass of the constituents of DM is essentially unconstrained over many orders of magnitude, while still being consistent with these observations. Furthermore, the composition of DM around us remains unclear, as it is yet to be determined whether it exists as elementary particles or as heavy composite objects *e.g.* primordial black holes [91]. The DM microscopic properties are consistent with a plethora of theoretical models [88]. As depicted in Fig. 2.2, a diverse range of viable DM models is evident, spanning an extensive mass spectrum from 10^{-22} eV up to the Planck mass $M_{\rm pl}$.

One way to classify DM candidates is based on spin. Candidates with mass below $\sim$ keV are often referred to as ultralight bosonic DM, which behaves as a coherent field and can form condensates. The lower bound is obtained by comparing the de Broglie wavelength of the DM with the size of the galactic halo. Possible models in this category include QCD axions [92], axion-like particles, and fuzzy DM [93, 94]. On the other hand, we have fermionic DM, where the lower bound $\sim$ keV is associated with the fact that accretion in a dwarf galaxy halo is bounded by the Pauli exclusion principle.

Thermal DM candidates within the $\text{MeV} - 100\ \text{TeV}$ mass window are among the most frequently explored models of DM, which can be produced through thermal processes within standard cosmology that are deemed plausible (see Section 2.3 for more details). Weakly Interacting Massive Particle (WIMP) is a simple and well-motivated thermal DM candidate living at the weak scale and linked to the electroweak sector that can thermally produce the observed DM relic abundance. The null results from direct detection experiments, as well as the decades of null results from indirect detection and collider searches, have cast doubt on the WIMP paradigm and motivated the pursuit of numerous alternative possibilities. Light DM with a sub-GeV mass is a theoretically well-motivated class of alternative thermal models motivated by the dark sector paradigm (see Section 2.5).

2.3 Particle DM Production Mechanisms

From the perspective of production mechanisms in the early universe, DM can be classified into two categories: thermal and non-thermal candidates [95]. The interaction strength of the DM particles with the visible sector determines whether they achieved thermal equilibrium with the thermal bath in the early universe.

2.3.1 Thermal Freeze-Out

In a thermal production scenario, DM particles are assumed to be in thermal and chemical equilibrium, annihilating as the Universe expands with scale factor $a(t)$ until the temperature of the thermal bath $T \propto a^{-1}$ drops below the DM mass $T \lesssim m_\chi$, so that their number density becomes Boltzmann suppressed, dropping exponentially as $e^{-m_\chi/T}$. This continues until the DM number density is diluted by the expansion of the Universe to the point that the number-changing processes through annihilation are no longer effective enough to maintain equilibrium and the DM number density asymptotically approaches a constant in comoving volume a^3. This process is referred to as *freeze-out*. Lighter DM particles take longer to become non-relativistic, impacting structure formation. Thermal DM candidates can be as light as $\sim$ MeV while remaining compatible with existing cosmological and astrophysical observations (and satisfying the warm DM bounds [96]), with the upper bound restricted by the unitarity bound on scattering amplitudes [97].

Let us briefly summarize the standard picture of the freeze-out mechanism and perform a back-of-the-envelope estimate for the predicted DM relic abundance. This is described quantitatively by the Boltzmann equation

$$\frac{dn_\chi}{dt} + 3Hn_\chi = -\langle \sigma_A v \rangle \left(n_\chi^2 - n_{\rm eq}^2 \right) \tag{2.3}$$

where n_χ is the DM number density, H is the Hubble parameter representing the expansion rate of the Universe, $\langle \sigma_A v \rangle$ is the thermally averaged annihilation cross-section times the relative velocity between two DM particles, and $n_{\rm eq}$ is the DM number density in thermal equilibrium, *e.g.* when $T \ll m_\chi$

$$n_{\rm eq} = g_\chi \left(\frac{m_\chi T}{2\pi} \right)^{3/2} e^{-m_\chi/T}, \tag{2.4}$$

where g_χ counts the number of internal degrees of freedom for DM particle χ. Freeze-out occurs when the interactions of the DM become slower compared to the expansion rate, a condition approximately given by $\Gamma_{\chi\bar{\chi}\to SM} \equiv n_\chi \langle \sigma_A v \rangle_{fo} = H(T_{fo})$. Solving the Boltzmann equation [98], the relic abundance of DM particles χ is determined by its thermally averaged annihilation cross section at the time of freeze-out

$$\Omega_\chi h^2 \equiv \frac{m_\chi n_{0,\chi}}{\rho_{c,0}} \approx 0.12 \times \frac{2 \times 10^{-26} \mathrm{cm}^3/s}{\langle \sigma_A v \rangle_{fo}}, \tag{2.5}$$

where Ω_χ is the present fraction of the energy density of the Universe made up of particle χ divided by the critical density of the Universe, defined as $\rho_{c,0} = 3H_0^2/8\pi G$, and the subscript 0 denotes the present-time values. From Eq. (2.5), it can be observed that the thermal relic density is inversely proportional to the thermally-averaged annihilation cross-section. A viable thermal candidate requires a minimum annihilation cross section of $\langle \sigma_A v \rangle_{fo} \sim 10^{-9}\,\mathrm{GeV}^{-2} \sim 1\,\mathrm{pb}$ to avoid DM overabundance, which is indeed the size of a weak scale cross-section. This is obtained by matching the predicted DM relic density in Eq. (2.5) to the observed relic abundance (2.1) and assuming that particle χ exclusively constitutes all the DM in the universe.

One of the simplest and most effective scenarios for the formulation of DM models is commonly known as the *Weakly Interacting Massive Particle* (WIMP) with a mass range from several GeV to several TeV and typical cross-sections consistent with the weak interactions. To explore this possibility, we can parametrize the thermally-averaged annihilation cross section from dimensional analysis by

$$\langle \sigma_A v \rangle = \frac{\alpha_\chi^2}{m_\chi^2} \times \left(a + b\, v^2 + \mathcal{O}(v^4)\right) \approx \left(\frac{\alpha_\chi}{\alpha_w}\right)^2 \left(\frac{1\,\mathrm{TeV}}{m_\chi}\right)^2 \frac{1}{10^9\,\mathrm{GeV}^2} \tag{2.6}$$

where $\alpha_\chi \equiv g_\chi^2/4\pi$, g_χ is the DM coupling to the visible sector and m_χ is assumed to be the only scale that determines the cross section for annihilation in the non-relativistic limit. The model-dependent factors a and b correspond to s- and p-wave annihilation, respectively. One observes that the weak-scale DM candidate confined to have interaction with visible matter only through the weak forces (EW gauge bosons or Higgs) with $\alpha_w \approx 0.03$ is a viable thermal relic, often referred to as a WIMP *miracle*. In this case, TeV-scale DM candidates are favored by relic density considerations. Although freeze-out provides a lower bound on the non-gravitational interaction rates with SM, it implies that the annihilation (scattering) to (with) ordinary matter must be efficient, which suggests strategies for detecting DM.

2.3.2 Thermal Freeze-In

Freeze-in DM [99, 100], as a non-thermal candidate, is among the alternative mechanisms proposed for producing the observed DM abundance. If the coupling to the visible sector is small enough, $\lesssim \mathcal{O}(10^{-7})$, DM was never in thermal equilibrium in the early universe. In this case, the DM abundance is slowly generated by rare (feeble) interactions within the SM thermal bath, such as the decay of heavy SM particles or $2 \to 2$ annihilation-type processes. This continues until the number densities of SM particles producing DM become Boltzmann-suppressed, ending the yield.

2.3.3 Other production mechanisms

Here we briefly name a list of alternative methods for producing the correct relic abundance of DM that go beyond the traditional thermal freeze-out scenario. Revising the underlying assumptions of thermal production, there are a variety of other recently proposed novel quasi-thermal DM production mechanisms such as Asymmetric DM models [101], co-annihilation[102], co-scattering [103], Self Interacting Massive Particles (SIMPs) [104], cannibal DM [105], and ELDER [106]. DM can also be produced via non-thermal mechanisms, for example through gravitational interactions in the early Universe or in the out-of-equilibrium decay of heavy particles.

2.4 Current Status of DM Searches

Thus far, all the searches to observe dark matter non-gravitationally using different approaches including direct and indirect detection and collider searches were not successful to capture any sign of the particle nature of DM [1, 107, 108]. Nevertheless, the particle searches have put impressive limits on the parameter space of WIMPs [108, 107].

2.4.1 Direct Detection

The landscape of existing exclusion limits from spin-independent direct detection is shown in Fig. 2.3, which are deep underground experiments searching for deposited recoil energy from scattering interactions between halo DM passing through matter in highly sensitive, low background detectors. The typical recoil energy for elastic scattering nuclei is given by $E_{\text{recoil}} = 2\mu_{\chi,N}^2 v_\chi^2/m_N$ [90], where $v \sim 200\,\text{km/s}$ is the local DM speed, and $\mu_{\chi,N}$ is the DM-nucleon reduced mass. As illustrated in Fig. 2.3, the sensitivity of direct detection to WIMP-nucleon interactions drops dramatically for DM masses $m_\chi \lesssim$ a few GeV due to the energy thresholds in the experiments. At high m_χ, the sensitivity weakens as the number density of the ambient DM inversely scales with DM mass. There are also new avenues in direct detection proposed to push the low-threshold experiments [24, 109, 110, 111] providing the possibility to probe a variety of light MeV to GeV-scale DM benchmark models. The sensitivities from DM-electron and DM-nuclear scattering direct detection experiments are complementary.

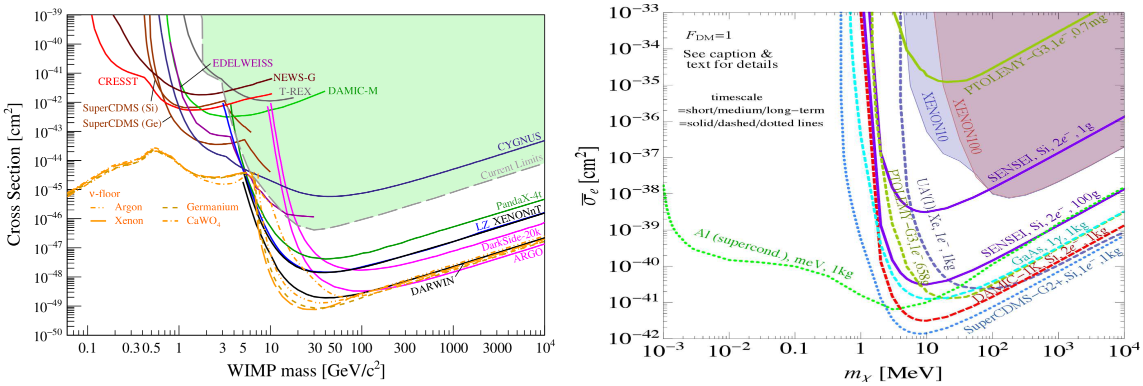

Figure 2.3: The experimental parameter space of WIMP from Ref. [2, 24], showing the existing constraints (shaded regions) and projections (colored lines) for spin-independent (**Left**) DM-nucleon and (**Right**) DM-electron elastic scattering cross section. The projected sensitivities to WIMP-nucleon scattering have improved even further recently by the result from LZ experiment [112]. The left plot is reprinted by permission from Julien Billard et al., Direct detection of dark matter-APPEC committee report, Rep. Prog. Phys. Vol. 85, Num. 056201, p. 34, DOI 10.1088/1361-6633/ac5754 ©IOP Publishing. Reproduced with permission. All rights reserved.

2.4.2 Indirect Searches

Indirect detection methods utilize astronomical techniques to search for indirect signals of DM-SM interactions through the annihilation or decay of DM particles at various locations within the local galaxy and beyond. This serves as a complementary approach to direct detection searches for DM with a focus on the ambient DM density near the Earth's surface. The annihilation rate scales with the square of local DM number density [113], n_χ^2, thus we are particularly interested in regions of very high DM density such as the galactic center of the Milky Way or dwarf spheroidal galaxies as DM-dominated objects in the Universe. However, the analysis of data from these locations is challenging due to the higher rate of backgrounds from the activity of baryon concentration.

Indirect detection experiments aim to detect the byproducts of the annihilation or decay of the ambient DM particles into SM states, with a particular focus on high-energy photons. Satellite telescopes and ground-based experiments have the capability to trace back the flux of gamma rays to their sources of DM. This is possible because gamma rays with energy below a few TeV can propagate through the universe with minimal interruption. Direct annihilation of (non-relativistic) DM into a pair of photons $\chi\chi \to \gamma\gamma$, produces a nearly monochromatic signal with an energy line at $E_\gamma = m_\chi$. However, for more complex annihilation scenarios, the photon energy spectrum can be significantly broader and exhibit characteristic features, such as bumps or cutoffs, depending on the masses and decay channels of the intermediate SM particles. The search for these gamma-ray signals has been carried out using satellite telescopes like Fermi Large Area Telescope [114, 115, 116] and ground-based gamma-ray instruments such as HESS [117, 118], and MAGIC [119, 120] to detect the elusive signatures of DM annihilation or decay within the night sky.

In addition to high-energy photons, the annihilation or decay of DM into stable charged particles and neutrinos is of great interest in indirect detection studies [121, 122, 123]. The cosmic-ray spectrum consists mainly of particles rather than antiparticles across all energy ranges. The observation of any excess in the relative fluxes of particle and antiparticle may be interpreted as a DM annihilation signal since equal amounts of matter and antimatter would be produced through annihilation. Cosmic rays in the form of high energy protons, antiprotons, electrons, and positrons can be detected using satellite experiments such as PAMELA [124] and AMS-II [125, 126], while large scale neutrino telescopes on Earth like IceCube [127] and ANTARES [128] are capable of searching for high-energy neutrinos from DM annihilation in local galaxy halo [129] or captured and accumulated by the Sun [130].

Energy injection of DM particles through annihilation or decay can lead to additional ionization of hydrogen atoms during recombination, affecting the CMB temperature fluctuations, and can be used to place indirect constraints on the DM candidates with a velocity-independent (*i.e.* s-wave) annihilation cross-section [131, 132, 133]. Recent constraints from the Planck Collaboration [76] provide robust limits on annihilating DM, particularly for masses below 10 GeV, with electron and photon channels being the most sensitive due to their significant influence on heating and ionizing the intergalactic medium.

2.4.3 Accelerator Searches

If DM has some coupling to the SM sector it can directly be produced in high-energy collisions at colliders. However, being weakly interacting and having a long cosmological lifetime, DM candidates are invisible and would likely escape detection within the collider detectors, resulting in a missing (transverse) energy signature. In this case, the presence of a single hard mono-X recoiling against the invisible DM particles serves as a powerful collider signature in DM searches [135]. This technique has been specifically developed to enhance the sensitivity of collider experiments to

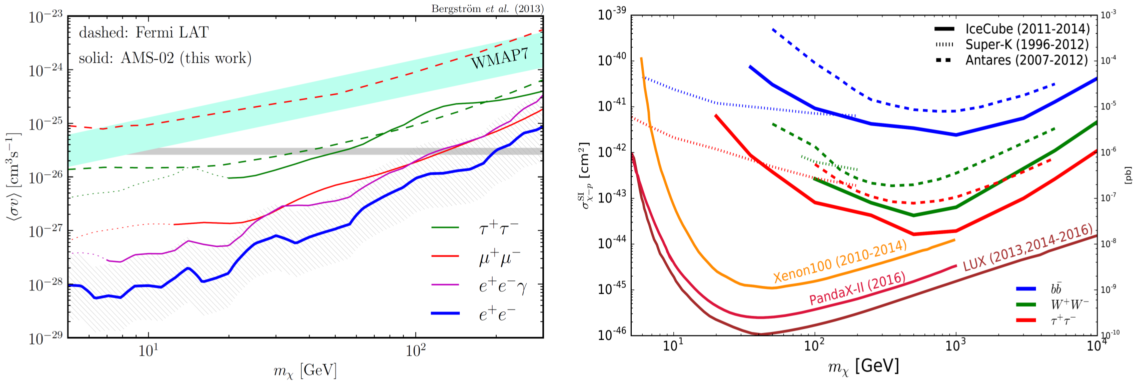

Figure 2.4: **Left:** A plot showing the limits on the annihilation cross section for the DM particles annihilating into various leptonic final states. These upper limits are obtained from the AMS-02 positron fraction measurement. The current strongest limit for the case of DM annihilating to $b\bar{b}$, which is not included in the presented plot, comes from a combined analysis of both Fermi-LAT and MAGIC collaborations [120]. Reprinted figure with permission from Bergstrom et. al., Phys. Rev. Lett., Vol. 111, pages 171101, 2013. © 2013 by the American Physical Society [134]. **Right:** Constraints on the (spin-independent) DM-nucleon cross-section, obtained from observation of the annihilation processes in the Sun and probed by neutrino telescopes, are compared to limits from direct detection experiments. From Ref. [130].

DM signals by simplifying the task of discriminating them from the SM background. The choice of X can vary and includes options such as jets, photons, or even the W/Z boson. Collider experiments, including the CMS [136, 137, 138] and ATLAS [139, 140, 141] experiments at the Large Hadron Collider (LHC), have conducted extensive searches utilizing the missing transverse energy techniques. Collider searches provide complementary sensitivities to direct and indirect detection bounds, especially in low-mass regions [142], where the comparisons are typically presented in the framework of effective field theories [143, 144, 145, 146, 147] and simplified models [148]. It is crucial to emphasize that the observation of missing energy in a collider search does not automatically imply that it is related to the elusive DM. Unlike direct detection methods, the stable particle that escaped detection within the collider apparatus is not necessarily a cosmic relic. Hence, collider signatures can only be considered as a potential DM discovery and additional evidence from direct or indirect detection methods is necessary.

Next, we turn to another important class of DM searches at beam dump experiments and fixed target facilities. DM can be probed experimentally through production generated by high-intensity proton/electron beams directed on fixed targets. The primary goal of the fixed target neutrino experiments is to produce large numbers of neutrinos in order to study neutrino physics. One expects copious numbers of hypothetical hidden mediators and DM particles to be produced alongside the neutrinos. These weakly interacting particles could be detected in the detector located tens to hundreds of meters away from the fixed target. Already existing or past fixed target experiments can provide low-cost direct detection signatures of light-dark states, which can impose strong constraints on the parameter space of different hidden sector scenarios [26, 27, 28, 149]. See Section 2.8 for further discussion of searching for the hidden sectors at fixed target experiments.

2.5 Motivation for Dark Sector DM

Over the past decades, there has been growing interest in sub-GeV DM, since the small mass provides a natural explanation for the null results of direct detection experiments, as depicted in Fig. 2.5 (see [24] for a review). For example, sub-GeV DM with feeble interaction can still have the correct relic abundance, an alternative thermal scenario known as the WIMPless miracle [150]. However, for lighter DM below the weak scale, both the mediator mass m_{med} and m_χ control the annihilation cross-section and enter the parametrization as

$$\langle \sigma_A v \rangle = \frac{\alpha_\chi \alpha_f m_\chi^2}{m_{\text{med}}^4} \approx \left(\frac{\alpha_\chi \alpha_f}{\alpha_w^2}\right) \left(\frac{m_\chi}{1\,\text{GeV}}\right)^2 \left(\frac{100\,\text{GeV}}{m_{\text{med}}}\right)^4 \frac{1}{10^9\,\text{GeV}^2}, \tag{2.7}$$

where α_χ and α_f indicate the mediator's coupling to the DM and SM fermions, respectively. If the *direct* annihilation cross-section of low mass DM into SM states is through weak interactions (with $m_{\text{med}} \approx 100\,\text{GeV}$), the thermal relic cross-section would be too small when $m_\chi <$ GeV to generate a consistent DM energy density in the early universe in comparison with what is observed. This leads to an overabundance of sub- GeV DM, commonly known as the Lee-Weinberg bound [3]. Therefore, a viable thermal relic density for a sub- GeV WIMP requires new annihilation channels through light states [4, 5].

A *hidden* (or *dark*) *sector* can be defined to be a collection of particles that do not interact directly with SM forces, or in other words, are uncharged under the SM gauge groups. In a minimal dark sector model, we could have a DM particle and a dark force mediator that couples weakly to the SM, and these two states can be populated during the early universe through thermal mechanisms such as freeze-in or freeze-out. However, the thermal history of dark states may differ from that of

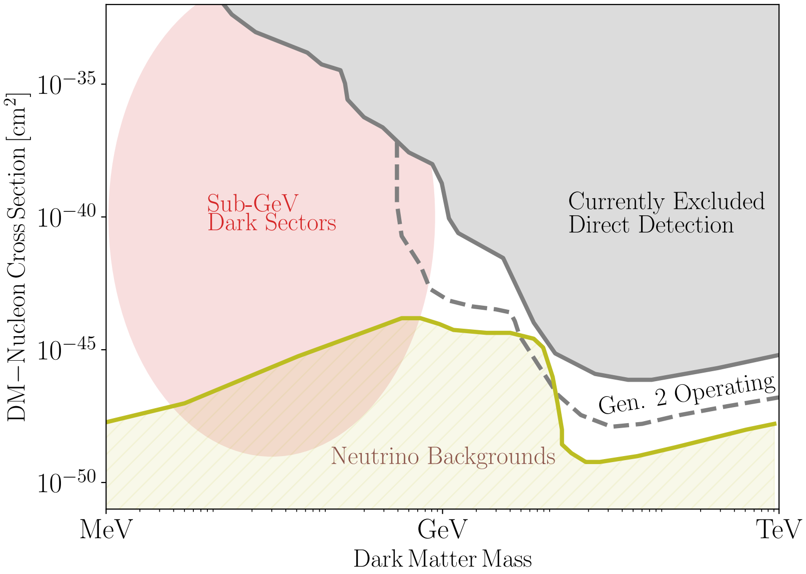

Figure 2.5: A schematic plot illustrating an unexplored region of Spin-independent DM-nucleon scattering cross-section space for scattering with nucleons. For sub- GeV DM, the direct detection sensitivity drops due to recoil thresholds.

the SM particles. Depending on the DM-dark mediator mass hierarchy, we can have *secluded* sector states [5, 151] that have their own separate thermal plasma with colder temperature $T_d \lesssim T_\gamma$, decoupled from the SM thermal bath. This secluded scenario is viable if $m_\chi > m_{\text{med}}$ and DM candidates χ annihilate to a lighter mediator state with cross-section scaling as $\langle \sigma_A v \rangle \sim \frac{\alpha_\chi^2}{m_\chi^2}$ during freeze-out but there is little or no annihilation to the visible sector.

A question arises here: how light can these additional dark states be from a cosmological perspective? Notably, an important cosmological scale exists around $\sim$ MeV. DM relics below this scale that are in thermal contact with the SM bath, are relativistic during BBN, when the temperature of the expanding Universe was around a few MeV. Sub- MeV thermal relics are subject to stringent constraints from BBN [152, 153, 154, 155, 156], as they can disrupt the light element abundances formed during BBN, and in particular alter the well-measured quantity $N_{\text{eff}} \approx 3$ [157, 76], the effective number of relativistic degrees of freedom. Preserving the success of BBN is crucial, given our confidence in understanding baryonic physics during this epoch. Therefore, DM candidates lighter than an MeV should have undergone thermal decoupling from the SM thermal bath well before the start of BBN.

Dark sectors are also motivated by many experimental puzzling results that could well be explained by introducing new hidden force carriers. There exist several anomalies in particle and astroparticle physics, that can be addressed by considering new force carriers, which couple to ordinary matter. Among these problems, the discrepancy between the calculated and measured anomalous magnetic moment of the muon is a long-lasting tension. The SM prediction of $g_\mu-2$ is 4.2σ away from the experimental results [158]. There are various dark sector model contributions to muon $g-2$ (*e.g.* [6, 159]). Astrophysical observations of the positron excess in cosmic rays by PAMELA [124, 160, 121] and then AMS II [134, 161] motivated analysis as a potential hint of enhanced dark matter annihilation mediated by light force carriers. As another anomalous observation, the Experiment to Detect the Global Epoch of Reionization Signature (EDGES) collaboration reported the anomalous 21 cm hydrogen absorption signal [162]. A fraction of DM with tiny electromagnetic interaction is a proposal to explain the EDGES anomaly [163, 54, 164].

The other empirical evidence for physics beyond the SM is the neutrino oscillations between different flavors [165, 166, 167]. This phenomenon arises from mixing between the flavor and mass eigenstates of neutrinos, which is absent in the SM. The mass matrix of the neutrino sector can be generated via the common *seesaw* mechanism by introducing one or more sterile neutrinos [168]. An eV-scale sterile neutrino [169] has been proposed as an explanation for the observed short-baseline oscillation anomalies in experiments such as MiniBooNE [170] and LSND [171]. To ensure cosmological viability, these sterile neutrinos could potentially belong to a hidden sector that is charged under a new light force carrier [172].

There are also a few fine-tuning puzzles in particle physics that motivate new physics beyond the SM. For example, the SM suffers from the hierarchy problem [173]; the mass of the SM Higgs gets a large quantum correction (due to the presence of virtual particles in the loop) which is much larger than the actual mass of the Higgs experimentally observed. This leads to a fine-tuning of the bare Higgs to cancel the quantum corrections.

2.6 The Standard Model of Particle Physics

Before delving into the discussion of the hidden sector models, it is important to review the Standard Model of particle physics. By understanding the fundamental particles and their interactions within the SM framework, we can lay the groundwork for exploring the connections between the visible and hidden sectors.

The SM is a relativistic gauge theory of quantum fields [174] which is invariant under the local symmetry group $SU(3)_c \otimes SU(2)_L \otimes U(1)_Y$, where the indices c, L, Y refer to the quantum numbers color, weak isospin and hypercharge, respectively. The gauge group $SU(3)_c$ corresponds to the strong interaction with associated gluonic gauge fields G^a_μ ($a = 1, \cdots, 8$) coupled to the color charges described by the Quantum Chromo Dynamics (QCD). The combination of the $SU(2)_L \otimes U(1)_Y$ produces the electroweak symmetry group with the associated weak W^i_μ ($i = 1, 2, 3$) and hypercharge B_μ gauge fields. The electroweak theory unifies electromagnetic and weak interaction.

The matter content of the SM is composed of spin-$\frac{1}{2}$ fields, which come in three identical copies called *generations*. These generations of fermions are *chiral*: left-handed and right-handed fields are assigned different isospin charges in agreement with observed parity violation in the weak interactions. Moreover, fermions neutral under $SU(3)_c$ transformations are called *leptons*, while *quarks* are color triplets. In the Standard Model, each generation of left-handed leptons and quarks pair up in $SU(2)$ doublets: the lepton doublet L consists of the left-handed neutrino ν_L and the left-handed charged lepton e_L, while the quark doublet Q contains the left-handed up-type quark u_L and the left-handed down-type quark d_L. On the other hand, the right-handed fermions u_R, d_R, and e_R are singlets under the weak interaction.

The SM Lagrangian has three components; gauge group structure, vacuum structure and matter content which can be summarized in the form

$$\mathcal{L} = \mathcal{L}_{\text{gauge}} + \mathcal{L}_{\text{Higgs}} + \mathcal{L}_{\text{Yukawa}} \tag{2.8}$$

The gauge term includes kinetic terms for the vector-boson fields, their self-interactions, and fermion-gauge boson couplings following gauge invariance

$$\begin{aligned}\mathcal{L}_{\text{gauge}} = -\frac{1}{4}(G^a_{\mu\nu})^2 - \frac{1}{4}(W^i_{\mu\nu})^2 - \frac{1}{4}(B_{\mu\nu})^2 \\ + \sum \overline{f} i\gamma^\mu D_\mu f,\end{aligned} \tag{2.9}$$

where $G^a_{\mu\nu} = \partial_\mu G^a_\nu - \partial_\nu G^a_\mu + g_s f^{abc} G^b_\mu G^c_\nu$ is the gluon field strength with f^{abc} the structure constants of $SU(3)_c$, and the sum in the last piece runs over the left- and right-handed field components of the leptons and quarks. Depending on the fermion species, each covariant derivative takes the form

$$D_\mu = \partial_\mu + ig_s T^a_c G^a_\mu + igT^i_L W^i_\mu + ig'YB_\mu, \tag{2.10}$$

where g and g' are the $SU(2)_L$ and $U(1)_Y$ gauge couplings, T_c^a and T_L^i denote the gauge group generators associated with the $SU(3)_c$ and $SU(2)_L$, respectively, and *hyphercharge* Y is the charge of the field under $U(1)_Y$ and is connected with the electric charge Q and the isospin T_L^3 by the relation $Y = (Q - T_L^3)$.

The Higgs Lagrangian contains the Higgs-gauge boson interactions and the potential of the Higgs self-interactions as

$$\mathcal{L}_{\text{Higgs}} = |D_\mu H|^2 - V(|H|^2), \tag{2.11}$$

where H is the Higgs complex isodoublet, and the Higgs potential $V(|H|^2) = -\mu^2|H|^2 + \lambda/2|H|^4$ with constant parameters $\mu^2, \lambda > 0$ determines the vacuum structure of the SM Lagrangian. The Higgs potential in (2.11) leads to spontaneous symmetry breaking which has important consequences. After symmetry breaking, the Higgs doublet gets a vacuum expectation value and may be expanded as $\langle H \rangle = (0\,,\, v + h/\sqrt{2})$, where $v = \sqrt{\mu^2/\lambda}$, and the real scaler field h is the excitation around the minimum of the potential and is called the Higgs boson.

Finally, the last term in the SM Lagrangian corresponds to the Higgs-fermion Yukawa couplings invariant under $SU(2)_L$

$$\mathcal{L}_{\text{Yukawa}} = \sum y_f^d \bar{f}_L^d H f_R^d + y_f^u \bar{f}_L^u \tilde{H} f_R^u + \text{h.c.}, \tag{2.12}$$

where we define $\tilde{H} \equiv i\sigma^2 H$ that couples to the up-type fermions. Inserting the vacuum expectation value for H into the expressions in (2.12), produces the Dirac mass terms $m_f = y_f v$ for the fermions.

Expanding the Higgs kinetic term around the minimum, expressions with the structure of mass matrix for gauge bosons appear, where the physical gauge bosons consist of the charged electroweak $W_\mu^\pm$ and the neutral Z_μ^0 bosons and the massless photon A_μ. These states can be identified with a linear combination $W_\mu^\pm = (W_\mu^1 \mp iW_\mu^2)/\sqrt{2}$, while the B_μ field and the neutral component of the W_μ^3 triplet field mix

$$\begin{pmatrix} Z_\mu \\ A_\mu \end{pmatrix} = \begin{pmatrix} \cos\theta_W & -\sin\theta_W \\ \sin\theta_W & \cos\theta_W \end{pmatrix} \begin{pmatrix} W_\mu^3 \\ B_\mu \end{pmatrix} \tag{2.13}$$

to form A_μ and Z_μ, where θ_W denotes the weak mixing angle defined by $\cos\theta_W = g/\sqrt{g^2 + g'^2}$.

The interaction of leptons and quarks with the mediating gauge bosons is obtained from (2.9). Using terms for W_μ^3 and B_μ from Eq. (2.13) and relation $Y = Q - T_L^3$, the weak charged current (CC), weak neutral current (NC), and electromagnetic neutral current are read as

$$\mathcal{L}_{\text{int}} = \frac{g}{\sqrt{2}}\big(W_\mu^+ J_\mu^- + W_\mu^- J_\mu^+\big) + \frac{g}{\cos\theta_W} Z^\mu \big(J_\mu^3 - \sin^2\theta_W J_\mu^{\text{EM}}\big) + g\sin\theta_W A^\mu J_\mu^{\text{EM}}, \quad (2.14)$$

where the electromagnetic coupling $e \equiv g\sin\theta_W$, and the Z_μ gauge boson couples to linear combinations of the $J_\mu^3 = \sum_f \bar{\psi}_f \gamma_\mu T_L^3 \psi_f$ (with T_L^3 acting only on left-handed fermions) and the electromagnetic current $J_\mu^{\text{EM}} = \sum_f Q_f \bar{\psi}_f \gamma_\mu \psi_f$.

2.7 Benchmark Models of Hidden Sector Portals

Models of a dark sector with diverse structures including feebly-interacting particles could exist theoretically, which may interact with SM matter through a number of *portals* respecting the symmetries of the SM. These portals can mediate non-gravitational interactions between DM and ordinary matter. Under the SM symmetries, many generic SM-neutral gauge-invariant interactions are allowed that couple the two sectors which are given as follows,

$$\mathcal{L}_{\text{mediation}} \sim \frac{\mathcal{O}_{\text{NP}}^{(l)} \mathcal{O}_{\text{SM}}^{(k)}}{\Lambda^n}, \quad (2.15)$$

where $\mathcal{O}$ denotes operators of dimensions k and l for SM and New Physics (NP) fields respectively, and Λ defines any arbitrary cut-off scale at a TeV or above. Also, $\mathcal{O}_{\text{NP}}$ must be gauge invariant under the SM gauge group. We limit our discussion here to the operators in the Lagrangian Eq. (2.15) of dimension up to 5, $k + l \leq 5$.

The dark sector framework relies on minimal assumptions, but effective field theory provides a simplifying perspective that helps to classify the portal interactions according to their dimensionality. Most of these interactions are irrelevant, but only a few are UV-complete with dimension ≤ 4. The relevant and marginal $n \leq 0$ interactions are of special importance and will be the focus of attention here. The Higgs, vector and neutrino portals, therefore, comprise a priori the leading couplings of the SM to a dark or hidden sector, given the presence of the associated vector (A'_μ), scalar (S), or singlet fermion (N) mediators. These lowest-dimensional operators that can couple the two sectors can be classified into the following types:

$$\mathcal{L}_{\rm mediation} \supset \begin{cases} \frac{\epsilon}{2\cos\theta_w} F'_{\mu\nu} B^{\mu\nu} & \text{Vector portal,} \\ (AS + \lambda S^2) H^\dagger H & \text{Higgs portal,} \\ y_N \bar{L} H\, N & \text{Neutrino portal,} \end{cases} \tag{2.16}$$

where $F'_{\mu\nu} = \partial_\mu A'_\nu - \partial_\nu A'_\mu$ is the field strength for the $U(1)$ vector mediator, which couples to the hypercharge field strength, $B^{\mu\nu}$, and H and L are the Higgs and lepton doublets respectively. The neutrino portal of course provides the simplest model of Majorana neutrino mass. Dirac masses are induced through the Yukawa interaction between the left-handed lepton doublet and the Higgs field after it acquires a vacuum expectation value. In fact, this coupling, along with the presence of Majorana mass terms for the right-handed state, results in the generation of small masses for the active neutrinos. Note that these are the only three relevant or marginal portal operators that are unsuppressed by a new (potentially high) energy scale.

2.7.1 Dark Photon

Significant theoretical and experimental effort has been invested in studying these portal interactions in Eq. (2.16), motivated in part by their importance for the phenomenology of light DM models [23, 24, 25]. In particular, much effort over the past decade has focused on the vector portal, which at low energies involves kinetic mixing between the photon and the dark vector (photon), $\epsilon F^{\mu\nu} F'_{\mu\nu}$, where the kinetic mixing parameter ϵ, can generically be very small [5]. The importance of the vector portal is in part because it is the least constrained scenario that allows for bi-linear mixing. It also provides the most scope for model building, including what has become the benchmark model for sub-GeV dark matter [23, 24]. It is also worth noting that the dark vector itself can remain cosmologically stable and be a viable DM candidate, provided that it is sufficiently light with mass below the di-electron threshold, preventing its decay into the visible sector. The dark photon DM relic abundance can be obtained, *e.g.* from cosmological initial conditions [175, 176, 177]

Depending on the energy of the processes considered, it is possible to embed the kinetic mixing into the Lagrangian by only mixing with the photon field. The more general kinetic mixing with the hypercharge associated with the $U(1)_Y$ gauge group of the SM, as in Eq. (2.16), should be replaced with the direct coupling to the photon after the electroweak symmetry breaking, which is relevant for the low-energy processes considered in the present thesis. Consider the Lagrangian of the massive dark photon with additional $U(1)'$ symmetry as

$$\begin{aligned}\mathcal{L} \supset -\frac{1}{4}F^{\mu\nu}F_{\mu\nu} - \frac{1}{4}F'^{\mu\nu}F'_{\mu\nu} - \frac{\epsilon}{2}F^{\mu\nu}F'_{\mu\nu} + \frac{1}{2}m_{A'}^2 A'_\mu A'^\mu \\ + eJ^\mu_{\text{EM}}A_\mu + g_D J^\mu_{\text{Dark}}A'_\mu,\end{aligned} \tag{2.17}$$

where the dark photon is taken to couple to the dark current J^μ_{Dark} made of dark sector matter with coupling g_D and its mass term may be obtained gauge-invariantly through the spontaneous symmetry breaking or the Stuckelberg mechanism [178, 179]. To diagonalize the kinetic terms in Eq. (2.17), one can rotate the gauge fields as [180]

$$\begin{pmatrix} A'_\mu \\ A_\mu \end{pmatrix} \mapsto \begin{pmatrix} \frac{1}{\sqrt{1-\epsilon^2}} & 0 \\ \frac{-\epsilon}{\sqrt{1-\epsilon^2}} & 1 \end{pmatrix} \begin{pmatrix} A'_\mu \\ A_\mu \end{pmatrix}, \tag{2.18}$$

which cancels the non-diagonal kinetic term and induces couplings of the dark photon A'_μ to the SM electromagnetic current $\mathcal{L}_{\text{int}} \simeq -\epsilon e J^\mu_{\text{EM}} A'_\mu$ [181]. This Lagrangian can be viewed as a low-energy description of interactions between dark and visible sectors.

Milli-charged dark sectors can be realized when considering the massless limit of kinetically mixed dark photons. In the transformation (2.18), an additional orthogonal rotation, represented by $\left(\begin{smallmatrix} \cos\theta & \sin\theta \\ -\sin\theta & \cos\theta \end{smallmatrix}\right)$, is always possible and introduces an angle θ which is arbitrary as long as the dark photon is massless. By choosing $\sin\theta = \epsilon$, the coupling of the dark photon becomes exclusive to the dark current, while the ordinary photon maintains couplings to both currents. Consequently, in the case of the massless dark photon, the presence of kinetic mixing gives rise to an interaction between the photon and the dark sector as $\mathcal{L}_{\text{int}} \simeq \epsilon g_D J^\mu_{\text{Dark}} A_\mu$. As a result, the dark sector exhibits milli-charged behaviour under the assumption that $\epsilon^2 \ll 1$. Note that the electromagnetic milli-charge can only arise if the dark photon is massless.

milli-Charged Particles

As another interesting model, we explore a simple extension of the SM which introduces a new particle with a very small charge, milli-Charged Particle (mCP). A mCP with electric fractional charge Q_χ can be modeled by a simple interaction as $\mathcal{L}_{\text{mCP}} \supset -\epsilon e(\bar{\chi}\gamma^\mu\chi)A_\mu$, where $\epsilon \equiv Q_\chi/e$. Searching for mCP particles provides an empirical test of charge quantization [182] as well as predictions from well-motivated High energy theories (*e.g.* grand unified theories (GUT) [183, 184]). As discussed above, the millicharged dark sectors can also arise as a low-energy consequence of a dark current coupled to a kinetically-mixed $U'(1)$ dark photon in the massless phase [181]. However, mCPs can also just be a particle with small hypercharge, with no connection to the existence of a dark photon.

mCPs not only serve as a simple extension of the SM but can also have important astrophysical and cosmological consequences. mCPs can be related to dark matter [185, 186, 187] and account for a fraction of the observed DM abundance. In this case, mCP fall into the category of milli-charged strongly interacting dark matter (mSIDM), in which these dark matter candidates cannot be probed by ground-based direct-detection experiments, due to the attenuation of the expected local dark matter flux through interaction in the Earth's atmosphere and crust before reaching a terrestrial detector [188, 189, 190]. Another interesting physics motivation of searching for mCPs is the connection to the explanation to the recently observed EDGES anomaly [162, 163, 49, 54, 164].

2.7.2 Dark Scalar

As another interesting benchmark model, we consider the minimal Higgs portal [191], the unique relevant operator that can couple the SM model to a hidden sector, $\mathcal{L}_{SH} \supset -ASH^\dagger H$ where A is a dimensional portal coupling. This coupling has intrinsic interest as a potential extension of the Higgs sector, but more generally is part of the small subset of renormalizable portal couplings that needs to be probed in order to test the hidden sector framework. It is also worth noting, that after the vector portal DM model, with $m_{A'} > m_{\mathrm{DM}}$, models involving a Higgs portal mediator with $m_S < 2m_{\mathrm{DM}}$ are one of the few scenarios that can escape stringent CMB constraints in the early universe [192]. We will not consider DM models explicitly for the Higgs and vector portal in this dissertation but take these remarks as motivation to explore these two portals in more detail.

Higher dimensional operators

Beyond the three UV-complete relevant or marginal portals discussed above, several additional UV-sensitive interactions at dimension 5 (and higher) can arise. One well-known example at dimension 5 is the axion portal, where a new pseudoscalar singlet (a) serves as a mediator of a new interaction between dark sectors and the SM. The Lagrangian of this interaction at a scale f_a takes the form,

$$\frac{1}{f_a}\, a\, \mathrm{tr}(G^{\mu\nu}\tilde{G}_{\mu\nu}) \qquad\qquad \text{Axion portal,} \tag{2.19}$$

where $G_{\mu\nu}$ is the gluon field strength with the dual tensor $\tilde{G}_{\mu\nu} = \frac{1}{2}\epsilon_{\mu\nu\rho\sigma}G^{\rho\sigma}$. The axion-like particles (ALPs), with masses below the electroweak scale, can appear in theories with broken global symmetries [193].

Electroweak extensions of the SM may contain heavy states, where their interactions with SM can be encoded in the higher dimensional operators. As stated before, the observation of neutrino mass and mixing requires physics beyond the SM, which in many models is accounted for by introducing right-handed singlet states (or so-called heavy neutral leptons), N, through the neutrino portal. However, the interaction of light-active neutrinos with heavy neutral N can also be realized through a dipole moment operator, often referred to as *dipole* portal, in the form

$$d\,\bar{\nu}_L\sigma_{\mu\nu}F^{\mu\nu}N \qquad\qquad \text{Dipole portal,} \tag{2.20}$$

where $\sigma^{\mu\nu} \equiv \frac{i}{2}[\gamma^\mu, \gamma^\nu]$, $F^{\mu\nu}$ indicates the electromagnetic field strength tensor, and ν_L is the SM left-handed neutrino field. This dimension-5 effective operator is not gauge invariant and resides below the electroweak scale. The UV-completion of this operator above a cut-off scale $\sim d^{-1}$ can be realized *e.g.* through a Higgs insertion [194].

2.8 Accelerator Probes of Dark Sectors

In this section, we discuss some experimental sensitivity to the hidden sector portals and dark matter. The SM portals and couplings to a dark sector discussed in Section 2.7 can be probed experimentally through production generated by high-intensity proton beams directed on fixed targets. These setups offer distinct advantages over high-energy colliders, such as the LHC, for exploring the light dark sector particles with masses below $\mathcal{O}(\text{ GeV})$ [149]. To see this first note that the interaction between the SM and the dark sector, mediated by benchmark portals (2.21), exhibits a production cross section that generally scales inversely with the beam energy, characterized by $\sigma \sim g_D^2/E^2$, where g_D represents the dimensionless coupling constant between the two sectors. High-luminosity fixed targets, with attainable proton intensities of $\sim 10^{21-22}$ protons on target (POT) per year, have the capability to overcome the feeble nature of the interactions and achieve remarkable production rates. In fact, a rough estimate shows that these rates can be several orders of magnitude larger than those achieved at colliders, providing fixed targets with a substantial advantage in terms of sensitivity to GeV-scale dark sector physics [26].

The strategy to achieve sensitivities to dark sectors at fixed targets involves modelling both the production and detection of such weakly interacting states. To estimate the number of produced dark particles in each scenario, one needs to calculate the contribution of various processes to a dark sector beam, such as hadronic decays, direct partonic production, and proton Bremsstrahlung. The production rates and distributions can be evaluated analytically or through Monte Carlo simulation. The next step is to evaluate the detection probability corresponding to the event, in which a dark particle reaches a specific detector and undergoes scattering, absorption, or decay within the detector volume. While the DM particle is cosmologically stable, the dark mediator may have a finite lifetime and depending on the mass hierarchy, it can visibly decay to SM particles. In the case of the decay signature at a downstream detector, long-baseline experiments like beam dumps can provide enhanced sensitivity. Our analysis necessitates two components. Firstly, we require the decay length of the long-lived dark mediator for mass ranges below a few GeV. Secondly, we need to account for the detector's sensitivity to the decay products.

Beyond the conventional fixed-target experiments with a near-detector setup, there are several proposed (relatively) inexpensive small dedicated detectors to explore further the sensitivity reach to dark sectors. The Forward Physics Facility (FPF) [195] located in the forward region of the LHC (approximately 480 m from the ATLAS interaction point) is one example out of several proposed experiments in this direction. The detectors at FPF can benefit from an intense and highly collimated beam of light and weakly interacting particles. The experiments in this facility (*e.g.* FASER [37, 196]) are sensitive to many Beyond the SM phenomena and can search for long-lived particles (*e.g.* dark gauge bosons, dark scalars, axion-like particles) or stable particles (dark matter, millicharged particles).

For the purpose of discussing production modes and detection strategies in proton beam facilities, we only consider the two benchmark dark sectors which couple to the SM via vector and/or scalar portal couplings of the form,

$$\mathcal{L} \supset -\frac{1}{2}\epsilon F^{\mu\nu}F'_{\mu\nu} - ASH^{\dagger}H + \cdots , \tag{2.21}$$

which induces couplings of the dark vector A'_{μ} to the electromagnetic current [181], and the dark scalar S to the scalar current which contains all scalar bilinears of charged fermions [191].

2.8.1 Production via Proton Beams

The most relevant production channels for dark force mediators are therefore of importance for associated searches at collider and fixed target facilities. In a proton collider or fixed target experiment, there are a variety of production modes, which proceed via an on or off-shell mediator A'_μ or S. The dominant production channels depend on the energy of the proton beam and the mass of the dark mediator. For the low sub-GeV mass range of interest, meson decays provide an important channel. For the vector portal, the decays $\pi^0/\eta \to \gamma + A'^*$, with subsequent visible or invisible decays of A'^* provide the dominant channel for $m_{A'} < 0.5$ GeV [26, 34], while for scalars, the decays $K \to \pi + S^*$ and $B \to K + S^*$ provide the dominant channels for a larger mass range if the beam is sufficiently energetic [11]. For proton beam fixed target experiments, secondary electromagnetic bremsstrahlung may also be important for very low masses [197]. On the other hand, for mediator masses well above the nucleon scale, Drell-Yan processes such as $q\bar{q} \to A'^*$ or loop-induced scalar production $gg \to S^*$ are relevant [28].

In the next chapters of the present dissertation, our focus is on the intermediate mass range $m_{A'/S} \sim$ GeV, where mixing of the dark states with vector or scalar mesons with the same quantum numbers can resonantly enhance the production rate. In the case of forward production, where the small sub-GeV momentum transfer allows us to treat the coupling of the dark sector state with the proton collectively, this channel amounts to "dark bremsstrahlung". For the scalar and vector portals, the induced coupling to protons, which will be relevant here, follows directly from Eq. (2.21),

$$\mathcal{L}_{\text{eff}} \supset -\epsilon e A'_\mu \bar{p}\gamma^\mu p - g_{SNN}\theta S\bar{p}p + \cdots , \tag{2.22}$$

where we have ignored higher multipole couplings for A'_μ, the $h{-}S$ mixing angle $\theta \simeq Av/m_h^2 \ll 1$ for the parameters of interest, and $g_{SNN} = 1.2 \times 10^{-3}$ can be obtained via the use of low energy theorems [198] (see also [199, 200]). In Chapter 4, we will consider a model for dark bremsstrahlung based on these couplings, while the underlying physics of proton-proton scattering is discussed in Appendix A.

2.8.2 Detection Signature

To clarify the detection strategy, consider an example of a dark scalar produced at a fixed target facility. Once produced, the probability that a dark scalar particle decays inside the detector is

$$P_{\text{decay}} = e^{-L_i/\gamma\beta\tau} - e^{-L_f/\gamma\beta\tau}, \tag{2.23}$$

where L_i (and L_f) denote the distances from production at which the scalar will enter (and exit) the detector, while τ is the lifetime and β is the velocity. This probability depends on the scalar's energy as well as its direction with respect to the beam axis.

In analyzing the fixed target detection signatures of S decays, we will also require the decay width of S. From the induced coupling of S to leptons, the dark scalar decay rate into leptonic final states is given by [11],

$$\Gamma(S \to \ell^+\ell^-) = \theta^2 \frac{m_\ell^2 m_S}{8\pi v^2} \left(1 - \frac{4m_\ell^2}{m_S^2}\right)^{3/2}, \tag{2.24}$$

where the branching ratio formulated as $\text{Br}(X \to f) = \Gamma_f/\Gamma_{\text{total}}$, is approximately $\text{Br}(S \to e^+e^-) \simeq 1$ for $2m_e < m_S < 2m_\mu$, while $\text{Br}(S \to \mu^+\mu^-) \simeq 1$ for $2m_\mu < m_S < 2m_\pi$. Just above the pion threshold, $\text{Br}(S \to \mu^+\mu^-) \simeq 0.1 - 0.2$ and various hadronic decay channels open up [201]. The branching ratios for the decay of the dark scalar are illustrated in Fig. 2.6.

The experimental signature of a massive dark photon depends on its decay modes. The dark photon with mass above $m_{A'} > 2m_e \sim 1\,\text{MeV}$ predominantly decays into pairs of charged leptons with decay width [26],

$$\Gamma(A' \to \ell^+\ell^-) = \frac{1}{3}\alpha\epsilon^2 m_{A'} \sqrt{1 - \frac{4m_\ell^2}{m_{A'}^2}} \left(1 + \frac{2m_\ell^2}{m_{A'}^2}\right), \tag{2.25}$$

where m_ℓ is the lepton mass. At larger masses, decay channels into hadronic states open up,

$$\Gamma(A' \to \text{hadrons}) = \Gamma(A' \to \mu^+\mu^-) \times R, \tag{2.26}$$

where $R \equiv \sigma(e^+e^- \to \text{had})/\sigma(e^+e^- \to \mu^+\mu^-)$ is the R-ratio [202]. The decay branching ratios for the dark photon are shown in Fig. 2.7.

The focus of the studies presented in this dissertation is on the *visible* scenarios where we assume that the decay of dark mediators into other states in the dark sector is kinematically forbidden, and the dark scalar/vector is visible only through

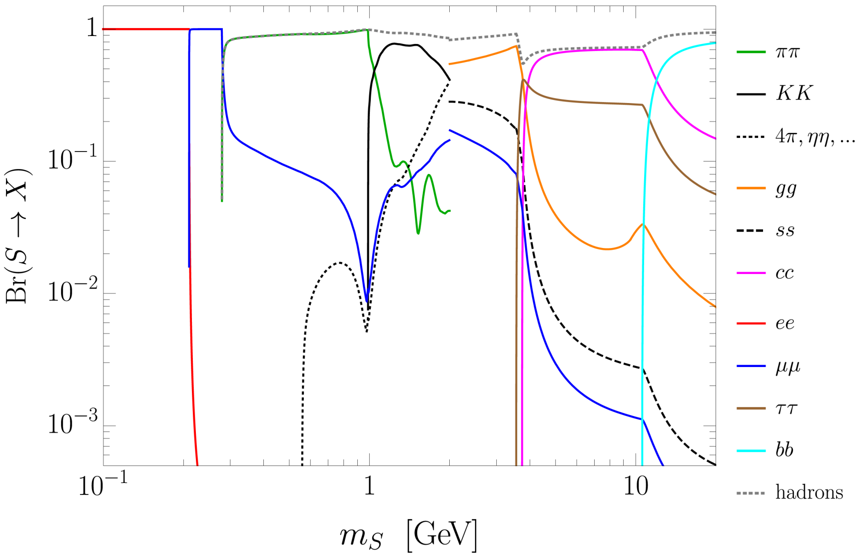

Figure 2.6: The decay branching ratios of dark scalar into different hadronic and leptonic final states. Reproduced with permission from B. Batell et al., "Dark Sector Studies with Neutrino Beams", in the Proceedings of the APS DPF Community Summer Study (Snowmass 2021), `https://www.slac.stanford.edu/econf/C210711/`, arXiv:2207.06898 [hep-ph], Copyright 2022 [149].

its decay into SM particles. However, it is possible for the dark photon to interact with other dark states in the dark sector. For example, the Lagrangian Eq. (2.21) can be expanded by introducing a scalar or pseudo-Dirac fermionic DM state χ charged under the $U(1)'$ symmetry, which produces a viable thermal relic DM model. In the case $m_{A'} > 2m_\chi$, the dark photon can decay with a non-vanishing branching ratio into invisible DM states given by the decay width,

$$\Gamma(A' \to \chi\bar{\chi}) = \frac{1}{3}\alpha_D m_{A'} \sqrt{1 - \frac{4m_\chi^2}{m_{A'}^2}} \left(1 + \frac{2m_\chi^2}{m_{A'}^2}\right), \tag{2.27}$$

where α_D is the dark coupling to the dark photon. This invisible channel would be the dominant decay mode if $\alpha_D \gg \alpha\epsilon^2$. Such invisible dark photon decay can be detected by using techniques like missing energy/momentum from dark photon production or the DM scattering off the matter in the detector.

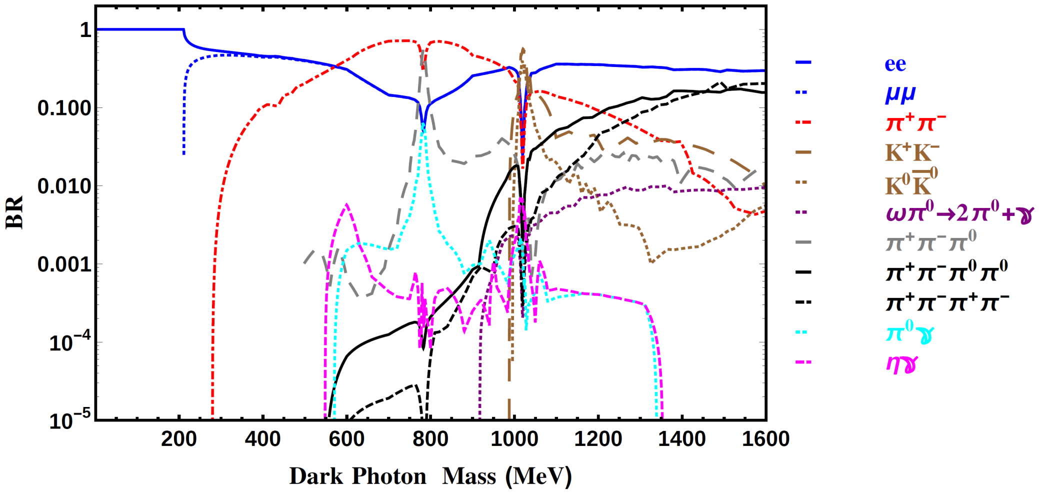

Figure 2.7: A plot from Ref. [161] displaying the decay branching ratios of dark photon into various final states as a function of mass.

Chapter 3

LSND Constraints on the Higgs Portal

This chapter is based on the content of a paper that was originally written in collaboration with Adam Ritz and is referenced in Ref. [203].

3.1 Introduction

In this chapter, we will consider the minimal Higgs portal [191], the unique relevant operator that can couple the SM model to a dark sector,

$$\mathcal{L}_{SH} \supset -ASH^{\dagger}H, \tag{3.1}$$

where S is a new scalar singlet, H is the SM Higgs doublet, and A is a dimensional portal coupling. Along with being one of the few renormalizable portal couplings to a dark sector, and a potential force mediator for thermal relic models of light dark matter, this interaction is of intrinsic interest as an extension of the SM Higgs sector.

The strongest existing constraints on the Higgs portal, in the low mass range where $\text{Br}(S \to l^+l^-) \sim 1$, arise from searches for leptonic decays at the CHARM fixed target experiment at CERN [204, 205, 206], and analysis of $K^+ \to \pi^+ S$ signatures at the Brookhaven E949 experiment, with S escaping the detector before decaying and thus being counted as missing energy in the search for $K^+ \to \pi^+ \nu\bar{\nu}$ [207, 205, 206]. The latter constraint is the most stringent, except in an S mass range relatively close to m_π where significant backgrounds limit the reach of E949. For higher S masses, a range of accelerator and meson decay constraints apply to the Higgs portal [11, 208, 205, 209, 201, 206, 210, 198, 211], while for smaller couplings, constraints from supernova cooling also apply [192, 212].

In the current study, we revisit the limits on the Higgs portal in the low mass $m_S <$

350 MeV region, by studying the sensitivity of the LSND experiment, that is known to provide important constraints on the dark photon [26, 27]. In particular, by analyzing a range of production channels in the interaction of the 800 MeV proton beam with the target, particularly proton bremsstrahlung [198], we find that existing LSND analyses with final state electrons and muons already impose the leading constraint on the Higgs portal in two mass windows between 100 and 350 MeV. Our final results are presented in Fig. 3.1, where we show LSND exclusions compared to existing limits e.g. from CHARM and E949, and recent projections for sensitivity at the Fermilab SBN facility [213]. For comparison, we also show the 1 and 2σ preferred regions if decays of K_L via S were to explain the recent KOTO anomaly [214, 215, 216, 217, 218].

The rest of this Chapter is organized as follows. In Section 3.2, we summarize some of the relevant couplings and decay rates of the Higgs Portal. In Section 3.3, the production of light scalars at LSND is discussed in some detail, and in Section 3.4 we present the sensitivity reach due to light scalars decaying to electrons and muons in the detector. Section 3.5 contains our concluding remarks.

3.2 Higgs portal

As introduced in Section 2.7, we extend the SM by adding a scalar singlet S, for which the leading relevant or marginal couplings to the Higgs doublet H comprise the Higgs portal [191],

$$\mathcal{L} \supset -(AS + \lambda S^2)H^\dagger H. \tag{3.2}$$

After electroweak symmetry breaking, and re-diagonalizing by shifting the physical Higgs field as $h \to h + \theta S$ to remove hS mixing, the induced linear couplings take the form

$$\mathcal{L} \supset -\frac{\theta}{v} S \left(\sum_f m_f \bar{f} f + m_Z^2 Z^\mu Z_\mu + 2m_W^2 W_\mu^+ W^{\mu +} \right),$$

where the mixing angle $\theta \simeq Av/m_h^2 \ll 1$ for the parameters of interest here.

Integrating out the electroweak-scale degrees of freedom induces further couplings of S to light hadronic states. For the sub-GeV mass range of interest here, the relevant interactions take the form,

$$\mathcal{L} \supset -\theta S \left(\frac{m_e}{v} \bar{e} e + g_{S\gamma\gamma} F_{\mu\nu} F^{\mu\nu} + g_{SNN} \bar{N} N + \cdots \right).$$

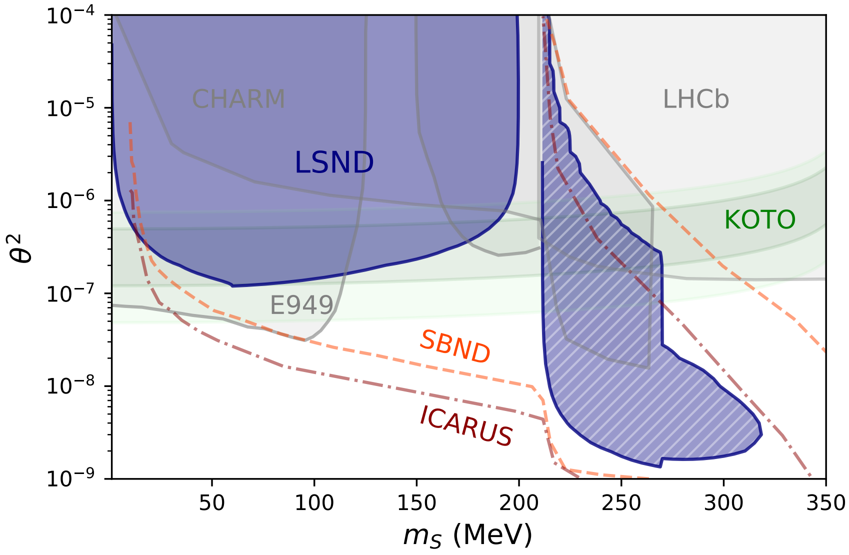

Figure 3.1: A summary of the sensitivity limits determined in this work for scalar S decays to electrons (solid) and muons (hatched) at LSND, shown in the plane of the coupling $\theta^2 \simeq (Av/m_h^2)^2$ versus dark scalar mass m_S. Exclusions from other sources (in gray) including LHCb [208], E949 $K \to \pi +$ invisible [207, 205, 206], and CHARM $S \to e^+e^-$, $\mu^+\mu^-$ [204, 205, 206] are shown. The 1 and 2σ preferred contours to explain the KOTO anomaly in K_L decays [214, 215, 216, 217], and the sensitivity projections for the on-axis SBND (orange) and off-axis ICARUS (purple) experiments at Fermilab [213], are also shown for comparison (see the text for further details).

Well-known 1-loop triangle diagrams generate the effective diphoton coupling [219],

$$g_{S\gamma\gamma} = \frac{\alpha}{8\pi v} F_\gamma(m_S), \tag{3.3}$$

where $F_\gamma(m_S \ll \text{GeV}) \sim \mathcal{O}(1)$ is a loop function [219, 220, 198]. The coupling to nucleons can in turn be obtained through the use of low energy theorems [198] (see also [199, 200, 221]),

$$\begin{aligned} g_{SNN} &\simeq \frac{2}{9}\frac{m_N}{v}\left(1 + \frac{7}{2}\sum_{q=u,d,s}\frac{m_q}{m_N}\langle N|\bar{q}q|N\rangle\right) \\ &\sim 1.2 \times 10^{-3}. \end{aligned} \tag{3.4}$$

In principle, this coupling should be extended to a form factor, but for the kinematic regime of interest in this work, there is no significant impact from hadronic scalar resonances, and the assumption that g_{SNN} is a constant will be sufficient.

3.3 Light scalar production at LSND

The LSND experiment comprises an 800 MeV proton beam impacting a thick target, that was either water or a high Z metal at various stages of the experimental program. Over its lifetime LSND accumulated one of the largest proton on target (POT) datasets of any fixed target experiment, with over 10^{23} POT in total [222, 223]. The relevance of LSND for Higgs portal phenomenology was briefly addressed in [209]. In this section, we will revisit the production rate of scalars for $m_S < m_\pi$ from a variety of channels.

Before we examine specific production modes, it is useful to compare this case to the scenario with a dark photon A'_μ kinetically mixed with the photon via the interaction $\frac{\epsilon}{2}F^{\mu\nu}F'_{\mu\nu}$. This induces a low energy coupling of A' to the electromagnetic current with strength $e\epsilon$, with ϵ the kinetic mixing parameter. The leading production mode at LSND for low mass dark photons is pseudoscalar meson decay, e.g. $\mathrm{Br}(\pi^0 \to A'\gamma) \sim \epsilon^2$. Thus, for sufficiently light dark photons, we can estimate the number of dark photons produced as $N_{A'}^{(\pi)} \sim \epsilon^2 N_\pi$. The large pion (and eta) production rate, combined with the large radiative branching for pseudoscalar mesons makes this channel by far the most efficient. For scalars coupled through the Higgs portal, the situation is somewhat different, as the only mesons with substantial scalar branching rates are kaons and B mesons, which are not kinematically accessible at LSND. We find instead that the dominant production mode in this case is proton bremsstrahlung, $p + N \to X + S$, with X the inclusive hadronic final state and $N_S \sim 0.5\theta^2 g_{SNN}^2 N_\pi \sim 10^{-6}\theta^2 N_\pi$, which is substantially lower than the dark photon production rate due to the reduced scalar coupling to hadrons. In the rest of this section, we will discuss this production mode in more detail, along with further production channels via Δ decay and the Primakov process for comparison.

3.3.1 Proton bremsstrahlung

Scalars can be produced through the SNN vertex via the proton-proton bremsstrahlung process $p + p \to S + X$, where we focus on pp scattering due to its resonantly enhanced rate, proceeding via the Δ^{++} intermediate state. At LSND beam energies, the beam protons are only moderately relativistic, and thus we will utilize two different procedures for the calculation adapted respectively to either sub-relativistic or highly

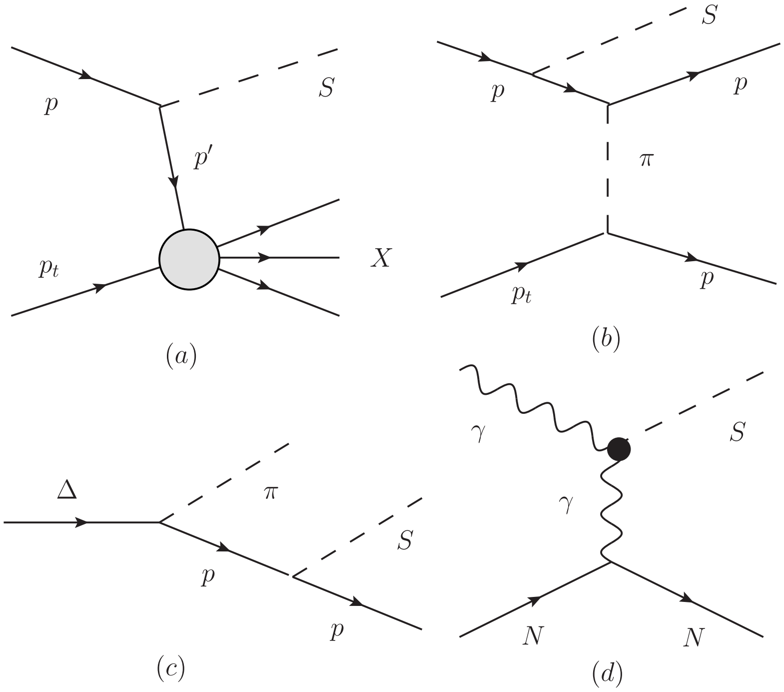

Figure 3.2: Production channels for the scalar S at LSND via (a) proton bremsstrahlung splitting function, (b) proton bremsstrahlung through one-pion exchange, (c) Δ decay and (d) the Primakov process.

relativistic beams. Comparing the scalar production rate using both techniques at LSND will allow for an assessment of the precision of the rate calculation.

Splitting function

We will first follow the approach of Altarelli-Parisi and formulate the bremsstrahlung calculation in quantum mechanical perturbation theory, as recently discussed in this context in [198]. Since the beam protons are not ultra-relativistic at LSND, this is an extension of the conventional Weizsacker-Williams (WW) approximation in which the beam protons are often considered in the infinite-momentum frame. Nonetheless, we find that the kinematic range at LSND will still allow us to approximate the required rate in terms of the proton-proton cross-section and a calculable sub-process [224, 225, 226, 198]. In this formalism, all states are on-shell and while 3-momentum is conserved, energy is not automatically conserved at each vertex, but only after summing all contributions.

The relevant diagram for the process is shown in Fig. 3.2(a). We denote the momentum of the incoming proton and emitted S in the target rest frame by $p_p^\mu = (E_p, \vec{0}, p_p)$

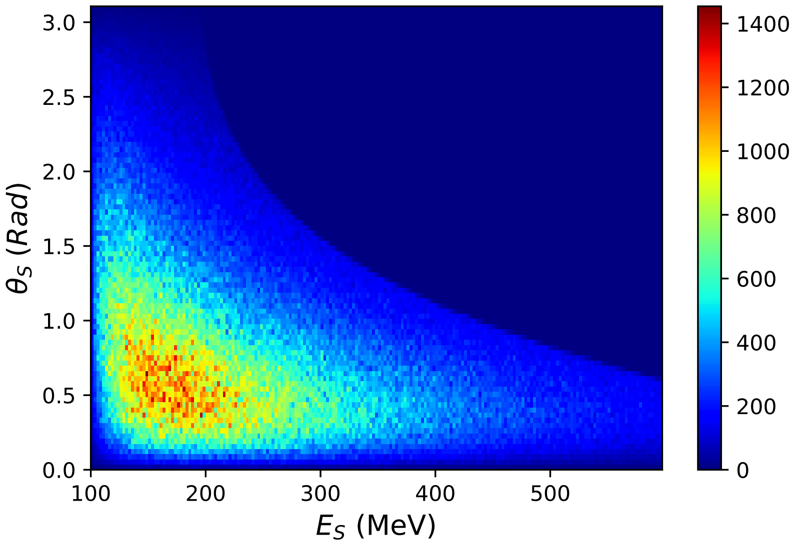

Figure 3.3: Energy-angle distribution of scalars with $m_S = 100$ MeV produced via the proton bremsstrahlung channel at the LSND beam energy of 0.8 GeV. This distribution uses the assumptions discussed in the text, and has an arbitrary overall normalization with the colour bar indicating the relative frequency.

and $p^\mu_S{=}(E_S, \vec{p}_T, zp_p)$, with $E^2_S{=}z^2p^2_p{+}p^2_T{+}m^2_S$. The momentum of the intermediate proton is denoted $p^\mu_{p'}{=}(E_{p'}, -\vec{p}_T, (1{-}z)p_p)$, with $E^2_{p'}{=}(1{-}z)^2p^2_p{+}p^2_T{+}m^2_p$, where p_T is the S transverse momentum with respect to the beam, and z is the fraction of longitudinal momentum carried by S.

The second order contribution to the matrix element, generically of the form $V_{fj}V_{ji}/(E_f - E_i)$ for a perturbation V, has two possible time orderings in this case for the process $p{+}p_t{\to}S{+}X$ exchanging the intermediate state p'. The two amplitudes can be written as [225, 198]

$$\mathcal{M}^{\text{emit}} = \frac{\mathcal{M}_{p\to p'S}\mathcal{M}_{pp'\to X}}{2E_{p'}(E_p - E_S - E_{p'})} \tag{3.5}$$

$$\mathcal{M}^{\text{absorb}} = \frac{\mathcal{M}_{p\to p'X}\mathcal{M}_{pp'\to S}}{2E_{p'}(E_S - E_p - E_{p'})} \tag{3.6}$$

where the intermediate proton's 3-momentum is fixed by $\vec{p}_{p'}{=}\vec{p}_p{-}\vec{p}_S$, while the energy is not automatically conserved at the $pp'S$ vertex. Denoting the energy denominators as $\Delta E_{\rm emit}{=}E_{p'}{+}E_S{-}E_p$ and $\Delta E_{\rm absorb}{=}E_{p'}{-}E_S{+}E_p$, then under the condition

$$\Delta E_{\rm emit} \ll \Delta E_{\rm absorb}, \tag{3.7}$$

we can neglect the matrix element $\mathcal{M}^{\rm absorb}$. This can be interpreted as the dominant contribution coming from initial state radiation. We have verified that this condition is satisfied to a few percent for LSND kinematics. Imposing a second condition,

$$\Delta E_{\rm emit} \ll m_p, \tag{3.8}$$

it is possible to write the differential cross section of the process $p{+}p_t{\to}S{+}X$ in the approximate form [198],

$$\frac{d\sigma_{pp_t\to SX}}{dzdp_T^2} \approx P_S^{\rm split}(z,p_T)\sigma_{pp}(s'), \tag{3.9}$$

where σ_{pp} is the total proton-proton scattering cross section, which varies between $\sim 30{-}45$ mb over the relevant energy range (see Fig. A.4 in Appendix A) [57], with $s'{=}2m_p(E_p{-}E_S{+}m_p)$ the center of mass energy. Denoting the momentum transfer as $q^\mu = (E_p{-}E_S, \vec{p}_p{-}\vec{p}_S)$, the differential splitting probability of the proton to emit a scalar $P_S^{\rm split}$ can be represented in the form,

$$\begin{aligned} P_S^{\rm split}(z,p_T) =& \frac{\theta^2 g_{SNN}^2}{16\pi^2}\frac{(E_pE_{p'}{-}(1{-}z)p_p^2{+}m_p^2)}{E_S(q^2{-}m_p^2)^2}\times \\ & \sqrt{(1{-}z)^2p_p^2+p_T^2}\left(1+\frac{E_p{-}E_S}{E_{p'}}\right)^2. \end{aligned} \tag{3.10}$$

The integration range for p_T and z is determined by the kinematic conditions Eq. (3.7), and Eq. (3.8), where we require the kinematic variable on the left of each inequality to be at most 10% of the right hand side. The conditions are satisfied for $z \in [0, 0.5]$ and $p_T < 300$ MeV at LSND. The resulting distribution of scalars is shown in Fig. 3.3, which we see reaches above $E_S \sim 300$ MeV.

One-pion exchange

We will now consider a complementary approach, modelling proton-proton scattering via one pion exchange, which is expected to provide the dominant hadronic (as opposed to electromagnetic) contribution to bremsstrahlung at sub-relativistic beam energies. Employing the one-pion exchange model described by $\mathcal{L} = g_{\pi NN}\bar{N}\gamma_5\tau\cdot\pi N$, with nucleon-pion coupling $g_{\pi NN}^2/(4\pi) \approx 13.5$, we find that the tree-level contribution provides a good fit for pp elastic scattering as depicted in Fig. A.4. See Appendix A.3 for details.

We now compute the rate for initial state radiation of S, $pp \to ppS$ via one pion exchange, according to Fig. 3.2(b). For the analysis below, we use the full tree-level calculation of the 2-body and 3-body final states. However, we can gain some intuition in the limit where Mandelstam $s \gg m_S^2$, where the cross section takes the form $\sigma_{pp\to ppS} = \frac{g_{SNN}^2}{8\pi^2}\sigma_{pp}f(m_S^2)$, with $f(m_S^2) \propto \log^2\frac{m_S^2}{s} + \cdots$ exhibiting the Sudakov double logarithim. For the finite-m_S kinematics of interest here, there are no sizeable IR/collinear effects, and so we will not need to include the corresponding loop contribution that is relevant in the $m_S \to 0$ limit.

To compare with the splitting function calculation above, we define the differential splitting probability of the proton to emit a scalar via one pion exchange in the form,

$$P_S^{\text{split,OPE}}(E_S,\Omega_S) = \frac{1}{\sigma_{pp}^{\text{Elastic}}}\frac{d\sigma_{pp\to ppS}^{\text{Elastic}}}{d\Omega_S dE_S} \tag{3.11}$$

The plot in Fig. 3.4 compares the two different methods of calculating the splitting probability as a function of the scalar energy E_S. Similar results hold for other choices of m_S. We observe that the ratio is $\mathcal{O}(1)$, with one pion exchange providing a rate that is slightly larger than the relativistic splitting function for LSND beam energies. This comparison nonetheless provides confidence in the rate calculation at the $\mathcal{O}(1)$ level.

Scalar production rate

Utilizing only the splitting function calculation Eq. (3.9) as a conservative approximation for the total rate, the total number of scalars N_S produced through the bremsstrahlung channel can be estimated numerically, where we normalize the rate to the number of π^+ produced, N_π, which is given at LSND energies by the Burman-Smith distribution [227]. For $m_S = 1$ MeV, we obtain $N_S \sim 0.5\theta^2 g_{SNN}^2 N_\pi$. This calculational approach should capture part of the primary production channel, but as is apparent from the discussion above, it is only anticipated to be accurate up to $\mathcal{O}(1)$ factors.

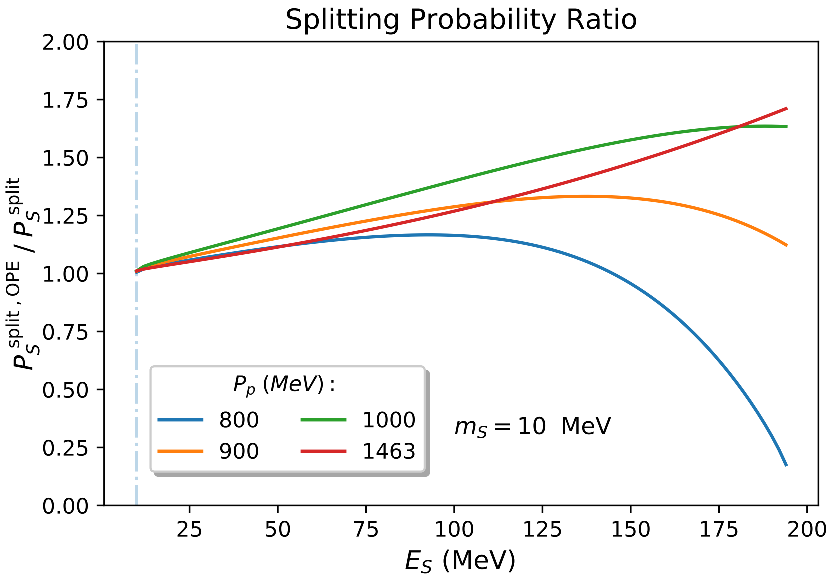

Figure 3.4: The ratio of the splitting probability of the initial state proton to emit a scalar calculated using the two techniques as a function of scalar energy. The LSND beam momentum corresponds to $P_p = 1463\,\mathrm{MeV}$.

3.3.2 Other production channels

In this subsection, we comment on a number of additional sub-leading scalar production channels.

Δ decay

At LSND beam energies, roughly half the total proton-proton scattering cross section involves an inelastic process with resonant production, e.g. of Δ^{++}, which subsequently decays to $p + \pi^+$. Indeed, the resonant excitation of Δ (and Σ) hadronic resonances is the primary channel for pion production at LSND. This is partially incorporated in the analysis of bremsstrahlung above, in that it contributes to the total cross-section, but there are additional channels involving S radiation from final states which are more problematic to calculate. A tractable contribution of this type involves 3-body Δ decay, $\Delta \to \pi + p + S$ [209], as shown in Fig. 3.2(c). Computing the 3-body decay rate, using a phenomenological pion-Delta-nucleon vertex at the low-energy given by $\mathcal{L}_{\mathrm{int}} = g_{\pi\Delta N}\bar{\Delta}^\mu N \partial_\mu \pi$, and assuming that the 2-body decay of Δ's saturates pion production inside the target, we can estimate the number of scalars from the 3-body decay via the following ratio, $N_S \sim N_\pi \times \frac{\Gamma_{\Delta\to p\pi S}}{\Gamma_{\Delta\to p\pi}}$. Evaluating the 3-

body phase space integral numerically for $m_S = 1$ MeV, we find $N_S \sim 0.04\theta^2 g_{SNN}^2 N_\pi$, which is consistent with the estimate in [209] and about an order of magnitude below the bremsstrahlung rate. Note that in the collinear limit, scalars are produced isotropically in the Δ rest frame. We have transformed the energy-angle distribution to the lab frame, using a Monte Carlo simulation, in which the energy-angle distribution of Δ baryons in the lab frame was reconstructed from the Burman-Smith parameterization of the pion distribution. As expected this distribution is almost isotropic, reflecting the fact that the Δ's are produced almost at rest, in comparison to the more forwarded-peaked distribution from bremsstrahlung. This further suppresses the event rate in the detector.

Primakov conversion

There are several additional decay channels that will contribute to S production, as discussed in [209], but none are estimated to be larger than the Δ-decay channel discussed above. We have also considered a different topology that utilizes the effective diphoton coupling Eq. (3.3), via which scalars can be produced via the Primakov conversion of photons $\gamma{+}N{\to}S{+}N$ in the presence of nuclei with atomic (number) mass $Z(A)$, as shown in Fig. 3.2(d). The dominant source of photons is provided by π^0 decays in the target [228]. The neutral pion decay length is roughly 0.1 μm at the LSND beam energy, and thus $\pi^0 \to \gamma\gamma$ decays can effectively be treated as a distribution of real photons in the target. Applying the analysis of [229] to scalar production, the total cross section can be written as $\sigma_S = \int dk_\gamma d\Omega_\gamma f_\gamma(k_\gamma, \Omega_\gamma) {\times} \sigma_{\gamma N \to NS}(k_\gamma)$, where $f_\gamma(k_\gamma, \theta_\gamma) dk_\gamma d\Omega_\gamma$ is the photon energy and angular distribution with angles $(\theta_\gamma, \phi_\gamma)$ defined with respect to the beam direction. The two-body cross section $\gamma{+}N \to S{+}N$ incorporates a Helm form factor [230], which is exponentially suppressed for momentum transfer above 200 MeV once coherence is lost [231]. Taking the Burman-Smith model of the pion distributions as an input, the dependence of the photon distribution on the energy and angle with respect to the beam axis was determined using a Monte Carlo simulation, and numerically evaluating the integrals for $m_S{=}1$ MeV, we estimate the number of scalars produced as $N_S{\sim}10^{-4}\theta^2 g_{SNN}^2 N_\pi$ where the factor of $g_{SNN}^2 \sim 10^{-6}$ has been inserted purely for comparison. This S-production process is forward-peaked, but is subleading at LSND.

3.4 Sensitivity at LSND

In this section, we focus on the dominant proton bremsstrahlung production mode and combine the rate and distribution of the last section with the experimental geometry and detection probability, in order to determine the LSND constraints on the Higgs portal. The LSND detector was a shielded 5.7m diameter cylinder of length 8.3m filled with 167 tons of mineral oil, that was on average at an angle of 14 degrees to the beamline, and at a distance of 30m from the target. Charged particles, such as electrons and muons, were detected via a combination of Cerenkov and scintillation light.

To estimate the sensitivity reach of the decay search at LSND, we use the probability that a produced S particle decays inside the detector defined in Section 2.8.2 as

$$P_{\text{decay}} = e^{-L_i/\gamma\beta\tau} - e^{-L_f/\gamma\beta\tau}, \tag{3.12}$$

which depends on the dark scalar's energy as well as its direction with respect to the beam axis. Due to the low beam energy at LSND, we do not consider scattering or Compton absorption signatures inside the detector, since the decay reach dominates the scattering reach by several orders of magnitude [209, 232].

To normalize the overall event rate at LSND, we have used N_{π^0}, the total number of neutral pions produced. In practice, the π^0 distribution is taken to be an average of the measured π^+ and π^- production rates in proton-nucleon collisions, which differ by $\mathcal{O}(1)$ factors. For the LSND beam energy, we use the parameterization of the production cross-section given by Burman and Smith [227], and denote the total cross section as σ_π^{BS}. With this normalization, the number of scalars produced via proton bremsstrahlung, that subsequently deposit their energy in the LSND detector, can be schematically represented as follows,

$$N_S^{\text{LSND}} \sim \varepsilon_{\text{eff}} \frac{N_\pi}{\sigma_\pi^{\text{BS}}} \int dE_S d\theta_S \left(\frac{d^2\sigma_{pp_t \to SX}}{dE_S d\theta_S} \right) \times P_{\text{decay}} \times \vartheta(E_S, \theta_S)$$

where $\vartheta(E_S, \theta_S)$ summarizes the experimental cut conditions and ε_{eff} is the corresponding detection efficiency. To determine the sensitivity to scalar decays to electrons, we use the analysis [222, 223], in which ν_e were detected via the inclusive charged-current reaction $\nu_e + {}^{12}C \to e^- + X$. Following [14], we make the assumption, based on the primary use of the scintillation to Cerenkov light ratio, that the e^+e^- pairs would be registered as indistinguishable from single electrons. Therefore, we assume that the scalar's energy would have been measured as the energy of a single-electron in the energy range 60 MeV to 200 MeV with the e^+e^- pair detection efficiency as for a single electron, *i.e.* $\varepsilon_{\text{eff}} \sim 0.1$. A similiar analysis [233] uses an energy cut between 160 MeV and 600 MeV on muons produced through the reactions $\nu_\mu(\bar{\nu}_\mu) + {}^{12}C \to \mu^{-(+)} + p(n) + X$ in order to identify muon neutrino-like beam excess events inside the detector. We can use this analysis to find the sensitivity to S decays to muon pairs, although the efficiency is harder to estimate in this case given that the $\mu^+\mu^-$ pair will have a lower boost than the corresponding electron decay. We will assume these events are also reconstructed as single-muon events with efficiency ~ 0.1 similar to the electron case, but show the results with hatching to indicate that the detection assumptions are distinct. In this case, we also account for the reduced branching fraction to muons when $m_S > 2m_\pi$. In both analyses, the number of beam-excess events does not exceed 20, which we take as the limit for both electron and muon decay channels.

Using the energy-angle distribution of scalars produced dominantly through proton bremsstrahlung, as outlined in Section 3.3, and considering the geometric acceptance of the LSND detector as well as kinematic cuts and detection efficiencies for the final state particles, we numerically determined the event yields at LSND. The resulting event number contours are shown in Fig. 3.5, while our final 20 event limit contour is shown in Fig. 3.1, which also summarizes the results in comparison to a number of existing constraints as detailed in the Figure caption. We see that the LSND sensitivity to electron decays provides the leading constraint in a small window in scalar mass from 120 to 180 MeV, while the sensitivity to muon decays provides the leading constraint from $2m_\mu$ up to 320 MeV.

3.5 Concluding Remarks

In this study, we have revisited the existing limits on one of the three UV-complete portals from the SM to a dark sector, namely the Higgs portal coupling to a singlet scalar. This portal is of particular interest as one of the generic mediation channels for the interaction with dark matter. We have shown that existing data from LSND, when combined with the dominant low energy production mode through proton bremsstrahlung, already excludes additional regions of parameter space for m_S between 100 and 350 MeV. Future analyses are possible, which can extend this reach further. For example, NA62 at CERN provides greater sensitivity to $K^+ \to \pi^+\nu\bar{\nu}$, and so the exclusion from E949 can be extended [211], while further sensitivity at

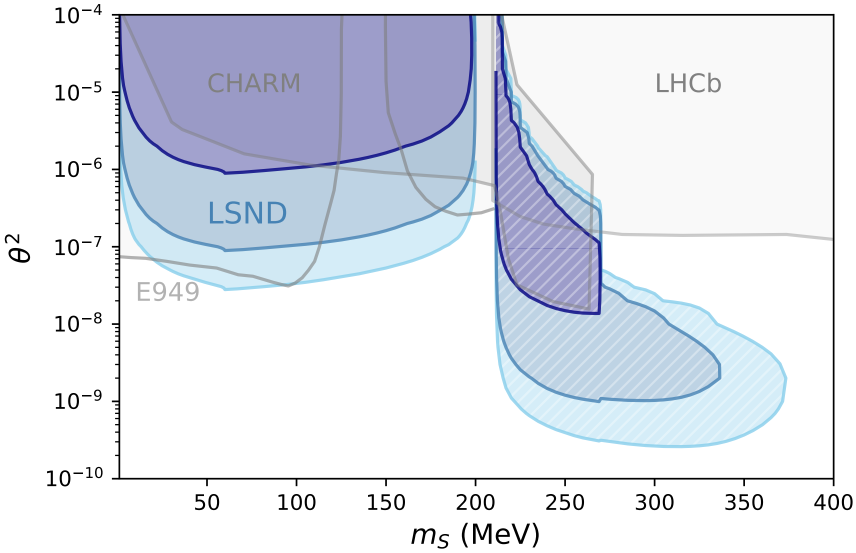

Figure 3.5: Sensitivity contours for scalar decays at LSND, with the three blue-shaded contour regions corresponding to 1 event (light), 10 events (medium) and 1000 events (dark). Solid shading indicates event rates from electron decays, while hatched shading indicates event rates from muon decays. Existing exclusions from other sources (in gray) include LHCb [208], E949 $K \to \pi + invisible$ [207, 205, 206], and CHARM $S \to e^+e^-$, $\mu^+\mu^-$ [204, 205, 206] analyses.

higher mass may come from Belle II [234]. Similarly, KOTO provides sensitivity through the neutral decay channel $K_L \to \pi^0\nu\bar{\nu}$ (see e.g. the recent discussions of an anomaly in current data in [214, 215, 216, 217, 218]). The short baseline neutrino (SBN) program at Fermilab will also provide new sensitivity to the Higgs portal, as recently analyzed in [213], and we exhibit the projected sensitivity for SBND and ICARUS from that reference in Fig. 3.1.

Chapter 4

Dark Sector Production via Proton Bremsstrahlung

This chapter is adapted from the paper originally written in collaboration with Adam Ritz, as referenced in Ref. [235].

4.1 Introduction

Experiments using proton beams at high luminosity colliders and fixed target facilities provide impressive sensitivity to new light weakly coupled degrees of freedom. The most relevant production channels for dark force mediators are discussed in Section 2.8, therefore of importance for associated searches at the experiments making use of proton beams. The dominant production channels depend on the energy of the proton beam and the mass of the dark mediator. Among them, bremsstrahlung of dark vectors and scalars can be particularly important over the dark sector mass range from about 500 MeV to a GeV. However, computing the bremsstrahlung production rate, particularly in the forward direction, is difficult as it involves the nonperturbative physics of the forward pp (or pn) cross section. Thus far, most analyses have relied on variants of the Weizsacker-Williams (WW) approximation, developed in the 1970's as a generalization of the successful approach used for electron beams.

In this chapter, we revisit the production of dark vectors and scalars via proton bremsstrahlung and build a model to describe this process in the context of pomeron-mediated forward scattering. We use this model to analyze the various production modes associated with initial and final state radiation in diffractive and non-diffractive proton scattering. We will focus our attention on proton-proton scattering, as a generic contribution relevant for both the High Luminosity-LHC (HL-LHC) and for

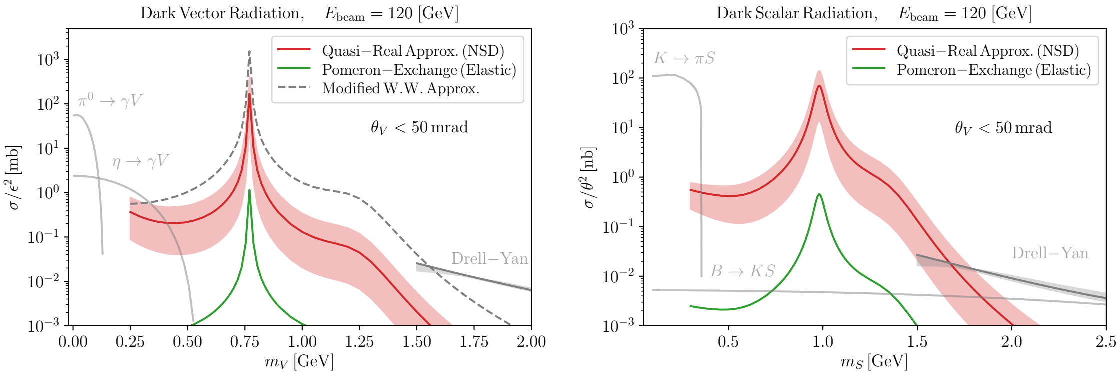

Figure 4.1: The production cross section of dark vectors and scalars for a 120 GeV fixed target beam as a function of mass and within $\theta < 50$ mrad of the beam axis (lab frame). The red curves denote the rates using the quasi-real approximation in non-single diffractive scattering, and the uncertainty band corresponds to varying the associated cut-off scale $\Lambda_p \in [1, 2]$ GeV with the central value 1.5 GeV. The green curves show the associated rates from initial and final state radiation in quasi-elastic scattering, where interference effects cause a significant suppression. Note the enhancement in the resonance region due to the mixing of the radiated dark state with vector mesons (ρ and ω) and scalar meson (f_0) with the same quantum numbers. In the vector case, the dashed grey curve uses the modified WW approximation of [236] with a cut on transverse momentum $p_T < 1$ GeV, while for both plots the lighter grey curves show other production channels from meson decay [26, 34], and parton-level Drell-Yan [28] processes relevant at higher mass. See the text in Section 4.2 and Section 4.3 for further details.

fixed target experiments. This analysis will allow us to test the impact of various approximations and kinematic constraints, and to compare this approach with the modified WW approximation [236]. Our final results for production rates are shown in Fig. 4.1 for a 120 GeV fixed target beam at Fermilab, and Fig. 4.2 for the 14 TeV LHC, along with various comparisons.

The rest of this chapter is organized as follows. In Chapter 2, we provided a concise overview of dark sector production channels in proton beam experiments (refer to Section 2.8.1). In Section 4.2, we now shift our focus to a detailed discussion of bremsstrahlung in forward proton scattering. We discuss the modeling of forward elastic and diffractive scattering via pomeron exchange, and then build a model for initial and final state radiation of dark vectors and scalars via this process, along with a more generic model for initial state radiation in non-single-diffractive scattering. We present our results in Section 4.3, along with comparisons to modified WW approaches. Finally, we conclude in Section 4.4.

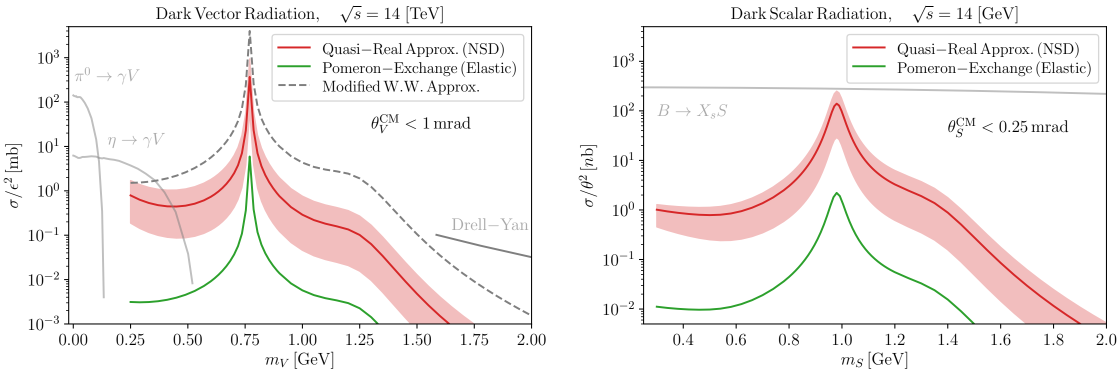

Figure 4.2: The production cross section of dark vectors and scalars at 14 TeV (centre of mass) energy as a function of mass and within $\theta < 1$ or 0.25 mrad of the beam axis (centre of mass frame). The curves are as described in Fig. 4.1. The lighter grey curves again show other production channels from meson decay [37, 237], and parton-level Drell-Yan [237] processes relevant at higher mass. See the text in Section 4.2 and Section 4.3 for further details.

4.2 Proton Bremsstrahlung

We will focus our attention in this chapter on bremsstrahlung, which is important for the forward production of dark sector mediators with hadronic scale mass, particularly due to the possibility of resonant mixing with hadronic states. This is a complex process to model for proton beams, and we will consider several different approximation strategies, which will allow an assessment of relative precision. In particular, we will compare four different approaches:

- ISR and FSR in quasi-elastic scattering
- ISR in non-single diffractive scattering via the quasi-real approximation
- Hadronic generalization of the WW approximation
- Modified WW approximation

These approaches are described in more detail below. In all cases, a timelike form factor for coupling to the proton provides resonant enhancements and is discussed separately.

4.2.1 ISR and FSR in quasi-elastic scattering

We can build a model of proton bremsstrahlung by adding initial state radiation (ISR) and final state radiation (FSR) to the pomeron exchange model for pp elastic scatter-

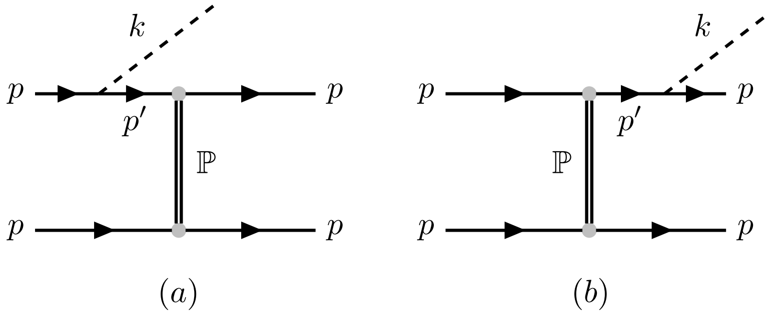

Figure 4.3: Dark state radiation from (a) initial state, and (b) final state proton bremsstrahlung through pomeron exchange. The label p' stands for the intermediate proton's momentum.

ing, as represented by the two Feynman diagrams in Fig. 4.3. Note that emission from the target proton into the forward region is negligible compared with that from the ultra-relativistic beam proton (as discussed for the photon bremsstrahlung in electron scattering [238]). Also note that u-channel (exchange) diagrams are sub-leading in the regime of high energy but soft (small-t) scatterings, since $t \ll u \sim s$.

We employ a popular parameterization to model the interaction of forward pp elastic scattering at high energies [239]. This parameterization encompasses single Pomeron exchange [240], and multiple exchanges [241, 242]. The details of this model are summarized in Appendix A, and we present a comparison of this model to data in Fig. A.3. The soft-pomeron exchange, relevant for small momentum transfer processes, emerges in the context of forward pp scattering and provides crucial insights into understanding diffractive phenomena [240, 243]. Soft-Pomeron trajectories and couplings are phenomenological numbers fitted from experiments. The single-Pomeron exchange effectively describes the measured pp total and elastic cross sections at high energies, as well as small-t processes. On the other hand, the QCD Pomeron represents a gluonic entity in a color singlet state in high-energy hadronic collisions with a large transverse momentum. Hard-Pomeron can be envisioned as a summation of multi-particle ladders formed by exchanging two t-channel gluons, and its corresponding couplings can potentially be computed using perturbative QCD [244, 245]. The Pomeron describes the asymptotic behaviour of elastic and inelastic hadron processes at high energies [246] (see Ref. [247] for a review).

To facilitate the computation of proton bremsstrahlung in quasi-elastic scattering, we express the parameterization of the pp elastic scattering in terms of a phenomenological soft pomeron propagator, denoted as $G_{\mathbb{P}}(s,t)g^{\mu\nu}$, and an effective proton-pomeron vertex $\Gamma^\mu_{\mathbb{P}}(t)$ as outlined in Appendix A. Utilizing the phenomenological pomeron propagator and vertices, we calculate the dark bremsstrahlung rate associated with the diagrams depicted in Fig. 4.3. Considering radiation from both incoming and outgoing beam protons with 4-momentum $k^\mu = (E_k, \vec{k})$, the contribution from the quasi-elastic process $pp \to ppD$ (where $D = V, S$) in the lab frame is given by

$$\frac{d^2\sigma^{\rm el}_{pp\to ppD}}{dE_k d\cos\theta_k} = \frac{1}{64(2\pi)^4 p_p m_p^2} \frac{|\vec{k}|}{|\vec{p}_p - \vec{k}|} \int dt d\phi \, |\overline{\mathcal{M}^{pp\to ppD}}|^2 \,, \tag{4.1}$$

where θ_k is the dark vector/scalar emission angle with respect to the beam, while ϕ denotes the azimuthal angle of the momentum transfer, which will be introduced shortly.

Here we present details of the calculation of the summed and averaged square of the 2 to 3 matrix element $|\overline{\mathcal{M}^{pp\to ppD}}|^2$ for the ISR plus FSR process,

$$p(p_1) + p(p_2) \to p(p_3) + p(p_4) + D(k), \tag{4.2}$$

where the dark state $D = \{S, V\}$ is emitted from either the beam or scattered proton with momentum p_1 and p_3, respectively (see e.g. [226]). We define the Mandelstam variables $s{=}(p_1{+}p_2)^2$, $s'{=}(p_1{+}p_2{-}k)^2$, and $t{=}q^2{=}(p_4{-}p_2)^2$. When $s \gg t$, the matrix elements for the bremsstrahlung processes depicted in Fig. 4.3 are given by,

$$i\mathcal{M}^{2\to 3}_S = i\bar{u}(p_4)\Gamma^\mu_{\mathbb{P}}(t)u(p_2)\bar{u}(p_3)S_\mu u(p_1), \tag{4.3}$$

$$i\mathcal{M}^{2\to 3}_V = i\bar{u}(p_4)\Gamma^\mu_{\mathbb{P}}(t)u(p_2)\bar{u}(p_3)V_{\mu\alpha} u(p_1)\epsilon^{\alpha\star}_k, \tag{4.4}$$

with

$$\begin{aligned} S^\mu = ig_S F^p_{1,S}(m_S^2)\Big[& G_{\mathbb{P}}(s',t)\Gamma^\mu_{\mathbb{P}}(t)F_{pp^\star D}\big((p_1{-}k)^2\big)\frac{i(\not{p}_1{-}\not{k}{+}m_p)}{(p_1{-}k)^2{-}m_p^2} + \\ & \frac{i(\not{p}_3{+}\not{k}{+}m_p)}{(p_3{+}k)^2{-}m_p^2}F_{pp^\star D}\big((p_3{+}k)^2\big)\Gamma^\mu_{\mathbb{P}}(t)G_{\mathbb{P}}(s,t)\Big], \end{aligned} \tag{4.5}$$

and

$$\begin{aligned} V^{\mu\alpha} = ig_V F^p_{1,V}(m_V^2)\Big[& G_{\mathbb{P}}(s',t)\Gamma^\mu_{\mathbb{P}}(t)F_{pp^\star D}\big((p_1{-}k)^2\big)\frac{i(\not{p}_1{-}\not{k}{+}m_p)}{(p_1{-}k)^2{-}m_p^2}\gamma^\alpha + \\ & \gamma^\alpha\frac{i(\not{p}_3{+}\not{k}{+}m_p)}{(p_3+k)^2{-}m_p^2}F_{pp^\star D}\big((p_3{+}k)^2\big)\Gamma^\mu_{\mathbb{P}}(t)G_{\mathbb{P}}(s,t)\Big], \end{aligned} \tag{4.6}$$

where the effective pomeron propagator $G_{\mathbb{P}}$ and vertex function $\Gamma^\mu_{\mathbb{P}}$ are introduced in Eq. (A.1), g_V and g_S are the effective dark vector and scalar couplings to the proton, and ϵ^μ is the final state dark vector polarization with $\sum_{\text{pol}} \epsilon^\mu_k \epsilon^\nu_k = -g^{\mu\nu} + k^\mu k^\nu / m_V^2$. When considering radiation from the proton p, the time-like vector and scalar proton form factors, $F^p_{1,V}(m_V^2)$ and $F^p_{1,S}(m_S^2)$, as well as the off-shell form factor $F_{pp^\star D}$, can be introduced in the form presented in Section 4.2.3.

The matrix element, averaged over spins and summed over the initial spins takes the form,

$$|\overline{\mathcal{M}_D^{2\to3}}|^2 = \frac{1}{4} \sum_{\text{spin}} |\mathcal{M}_D^{2\to3}|^2 = T_{\mu\nu} B_D^{\mu\nu}\,, \tag{4.7}$$

where the initial spin-averaged target and beam proton tensors are given by,

$$T^{\mu\nu} = \frac{1}{2} \mathrm{Tr}\big[(\not{p}_4 + m_p)\Gamma^\mu_{\mathbb{P}}(\not{p}_2 + m_p)\Gamma^{\nu\star}_{\mathbb{P}}\big], \tag{4.8}$$

$$B_V^{\mu\nu} = \frac{1}{2} \mathrm{Tr}\big[(\not{p}_3 + m_p)V^{\mu\alpha}(\not{p}_1 + m_p)V^{\beta\nu\star}\big](-g_{\alpha\beta} + \frac{k_\alpha k_\beta}{m_V^2}), \tag{4.9}$$

$$B_S^{\mu\nu} = \frac{1}{2} \mathrm{Tr}\big[(\not{p}_3 + m_p)S^{\mu}(\not{p}_1 + m_p)S^{\nu\star}\big]. \tag{4.10}$$

The differential cross section for the process Eq. (4.2) in the lab frame,

$$\begin{aligned} d\sigma = {} & \frac{1}{4|\vec{p}_1| m_p} |\overline{\mathcal{M}_D^{2\to3}}|^2 (2\pi)^4 \delta^{(4)}(p_1 + q - k - p_3) \\ & \times \frac{d^3\vec{p}_3}{(2\pi)^3 2E_3} \frac{d^3\vec{p}_4}{(2\pi)^3 2E_4} \frac{d^3\vec{k}}{(2\pi)^3 2E_k}\,, \end{aligned} \tag{4.11}$$

takes the following form after integrating over $\vec{p_3}$ and changing variables from $\vec{p_4}$ to $\vec{q}$ (the three-momentum of $q^\mu = (p_2^\mu - p_4^\mu)$), and using the remaining δ-function to integrate out $|\vec{q}|$,

$$d\sigma = \frac{|\overline{\mathcal{M}_D^{2\to3}}|^2 \, d^3\vec{k}}{32(2\pi)^5 |\vec{p}_1| m_p E_k} \frac{Q^2 \, d\cos\theta_q d\phi_q}{\big[Q(E_3 + E_4) - R E_3 \cos\theta_q\big]}\,. \tag{4.12}$$

Here θ_q and ϕ_q are the polar and azimuthal angles of $\vec{q}$ in the direction of $\vec{R} = \vec{k} - \vec{p}_1$, $Q = |\vec{q}|$, $R = |\vec{R}|$, and $\cos\theta_q = (m_p^2 + R^2 + Q^2 - E_3^2)/(2QR)$.

Next we change variables from θ_q to $t = q^2$ to obtain

$$\frac{d^2\sigma}{dE_k d\cos\theta_k} = \frac{1}{64(2\pi)^4 p_1 m_p^2} \frac{|\vec{k}|}{|\vec{p}_1 - \vec{k}|} \int_{t_{min}}^{t_{max}} dt \int_0^{2\pi} d\phi_q \, |\overline{\mathcal{M}^{pp\to ppD}}|^2\,, \tag{4.13}$$

where $t = 2m_p(m_p - \sqrt{Q^2 + m_p^2})$, and the integration boundaries of t correspond to

$$[Q]^{\pm} = \frac{R}{2} \pm \frac{(E_1 - E_k + m_p)}{2}\sqrt{1 - \frac{4m_p^2}{(E_1 - E_k + m_p)^2 - R^2}}. \tag{4.14}$$

The equivalent center of mass (CM) version of Eq. (4.13) has a similar form,

$$\frac{d^2\sigma}{dE_k^\star d\cos\theta_k^\star} = \frac{1}{64(2\pi)^4 p_{\rm CM} E_{\rm CM}^2}\int_{\tilde{t}_{min}}^{\tilde{t}_{max}} d\tilde{t}\int_0^{2\pi} d\phi_{\tilde{q}}\, |\overline{\mathcal{M}^{pp\to ppD}}|^2\,, \tag{4.15}$$

where we defined the invariant $\tilde{t} \equiv (p_1 + p_2 - p_4)^2 = m_p^2 + E_{\rm CM}(E_{\rm CM} - 2\sqrt{\tilde{Q}^2 + m_p^2})$, and starred ($\star$) variables are defined in the CM frame. The integration boundaries for $\tilde{t}$ correspond to

$$[\tilde{Q}]^{\pm} = \frac{k^\star}{2} \pm \frac{(E_{\rm CM} - E_k^\star)}{2}\sqrt{1 - \frac{4m_p^2}{(E_{\rm CM} - E_k)^2 - k^2}}. \tag{4.16}$$

To compare with the other approximate methods of calculation, we will find it convenient to define the differential splitting probability of the proton to emit a dark state in the form,

$$d\mathcal{P}_D^{\rm split.} = \frac{1}{\sigma_{pp}^{\rm el}(s)}\frac{d^2\sigma_{pp\to ppD}^{\rm el}}{dE_k d\cos\theta_k}. \tag{4.17}$$

The resulting splitting probability of dark state emission as a function of the scalar/vector energy E_k and angle θ_k is shown in the next section in Fig. 4.5 and Fig. 4.6, respectively. In the plots, we also compare the complete ISR + FSR calculation via pomeron exchange with the result from ISR only, which as discussed below can be associated with NSD scattering with various final states. In considering radiation during quasi-elastic scattering, we observe a strong interference between the ISR and FSR amplitudes, and a significant cancelation which suppresses the final result as a generic feature of bremsstrahlung [248, 249] for both scalar and vector cases. Similar results hold for varied choices of m_D, and emitted angles and energies. For completeness, we note that these radiative topologies are subject to soft and collinear divergences when the radiated particle is parametrically light, and certain divergences are only canceled on considering loop corrections to the underlying scattering process. We will not account for these effects here, as the mediator mass in the regimes of interest provides an infrared regulator that is sufficient to cut off those divergences.

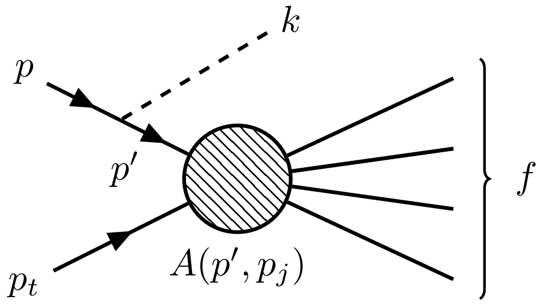

Figure 4.4: Dark sector initial state radiation in a generic non diffractive scattering event.

Using the single diffractive cross section in Eq. (A.14), one can also calculate the differential cross section for dark state radiation through pp bremsstrahlung. This computation has not been done explicitly in this study, but based on the large cancellation observed in the quasi-elastic regime, we anticipate a similar cancellation to also occur in the case of single diffractive topologies. In addition, since single diffractive events make up at most 10% of the total cross-section at the relevant energies, we will focus now on the non-single diffractive topologies.

4.2.2 ISR in non-single diffractive scattering and the quasi-real approximation

In quasi-elastic and single diffractive scattering, radiation from both initial and final protons is tightly connected, and as observed above significant interference between the two amplitudes leads to a suppression of the total rate as compared to ISR or FSR alone. As a result, in order to identify the leading processes, we consider radiation in pp non-single diffractive topologies, where both the beam proton and target proton dissociate after scattering. In such processes, radiation from particles other than proton in the final state should not interfere destructively with proton ISR, thus one expects no significant cancellation between ISR and FSR in non-single diffractive events.

The ISR contribution can be estimated by artificially turning off the FSR amplitude in the consideration of quasi-elastic scattering above. However, to test this estimate, we now discuss another approach for evaluating the proton bremsstrahlung cross-section, where instead of limiting the final state, the intermediate fermion propagator in the ISR diagram is approximated [250, 251, 252, 253] within an on-shell approach (also known as time-ordered perturbation theory) used by Altarelli-Parisi [225]. We will refer to this as the "quasi-real approximation".

We can compare the process of scattering of a beam proton by a target proton $pp_t \to X$, with another process, $pp_t \to X + D$ involving an additional dark state D emitted from the incoming proton as shown in Fig. 4.4, along with any possible particles in the final state X. Under certain kinematic conditions, to be formulated below, the cross-section for the second process can be expressed in terms of the cross section of its sub-process, along with the splitting probability of emission of a single dark state in the collision. Let us denote the corresponding amplitude for the hard scattering process without radiation as $\mathcal{M}_r^{pp_t\to f} = A(p,p_j)u^r(p)$, where $u^r(p)$ is the spinor of the incoming proton with helicity r and momentum p, and $A(p,p_j)$ is the remaining part of the amplitude for the hard scattering with p_j denoting the momenta of the other particles in the process. The amplitude for dark ISR off the incoming proton with momentum k can then be obtained from the amplitude for the original process by adding an external dark state line,

$$A(p,p_j) \to A(p-k,p_j)\frac{i(\not{p}-\not{k}+m_p)}{(p-k)^2-m_p^2}. \tag{4.18}$$

In the framework of the quasi-real approximation, which is best suited to the high energy limit, the intermediate proton propagator can be approximated as

$$\frac{i(\not{p}-\not{k}+m_p)}{(p-k)^2-m_p^2} \approx \frac{i}{2E_{p'}}\frac{\sum_{r'} u^{r'}(p-k)\bar{u}^{r'}(p-k)}{E_p-E_k-E_{p'}}, \tag{4.19}$$

where E_p, E_k, and $E_{p'} = \sqrt{(\vec{p}-\vec{k})^2+m_p^2}$ are the energy of the incoming proton, the radiated dark state, and the intermediate proton, respectively. Using this approximation, at the cost of being non-covariant, the numerator of the intermediate proton propagator in Eq. (4.18) can be replaced by the polarization sum for an on-shell proton resulting in the following matrix element for dark state emission off the initial state proton,

$$\mathcal{M}_r^{pp_t\to Df}(p,k,p_j) \approx \sum_{r'} \mathcal{M}_{r'}^{pp_t\to f}(p',p_j)\left(\frac{V^D_{r'r}}{2k\cdot p-m_D^2}\right). \tag{4.20}$$

Here we have defined the vertex functions $V^S_{r'r} = g_S\bar{u}^{r'}(p')u^r(p)$ and $V^V_{r'r,\lambda} = g_V\bar{u}^{r'}(p')\not{\epsilon}^\star_\lambda(k)u^r(p)$, corresponding to dark scalar and dark vector radiation, respectively. Note that now the matrix element $\mathcal{M}^{pp_t\to f}$ involves the modified on-shell momentum $p' \sim p - k$. Now by integrating over the phase space of the remaining particles in the final state X, the cross-section for the process with dark state emission can be factorized as follows (with further technical details to be discussed later in this section),

$$d\sigma^{pp_t\to Df}(s) \approx d\mathcal{P}_{p\to p'D} \times \sigma_{pp}^{\rm NSD}(s'), \tag{4.21}$$

where we have again introduced the differential splitting probability,

$$d\mathcal{P}_{p\to p'D} \equiv w^D(z, p_T^2)dp_T^2dz, \tag{4.22}$$

for radiating a dark state given a longitudinal momentum fraction z of the proton beam momentum and transverse momentum p_T. We take into account only the non-single diffractive cross section $\sigma_{pp}^{\rm NSD}(s')$, since as discussed above radiation in quasi-elastic processes is suppressed by ISR and FSR interference. The residual scattering cross section involves $s' = 2m_p(p(1-z)+m_p)$ which accounts for the momentum of the emitted dark state. Deferring the details to Section 4.2.2, the resulting splitting functions read

$$\begin{aligned} w_S(z, p_T^2) = &\frac{\alpha_\theta}{2\pi}F_S^2(m_S^2, m_p^2 - H/z) \\ &\times \frac{1}{2H}\left[z + z(1-z)\left(\frac{4m_p^2 - m_S^2}{H}\right)\right], \end{aligned} \tag{4.23}$$

and

$$\begin{aligned} w_V(z, p_T^2) = &\frac{\alpha_\epsilon}{2\pi}F_V^2(m_V^2, m_p^2 - H/z) \\ &\times \frac{1}{H}\left[z - z(1-z)\left(\frac{2m_p^2 + m_V^2}{H}\right) + \frac{H}{2zm_V^2}\right], \end{aligned} \tag{4.24}$$

with $\alpha_\theta = g_{SNN}^2\theta^2/4\pi$, $\alpha_\epsilon = \alpha_{\rm em}\epsilon^2$, and the kinematic structure function is given by

$$H(z, p_T^2) \equiv p_T^2 + z^2m_p^2 + (1-z)m_D^2. \tag{4.25}$$

The functions $F_S(k^2)$ and $F_V(k^2)$ are scalar and vector nucleon form factors, which are discussed in detail below in Section 4.2.3. The expression in Eq. (4.23) agrees with the result of Ref. [198] in the case of scalar bremsstrahlung.

Note that the terms appearing in Eq. (4.23) and Eq. (4.24) have poles when the structure function $H(z,p_T^2) \to 0$. In the massless and collinear limit, the approximation gives the standard soft photon bremsstrahlung result with a $1/H \sim 1/p_T^2$ singularity [43]. Indeed, assuming a smooth limit as $m_V \to 0$, one restores the Altarelli-Parisi splitting kernel, $w_V \propto \frac{\alpha}{2\pi}\frac{1}{p_T^2}\frac{1+(1-z)^2}{z}$, for $m_p \ll p_T$. However, finite $m_D = m_V, m_S$ regulates this singularity, leading to $1/H \approx 1/m_D^2$. The final term in Eq. (4.24) proportional to $1/m_V^2$ arises due to the longitudinal polarization of the massive vector, so the $m_V \to 0$ limit is not smooth, but this term is not numerically important for the parameters considered here.

The applicability of this approximation in which the ISR process is factorized from the underlying hard scattering depends on a number of kinematic conditions. First, we observe that the shift from the mass shell $p'^2 - m_p^2 = (p-k)^2 - m_p^2 = 0$ for the intermediate proton in the $pp^\star D$ vertex must be considerably smaller than the momentum transfer in the hard scattering denoted by the shaded central block of Fig. 4.4. Fortunately, the required suppression when the intermediate proton line goes far off-shell at the $pp^\star D$ vertex is accounted for by the off-shell (or transition) form-factor Eq. (4.53) described in the next section. The form factor is constructed to reach its maximum value $(= 1)$ if the invariant $p'^2 - m_p^2 \approx -H/z$ is much less than a specified cut-off value $\Lambda_p \sim m_p$ associated with the hard scattering. We will vary the hard scale over the range $1 \lesssim \Lambda_p \lesssim 2$ GeV, with the central value of 1.5 GeV, to assess the impact of this kinematic constraint. As a second kinematic condition, the propagator approximation in Eq. (4.19) requires $E_{p'} - (E_p - E_k) \ll 2E_{p'}$. Along with the generic requirements that the process is relativistic with the beam energy being the dominant kinematic variable, this leads to two further kinematic consistency conditions,

$$\frac{H}{4z(1-z)^2 p_p^2} \ll 1, \tag{4.26}$$

$$p_T,\, m_p\,(m_D) \ll E_p\,(E_k). \tag{4.27}$$

For concreteness, we demand that the variable on the left of each inequality in Eq. (4.26) and Eq. (4.27) be at most 20% of the right hand side.

In combination, these kinematic conditions lead to a restricted range for z, as well as an upper bound on p_T which depends on m_D and the characteristic scale Λ_p. As discussed further below, varying Λ_p as described above leads to the red shaded bands in Fig. 4.1 and Fig. 4.2. This serves as an estimate for the theoretical uncertainty in our calculation, as the systematic uncertainty in the non-diffractive cross section in Eq. (4.21) is somewhat smaller.

Initial State Radiation

Let us now proceed to discuss the technical details of calculating the Initial State Radiation. Consider the process of scattering of a beam proton by a target proton $pp_t \to X$, where X denotes any number of charged (and neutral) particles in the final state. Along with this process, let us consider another process, $pp_t \to f + D$, involving an additional dark state D which is emitted from the incoming proton as shown in Fig. 4.4. Under certain kinematic conditions (formulated below), the cross-section for the second process can be represented as a product of two independent factors, the cross-section of the former sub-process and the splitting probability for the emission of a single dark state in the collision.

The corresponding amplitude for the hard process $pp_t \to X$ can be written as

$$\mathcal{M}_r^{pp_t \to f} = A(p, p_j) u^r(p), \tag{4.28}$$

where $u^r(p)$ is the spinor of the incoming proton with the helicity r and momentum p, and $A(p, p_j)$ the remaining part of the amplitude for the hard scattering with p_j denoting the momenta of the other particles in the scattering.

For the process of dark state emission from the incoming proton in the initial state, the matrix element can be obtained from that for the original process by adding an external dark state line, and reads

$$\mathcal{M}_r^{pp_t \to Sf}(p, k, p_j) = i g_S A(p-k, p_j) \frac{i(\not{p} - \not{k} + m_p)}{(p-k)^2 - m_p^2} u^r(p), \tag{4.29}$$

$$\mathcal{M}_{r\lambda}^{pp_t \to Vf}(p, k, p_j) = i g_V A(p-k, p_j) \frac{i(\not{p} - \not{k} + m_p)}{(p-k)^2 - m_p^2} \not{\epsilon}_\lambda^\star(k) u^r(p), \tag{4.30}$$

where k and $p' = p - k$ denote the four-momenta of the dark state and the internal proton, respectively.

When the transverse momentum p_T of the radiated particle is small compared to the dominant longitudinal component, the kinematic variables within the infinite momentum frame of the rapidly moving beam proton can be parametrized as follows:

$$\begin{aligned} p^\mu &= (p_p + \frac{m_p^2}{2p_p}, \mathbf{0}, p_p), \\ k^\mu &= (zp_p + \frac{p_T^2 + m_D^2}{2zp_p}, \mathbf{p}_T, zp_p), \\ p'^{\,\mu} &= ((1-z)p_p + \frac{p_T^2 + m_p^2}{2p_p(1-z)}, -\mathbf{p}_T, (1-z)p_p), \end{aligned} \tag{4.31}$$

where z is the fraction of longitudinal momentum carried by D, and the transverse momentum $\mathbf{p}_T = (p_T \cos\phi, p_T \sin\phi)$ is a measure of the non-collinearity of the radiated scalar which determines how far off shell the intermediate proton is, as given by $(p-k)^2 = m_p^2 - H/z$, where we have defined the kinematic structure function

$$H(z, p_T^2) \equiv p_T^2 + z^2 m_p^2 + (1-z)m_D^2. \tag{4.32}$$

We use the representation for the intermediate proton propagator of Eq. (4.29) in the framework of the quasi-real approximation which appears suitable for evaluating the cross section in the high energy limit. The intermediate proton propagator corresponding to two possible time orderings can be decomposed as follows,

$$\frac{i(\not{p} - \not{k} + m_p)}{(p-k)^2 - m_p^2} = \frac{i}{2E_{p'}} \sum_{r'} \left[\frac{u^{r'}(p-k)\bar{u}^{r'}(p-k)}{E_p - E_k - E_{p'}} + \frac{v^{r'}(-p-k)\bar{v}^{r'}(-p-k)}{E_p - E_k + E_{p'}} \right], \tag{4.33}$$

where E_p, $E_{p'}$, and E_k are defined in Eq. (4.31) as the energy of the incoming proton, the intermediate proton and the radiated dark state.

In the collinear limit, $k \cdot p/p_p^2 \ll 1$, where the dark states are radiated almost parallel to the energetic beam proton, the denominator of the first term on the right hand side of Eq. (4.33) is small relative to the denominator of the second term, $E_{p'} + E_k - E_p \ll E_{p'} - E_k + E_p$, which implies,

$$\frac{H}{4z(1-z)^2 p_p^2} \ll 1. \tag{4.34}$$

Provided that the above kinematic condition is satisfied, one can retain the first term while neglecting the second. Thus the numerator of the proton propagator in Eq. (4.29) can be replaced with the polarization sum of an on-shell fermion, with the result

$$\mathcal{M}_r^{pp_t\to Sf} \approx -A(p',p_j)\sum_{r'} u^{r'}(p')\frac{\left(g_S\bar{u}^{r'}(p')u^r(p)\right)}{(p-k)^2-m_p^2}$$
$$= \sum_{r'}\mathcal{M}_{r'}^{pp_t\to f}(p',p_j)\left(\frac{z}{H}\right)V_{r'r}^S, \tag{4.35}$$

$$\mathcal{M}_{r,\lambda}^{pp_t\to Vf} \approx -A(p',p_j)\sum_{r'} u^{r'}(p')\frac{\left(g_V\bar{u}^{r'}(p')\not{\epsilon}_\lambda^\star(k)u^r(p)\right)}{(p-k)^2-m_p^2}$$
$$= \sum_{r'}\mathcal{M}_{r'}^{pp_t\to f}(p',p_j)\left(\frac{z}{H}\right)V_{r'r,\lambda}^V, \tag{4.36}$$

where we defined the vertex functions $V_{r'r}^S = g_S\bar{u}^{r'}(p')u^r(p)$ and $V_{r'r,\lambda}^V = g_V\bar{u}^{r'}(p')\not{\epsilon}_\lambda^\star(k)u^r(p)$. Note that now the matrix element $\mathcal{M}^{pp_t\to f}$ involves the reduced momentum $p' \sim (1-z)p$.

To calculate the vertex functions above, we use the Pauli representations of the right-handed and left-handed helicity states $u^r(p)$, for $r=\pm$, with momentum $\mathbf{p} = |\vec{p}|\,(\sin\theta\cos\phi, \sin\theta\sin\phi, \cos\theta)$, normalized to $u^\dagger u = 2E$ particles per unit volume, which take the form,

$$u^{(+)}(p) = \sqrt{E+m}\Big(c, s\,e^{i\phi}, \frac{|\vec{p}|}{E+m}c, \frac{|\vec{p}|}{E+m}s\,e^{i\phi}\Big)^T,$$
$$u^{(-)}(p) = \sqrt{E+m}\Big(-s, c\,e^{i\phi}, \frac{|\vec{p}|}{E+m}s, \frac{-|\vec{p}|}{E+m}c\,e^{i\phi}\Big)^T, \tag{4.37}$$

where $s \equiv \sin(\theta/2)$ and $c \equiv \cos(\theta/2)$. The expressions for the circular and longitudinal polarization vectors associated to the dark vector with momentum $\mathbf{k} = |\vec{k}|\,(\sin\theta\cos\phi, \sin\theta\sin\phi, \cos\theta)$ also read,

$$\epsilon_\pm^\mu(k) = \frac{e^{\pm i\phi}}{\sqrt{2}}\Big(0, \mp\cos\theta\cos\phi+i\sin\phi, \mp\cos\theta\sin\phi-i\cos\phi, \pm\sin\theta\Big),$$
$$\epsilon_L^\mu(k) = \frac{1}{m_V}\Big(|\vec{k}|, E_k\sin\theta\cos\phi, E_k\sin\theta\sin\phi, E_k\cos\theta\Big). \tag{4.38}$$

Thus, by using the kinematic variables defined in Eq. (4.31), one finds the following explicit expressions for the spinors

$$\begin{aligned} u^{+}(p)&=\left(\sqrt{E_p+m_p}, 0, \frac{p_p}{\sqrt{E_p+m_p}}, 0\right)^T, \qquad (4.39)\\ u^{-}(p)&=\left(0, \sqrt{E_p+m_p}, 0, \frac{-p_p}{\sqrt{E_p+m_p}}\right)^T,\\ u^{+}(p')&=\sqrt{E_{p'}+m_p}\left(1, \frac{p_T\, e^{i(\phi+\pi)}}{2(1-z)p_p}, \frac{(1-z)p_p}{E_{p'}+m_p}, \frac{\frac{1}{2}p_T\, e^{i(\phi+\pi)}}{E_{p'}+m_p}\right)^T,\\ u^{-}(p')&=\sqrt{E_{p'}+m_p}\left(\frac{-p_T}{2(1-z)p_p}, e^{i(\phi+\pi)}, \frac{\frac{1}{2}p_T}{E_{p'}+m_p}, \frac{-(1-z)p_p\, e^{i(\phi+\pi)}}{E_{p'}+m_p}\right)^T, \end{aligned}$$

and the polarization vectors,

$$\epsilon^{\mu}_{\pm}(k) = \frac{1}{\sqrt{2}}\Big(0, 1, \pm i, -\frac{p_T}{z p_p}e^{\pm i\phi}\Big), \qquad (4.40)$$

$$\epsilon^{\mu}_{L}(k) = \frac{1}{m_V}\Big(z p_p, p_T\cos\phi, p_T\sin\phi, z p_p\Big). \qquad (4.41)$$

Straightforward algebra then yields the following vertex functions up to $\mathcal{O}(m_p^2, p_T^2)$,

$$V^S_{r'r} = \frac{g_S}{\sqrt{1-z}} e^{i(\frac{r-1}{2})\phi}\Bigg[r(2-z)m_p\delta_{r'r} - p_T\delta_{r',-r}\Bigg], \qquad (4.42)$$

$$V^V_{r'r,\lambda=\pm} = \frac{g_V\sqrt{2}}{z\sqrt{1-z}} e^{-i\lambda\phi} e^{i(\frac{r-1}{2})\phi}\Bigg[p_T\big((1-z)\delta_{r,-\lambda} - \delta_{r\lambda}\big)\delta_{r'r} - \lambda z^2 m_p \delta_{r\lambda}\delta_{r',-r}\Bigg], \qquad (4.43)$$

$$V^V_{r'r,\lambda=L} = \frac{g_V}{z\sqrt{1-z}} \frac{r e^{i(\frac{r-1}{2})\phi}}{m_V} \times \Bigg(p_T^2 + z^2 m_p^2 - (1-z)m_V^2\Bigg)\delta_{r'r}, \qquad (4.44)$$

We then obtain

$$V^S_{r',r}\big(V^S_{r'',r}\big)^{\star} = g_S^2\Bigg(\mathcal{I}_S\,\delta_{r'r}\delta_{r'',r'} + \mathcal{J}_S\, r'\,\big(\delta_{r'r} - \delta_{r',-r}\big)\delta_{r'',-r'}\Bigg), \qquad (4.45)$$

and

$$\sum_{\lambda=\pm,L} V^V_{r',r,\lambda}\big(V^V_{r'',r,\lambda}\big)^{\star} = g_V^2\Bigg(\mathcal{I}_V\,\delta_{r'r}\delta_{r'',r'} + \mathcal{J}_V\, r'\,\big(\delta_{r'r} - \delta_{r',-r}\big)\delta_{r'',-r'}\Bigg),$$

which involves the functions,

$$
\begin{aligned}
\mathcal{I}_S &= \frac{(2-z)^2 m_p^2 + p_T^2}{1-z}, \\
\mathcal{J}_S &= -\frac{(2-z)}{1-z} m_p p_T, \\
\mathcal{I}_V &= \frac{2}{(1-z)} \Bigg(\frac{1+(1-z)^2}{z^2} p_T^2 + z^2 m_p^2 \\
&\qquad\qquad + \frac{1}{2z^2 m_V^2} \Big(p_T^2 + z^2 m_p^2 - (1-z) m_V^2 \Big)^2 \Bigg), \\
\mathcal{J}_V &= 0, \qquad (4.46)
\end{aligned}
$$

which are independent of ϕ. Note that the last term in $\mathcal{I}_\mathcal{V}$ arises only for the massive vector boson, due to the longitudinal polarization given in Eq. (4.41).

Inserting the vertex functions Eq. (4.45) and Eq. (4.46) into Eq. (4.35), the absolute square of the matrix element summed over polarizations of the final proton can now be expressed in the form,

$$
\begin{aligned}
&\frac{1}{2} \sum_{r(,\lambda)} |\mathcal{M}_{r(,\lambda)}^{pp_t \to Df}(p,k,p_j)|^2 \\
&= \Big(\frac{z}{H}\Big)^2 \sum_{r,r',r''(,\lambda)} V_{r',r(,\lambda)}^D \big(V_{r'',r(,\lambda)}^D\big)^\star \times \frac{1}{2} \mathcal{M}_{r'}^{pp_t \to f}(p',p_j) \Big(\mathcal{M}_{r''}^{pp_t \to f}(p',p_j) \Big)^* \\
&= g_D^2 \Big(\frac{z}{H}\Big)^2 \mathcal{I}_D |\overline{\mathcal{M}^{p'p_t \to f}}|^2, \qquad (4.47)
\end{aligned}
$$

which importantly is proportional to the matrix element squared for the subprocess $pp_t \to X$. Note that terms with $\big(\delta_{r'r} - \delta_{r',-r}\big)\delta_{r'',-r'}$ in Eq. (4.45) and Eq. (4.46) vanish. This is because collinear emission does not change the proton's helicity and only transitions in which the helicity is conserved contribute to the unpolarized matrix element in Eq. (4.47).

Finally, by integrating over the final state phase space, the cross section for dark state emission is expressed via the unpolarized cross section of the sub-process $pp_t \to$

X without radiation at the reduced momentum $(1-z)p_p$,

$$\begin{aligned} d\sigma^{pp_t\to Df}(s) &= \frac{1}{4E_pE_{p_t}}\frac{d^3k}{(2\pi)^3 2E_k}\prod_f \frac{d^3p_f}{(2\pi)^3 2E_f}|\overline{\mathcal{M}^{p'p_t\to Df}}|^2(2\pi)^4\delta(p+p_t-k-p_f) \\ &\approx g_D^2\Big(\frac{z}{H}\Big)^2\mathcal{I}_D\frac{dp_T^2dz}{16\pi^2 z}\frac{E_{p'}}{E_p}\int\frac{1}{4E_{p'}E_{p_t}}\prod_f\frac{d^3p_f}{(2\pi)^3 2E_f}|\overline{\mathcal{M}^{p'p_t\to f}}|^2(2\pi)^4\delta(p'+p_t-p_f) \\ &\approx w_D(z,p_T^2)dp_T^2dz\,\sigma^{pp_t\to f}(s')\equiv d\mathcal{P}_{p\to p'D}\times\sigma^{pp_t\to f}(s'), \end{aligned} \tag{4.48}$$

where the difference in the energy conservation arguments in the delta-functions is neglected in the collinear limit, $p_T \ll p_p$. Here we have introduced the differential splitting probability $d\mathcal{P}_{p\to p'D} = w_D(z,p_T^2)dp_T^2dz$ for radiating a dark state with longitudinal momentum fraction z of the initial beam proton and transverse momentum p_T. The splitting functions have the form,

$$w_S(z,p_T^2) = \frac{\alpha_\theta}{2\pi}\frac{1}{2H}\left[z+z(1-z)\left(\frac{4m_p^2-m_S^2}{H}\right)\right], \tag{4.49}$$

and

$$w_V(z,p_T^2) = \frac{\alpha_\epsilon}{2\pi}\frac{1}{H}\left[z-z(1-z)\left(\frac{2m_p^2+m_V^2}{H}\right)+\frac{H}{2zm_V^2}\right], \tag{4.50}$$

with $\alpha_\theta = g_{SNN}^2\theta^2/4\pi$, $\alpha_\epsilon = \alpha_{\rm em}\epsilon^2$. The expression in Eq. (4.49) agrees well with the result of [198] in the case of scalar bremsstrahlung. Adding the time-like and off-shell form factors introduced in Section 4.2.3 to the splitting functions above is straightforward.

4.2.3 Time-like and off-shell form factors

The coherent emission of a dark vector or scalar from a proton, having timelike momentum, requires the incorporation of a timelike form-factor to properly account for both the loss of coherence for momentum transfers above a GeV, and resonant enhancement due to the mixing of the radiated dark state with hadronic degrees of freedom with the same quantum numbers.

The vector case coincides with the proton electromagnetic form factor $F_{1,p}(q^2)$, which can be extracted from elastic scattering and annihilation reactions (see Ref. [254] for a recent review). Numerous data sets in the spacelike kinematic region have allowed high-precision parametrizations, but the timelike region is more complex and statistics over the kinematic threshold, $q^2 > 4m_p^2$, are limited [255, 256], but it is this region involving low mass vector resonances that is of most interest to us. To make use of the data that exists, parametrizations in the low invariant mass regime have made use of the vector meson dominance (VMD) approach [257, 258] (see Ref. [259] for a recent review). Following [34], we make use of the following form-factor parametrization with a minimal number of free parameters which still achieves a good fit to data away from the threshold [258],

$$F_{1,V}^p(k_V^2) = \sum_{\rho,\omega} \frac{f_{\rho,\omega} m_{\rho,\omega}^2}{m_{\rho,\omega}^2 - k_V^2 - i m_{\rho,\omega} \Gamma_{\rho,\omega}}. \tag{4.51}$$

The fit parameters are $f_\rho = \{0.616, 0.223, -0.339\}$, and $f_\omega = \{1.011, -0.881, 0.369\}$, which account for mixing with ρ and ω resonances. In the mass region of interest, we only consider the three lightest mesons, accounting for each isovector and isoscalar mixing.

Following Ref. [260], lacking any data in the scalar channel, we take the same approach for the timelike scalar-nucleon form factor, incorporating mixing with isoscalar (and in principle isovector) $J^{PC} = 0^{++}$ scalar resonances through a sum of Breit-Wigner components,

$$F_{1,S}^p(k_S^2) = \sum_{\phi=f_0} \frac{f_\phi m_\phi^2}{m_\phi^2 - k_S^2 - i m_\phi \Gamma_\phi}, \tag{4.52}$$

where the parameters $f_{f_0} = \{0.28, 1.8, -0.99\}$ account for mixing with the three low-lying scalar f_0 resonances.

The timelike form-factors assume all legs are on-shell. However, the intermediate proton in ISR and FSR is off-shell, and to account for the off-shell leg at the $pp^\star D$ vertex, as in Ref. [261] we introduce a further hadronic form factor,

$$F_{pp^\star D}(p'^2) = \frac{\Lambda_p^4}{\Lambda_p^4 + (p'^2 - m_p^2)^2}, \tag{4.53}$$

which depends on the momentum of the intermediate proton $p'^2 = (p-k)^2$ rather than just the momentum transfer. The form factor is constructed to reach its maximum value ($= 1$) if the invariant $p'^2 - m_p^2 \approx -H/z$, which measures how far the intermediate proton line is off-shell, is much less than a specified cut-off value $\Lambda_p \sim m_p$. This off-shell hadronic form factor has been utilized in *e.g.* π and η [262, 263], kaon [264], and ω [265] photoproduction reactions, and also in meson- and photon-induced reactions on the nucleon [266, 267] to insure the gauge invariance of different contributions [268]. We vary the hard scale over the range $1 \lesssim \Lambda_p \lesssim 2$ GeV, with the central value of 1.5 GeV, to generate the results shown in Fig. 4.1 and Fig. 4.2.

To account for both effects discussed above, we define the product of the timelike form-factors in Eq. (4.51), Eq. (4.52) and the off-shell form factor in Eq. (4.53),

$$F_D(k^2, p'^2) \equiv F_{pp^\star D}(p'^2) \times F^p_{1,D}(k^2). \tag{4.54}$$

4.3 Results and comparisons

In this section, we present our results for the production rates of dark states via proton bremsstrahlung, and compare them with modifications of the Weizsacker-Williams approximation [269, 43] which is particularly successful in modeling high energy electron bremsstrahlung.

Using the results of the last Section 4.2, differential splitting probabilities for the various approaches are shown in Fig. 4.5 and Fig. 4.6 for vector and scalar dark sector radiation respectively. These results for the differential splitting functions illustrate a number of features. In particular, we see that the quasi-real approximation for ISR agrees very well with the full 2 to 3 calculation of pure ISR in the pomeron exchange model. We emphasize that although these processes in principle involve distinct final states, the ratio taken in forming the splitting functions restores the normalization. Similarly, we see that the full 2 to 3 calculation of ISR plus FSR in quasi-elastic scattering using the pomeron exchange model is well described by a hadronic generalization of the WW approximation described below. Finally, we have included the result from another modification of the WW approximation, presented in [236], which we also discuss below and which leads to a slightly higher production rate. The form factor at the radiation vertex, as defined in Eq. (4.54), is used in all approaches except for the modified WW approximation, where following [37] we use only a time-like form factor but restrict the transverse momentum of the radiated dark vector, $p_T < 1$ GeV.

Integrating these differential distributions, and incorporating the appropriate form-factors, our final results for the production rates of dark vectors and scalars are shown in Fig. 4.1 and Fig. 4.2. For illustrative purposes, in these figures, we choose angular cuts that are relevant for dark sector production in a 120 GeV fixed target beam at the Fermilab SeaQuest detector ~ 10 m away from the beam collision, and at FASER

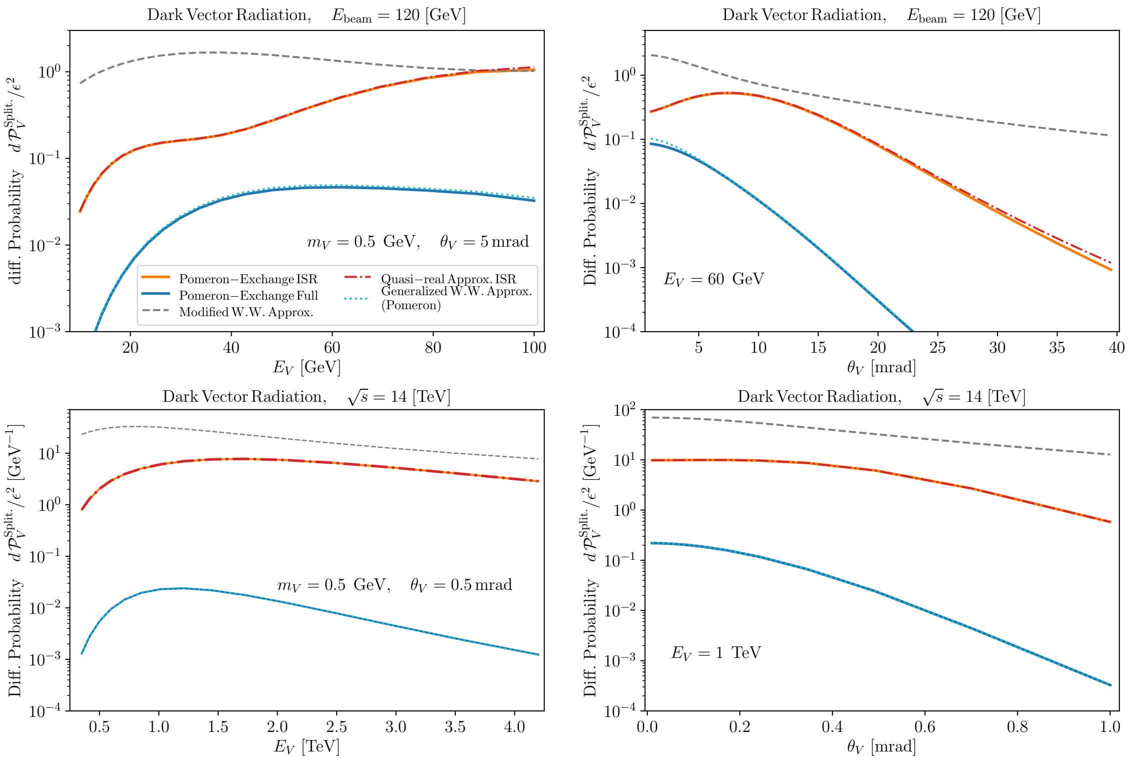

Figure 4.5: The splitting probability for the proton to emit a dark vector with $m_V = 0.5$ GeV as a function of energy (left) and radiated angle (right), corresponding to beam energies $E_{\rm beam} = 120$ GeV and $\sqrt{s} = 14$ TeV. The curves denote the contributions from the quasi-elastic emission from both initial and final state protons (solid blue), emission from the initial state only (solid orange), compared with the approximate splitting probability using the WW approximation with an effective pomeron cloud (dotted cyan) and the quasi-real ISR (dot-dashed red) methods. The agreement between these approximate approaches and the full results is very good, with the latter dotted and dot-dashed curves overlapping with the corresponding solid curves. Emission from both the initial and final state proton is subject to large interference and cancellations, in comparison to purely initial state radiation. The modified WW approximation of [236] is also shown for comparison (dashed gray).

in the forward region of the 14 TeV LHC.

4.3.1 Versions of the WW approximation

The equivalent photon method (or Fermi-Weizsacker-Williams (WW) approximation) has been used successfully as an approximate method to evaluate cross sections for various QED processes at high energies (see e.g. [269, 252, 238]), wherein one replaces the target charge with its effective electromagnetic field. In this method, which is

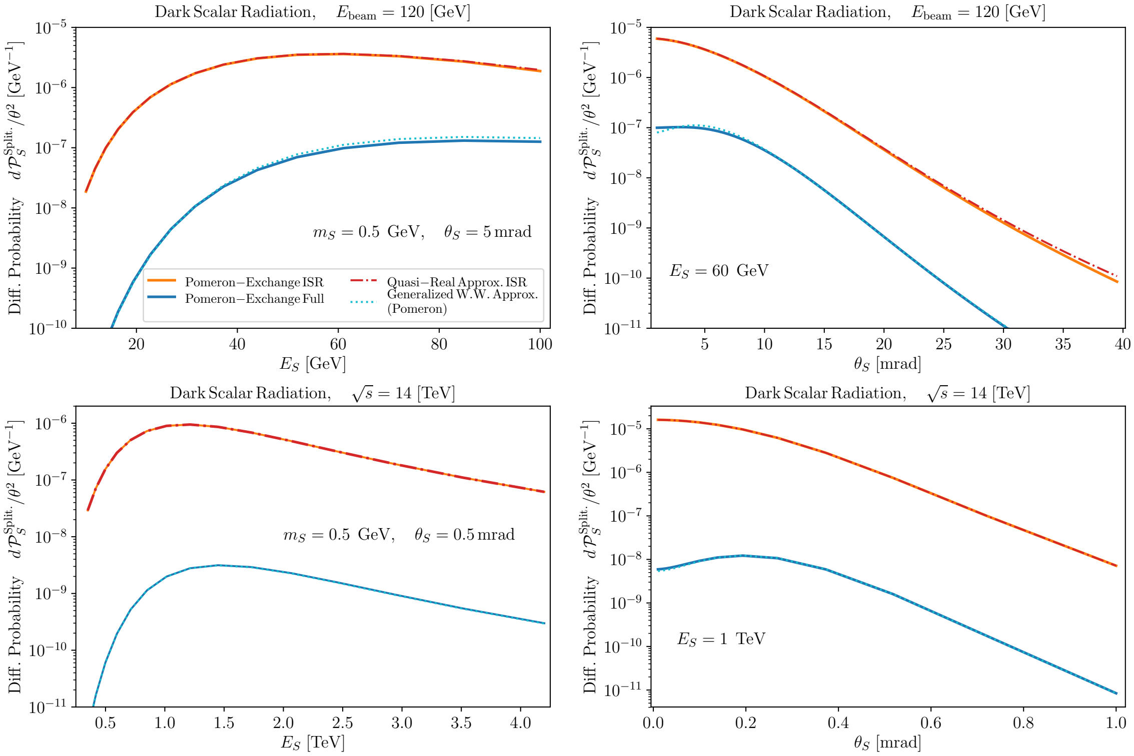

Figure 4.6: The splitting probability of the proton to emit a dark scalar with $m_S = 0.5$ GeV as a function of energy (left) and radiated angle (right), corresponding to beam energies $E_{\rm beam} = 120$ GeV and $\sqrt{s} = 14$ TeV. The curves denote the contributions from the quasi-elastic emission from both initial and final state protons (solid blue), emission from the initial state only (solid orange), compared with the approximate splitting probability using the WW approximation with an effective pomeron cloud (dotted cyan) and the quasi-real ISR (dashed-dotted red) methods. As in Fig. 4.5, the agreement between these approximate approaches and the full results is again very good, with the latter dotted and dot-dashed curves overlapping with the corresponding solid curves.

based on the mediator pole approximation, the 2 to 3 cross section is dominated by the photon pole at small t corresponding to small photon virtuality. This approach has successfully been used for electron beams [43, 49, 226], where in this case the scattering of the highly energetic beam electrons off the target reduces to a real photon interaction with the same target.

Generalizing this argument to high energy proton-proton elastic scattering, we would have a cloud of effective bosons (here hypothetical pomerons) from the target proton denoted by $\chi_{\mathbb{P}}$, which the beam proton scatters to radiate a collinear dark state. In this case the cross-section for the full process can be expressed in terms of the 2 to 2 process $p+\mathbb{P} \to p'+D$, a subprocess of the full 2 to 3 interaction. Following [269, 43, 226] we have,

$$\left(\frac{d\sigma^{\rm el}_{pp\to ppD}}{dz dp_T^2}\right)_{\rm WW} \cong \frac{\alpha_D}{16\pi^2} F_D^2(m_D^2, m_p^2 - H/z)\frac{z(1-z)}{H^2}(A_D^{22}|_{t=t_{min}})\,\chi_{\mathbb{P}}, \tag{4.55}$$

with

$$\chi_{\mathbb{P}} \equiv \int_{t_{min}}^{t_{max}} dt\,(t-t_{min})|\mathcal{A}_{\rm el}(s,t)|^2 \simeq 64\pi^2\left(\frac{\sigma_{\rm el}(s)}{\sigma_{\rm tot}(s)}\right)^2 \exp(-Bt_{\rm min}), \tag{4.56}$$

where $t_{min}{\approx}-H^2/(2z(1{-}z)p_p)^2$, $t_{max}{\approx}-2(1{-}z)m_p p_p$, and we have replaced $1/t$ for the photon propagator with the effective pomeron exchange amplitude, $\mathcal{A}_{\rm el}(s,t)$ defined in Eq. (A.7). The function $\chi_{\mathbb{P}}(s)$ depends on the kinematics of the radiation and can be approximated in terms of the elastic scattering using the optical theorem Eq. (A.5), where the $B(s)$ is the diffractive slope defined in Eq. (A.6).

Finally, A_D^{22} at $t{=}t_{min}$ corresponds to the 2 to 2 process $p+\mathbb{P} \to p'+D$, a subprocess of the full 2 to 3 interaction that is relevant for the WW approximation. The matrix elements take the form,

$$\begin{aligned} i\mathcal{M}_V^{22} = i g_V F^p_{1,V}(m_V^2)\tilde{\epsilon}^\mu_q \epsilon^{\nu\star}_k \bar{u}_{p'}\Bigg[&F_{pp^\star D}\big((p{-}k)^2\big)\Gamma_{\mu,\mathbb{P}}(q^2)\frac{i(\not{p}{-}\not{k}{+}m_p)}{(p{-}k)^2{-}m_p^2}\gamma_\nu + \\ &\gamma_\nu\frac{i(\not{p}'{+}\not{k}{+}m_p)}{(p'+k)^2{-}m_p^2}F_{pp^\star D}\big((p'{+}k)^2\big)\Gamma_{\mu,\mathbb{P}}(q^2)\Bigg]u_p, \end{aligned} \tag{4.57}$$

$$\begin{aligned} i\mathcal{M}_S^{22} = i g_S F_{1,S}(m_S^2)\tilde{\epsilon}^\mu_q \bar{u}_{p'}\Bigg[&\Gamma_{\mu,\mathbb{P}}(q^2)F_{pp^\star D}\big((p{-}k)^2\big)\frac{i(\not{p}{-}\not{k}{+}m_p)}{(p{-}k)^2{-}m_p^2} + \\ &\frac{i(\not{p}'{+}\not{k}{+}m_p)}{(p'+k)^2{-}m_p^2}F_{pp^\star D}\big((p'{+}k)^2\big)\Gamma_{\mu,\mathbb{P}}(q^2)\Bigg]u_p, \end{aligned} \tag{4.58}$$

where p, p' and k are the momenta of the incoming and outgoing protons and the radiated dark state $D = V, S$, while $\tilde{\epsilon}^\mu_q$ stands for the phenomenological polarization of pomeron with momentum q^μ, and the polarization sum is $\sum_{\rm pol}\tilde{\epsilon}^\mu_q\tilde{\epsilon}^\nu_q{=}-g^{\mu\nu}$. We assume that the on-shell pomeron state is massless, and in the following we set the virtuality $t = q^2$ effectively to zero.

The squared matrix element, averaged (summed) over the initial (final) spins takes the form,

$$|\overline{\mathcal{M}_D^{22}}|^2 = \frac{1}{4}\sum_{\text{spin}} |\mathcal{M}_D^{22}|^2 \approx g_D^2 |F_D(m_D^2, m_p^2 + U)|^2 Y_{\mathbb{P}}^2 F_{\mathbb{P}}^2(t) A_D^{22}, \tag{4.59}$$

where

$$A_V^{22} = 4\left(2m_p^2 + m_V^2\right)\left[m_p^2\left(\frac{S+U}{SU}\right)^2 + \frac{S+U-m_V^2}{SU} - 2\frac{S^2+U^2}{SU}\right], \tag{4.60}$$

and

$$A_S^{22} = -2\left(4m_p^2 - m_S^2\right)\left[m_p^2\left(\frac{S+U}{SU}\right)^2 + \frac{S+U-m_S^2}{SU} - \frac{(S+U)^2}{SU}\right], \tag{4.61}$$

We have defined the following invariant quantities

$$U \equiv (p-k)^2 - m_p^2 = m_D^2 - 2p\cdot k, \tag{4.62}$$

$$S \equiv (p'+k)^2 - m_p^2 = m_D^2 + 2p'\cdot k. \tag{4.63}$$

In the infinite momentum frame, these invariants are related to the kinematic structure function $H(z, p_T^2)$ and take the following simple form

$$U = -\frac{H}{z}, \qquad S = \frac{H}{z(1-z)}. \tag{4.64}$$

Note that we have approximated $F_{pp^\star D}(m_p^2 + S) \approx F_{pp^\star D}(m_p^2 + U)$ in Eq. (4.59) in the soft radiation limit.

In Fig. 4.5 and Fig. 4.6 we show the splitting probability using this generalized WW approximation compared to the approaches described above. The Jacobian $\partial(z, p_T^2)/\partial(E_k, \cos\theta_k) = 2kE_k/p_p$ is taken into account for comparing the splitting probability in Eq. (4.17) with the corresponding one obtained from Eq. (4.55). We observe that this approximation agrees very well with the full 2 to 3 calculation in quasi-elastic scattering using pomeron exchange, and indeed is suppressed by a similar interference of ISR and FSR contributions.

Next, we discuss a different variant of the WW approximation. The procedure outlined in Ref. [236] is a *modified* version of both fermion-pole [251, 225] and photon-pole approaches [269] (used for electron beams), and applied to the process of dark vector radiation in a high-energy proton beam dump. In this prescription, the following splitting function,

$$w_V(z,p_T^2) = \frac{\alpha_\epsilon}{2\pi}|F^p_{1,V}(m_V^2)|^2\frac{1}{H}\Bigg[\frac{1+(1-z)^2}{z}-2z(1-z)\Big(\frac{2m_p^2+m_V^2}{H}-z^2\frac{2m_p^4}{H^2}\Big) \\ +2z(1-z)(1+(1-z)^2)\frac{m_p^2m_V^2}{H^2}+2z(1-z)^2\frac{m_V^4}{H^2}\Bigg],$$

was determined using the matrix element for the WW sub-process $p + b \to p' + V$, where the nature of the exchanged vector boson b was not specified in [236], but the pomeron is a viable candidate. This result notably includes terms of up quartic order in the mass scales and reduces to the well-known Altarelli-Parisi function in the massless limit. The splitting function was then convoluted with the total pp cross section $\sigma_{pp}^{\text{tot}}(s')$ at a reduced scale $s' = 2m_p(p_p(1-z)+m_p)$, and this approach, augmented with a timelike form-factor to account for mixing with hadronic states, has been widely used in estimating the bremsstrahlung production of dark vectors in recent years [34, 37, 270, 271]. We present the splitting probability from this prescription in Fig. 4.5 to compare with the other approaches discussed in this Chapter. We observe that this rate is slightly higher than the one obtained using the quasi-real approximation for ISR. We also impose a constraint on either $p_T < 1$ GeV or the maximum angle from the beam θ_V when presenting the corresponding results in Fig. 4.1 and Fig. 4.2.

4.3.2 Sensitivity to visible dark vector decays

The impact of various bremsstrahlung production models can be assessed by studying the experimental sensitivity in the minimal scenario that the dark sector particle decays visibly, e.g. to leptons. In Fig. 4.7 we illustrate the impact on the sensitivity reach of FASER [37] experiment at CERN for dark vector searches. In producing this plot, we made use of the FORESEE [237] software package which determines the 90% confidence limit contours for the sensitivity of detectors placed in the LHC forward direction, and incorporates dark sector production via meson decays and Drell-Yan, in addition to bremsstrahlung, and accounts for dark sector particle lifetimes and branching fractions. The modified WW approximation [236] described above has been used extensively to determine the sensitivity to dark vectors from bremsstrahlung at high luminosity proton colliders and fixed target facilities. Replacing the modified WW approximation with the quasi-real approximation for dark vector radiation as derived in this study, modifies the sensitivity reach in parameter space near the ρ/ω

resonant peak, with $m_{A'}$ between 0.5 and 1 GeV. We illustrate both approaches in Fig. 4.7 for comparison. As anticipated, the sensitivity reach is degraded slightly on adopting the quasi-real approximation. The red band for the quasi-real approximation was determined as in Fig. 4.2 by varying the associated cut-off scale Λ_p from 1 to 2 GeV, and illustrates the dominant uncertainty.

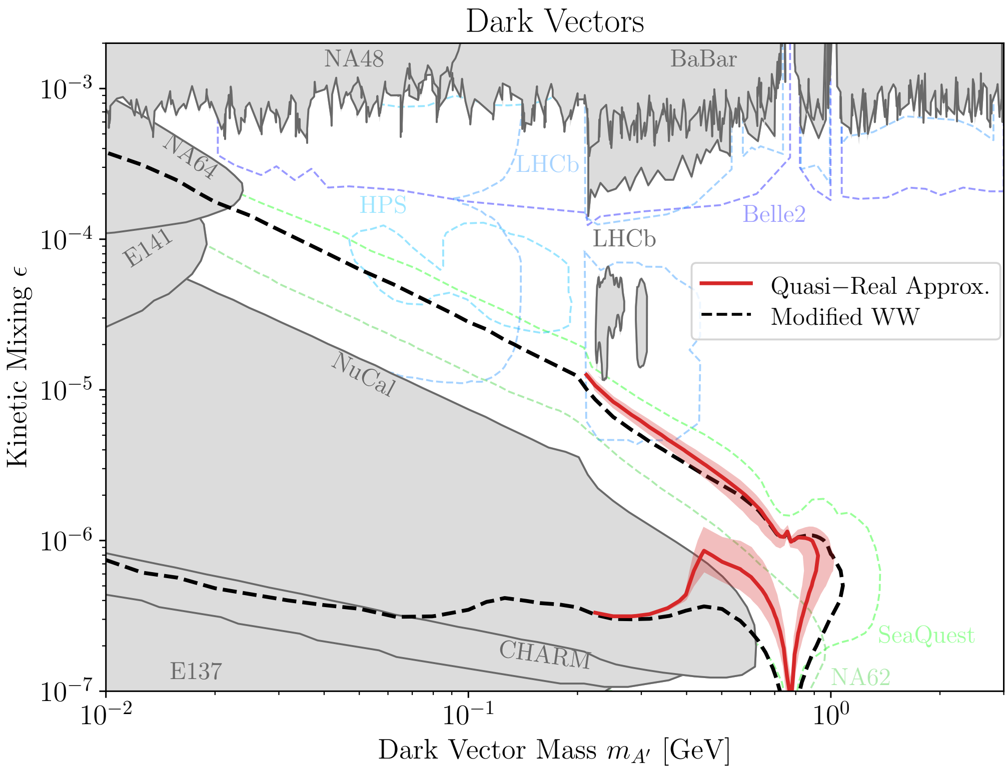

Figure 4.7: The sensitivity reach for dark photon decays at the FASER experiment, comparing bremsstrahlung production via the quasi-real approximation (solid red) with the modified WW approximation (dashed black). This plot was generated using the FORESEE [237] software package, and it includes various existing constraints and projections, and accounts for additional dark photon production modes.

4.4 Concluding remarks

In this chapter, we have revisited one of the primary production channels for dark sector mediators (kinetically mixed vectors and Higgs portal scalars) at proton beam facilities, namely proton bremsstrahlung. The production rate is nontrivial to estimate in the forward region as it involves nonperturbative QCD. However, it is also important for a number of fixed target and accelerator based searches for dark sectors and light dark matter (including at the proposed Forward Physics Facility at the HL-LHC), as this production channel is enhanced by resonant hadronic mixing in the $0.5-1.0$ GeV mass range. The analysis in the current study has focused solely on the production rates for the dark mediators. However, the production distributions obtained can straightforwardly be convoluted with decay distributions for either visible or hidden final states in the decays of dark vectors or scalars.

Our approach has been to compare ISR and FSR channels in an explicit model for the underlying diffractive pp scattering process with various approximations that instead use parametrizations of the hard scattering event. One of our primary goals was to compare the efficacy of these different approaches and attempt to quantify the level of precision and distinct kinematic constraints. Our results for production distributions are summarized in Fig. 4.5 and Fig. 4.6, while the final integrated results for the overall cross sections are shown in Fig. 4.1 and Fig. 4.2. The parameters chosen for these figures are representative of fixed target experiments close to the 120 GeV main injector beamline at Fermilab, and detectors such as FASER in the forward region of the ATLAS interaction point at the 14 TeV LHC. Overall, we find that radiation in quasi-elastic 2 to 3 scattering is suppressed by destructive interference between the t-channel ISR and FSR diagrams, while various approximations point to the dominant forward production channel being from ISR in non-single diffractive scattering. This calculation has an uncertainty associated with the choice of cutoff scale Λ_p in the vertex form-factor. Further progress in determining parton distribution functions at very small x may allow for an alternate parton-level calculation, and progress in reducing the uncertainty in estimating production rates via bremsstrahlung.

As an additional investigation to evaluate the effectiveness of current methods for calculating the proton bremsstrahlung rate, it is possible to compare and benchmark the bremsstrahlung distribution with very-forward particle production rates within the SM. For instance, in the case of the vector portal, analyzing and comparing the bremsstrahlung spectrum with data on inclusive distributions of forward neutral vector mesons can serve as a benchmark. Currently, work is in progress being carried out to benchmark the proton bremsstrahlung rates in relation to data for ρ^0 production [272]. Furthermore, it would be valuable to test various approaches for approximating the production rates via proton bremsstrahlung in specific kinematic limits, such as comparing our method with the soft photon approximation [273, 274].

Chapter 5

Millicharged Dark Sector Studies with Proton Beams

This chapter is adapted from Ref. [275], a paper originally written in collaboration with Felix Kling, and Yu-Dai Tsai.

5.1 Introduction

Searching for milli-Charged Particles, or mCPs, provides an empirical test of charge quantization [182] as well as predictions from well-motivated UV theories, including grand unified theories (GUT) [183, 184] and string theory [276, 277]). As introduced in Section 2.7, mCPs can also arise as a low-energy consequence of a theory with a massless kinetic-mixing dark photon [181]. Recently, the consideration of mCPs as dark matter (DM) [185, 186, 187] and the connection to the explanation to the EDGES anomaly [162, 163, 49, 54, 164] rekindle the experimental mCP program.

Within the past few decades, the search for mCPs has encompassed terrestrial experiments at fixed target and collider facilities, as well as astrophysical and cosmological observations [278, 279, 280, 281, 282, 283, 284, 285, 286, 287, 288]. A dedicated experiment, milliQan [285], was proposed at LHC that would detect mCPs produced by proton collisions using scintillator-based detectors. Later, FerMINI [289] with a similar setup was considered for proton fixed-target and neutrino experiments, primarily targeting Fermilab proton beamlines or CERN SPS beam. Recently, this idea has motivated a proposal at J-PARC proton fixed-target facilities [290].

In general, there is great promise in using experiments at the intersection of the high-energy and high-intensity frontiers to study dark-sector or long-lived particles. Traditionally such searches are done either in the LHC transverse region or at proton fixed-target experiments [26, 14, 27, 29, 291, 292, 293, 209, 294, 194, 271, 288, 295, 296, 297, 298, 299, 300, 301, 302, 289, 303, 304, 228, 305, 306]. However, we note that the production rates for dark-sector particles available in the forward direction of high-energy colliders are comparable to those achieved at beam dump experiments, so one can view the detectors located at the LHC forward regions as *very energetic beam-dump experiments* given the high statistics one can accumulate in this region [37]. The LHC's forward region can be regarded as a true intersection between high energy and high intensity: this is where one can get a high flux of low-mass dark sector particles through direct production and meson decays. However, until recently, this region has been neglected.

In this study, we consider two scenarios featuring millicharged particles in the LHC forward physics region. First, we consider installing a minimal mCP detector in a tunnel next to the current FASER experiment (see the left panel of Fig. 5.2 for more details), which we call FORMOSA-I for convenience. Second, we consider constructing a full-size milliQan-type detector in the Forward Physics Facility (FPF, an expanded UJ12 hall [55]), referred to as FORMOSA-II. One can also consider moving the proto-milliQan detector [307] to the forward physics region, but given the higher beam-related background rate compared to the transverse region [39] a more detailed study of the sensitivity is required.

5.2 Location

We propose locating FORMOSA in the far-forward direction, close to the beam collision axis, where it can benefit from an enhanced mCP production cross-section compared to the transverse direction.

A suitable location is available roughly 500 m downstream from the ATLAS interaction point in the cavern UJ12 or the tunnel TI12, shown in the left panel of Fig. 5.2. One can also consider the nearly symmetrical TI18 and UJ18 on the opposite side of ATLAS. During Run 3 of the LHC, TI12 will host the FASER experiment to search for long-lived particles [37, 315, 316, 317, 270, 39, 306, 318, 319], and study neutrino interactions [320, 321], with continuations being proposed for the HL-LHC era [322, 323]. For this reason, TI12 and UJ12 are equipped with lighting, power, stairs, and support structures to safely transport detector components around the LHC. Recently, it has also been proposed to enlarge the UJ12 cavern to create a FPF, which could house FORMOSA and other forward experiments [55].

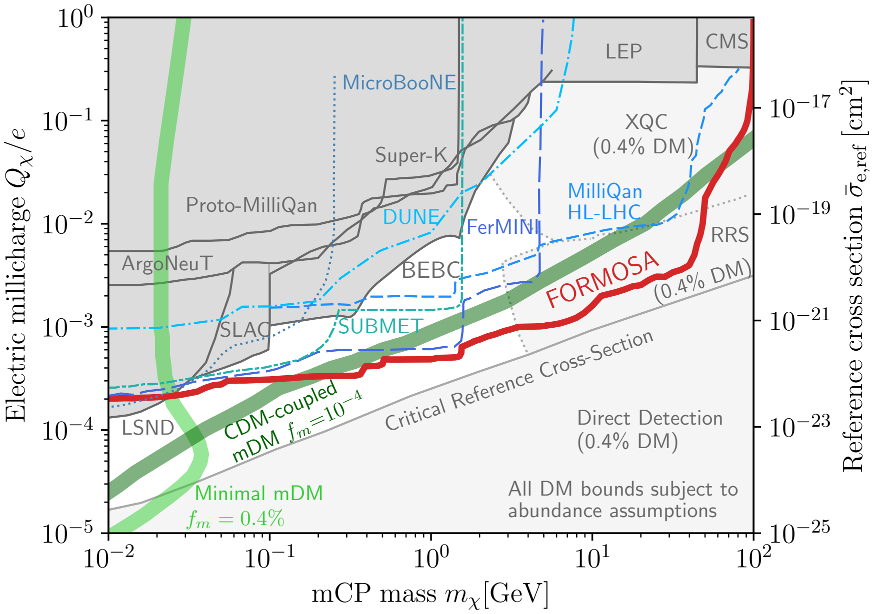

Figure 5.1: Parameter space for mCPs shown in the $(m_\chi, Q_\chi/e)$ plane. The sensitivity reach of FORMOSA is shown as a solid red curve. Exclusions from previous accelerator searches are shown in dark gray [279, 308, 280, 309, 310, 288, 311, 307, 190], and projections for proposed searches are shown as blue dashed lines [312, 289, 290, 311, 194]. In this case of millicharged SIDM, additional constraints arise from underground direct-detection, balloon, and satellite experiments [189, 188, 313, 314], assuming a mSIDM only contributes 0.4% to the DM abundance. The green bands correspond to the millicharged dark matter (mDM) that provides an explanation for the EDGES anomaly [164].

TI12 and UJ12 are shielded from the ATLAS IP by the forward LHC infrastructure, which consists of magnets and absorbers, as well as 100 m of rock. Particle fluxes and radiation levels have been simulated using FLUKA [324] and validated experimentally [39, 321], indicating that the particle fluxes at this location are low.

5.3 mCP Production

We study mCP χ with electric charge Q_χ, mass m_χ and define $\epsilon \equiv Q_\chi/e$. The small electric charge can come from directly introducing a tiny $U(1)$ hypercharge to χ. It can also be generated by a massless dark photon, kinetically mixed with SM, that couples to χ and induces the millicharge of χ in a convenient basis [325, 181].

We perform a dedicated Monte Carlo study to estimate the flux of mCP produced at the LHC. The different production channels and their corresponding production

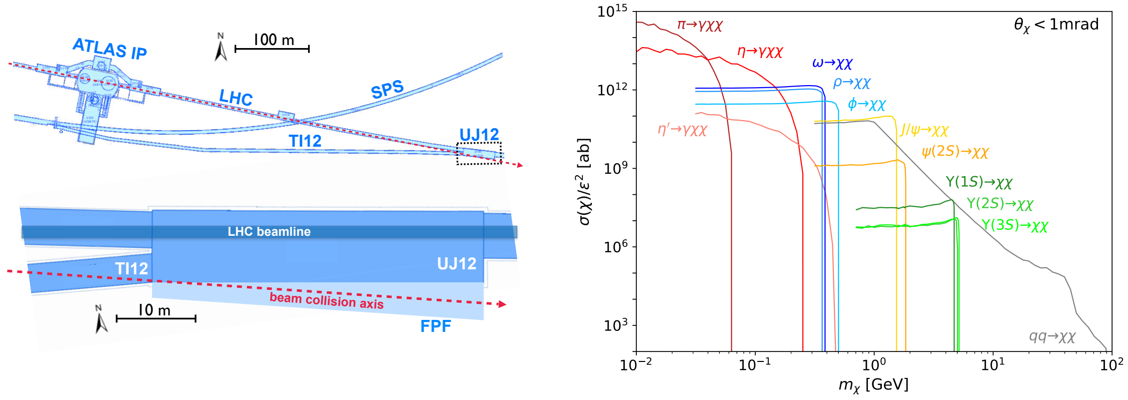

Figure 5.2: **Left:** the proposed location of FORMOSA in the cavern UJ12 or side tunnel TI12 (blue) close to the beam collision axis (red). The Forward Physics Facility (FPF) extension is shown as a light-blue area. **Right:** production cross section of mCP in the forward direction, $\theta_\chi < 1$ mrad, for different production modes and mCP masses.

cross sections in the forward direction, within $\theta_\chi < 1$ mrad of the beam collision axis, are summarized in the right panel of Fig. 5.2.

If the mCP is light, it is primarily produced in both pseudoscalar meson decays such as $\pi^0 \to \gamma\chi\chi$ and vector meson decays such as $\omega, J/\psi, \Upsilon \to \chi\chi$. We generate the spectra of light mesons using `EPOS-LHC` [326]. The spectra of the charmonium and bottomonium states are simulated using `Pythia 8` [327], which we have calibrated with their spectra as measured at LHCb [328, 329, 330]. More details on the simulation and validation of forward meson production at the LHC and their decay into mCPs are provided in the Section 5.3.1.

Heavy mCPs are primarily produced in partonic scattering $qq \to \chi\chi$. We simulate this Drell-Yan production mode using `MadGraph 5` [331] and `Pythia 8`. To ensure that the PDFs are well defined, we require the invariant mass of the mCP pair to be larger than 2 GeV, which leads to a constant mCP production cross sections for $m_\chi < 1$ GeV.

It is important to note that particle production rates are enhanced in the forward direction. According to Feynman scaling arguments [332], in the limit where $m_\chi \ll p_T$, mCP production is approximately flat in pseudorapidity, $dN/d\eta \approx$ constant. Comparing the flux of mCPs going through a 1 m × 1 m area at a transverse location (T) similar to milliQan, and a forward location (F) about 500 m downstream and off-set by 2 m from the beam axis, we find $N_\mathrm{F}/N_\mathrm{T} \sim \Delta\eta_F/\Delta\eta_T \times \Delta\phi_\mathrm{F}/\Delta\phi_\mathrm{T} \sim 250$, indicating that the forward particle flux is indeed strongly enhanced.

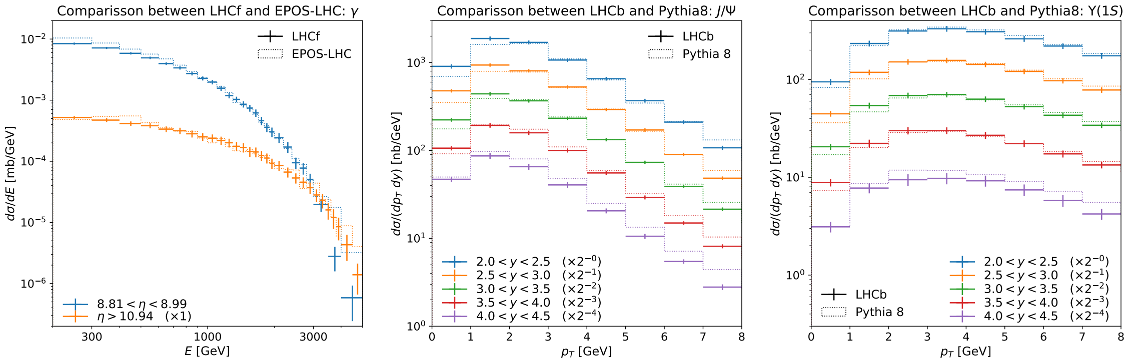

Figure 5.3: Validation of forward meson production. Forward photon production predicted by `EPOS-LHC` (left), J/ψ production (center) and $\Upsilon(1S)$ production predicted by `Pythia 8` compared to measurements by LHCf [333] and LHCb [328, 329] at 13 TeV LHC.

5.3.1 mCP Production in Meson Decays

If the mCP χ is sufficiently light, $m_\chi \lesssim 5$ GeV, it can be produced in the decay of SM mesons M. This requires a reliable description of forward particle production, best validated with or tuned to available data.

The production of light mesons, $M = \pi^0, \eta, \eta', \omega, \rho$ and ϕ, is simulated using `EPOS-LHC` [326], as implemented in the simulation package `CRMC` [334], which is a dedicated Monte-Carlo generator designed to describe minimum bias hadronic interactions at both particle colliders and cosmic ray experiments. In the left panel of Fig. 5.3 we compare the predicted energy spectra of far forward photons (mainly from π^0 decay) produced in 13 TeV collisions to those measured at LHCf [333], and find good agreement over the full spectrum.

In addition, we simulate the production of charmonium and bottomonium using `Pythia 8` [327]. Since the default setup of `Pythia 8` tends to overestimate their production rate at small transverse momenta p_T, we use the predefined `SuppressSmallPT` user hook to suppresses the production rate by a factor

$$\left(\frac{p_T^2}{k^2 p_{T0}^2 + p_T^2}\right)^2 \left(\frac{\alpha_S(k^2 p_{T0}^2 + Q_{\rm ren}^2)}{\alpha_S(Q_{\rm ren}^2)}\right)^n , \tag{5.1}$$

where p_{T0} is the same energy-dependent dampening scale as used for multiparton interactions and Q_{ren} is the renormalization scale. Good agreement between the simulation and measurements at LHCb [328, 329, 330] are obtained for $k = 0.35$ and $n = 3$, as shown in the center and right panel of Fig. 5.3.

In the next step, we use a MC simulation to subsequently decay the mesons into mCPs χ. The pseudoscalar mesons $M = \pi^0, \eta, \eta'$ can undergo the 3-body decay $M \to \gamma\chi\bar{\chi}$. Following Ref. [304, 335], the differential branching fraction for this process is given by

$$\begin{aligned}\frac{d\mathrm{BR}(M\!\to\!\gamma\chi\chi)}{ds\,d\!\cos\theta} &= \frac{\epsilon^2\alpha}{4\pi s}\left[1\!-\!\frac{s}{m_M^2}\right]^3\left[1-\frac{4m_\chi^2}{s}\right]^{\frac{1}{2}} \\ &\times\left[2-\left(1-\frac{4m_\chi^2}{s}\right)\sin^2\theta\right]\times\mathrm{BR}(M\!\to\!\gamma\gamma),\end{aligned} \tag{5.2}$$

where $s = (p_\chi + p_{\bar{\chi}})^2$ is the invariant mass of the off-shell photon producing the mCP pair and θ is the angle between the momentum of χ in the off-shell photon's rest frame and the boost direction of the off-shell photon.

In addition, the vector mesons $M = \rho, \omega, \phi, J/\psi, \psi(2S)$ and $\Upsilon(nS)$ can decay directly into a pair of mCPs, $M \to \chi\bar{\chi}$. Following Ref. [289], the corresponding branching fraction is given by

$$\frac{\mathrm{BR}(M\!\to\!\chi\bar{\chi})}{\mathrm{BR}(M\!\to\!ee)} = \epsilon^2\frac{(m_M^2\!+\!2m_\chi^2)(m_M^2\!-\!4m_\chi^2)^{1/2}}{(m_M^2\!+\!2m_e^2)(m_M^2\!-\!4m_e^2)^{1/2}}\ . \tag{5.3}$$

5.4 Detector and Signature

We will consider a minimal detector (FORMOSA-I) and a full mCP detector (FORMOSA-II). For FORMOSA-I we consider a setup similar to the milliQan demonstrator with size 0.2 m × 0.2 m × 4 m, which consists of 4 layers each containing 16 scintillator bars coupled to a PMT. FORMOSA-II would be a 1 m × 1 m × 4 m array consisting of 4 layers of 400 scintillator bars. In our analysis we place FORMOSA-I in the UJ12/TI12 hall and 2 meters off-axis, and we take FORMOSA-II to be on-axis and located in the proposed FPF (expanded UJ12 hall).

When an mCP traverses the detector, photoelectrons (PE) are produced from ionization energy deposition within each stack of scintillator. The average number of PEs collected with detection efficiency $\varepsilon_{\mathrm{det}}$ in a scintillator bar with density ρ_s and length L_s can be estimated as $\bar{N}_{\mathrm{PE}} \approx \varepsilon_{\mathrm{det}}\,\rho_s\,L_s\!\times\!\langle -dE/dx\rangle\!\times\!Y_\gamma$, where the mean rate of energy deposition $\langle -dE/dx\rangle$ scales as ϵ^2 and is a function of the mCPs energy [57]. $Y_\gamma \sim 1.1\times10^4\ \ \mathrm{MeV}^{-1}$ is the photon yield deposited in the typical plastic scintillators [336]. Like the milliQan collaboration [286], we assume a detection efficiency of $\varepsilon_{\mathrm{det}} \approx 10\%$.

For FORMOSA, we search for a quadruple coincidence of hits with $\bar{N}_{\mathrm{PE}} \geq 1$ in each stack within a 20 ns time window. The probability of detecting a mCP follows the Poisson distribution, $P_{\mathrm{det}} = (1 - \exp(-\bar{N}_{\mathrm{PE}}))^4$. Considering the number of mCPs passing through the detector N_χ, the total number of signal events is $N_\chi \cdot P_{\mathrm{det}}$.

5.5 Background

The potential background sources of an mCP detector at the forward physics region can be classified as beam related and beam unrelated. According to the proto-milliQan study [307], in the transverse region, the beam-unrelated background dominates, and it can be controlled by adding an additional layer to the original three-layer milliQan design. However, in the forward region at the LHC considered in this study, we find that the beam-related background could be much more important. The background reduction strategy and the choices of PMTs need to be reconsidered accordingly. We will first review the beam unrelated background and its reduction strategy, and then discuss the beam-related background.

The beam unrelated background of FORMOSA can come from cosmic muons and dark current, and their combined coincident signatures. The cosmic muons interacting with the cavern walls generate a spray of electrons and gamma rays. The subsequent shower causing scintillation in the detector is a significant background source for the proto-milliQan detector [307]. In addition, due to the random emission of thermal electrons from the photo-cathode, dark current pulses can be produced in each PMT. These two sources of detector background lead to the similar signature to mCPs.

Several techniques have been developed to reduce these beam-unrelated background events [285, 286]. These strategies can be summarized as requiring multiple-coincidence as a detection signature; implementing a veto of large-PE events; shifting or enlarging the middle detector array (to eliminate coincident low-PE pulses caused by energetic muons scraping through the surface of the scintillator layers); and considering a dead-time veto of the afterpulses. In addition to scintillator bars, the milliQan prototype design has considered components such as the scintillator panels and four scintillator slabs along the length of the detector for further reduction of backgrounds [307]. The scintillator panels are used as shields for the bars from the top and sides to reject backgrounds due to cosmic muon showers. The slabs provide time information, shielding from neutron radiation, and help to veto deposits due to beam and cosmic muons passing the bars. As demonstrated by the milliQan collaboration, the beam unrelated background can be reduced to nearly zero with all these background reduction strategies.

The quadruple coincidence requirement has the advantage of lowering the dark-current background rate by a factor of $\mathcal{O}(10^{-4})$ compared to the original milliQan design, which is expected to have ~ 300 dark current background events per year [286, 289]. The same conclusion taking into account other beam unrelated background is also shown in [312].

A new challenge arises for the dedicated mCP search in the forward physics region, given a large flux of high-energy muons from the beam collisions. For FORMOSA-I, we consider a location inside the cavern UJ12, where a muon rate $\lesssim 1$ Hz/cm^2 can be achieved [320] (one can consider the same muon rate for FORMOSA-II). These energetic muons (and the secondary particles they produce inside the detector) can cause large pulses in the PMT. One can implement online-vetos of large-PE pulses to avoid the readout deadtime and ensure a high signal efficiency.

In addition, afterpulses, which can appear with a delay time of a few μs after the initial pulse, could become sources of background events. These smaller pulses can appear correlated in the τ time window. Thus, they may be indistinguishable from the small PE events and cannot be vetoed by the large PE cuts. However, the rate of the afterpulses with a delay time of $\delta t \gtrsim 10\ \mu$s drops below the dark current rate for most of the PMTs [337, 338]. We can therefore remove the afterpulse background using a veto: assuming one muon every 100 μs for FORMOSA-II and an afterpulsing duration of $\sim$ 10 μs, roughly 10% of the data needs to be vetoed, resulting in a live-time efficiency of $\sim$ 0.9. For FORMOSA-I, this is a much smaller issue since it has a smaller detector area and thus a lower total muon rate. Considering better PMTs with reduced afterpulse duration can improve the live-time efficiencies for both FORMOSA-I and II.

Interactions of high-energy neutrinos produced at the LHC with the FORMOSA detector provide another beam-related background source. According to [321], we estimate $\mathcal{O}(10^6)$ interactions with FORMOSA during the HL-LHC. These interactions cause energetic events with a very large number of PE throughout the detector, which is very different from the mCP signal. Furthermore, neutrinos interacting with the material surrounding FORMOSA can produce particles that form a hadronic shower. In a 2.5 m volume of rock in front of FORMOSA (corresponding to $\sim 10\,\lambda_{\text{int}}$ which a hadronic shower should be mostly absorbed) $\mathcal{O}(10^6)$ neutrino interactions is expected during the HL-LHC. This corresponds to a rate of $\mathcal{O}(1)$ interaction per minute, which

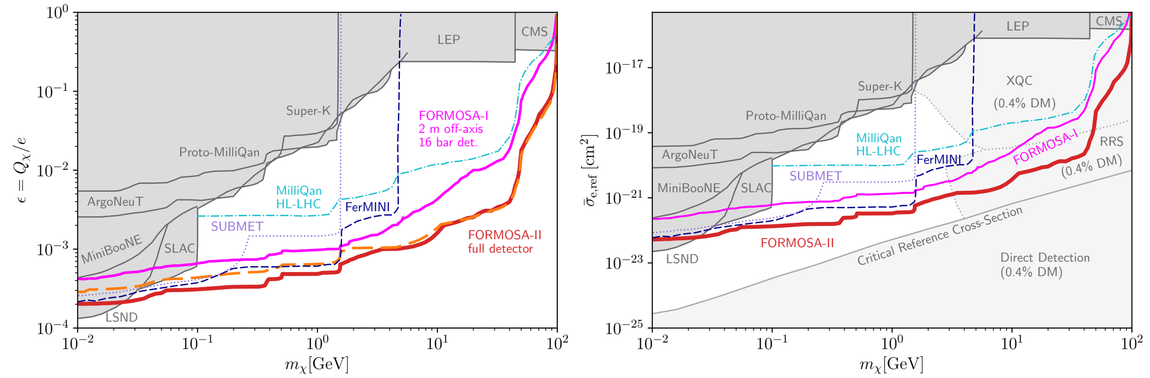

Figure 5.4: Sensitivity of FORMOSA in the mCP parameter space (left) and mSIDM parameter space (right) alongside existing accelerator constraints (dark gray), direct-detection experiments (light gray, assuming 0.4 % DM abundance for the direct-detection experiments) and other proposals (dashed lines). FORMOSA-II 2 m off-axis is plotted orange and dashed. See text for details.

is sub-leading compared to the expected rate of muons passing through the detector.

Other beam-related background sources come from beam-gas and beam halo collisions with the beam pipe, which require special attention. Based on a FLUKA study[1] performed for the FASER experiment [39, 324], we expect that particles produced in proton losses and beam-gas collisions near TI12/UJ12 would typically point toward the direction of the nearby LHC beam pipe rather than the ATLAS IP. This lead us to suggest i) additional shielding and ii) vetoes around the detector, combined with pointing the long axis of FORMOSA toward the IP, to reduce possible backgrounds associated with such particles. Note that the FLUKA simulations do not include any non-beam backgrounds such as cosmic ray muons, and thus are insufficient to quantitatively estimate the background rate for the new detector. As we mentioned, one can install the proto-milliQan at this location to conduct an in-situ study of the background to address this issue.

5.6 Sensitivity

In the left panel of Fig. 5.4, we present the projected sensitivity reaches of FORMOSA-I and II in terms of the mCP mass m_χ and charge ratio $\epsilon \equiv Q_\chi/e$, assuming an integrated luminosity of 3 ab^{-1} at the HL-LHC. We require 3 signal events, and a

---

[1] This simulation from Refs. [39, 324] were performed for TI18/UJ18 location, which is nearly identical to TI12/UJ12 and located on the opposite side of ATLAS. The results presented in Ref. [39] assumes LHC Run 3 conditions with a luminosity of $2 \cdot 10^{34}\mathrm{cm}^{-2}\,\mathrm{sec}^{-1}$, while the original FLUKA study presented in Ref. [324] assumed HL-LHC conditions with a luminosity of $5 \cdot 10^{34}\mathrm{cm}^{-2}\,\mathrm{sec}^{-1}$.

0.9 live-time efficiency. The choice of 3 events is based on the discussions in the background section that the beam-unrelated background can be reduced to a negligible level with the requirement of quadruple coincidence. The line corresponding to FORMOSA-I placed 2 m off-axis is colored magenta. FORMOSA-II on-axis (2 m off-axis) is plotted red (orange and dashed).

We plot the existing constraints as gray-shaded regions. These include bounds from SLAC [279], LEP [308, 280], CMS [309, 310], LSND and MiniBooNE [288], ArgoNeuT at Fermilab [311], proto-milliQan at LHC [307], and the constraint on cosmic-ray produced mCPs from Super-K [190]. For comparison, we also show the sensitivity projections from the full milliQan experiment at the 14 TeV LHC with 3 ab^{-1} integrated luminosity [286], the proposed FerMINI experiment at LBNF/DUNE with a beam energy of 120 GeV and 10^{21} POT (also considered for NuMI/MINOS hall and the sensitivity reach is similar) [289], and the proposed SUBMET experiment assuming 10^{22} POT at the 30 GeV proton beam at J-PARC [290].

Based on our analysis, one can see that FORMOSA-I, a minimal detector to be placed in UJ12, would provide a better sensitivity reach in comparison to the full milliQan run. As discussed above, this is due to an enhanced flux of mCP in the forward region, in comparison to that of the transverse region. Up to $\mathcal{O}(10^6)$ signal events at $m_\chi = 1$ GeV near the proto-milliQan bound are possible. We also find that with 300 fb^{-1} (1/10 of the full luminosity of the HL-LHC), the FORMOSA-I has a better sensitivity than the full HL-LHC milliQan for $m_\chi \lesssim 10$ GeV.

Also note that, although we derive our sensitivity projections based on the luminosity of HL-LHC, it could be possible to employ a similar setup already during Run 3 of the LHC. In particular, one could install the proto-milliQan detector in the TI12 cavern and perform a test run for FORMOSA to better understand the detector environment and experimental challenges.

We further show that FORMOSA-II provides leading sensitivity projections in a large window of mCP mass from 100 MeV to 100 GeV, exceeding the reaches of other similar proposals. We also see that, even if the detector is placed a few meters off the beam axis, the sensitivity would not be strongly affected. This allows us to place FORMOSA inside the existing cavern UJ12.

5.7 Millicharged Strongly-Interacting DM

mCPs in this region of parameter space can account for a fraction of the DM abundance, but cannot be detected by the direct-detection experiments when the cross-section is larger than certain critical values (derived in [189, 188]). The ambient DM (DM in our local galaxy with Standard distribution and velocity dependence [339]) with a substantial cross-section with SM particles can lose most of its kinetic energy through interactions with SM particles. For some model parameters, the DM particles lose most of their energy and hence cannot be detected by ground-based direct detection experiments after interacting with the atmospheric particles and the crust. These DM particles are generally referred to as strongly interacting DM (SIDM) [314, 340]. In [189, 188, 190], an unconstrained region of parameter space is identified, which can be referred to as a millicharged SIDM (mSIDM) window, and FORMOSA can provide strong sensitivity in this parameter space.

In the right panel of Fig. 5.4, we show our results in terms of m_χ and the conventional "reference cross section" $\bar{\sigma}_{\rm e,ref} = 16\pi\alpha^2\epsilon^2\mu_{\chi e}^2/q_{\rm d,ref}^4$. Here, $q_{\rm d,ref}$ is chosen to be the typical momentum transfer in $\chi - e$ scattering for semiconductor or noble-liquid targets (taken to be αm_e [188]) and $\mu_{\chi e}$ is the reduced mass of the electron and χ.

We include bounds from terrestrial direct detection experiments [189, 188], XQC [313] and RRS [314]. We do not plot the constraints based on the millicharged DM accelerated by astrophysical sources [341, 342, 343, 344], as they require additional assumptions beyond local DM properties. When presenting the bounds, we follow Ref. [188] and assume 0.4 % of the DM to be mCP to avoid strong cosmological constraints [345, 346, 347]. In addition, the CMB constraint is preventing the DM from being composed of majority of mCP, and 0.4 % of DM being mCP is allowed by the current constraint (see, e.g., [132]). For different assumptions of DM being mCP, the existing constraints from direct-detection experiments would be different. It is also demonstrated that 0.4 % of DM being mCP could potentially explain the EDGES anomaly, although subjecting to other constraints (see, e.g. [163, 348]).

We show that FORMOSA can help cover a large part of the millicharged DM region that is previously unconstrained. Our study also demonstrates two strong advantages of accelerator probes of DM in general: (i) the accelerator probes are not sensitive to the material's attenuation, given that the particles produced from beam interactions have large kinetic energy (unlike the ambient DM, which has much lower kinetic energy), and (ii) the accelerator constraints are independent of the fractional

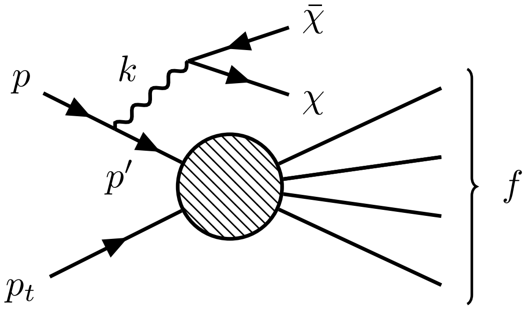

Figure 5.5: Pair production of $\chi\bar{\chi}$ in initial state radiation in a generic non-diffractive scattering event.

composition of DM (unlike the direct-detection or cosmological probes [345, 346, 347]).

5.8 Pair Production via Proton Bremsstrahlung

This section has not been included in the original study presented in this chapter. In our analysis thus far, we have focused on mCP production in proton fixed-target experiments and colliders via neutral meson decays and Drell-Yan processes. Here, we consider mCP pair production via proton bremsstrahlung, making use of the approximate method we developed in Chapter 4. We compute the scattering cross-section of proton-proton collision with a $\chi\bar{\chi}$ pair emitted from the incoming beam proton into an inclusive hadronic final state f,

$$p(p) + p(p_t) \to \chi(p_\chi) + \bar{\chi}(p_{\bar{\chi}}) + f(p_f). \tag{5.4}$$

In the framework of the quasi-real approximation, the matrix element of process, $pp_t \to \chi + \bar{\chi} + f$, involving a $\chi\bar{\chi}$ pair emitted from the beam proton can be represented in terms of product of the matrix element of $p \to \chi + \bar{\chi} + p'$ reaction and the subprocess $p'p_t \to f$, where p' is the momentum of the intermediate proton.

The matrix element of the emission process, depicted in Fig. 5.5 reads,

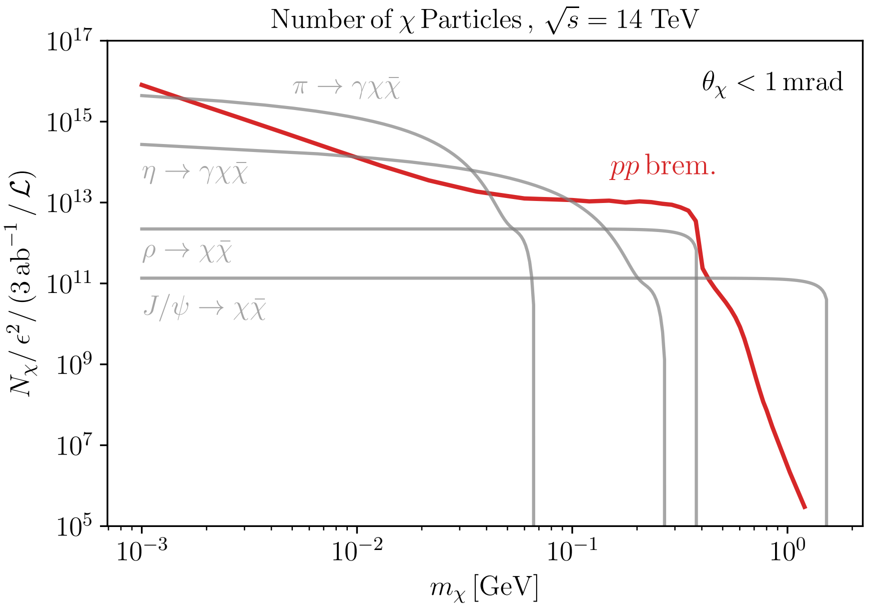

Figure 5.6: The number of produced mCPs in the forward direction, $\theta_\chi < 1$ mrad for different production modes and mCP masses.

$$\begin{aligned}
|\overline{\mathcal{M}^{p\to p'\chi\bar{\chi}}}| &= \frac{1}{2}\sum_{\text{spin}} |\mathcal{M}^{p\to p'\chi\bar{\chi}}|^2 = \frac{1}{2}\frac{\epsilon^2 e^4}{k^4}|F(k^2,p'^2)|^2 \times \\
&\quad \mathrm{Tr}[(\not{p}'{+}\mathrm{m_p})\gamma^\mu(\not{p}{+}\mathrm{m_p})\gamma^\nu]\mathrm{Tr}[(\not{p}_\chi{+}\mathrm{m}_\chi)\gamma_\mu(\not{p}_{\bar{\chi}}{-}\mathrm{m}_\chi)\gamma_\nu] \\
&\quad = \frac{16\epsilon^2 e^4}{k^4}|F(k^2,p'^2)|^2 \Big[(p'\cdot p_\chi)(p\cdot p_{\bar{\chi}}) + (p\cdot p_\chi)(p'\cdot p_{\bar{\chi}}) \\
&\qquad + m_\chi^2(p\cdot p') - m_p^2(p_\chi\cdot p_{\bar{\chi}}) - 2m_\chi^2 m_p^2\Big]
\end{aligned} \tag{5.5}$$

Note that a 3-body phase space corresponding to the emission shown in Fig. 5.5 has 9 degrees of freedom, and 3 of them can be reduced by the momentum conservation, since at the $pp'\gamma^\star$ vertex only the momentum is conserved in quasi-real approximation, thus $E_{p'} = \sqrt{(\vec{p}{-}\vec{p}_\chi{-}\vec{p}_{\bar{\chi}})^2{+}m_p^2}$. Among the six independent Lorentz invariants built by the scalar product of $p, p', p_\chi, p_{\bar{\chi}}$, one can be related to the rotation along the axis of $\vec{p}$, which is redundant. Following the previous study [235], the differential cross section for the full process then reads,

$$d\sigma^{pp_t\to\chi\bar{\chi}f} = \frac{|\overline{\mathcal{M}^{p\to p'\chi\bar{\chi}}}|}{\left((p{-}k)^2{-}m_p^2\right)^2}\frac{E_{p'}}{E_p}\frac{d^3p_\chi}{2E_\chi(2\pi)^3}\frac{d^3p_{\bar{\chi}}}{2E_{\bar{\chi}}(2\pi)^3}\sigma^{pp_t\to f}(s') \tag{5.6}$$

In Fig. 5.6 we show the expected number of mCPs to reach a detector with $\theta <$

1 mrad from pp collision with $\sqrt{s} = 14$ TeV. For a discussion on how to handle the numerical divergence in cases where the exchanged photon is extremely soft, refer to Ref. [197].

5.9 Concluding remarks

In this Chapter, we proposed a new mCP search in the forward region of the LHC ATLAS interaction point. FORMOSA, a milliQan-like experiment placed ~ 500 m downstream from ATLAS, would take advantage of enhanced mCP production in the forward direction and can provide leading sensitivity to mCPs in the 10 MeV to 100 GeV mass window.

We also find that, unlike the current milliQan location, beam-related backgrounds associated with the sizable flux of forward muons, such as PMT afterpulses, become important in the forward direction. This motivates additional detector design considerations, such as the use of PMTs with low afterpulse duration or the application of vetoes to control the afterpulse background.

In addition to mCPs, FORMOSA has the potential to search for other beyond standard model (BSM) particles, such as heavy neutrinos and DM with electric dipoles [349, 350, 351, 352]. Furthermore, FORMOSA's location in the far forward direction allows further extensions of its physics objectives. For example, one would expect about 10^6 neutrino interactions in the FORMOSA-II detector, providing additional opportunities for neutrino physics [320, 353, 323] and forward particle production measurements, and indicating a physics potential of FORMOSA and the Forward Physics Facility that remains to be explored.

Chapter 6

Neutrino Electromagnetic Properties and the Weak Mixing Angle at the LHC Forward Physics Facility

This chapter is adapted from Ref. [354], a paper originally written in collaboration with Roshan M. Abraham, Felix Kling, and Yu-Dai Tsai.

6.1 Introduction

Neutrino properties are crucial to understanding our Universe and have been prime targets of particle physics experiments. The electromagnetic (EM) properties of neutrinos, in particular, can be tested in existing and future experiments. These measurements include the mass-dimension 4 neutrino millicharge, the mass-dimension 5 neutrino dipole moments, and the mass-dimension 6 neutrino charge radius. These properties can, for example, be used to determine whether neutrinos have a Dirac or Majorana nature [355, 356] and to probe new physics beyond the Standard Model (SM) [52]. These neutrino properties could be linked to intriguing experimental anomalies, including the NuTeV anomaly [53] and the Xenon 1T excess [357] (although the latter was determined most likely to be from an SM background [358]). Large neutrino dipole moments, for example, can also affect the mass gap of black holes [359, 360]. Interesting models were proposed to generate neutrino EM couplings much larger than the SM predictions [361, 362, 363, 364, 365, 366] and to connect the anomalies to the neutrino properties [367]. Currently, the SM predictions of these properties are several orders of magnitude smaller than the present upper bounds, obtained from reactor neutrinos [368, 369], accelerator neutrinos [370, 371, 372], and solar neutrinos [373, 374, 375, 358, 376, 112], to name a few. For a connection between neutrino electromagnetic properties and CP phases, see Ref. [377].

The LHC provides one of the most exciting opportunities in studying high-energy neutrinos and tau neutrinos, given its high center-of-mass energy. The forward region at the LHC, in particular, provides a large flux of neutrinos coming from meson decays [320]. The Forward Physics Facility (FPF) [195] at the LHC is ideally placed on studying these TeV energy neutrinos. Previously, interesting signatures from the neutrino dipole portal [194, 378], were studied at FPF [379] and FASER [380], but a proper analysis of the future capability of FPF on neutrino EM properties are sorely lacking at this moment.

In this work, we utilize the FPF to study interesting properties of neutrinos: the neutrino millicharge, magnetic moment, and charge radius. By looking at low recoil energy electron scattering and neutral current deep inelastic scattering (DIS) events, we show that we can reach competitive sensitivity for these properties. Most excitingly, we can set the world's leading limit on neutrino charge radius for the electron neutrino, while for the muon neutrino, we come within a factor of a few from the SM prediction. For the tau neutrino, FPF's limits on the magnetic moment exceed the DONUT results [371] by an order of magnitude. Additionally, the bounds on millicharge and charge radius constitute some of the few measurements available for the tau neutrino.

The neutrino interaction with the target material, investigated in this study, also depend sensitively on electroweak parameters. In this context, the precise measurement of the neutral current neutrino DIS rate can also be translated to a precise measurement of the weak mixing angle. This would allow one to test the anomalous result obtained by NuTeV [53].

This Chapter is organized as follows. We briefly review neutrino EM properties in Section 6.2 and introduce the detectors under consideration at the FPF in Section 6.3. In Section 6.4, we discuss our signal characteristics. We present our results on the neutrino EM properties in Section 6.5 and discuss the measurement of the weak mixing angle in Section 6.6. We conclude in Section 6.7.

6.2 Neutrino EM Properties

The electric charge of neutrinos is zero in the SM. However, electromagnetic properties can arise at the quantum loop level (or via BSM physics) allowing electromagnetic interactions of neutrinos with photons and charged particles. Considering neutrinos as massive fermions, the electromagnetic properties of neutrinos in the one-photon approximation can be assembled in the matrix element of the neutrino effective electromagnetic current [381, 382] as

$$\langle \nu_f(p_f)|j^{\mu}_{\nu,\mathrm{EM}}|\nu_i(p_i)\rangle = \overline{u}_f(p_f)\Lambda^{\mu}_{fi}(q)u_i(p_i), \tag{6.1}$$

where q is the four-momentum transferred to the photon. The vertex function $\Lambda^{\mu}_{fi}(q)$ is a 3×3 matrix in the neutrino mass eigenstates space that encodes the electromagnetic properties of neutrinos. We are interested in the ultra-relativistic limit where, at low-q^2, it simplifies to,

$$\Lambda^{\mu}_{fi}(q) = \gamma^{\mu}(Q_{fi} - \frac{q^2}{6}\left\langle r^2\right\rangle_{fi}) - i\sigma^{\mu\nu}q_{\nu}\mu_{fi} \tag{6.2}$$

with $f = i$ for diagonal and $f \neq i$ for transition electromagnetic properties. Note that in theories of massive neutrinos, the transition electromagnetic properties can be generated through mixing, even if the matrices in Eq. (6.2) are diagonal in the mass basis [383].

In this work, we conduct a phenomenological study of effective neutrino electromagnetic properties: the millicharge Q, the magnetic moment μ, and the charge radius $\langle r^2\rangle$ at the FPF. Effective here implies the possible inclusion of contributions coming from electric and anapole moments to the magnetic moment and charge radius [384], respectively. Also, the neutral current interaction we study here has no information on the outgoing neutrino flavor. Therefore, we implicitly assume a sum over all final state neutrino flavors [385, 386]. Note that when recasting the results obtained here for e.g. Majorana neutrinos have only transition magnetic moment and millicharge.

The electric neutrality of neutrinos in the SM is guaranteed by charge quantization [387, 388]. But in some BSM theories, neutrinos can have a very small electric charge [389] enabling it to couple to the photon. This BSM interaction can be described by an effective term in the Lagrangian $\mathcal{L} \supset Q_{\nu}(\bar{\nu}\gamma_{\mu}\nu)A^{\mu}$.

Neutrino magnetic moments, on the other hand, do arise in the SM at one loop level [390, 391]. The diagonal magnetic moment for a massive Dirac neutrino is given by

$$\mu_{\nu} \approx \frac{3eG_F}{8\sqrt{2}\pi^2}m_{\nu} \approx 3\cdot 10^{-19}\mu_B\left(\frac{m_{\nu}}{1\ \mathrm{eV}}\right). \tag{6.3}$$

where m_ν is the neutrino mass, e is the electric charge, G_F is the Fermi constant and $\mu_B = e/(2m_e)$ is the Bohr magneton. This very small value is beyond the scope of terrestrial and astrophysical probes currently. The values for transition magnetic moments for Majorana neutrinos are even smaller [392]. However, an additional contribution to the magnetic moment of neutrinos could arise from BSM physics [364, 362, 393]. In an effective field theory approach, this can be parametrized in terms of a higher dimensional operator $\mathcal{L} \supset \mu_\nu(\bar{\nu}\sigma_{\alpha\beta}\nu)F^{\alpha\beta}$ for Dirac neutrinos (for Majorana neutrinos one replaces $\bar{\nu}$ with $\bar{\nu}^c$ for only the left-handed neutrino fields (ν_L) above, and only transition moments are allowed).

Measuring the magnetic moment of neutrinos is important, as it can also in principle shed light on the Dirac vs. Majorana nature of neutrinos. Dirac neutrinos can have diagonal and transition magnetic moments, whereas Majorana neutrinos only have transition magnetic moments. Large transition magnetic moments for Majorana neutrinos could be realized in certain BSM models [394, 395], which are not too far from the current experimental limits, but the off-diagonal moments could be hard to measure, as we do not probe the outgoing neutrino flavor.

Neutrinos also have non-zero charge radii in the SM from radiative corrections given by [396, 397]

$$\langle r^2_{\nu_\ell}\rangle_{\rm SM} = \frac{G_f}{4\sqrt{2}\pi^2}\left[3 - 2\log\frac{m_\ell^2}{m_W^2}\right]. \tag{6.4}$$

where m_ℓ are the lepton masses ($\ell = e, \mu, \tau$) and m_W is the W boson mass. Note that in the SM where neutrinos are massless, the charge radii of neutrinos are restricted to being flavor diagonal, as a consequence of the conservation of lepton numbers. The SM values are then found to be 4.1×10^{-33} cm^2 for ν_e, 2.4×10^{-33} cm^2 for ν_μ and 1.5×10^{-33} cm^2 for ν_τ. These values differ by at most one or two orders of magnitude from current terrestrial bounds, and hence testing the SM prediction of neutrino charge radius is a compelling challenge.

6.3 Detectors at the FPF

An unexpected but powerful source of light and weakly coupled particles can be found at the LHC [37]. In the forward direction, the LHC produces an intense and strongly collimated beam of neutrinos of all three flavors coming mainly from the decays of mesons produced at the interaction point. Currently, there are two experiments taking advantage of this opportunity: FASERν [320, 321] and SND@LHC [398, 399].

In particular, both experiments are expected to obtain about 20 tau neutrino interactions, which exceeds the number of events recorded by the DONuT [400] and OPERA [401] experiments.

Several improved neutrino detectors are planned for the HL-LHC era. They will be housed in the FPF [195, 402] along with an array of other detectors with a wide range of physics potential, to be located in a cavern 620 m downstream from the ATLAS interaction point. Our analysis focuses on two detector technologies at FPF which are sensitive to TeV range neutrino interactions: FLArE, which is a liquid argon time projection chamber, and FASERν2, which is an emulsion-based neutrino detector. In the following, we present the detector details relevant to the phenomenological study at hand:

- **FLArE**, the Forward Liquid Argon Experiment, is composed of a 10 tonne liquid argon time projection chamber with a fiducial volume of $1\text{m} \times 1\text{m} \times 7\text{m}$ [41]. Liquid argon time projection chambers are a proven technology for neutrino physics, having been used at Fermilab's Short-Baseline Neutrino Program [403] and at the future DUNE experiment [404]. They offer the dual advantage of very low energy thresholds of down to 30 MeV and excellent timing resolution, achieved through a light collection system. This will allow one to control possible muon induced backgrounds by vetoing events in coincidence with a muon track, which is critical to the feasibility of our study. FLArE is a 10 tonne detector. We also include in our study a larger 100 tonne detector, dubbed **FLArE-100**, with a fiducial volume of $1.6\text{m} \times 1.6\text{m} \times 30\text{m}$. This is meant to illustrate how sensitivities would scale with target mass.

- **FASERν2** is an emulsion detector designed as a much larger successor to the approved FASERν detector [323]. In the HL-LHC era, FASERν2 is envisioned as a 10 tonne neutrino detector composed of emulsion layers interleaved with tungsten sheets acting as target material. Emulsion detectors are capable of detecting charged tracks with high spatial resolution. The major drawback of emulsion detectors is a lack of timing information associated with the recorded events. FASERν2 aims to mitigate this by introducing tracking layers between and at the end of the emulsion layers. Timing information can then be obtained by successfully matching the event in the emulsion and the tracker. This is helpful in the search for a coincident muon track, which can be used to reduce muon induced backgrounds. We assume that in FASERν2 all muon induced backgrounds can be eliminated with the help of timing information. The fiducial volume we consider is 0.5 m × 0.5 m × 2 m [42]. Since the charged particle has to pass through a sufficient number of emulsion layers to leave a distinguishable track, a minimum particle momentum of 300 MeV [42] is required. This sets the energy threshold of the detector.

In Chapter 5, we discussed the FORMOSA experiment as a potential avenue for studying millicharged particles. While FORMOSA, based on scintillation signatures, offers the advantage of potentially providing stronger sensitivity to millicharged particles than a liquid argon detector like FLArE, it faces limitations at very low charge values due to multiple coincidences. We, therefore, do not consider FORMOSA here, as the feasibility of using scintillation-based experiments to study neutrino millicharge is limited. In contrast, the huge flux of neutrinos enables FLArE to exhibit greater sensitivity in single scattering events, making it more favourable in this regard.

The two processes we study here are neutrino electron elastic scattering and neutral current DIS. The main backgrounds for the former are similar to those studied in Refs. [41, 405] and the latter was studied in the context of FASERν in Ref. [406]. Here we briefly summarize the relevant results.

A major source of similar backgrounds for both processes is muon-induced events. Muons passing through the detector can, for example, emit photons through bremsstrahlung or produce high energy neutral hadrons in inelastic scatterings. The photons could then pair convert to e^+e^- and if one of them is missed, it can mimic our electron scattering signal. Neutral hadron scattering, on the other hand, would look similar to the neutral current DIS neutrino interactions. In both cases, the inclusion of timing capabilities in the detectors allows vetoing such backgrounds by associating such events with the accompanying muon. For example, the currently operating FASER detector employs several scintillating veto layers at its front, each of which has a muon detection efficiency of more than 99.99% [407]. In this study, we assume such muon-induced backgrounds can be reduced to negligible levels.

An irreducible source of backgrounds to both processes is the SM contribution to neutral current neutrino scattering. For neutrino electron elastic scattering, we employ the use of kinematic cuts to enhance the signal-to-background ratio, as described in the next section. This is where a low energy threshold detector like FLArE is advantageous.

Throughout this work, we use the neutrino fluxes presented in Ref. [42] for the

HL-LHC era. They were obtained using the event generator `SIBYLL 2.3d` [408, 409, 410, 411] implemented via `CRMC` [334] which simulates the primary collision. Ref. [412] introduced a fast neutrino flux simulator which models the propagation and decay of long-lived hadrons within the SM in the forward direction at the LHC. Currently, there exist sizeable uncertainties on the neutrino flux. However, this is expected to be brought under control using the charged current scattering event rate once the detector starts to take data [320].

6.4 Neutrino EM Interaction Rate

The signature we investigate in our study is the excess (or deficit) of neutrino neutral current scattering events in the detectors with respect to the expected rate predicted by the SM in the absence of any neutrino EM properties.

We first consider the neutrino electron elastic scattering where the SM cross section, in terms of the electron recoil energy E_r, is given by [413, 52]

$$\left(\frac{d\sigma_{\nu_\ell e}}{dE_r}\right)_{\text{SM}} = \frac{G_F^2 m_e}{2\pi}\left[(g_V^\ell - g_A^\ell)^2\left(1-\frac{E_r}{E_\nu}\right)^2 + (g_V^\ell + g_A^\ell)^2 + \left((g_A^\ell)^2-(g_V^\ell)^2\right)\frac{m_e E_r}{E_\nu^2}\right] \tag{6.5}$$

with the standard vector and axial vector coupling constants g_A^ℓ and g_A^ℓ given by

$$g_V^\ell = 2\sin^2\theta_w - \frac{1}{2} + \delta_{\ell e}\ ,\ g_A^\ell = -\frac{1}{2} + \delta_{\ell e}\ . \tag{6.6}$$

Here G_F is the Fermi constant, θ_W is the weak mixing angle, and E_ν is the neutrino energy. For antineutrinos, one must replace g_A^ℓ by $-g_A^\ell$. There is an extra term for the electron neutrino coming from the exchange of the W boson, which is not present for muon and tau neutrinos. In the presence of non-negligible values for the neutrino electromagnetic properties, the event rate and distribution can be sufficiently distorted.

As detailed below, the most significant effect of including these BSM physics is in the event rate, especially at low recoil energies for the magnetic moment and millicharge. This motivates looking at E_r as the main kinematic variable in our study. One could also look at the recoil angle of the electron, as was studied in Ref. [41]. For neutrino electron scatterings at the energies of interest, so E_ν and $E_r \gg m_e$, the recoil angle is correlated with the recoil energy via $\cos\theta_r \approx 1 - m_e/E_r$. Although, this does not help to distinguish different neutrino electron scattering events but provides another handle to remove backgrounds coming from neutrino nuclear scattering events with a single particle recoiling in the final state. Since we will be imposing a strong kinematic cut on the electron recoil energy that suppresses the background sufficiently, we do not include the recoil angle of the electron as an additional observable. We note, however, the strong correlation between the recoil energy and the recoil angle of the electron can be used to improve energy resolution at small energies.

In some cases, it might be beneficial to also consider nuclear scattering, where one could benefit from higher event rates. As can be seen in Eq. (6.5), the neutral current scattering rate in the SM roughly scales proportionally to the target mass. If the new physics signal count decreases or doesn't increase commensurately, then moving to a heavier target will only degrade the sensitivity. This is the case with neutrino magnetic moment and millicharge, and hence we stick to electron scattering events for both of them. As we will see below, a charge radius essentially induces a shift in the vector coupling constant, g_V and hence we can expect higher rates of signal if we use a heavier target. We therefore also consider neutral current neutrino DIS in the charge radius case, which will result in significantly higher signal event rates and hence improve the bounds on $\langle r^2_{\nu_\ell} \rangle$.

At leading order, the double differential cross section for neutral current neutrino-nucleon DIS is given by [414]

$$\begin{aligned}\frac{d\sigma(\nu N \to \nu X)}{dx\ dy} &= \frac{2G_F^2 m_p E_\nu}{\pi} \frac{m_Z^4}{(Q^2+m_Z^2)^2} \times \\ \sum_{q=u,d,s,c} &\Big[g_{q,L}^2[xf_q(x,Q^2) + xf_{\bar{q}}(x,Q^2)(1-y)^2] + \\ &\quad g_{q,R}^2[xf_q(x,Q^2)(1-y)^2 + xf_{\bar{q}}(x,Q^2)]\Big]\end{aligned} \tag{6.7}$$

for neutrino scattering and

$$\begin{aligned}\frac{d\sigma(\overline{\nu} N \to \overline{\nu} X)}{dx\ dy} &= \frac{2G_F^2 m_p E_\nu}{\pi} \frac{m_Z^4}{(Q^2+m_Z^2)^2} \times \\ \sum_{q=u,d,s,c} &\Big[g_{q,L}^2[xf_q(x,Q^2)(1-y)^2 + xf_{\bar{q}}(x,Q^2)] + \\ &\quad g_{q,R}^2[xf_q(x,Q^2) + xf_{\bar{q}}(x,Q^2)(1-y)^2]\Big]\end{aligned} \tag{6.8}$$

for anti-neutrino scattering, where X stands for the final states that are a byproduct of the DIS other than the neutrino. Here m_p is the mass of the target proton, m_Z is the Z boson mass, and $g_L^q, g_R^q = T^3 - Q_q \sin^2\theta_W$ are the left and right-handed neutral current couplings of the quarks with Q_q being the charge of the quarks in units of e. The differential cross section is expressed in terms of the DIS variables x, y and Q^2, where x is the partonic momentum fraction, $y = E_{\mathrm{had}}/E_\nu$ is the fraction of neutrino's energy that is transferred to the hadronic system, and $Q^2 = 2m_p E_\nu xy$ is the squared 4-momentum transfer. Here E_ν is the incident neutrino energy, and E_{had} is all the energy contained in the hadronic system. The functions $f_q(x, Q^2)$ are the nucleon parton distribution function. Here we use nCTEQ15 which includes nuclear effects of the target nucleus [415].

6.4.1 Neutrino Magnetic Moment

The presence of a BSM contribution to the neutrino magnetic moment can lead to an excess in the number of electron recoil events, especially at low recoil energies. The differential cross section with respect to the electron recoil energy for the elastic scattering of a neutrino (or antineutrino) with incoming flavor ℓ and energy E_ν off an electron in the presence of a magnetic moment is given by [416, 366]

$$\left(\frac{d\sigma_{\nu_\ell e}}{dE_r}\right)_{\mathrm{NMM}} = \left(\frac{d\sigma_{\nu_\ell e}}{dE_r}\right)_{\mathrm{SM}} + \frac{\pi^2}{m_e^2}\left(\frac{1}{E_r} - \frac{1}{E_\nu}\right)\left(\frac{\mu_{\nu_\ell}}{\mu_{\mathrm{B}}}\right)^2, \tag{6.9}$$

where μ_{ν_ℓ} is the effective neutrino magnetic moment, and μ_B is the Bohr magneton. Note that the two contributions in Eq. (6.9) add incoherently in the cross section due to the following helicity argument [417]: in the ultra-relativistic limit, the SM weak interaction conserves the neutrino helicity while the helicity flips in the neutrino magnetic moment interaction. Hence, one is always guaranteed an excess of events in this case.

The two contributions in the cross section exhibit quite different dependencies in the electron recoil energy E_r, as illustrated in Fig. 6.1 top left panel for an incoming neutrino beam with 1 TeV energy. The signal cross section associated with the neutrino magnetic moment exceeds the SM background in the range,

$$E_r \lesssim 10\ \mathrm{GeV} \times \left(\frac{\mu_{\nu_\ell}}{10^{-8}\,\mu_{\mathrm{B}}}\right)^2. \tag{6.10}$$

This leads to an increase in the elastic neutrino-electron events above the SM predicted value at low values of E_r. This can be seen as arising from the $1/E_r$ term in

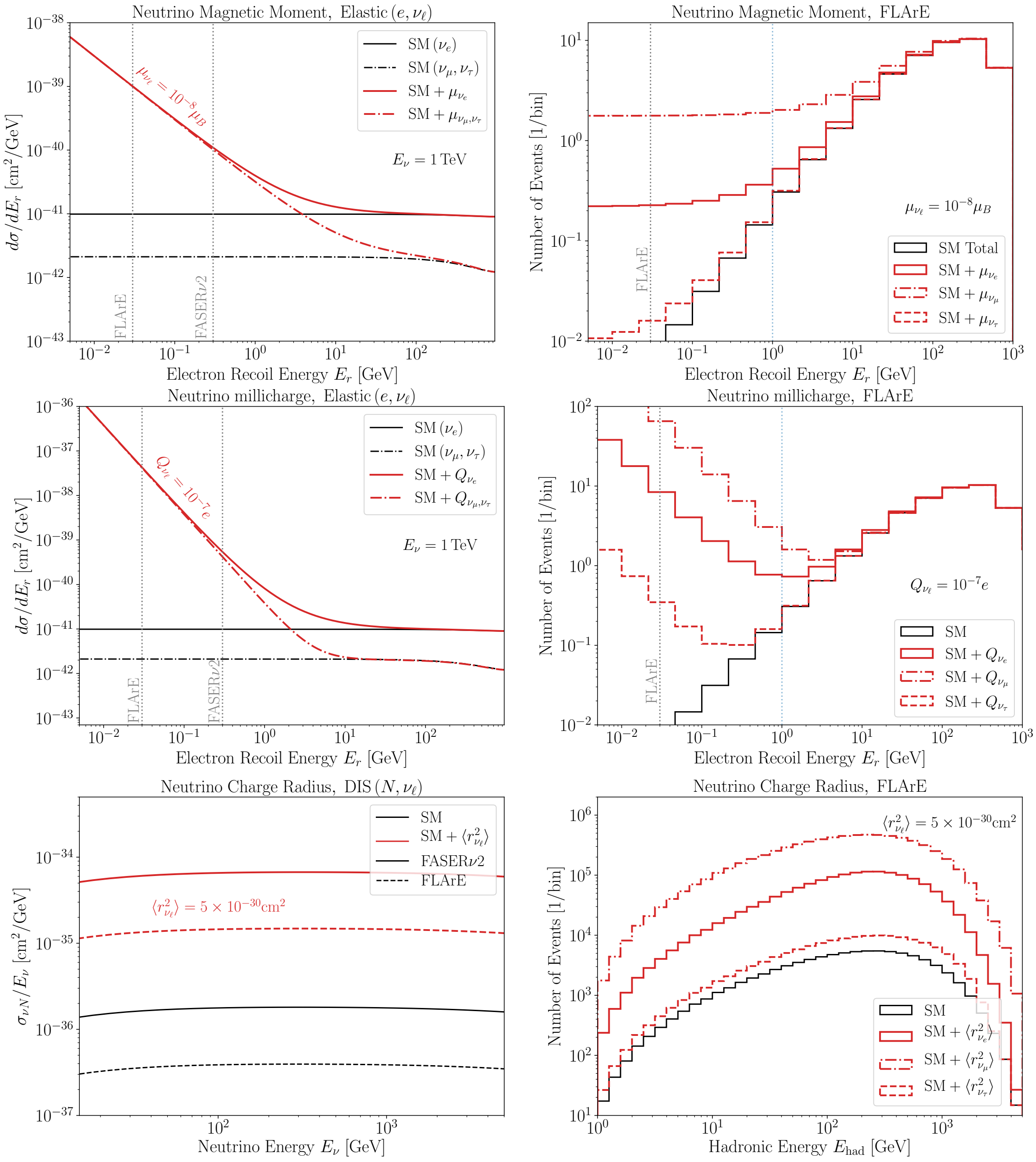

Figure 6.1: **Top and Middle Left:** Differential cross-section of neutrino elastic scattering on the electron as a function of electron recoil energy, corresponding to the incoming neutrino energy of 1 TeV. **Top and Middle Right:** The expected number of events at FLArE, considering the estimated neutrino flux at the FPF in the HL-LHC phase. The magnetic moment and millicharge electromagnetic contributions (red) exceed the SM background (black) at lower recoil energies. The FLArE and FASERν2 detector recoil energy thresholds of 30 and 300 MeV, as well as the 1 GeV upper cutoff, are indicated by vertical dotted lines. **Bottom Left:** Cross section of neutrino-nucleus deep-inelastic scattering in FASERν2 (solid) and FLArE (dashed) as a function of neutrino energy, within the SM (black) and in the presence of the charge radius. **Bottom Right:** Expected event rate at FLArE as a function of the energy of the hadronic system.

the BSM cross section expression. The lines for ν_e and $\nu_{\mu,\tau}$ look different due to the additional diagram coming from the W boson exchange that is only present for ν_e.

Given the neutrino flux at the FPF, the electron recoil energy spectrum at FLArE and FASERν2 detectors can be calculated. Fig. 6.1 top right panel shows the total expected event rate for a benchmark value of $\mu_{\nu_\ell} = 10^{-8}\ \mu_B$ for all three flavors at FLArE, as well as the SM event rate. The three flavors of neutrinos have different fluxes at FPF, resulting in distinct predictions for the event spectrum. The excess events in the low recoil energy bins serve as an experimental signature to look for neutrino magnetic moment.

6.4.2 Neutrino Millicharge

The FPF is an ideal environment to search for millicharged particles in the dark sector [275, 418] and can also be used to probe neutrino millicharge. The inclusion of a non-zero electric charge for the neutrino changes the neutrino-electron elastic scattering cross section as [383, 419, 52]

$$\left(\frac{d\sigma_{\nu_\ell e}}{dE_r}\right)_{\text{NMC}} = \left(\frac{d\sigma_{\nu_\ell e}}{dE_r}\right)_{\text{SM}} + \left(\frac{d\sigma_{\nu_\ell e}}{dE_r}\right)_{\text{Int}} + \left(\frac{d\sigma_{\nu_\ell e}}{dE_r}\right)_{\text{Quad}} . \tag{6.11}$$

The first term is the above SM expression as before. The interference term is,

$$\begin{aligned}\left(\frac{d\sigma_{\nu_\ell e}}{dE_r}\right)_{\text{Int}} = \frac{\sqrt{8\pi}G_F\alpha}{E_\nu^2 E_r}\left(\frac{Q_{\nu_\ell}}{e}\right)\Big[g_V^\ell\big(2E_\nu^2 + E_r^2\\ - E_r(2E_\nu + E_r)\big) + g_A^\ell\big(E_r(2E_\nu - E_r)\big)\Big]\end{aligned} \tag{6.12}$$

with g_V^ℓ, g_A^ℓ defined as before, and the quadratic term is given by

$$\left(\frac{d\sigma_{\nu_\ell e}}{dE_r}\right)_{\text{Quad}} = 4(\pi\alpha)^2\left(\frac{Q_{\nu_\ell}}{e}\right)^2\left[\frac{2E_\nu^2{+}E_r^2{-}2E_\nu E_r}{m_e E_r^2 E_\nu^2}\right], \tag{6.13}$$

where Q_{ν_ℓ} is the electric charge of the neutrino. For anti-neutrino, we replace g_A with $-g_A$ similar to the SM case. The presence of the interference term $\sim \big(Q_{\nu_\ell}/e\big)$ means we are now sensitive to the sign of the neutrino millicharge and depending on the value of Q_{ν_ℓ} we can expect an increase or decrease in the number of events. However, it turns out that, for the values of the millicharge that can be probed at the FPF, the quadratic term always dominates, therefore, an excess of events is expected. For a benchmark value of $Q_{\nu_\ell} = 10^{-7}e$ we see an even steeper increase in cross section at lower recoil energies than for the magnetic moment, as the quadratic term grows proportionally to $1/E_r^2$. This is shown in Fig. 6.1 middle left panel, while the middle right panel shows the event spectrum at FLArE.

Alternatively, neutrino millicharge can also be probed at FORMOSA [275], a proposed experiment located within the FPF to search for millicharged particles. If neutrino possesses a millicharge, then it will ionize the material and deposit energy as it passes through the detector, resulting in a scintillation signature. FORMOSA is a dedicated detector to detect low-charge scintillation signals consisting of an array of plastic scintillators with multiple layers, sensitive to low-energy deposits down to one single photoelectron. The mean ionization energy loss for a millicharged neutrino travelling through the plastic material can be estimated by Bethe-Bloch formula [420] that goes as $\langle dE/dx\rangle \sim (Q_\nu/e)^2 \times 5$ MeV/cm, and is quite insensitive to the neutrino energy and mass. The average number of photoelectrons produced within a scintillator bar N_{PE} is proportional to the ionization energy deposition, the bar length, and the scintillation light yield. To suppress the background noise in the photomultiplier tubes attached to the scintillation bars that collect the produced photoelectrons, the low-energy scintillation signal candidates are required to have multiple coincidences of hits. To detect a millicharged neutrino, at least one photoelectron in each layer of the scintillator must be observed. The detection probability $P = (1-\exp(-N_{\mathrm{PE}}))^n$ follows the Poisson distribution, where n is the number of layers. Conclusions about the relative sensitivity of FORMOSA versus other experiments will be given in Section 6.5.

6.4.3 Neutrino Charge Radius

From Eq. (6.2), one sees that a non-zero value of charge radius amounts to a shift in the vector term of the neutrino vertex function. Within the SM, only diagonal charge radii are allowed, as generation lepton numbers are conserved. However, some BSM scenarios also allow for off-diagonal charge radii [421, 422, 423]. If we only consider diagonal elements in the flavor basis, it was shown in Ref. [391] that this amounts to a modification of the vector coupling constant in Eq. (6.6) as,

$$g_V^\ell \rightarrow g_V^\ell + \frac{2}{3} m_W^2 \langle r_{\nu_\ell}^2 \rangle \sin^2\theta_w. \tag{6.14}$$

This introduces additional linear and quadratic terms in $\langle r_{\nu_\ell}^2\rangle$ to the cross section in Eq. (6.5). Therefore, similar to the neutrino millicharge case, we are sensitive to the sign of $\langle r^2_{\nu_\ell} \rangle$. Also, note that the antineutrino charge radius contribution comes with a negative relative sign to the above shift [52]. For quarks, this shift is modified by the quark-to-electron electric charge ratio as,

$$g^q_V \to g^q_V - \frac{2}{3} Q_q m^2_W \langle r^2_{\nu_\ell} \rangle \sin^2 \theta_w. \tag{6.15}$$

which modifies the left and right-handed neutral current couplings of the quarks $g^q_{L/R} = (g^q_V \pm g^q_A)/2$ in Eqs. (6.7) and (6.8).

In the bottom left panel of Fig. 6.1, we show the DIS cross section rates for a neutrino scattering off the argon nucleus in the FLArE detector and tungsten nucleus in the FASERν2 detector as a function of the incoming neutrino energy, E_ν. FASERν2 with a target atom with a higher atomic number has more nucleons for the neutrino to scatter off and hence has a higher cross section value. In the presence of a non-zero charge radius, the cross section enhancement is almost uniform across the incoming neutrino energy range. In the bottom right panel, we show the event spectrum as a function of $E_{\rm had}$ at FLArE for a benchmark value of $\langle r^2_{\nu_\ell} \rangle = 5 \times 10^{-30}$ cm^2. At the neutrino energies available at FPF and the values of $\langle r^2_{\nu_\ell} \rangle$ we are sensitive to, it is the quadratic term that is dominant, and we observe an excess in events across the spectrum.

Let us now proceed to discuss the technical details of deriving Eq. (6.14) and Eq. (6.15). Starting from the SM interaction defined in Eq. (2.14), the matrix element for the scattering process of $\nu_e + e \to \nu_e + e$ through neutral current interaction can be expressed as follows

$$\begin{aligned} i\mathcal{M}_{\rm NC} =& \left(\frac{ie}{\sin\theta_W \cos\theta_W} \right)^2 \Big[g^\nu_L \bar{\nu}_L \gamma^\mu \nu_L \Big] \frac{-ig_{\mu\nu}}{q^2 - m^2_Z} \Big[g^e_L \bar{e}_L \gamma^\nu e_L + g^e_R \bar{e}_R \gamma^\nu e_R \Big] \\ \approx& \frac{-iG_F}{\sqrt{2}} \Big[\bar{\nu} \gamma^\mu (1+\gamma^5) \nu \Big] \Big[\bar{e} \gamma_\mu (g_V + g_A \gamma^5) e \Big], \end{aligned} \tag{6.16}$$

where the left- and right-handed couplings, with values $g^\nu_L = 1/2$, $g^e_L = -1/2 + \sin^2\theta_W$, and $g^e_L = \sin^2\theta_W$, are incorporated into the parameters $g_V \equiv 2g^\nu_L(g^e_L + g^e_R)$ and $g_A \equiv 2g^\nu_L(g^e_L - g^e_R)$, representing the vector and axial couplings, respectively. We used the Fermi constant $4\sqrt{2}G_F \equiv e^2/(\sin^2\theta_W \cos^2\theta_W m^2_Z)$ in the second line.

For the same neutrino scattering process involving electrons, we also have the charged current (CC) interaction given by

$$\begin{aligned} i\mathcal{M}_{\rm CC} =& \left(\frac{ie}{\sqrt{2}\sin\theta_W}\right)^2 \Big[\bar{\nu}_L\gamma^\mu e_L\Big]\frac{-ig_{\mu\nu}}{q^2-m_W^2}\Big[\bar{e}_L\gamma^\nu\nu_L\Big] \\ \approx& \frac{-iG_F}{\sqrt{2}}\Big[\bar{\nu}\gamma^\mu(1+\gamma^5)e\Big]\Big[\bar{e}\gamma_\mu(1+\gamma^5)\nu\Big] \\ =& \frac{-iG_F}{\sqrt{2}}\Big[\bar{\nu}\gamma^\mu(1+\gamma^5)\nu\Big]\Big[\bar{e}\gamma_\mu(1+\gamma^5)e\Big], \end{aligned} \tag{6.17}$$

where in the last line, we used the Fierz identity, which allows for the interchange of the two spinor bilinears. This interferes with the result of the NC interaction as given in Eq. (6.16), resulting in a change where $g_V \to g_V + 1$ and $g_A \to g_A + 1$, but only for electron neutrinos.

Now, taking into account the neutrino charge radius, we obtain an additional contribution to the matrix element of neutrino scattering off fermion f, where f can be either an electron or a quark. This additional contribution can be expressed as

$$\begin{aligned} i\mathcal{M}_{\langle r^2\rangle} =& (ieQ_f)\left(\frac{ieq^2}{6}\langle r^2_{\nu_\ell}\rangle\right)\Big[\bar{\nu}_L\gamma^\mu\nu_L\Big]\frac{-ig_{\mu\nu}}{q^2}\Big[\bar{f}\gamma^\nu f\Big] \\ =& \frac{iG_F}{\sqrt{2}}\left(\frac{2}{3}(Q_f)m_W^2\sin^2\theta_W\langle r^2_{\nu_\ell}\rangle\right)\Big[\bar{\nu}\gamma^\mu(1+\gamma^5)\nu\Big]\Big[\bar{f}\gamma_\mu f\Big] \\ =& \frac{iG_F}{\sqrt{2}}\Big[\bar{\nu}\gamma^\mu(1+\gamma^5)\nu\Big]\Big[\bar{f}\gamma_\mu(\delta+0\gamma^5)f\Big], \end{aligned} \tag{6.18}$$

where $\delta \equiv \dfrac{2}{3}(Q_f)m_W^2\sin^2\theta_W\langle r^2_{\nu_\ell}\rangle$. As a result, the neutrino charge radius contribution introduces a shift in the vector coupling, where g_V is modified to $g_V - \delta$.

6.5 Sensitivity for Neutrino EM Properties

We are now ready to turn to our analysis. As described in the previous section, both the neutrino magnetic moment and neutrino millicharge would manifest themselves through an enhanced rate of neutrino-electron scattering events with low electron recoil energy. To isolate this effect, we select events within the energy range $E_{\rm thr} < E_r < 1$ GeV. Here we assume a lower energy threshold of $E_{\rm thr} = 30$ MeV for FLArE and 300 MeV for FASERν2. According to Refs. [41, 418], after applying these kinematic cuts, we expect less than $\mathcal{O}(1)$ neutrino-electron scattering events in the SM. Considering statistical uncertainties only, we then set limits on the neutrino magnetic moment and millicharge. Systematic uncertainties are expected to be under control since the neutrino-electron cross section is well understood and the neutrino

Neutrino EM Property		FASERν2	FLArE	FLArE-100
μ_{ν_ℓ} $[10^{-8}\mu_B]$	ν_e	1.78	1.35	0.73
	ν_μ	0.67	0.48	0.25
	ν_τ	10.7	6.59	3.08
Q_{ν_ℓ} $[10^{-8}e]$	ν_e	[-13.1 , 8.92]	[-4.03 , 3.21]	[-2.21 , 1.52]
	ν_μ	[-3.92 , 4.12]	[-0.96 , 1.27]	[-0.24 , 0.30]
	ν_τ	[-64.9 , 65.1]	[-17.9 , 17.9]	[-8.33 , 8.36]
$\langle r^2_{\nu_\ell}\rangle$ $[10^{-32}\text{cm}^2]$ Nuclear Scattering	ν_e	[-3.57 , 4.46]	[-3.47 , 4.29]	[-1.43 , 1.55]
	ν_μ	[-0.65 , 0.67]	[-0.62 , 0.64]	[-0.25 , 0.25]
	ν_τ	[-58.9 , 96.1]	[-41.3 , 78.4]	[-17.3 , 54.8]
$\langle r^2_{\nu_\ell}\rangle$ $[10^{-31}\text{cm}^2]$ Electron Scattering	ν_e	[-1.11 , 0.85]	[-1.62 , 1.10]	[-0.54 , 0.47]
	ν_μ	[-0.86 , 1.70]	[-1.03 , 1.79]	[-0.56 , 1.29]
	ν_τ	[-16.4 , 16.6]	[-14.5 , 14.8]	[-7.53 , 8.04]

Table 6.1: Projected 90% C.L. sensitivity on neutrino electromagnetic properties (μ_{ν_ℓ}, Q_{ν_ℓ}, $\langle r^2_{\nu_\ell}\rangle$) from FASER$\nu$2, FLArE, FLArE-100 detectors for all three flavors, assuming 3 ab^{-1} of integrated luminosity at HL-LHC. For completeness, we also show the charge radius bounds from electron scattering in the last row, which, as expected, are much weaker compared to those from nuclear scattering.

fluxes can be constrained by the same experiment through a measurement of the event rate of neutrino charged current scattering.

We present projected sensitivity on neutrino magnetic moment and millicharge in the upper part of Table 6.1. The upper bounds are given for different flavors at FASERν2, FLArE, and FLArE-100, considering an integrated luminosity of 3 ab^{-1} at HL-LHC. Note that the bounds are slightly sensitive to the sign of the neutrino millicharge due to the presence of the interference terms.

Unlike the other two neutrino properties, the effect of a neutrino charge radius is not confined to a specific energy region. Instead, we search for an increased neutrino neutral current event rate across the whole energy spectrum. For this, we consider both the electron scattering and nuclear scattering channel, where the latter will turn out to be more sensitive due to the significantly larger overall event rate. As this is essentially a precision measurement of the total neutral current scattering rate, it is subject to systematic uncertainties, which we discuss below.

One major source of systematic uncertainties is associated with the neutrino flux. While the uncertainties on the LHC neutrino flux predictions are currently large [412, 353, 424, 425], a measurement of the charged current event rate will constrain the fluxes once the experiment starts taking data. In our analysis, we take this into account by considering the statistical uncertainty expected in the measurement of charged current events as a proxy for the uncertainty on the flux estimates.

Another source of uncertainty is associated with the modelling of the neutrino-nucleus interaction cross section. This includes for example parton distribution functions, quark mass effects, higher order radiative corrections, nuclear shadowing and anti-shadowing effects, the modelling of parton shower and hadronization inside the target nucleus, as well as final state interactions. As for the neutrino fluxes, measurement of charged current neutrino-nucleus interactions at the FPF will provide valuable input to constrain these uncertainties [195, 402] and we will neglect them for the purpose of this study.

Finally, there could be uncertainties arising from the experimental setup, for example, related to energy reconstruction, detection efficiency, particle identification, and event classification. Since the detector designs are still under development, the details on the detector performance are not yet available. However, this also leaves room to consider the signatures under discussion in this study as a benchmark for detector design and optimize them accordingly. In the following, we assume that detector-related uncertainties can be sufficiently reduced to be smaller than the statistical uncertainties of the measurement.

The projected sensitivity on neutrino charge radius, considering statistical uncertainties along with systematic uncertainty coming from the neutrino flux, are presented in the lower part of Table 6.1. As expected, the bounds obtained from the electron scattering signature are much weaker compared to those from nuclear scattering.

The obtained sensitives to the neutrino EM properties are also presented in Fig. 6.2, alongside existing constraints and relevant benchmark scenarios. Here we show only the positive bounds, as the negative values are very similar in absolute value. A recent projection on the sensitivity for electron and muon neutrinos at DUNE, as obtained in Ref. [419], is also shown for comparison.

The left panel shows the results for the neutrino magnetic moment. Shown as dark gray shaded regions are current constraints obtained by purely laboratory experiments using reactor and accelerator neutrinos from GEMMA [368], TEXONO [369], LAMPF [372], LSND [370] and DONUT [371]. The light gray shaded region corresponds to measurements using solar neutrinos at Borexino [374], XENONnT [358,

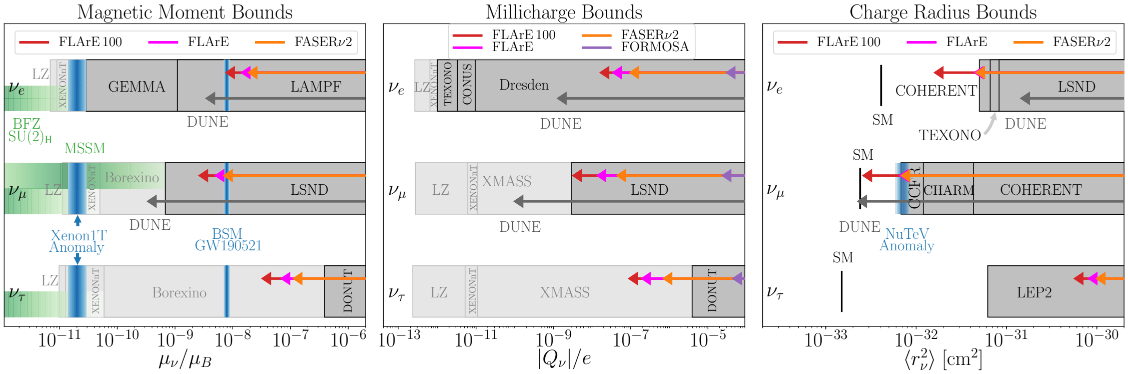

Figure 6.2: Comparison of experimental bounds on neutrino electromagnetic properties: effective magnetic moment (left), millicharge (middle), and charge radius (right). The projected sensitivity of FASERν2 (orange), FLArE (magenta), and FLArE-100 (red) shown alongside existing accelerator and reactor constraints (dark gray shaded), direct detection limits from solar neutrino flux (light gray shaded) and projections from other proposed searches (gray arrow). The blue-shaded regions correspond to the magnetic moment and charge radius values that explain the XENON1T, NuTeV anomaly, and gravitational waves signal from black hole mergers. The contribution of BSM benchmark models to large magnetic moments is presented in green. FLArE can set the world's leading laboratory-based limits on neutrino magnetic moment and millicharge for tau neutrino, and set the world's leading limit for electron neutrino charge radius. The limits on muon neutrino charge radius for FLArE come within a factor of a few from the SM prediction.

426, 376] and LZ [112, 376]. We can see that FLArE will be able to provide the leading sensitivity to tau neutrino magnetic moment obtained using a pure laboratory measurement and constrain $\mu_{\nu_\tau} \lesssim 7 \times 10^{-8} \mu_B$. This is due to the large flux of tau neutrino at the LHC location compared with other laboratory neutrino sources.

Throughout the years, a variety of new physics models predicting large neutrino magnetic moments have been proposed [363, 393, 362]. Such scenarios have been revisited recently in Refs. [365, 366]. The authors conclude that models of Dirac neutrinos with large diagonal neutrino magnetic moments do not seem possible anymore unless one is willing to accept it to be fine-tuned. An example of such a scenario was found in Ref. [364] in a scan over the MSSM parameter space, where a muon magnetic neutrino magnetic moment as large as 10^{-9} μ_B was found. In contrast, for Majorana neutrinos, large transition moments can be realized, for example using a $SU(2)_H$ horizontal symmetry [394] or a BFZ model [395]. We illustrate those scenarios as the green region in Fig. 6.2. In addition, large neutrino magnetic moments have been considered as a solution to the XENON1T anomaly [357] and to explain the existence of black holes in the mass-gap region that have been detected in the gravitational wave event GW190521 [360]. The corresponding regions are marked in blue.

We present the results for neutrino millicharge in the middle panel of Fig. 6.2. As before, the dark-shaded regions show purely laboratory constraints from DONUT [371, 389], LSND [370, 389], Dresden-II [427], CONUS [428], TEXONO [283, 429], and GEMMA [430, 429]. Upper limits on neutrino millicharge have been also obtained using solar neutrinos by XMASS [431], XENONnT [358, 426, 376] and LZ [112, 376] as shown by the light gray shaded regions. Not included in this figure are additional constraints from astrophysical considerations, since they are subject to additional underlying assumptions and uncertainties compared to pure laboratory constraints. In particular, the neutrino millicharge can have an impact on astrophysical phenomena such as red giant or solar cooling [432], the rotation of magnetized neutron stars [433], and the arrival time of SN 1987A supernova neutrinos [434], resulting in approximate upper limits on the effective charge of electron neutrino in the range $|Q_{\nu_e}| \lesssim 10^{-14} - 10^{-19}$. Even stronger constraints than astrophysical arguments on the electron neutrino millicharge can be obtained from electric charge conservation in neutron beta decay, along with the experimental bounds on the neutron charge and the non-neutrality of matter giving $|Q_{\nu_e}| \lesssim 10^{-21}e$ [432]. We find that FLArE is potentially capable of providing the most stringent laboratory-based limit on the effective electric charge of tau neutrino, with an upper limit of $|Q_{\nu_\tau}| \lesssim 10^{-7}e$.

Following the study of millicharged particles using the scintillator-based experiment [289, 275], we can expect to bound the neutrino millicharge at FORMOSA to $|Q_{\nu_e}| \lesssim 2.8 \times 10^{-5}e$, $|Q_{\nu_\mu}| \lesssim 2.2 \times 10^{-5}e$, and $|Q_{\nu_\tau}| \lesssim 4.1 \times 10^{-5}e$ with 90% C.L., corresponding to a scintillator detector with quadruple coincidence. These upper bounds on neutrino millicharge, which are weaker than FLArE results, are presented in the middle panel of Fig. 6.2. These projected sensitivities are almost independent of the neutrino flux, as the sensitivity is limited by the fact that below $Q_\nu \sim 5 \times 10^{-4}e$, the probability of photoelectron production drops significantly. The analysis of FORMOSA with 4 layers is considered almost background free. To demonstrate the sensitivity reach, we also assume zero background for a detector with triple coincidence and find the 90% C.L. upper bounds $|Q_{\nu_e}| \lesssim 0.8 \times 10^{-5}e$, $|Q_{\nu_\mu}| \lesssim 0.5 \times 10^{-5}e$, and $|Q_{\nu_\tau}| \lesssim 1.3 \times 10^{-5}e$. This background-free assumption can in principle be achieved, for example, by using better photomultiplier tubes (PMTs) that have less background noise.

The right panel shows the results for the neutrino charge radius. The dark gray shaded regions are current constraints obtained by purely laboratory experiments using reactor and accelerator neutrinos from COHERENT [427, 435], CHARM-II [436], LSND [370], CCFR [437, 438], LEP2 [438], TEXONO [439]. FLArE can set the world's leading limit for electron neutrino and set highly competitive limits for muon neutrino where it comes within a factor of a few from the SM prediction. The deviation of the weak mixing angle from the SM observed by the NuTeV Collaboration [53] could also be interpreted as a measurement of the muon neutrino charge radius $\langle r^2_{\nu_\mu} \rangle = 4.20 \times 10^{-33}$ within 1σ error [438]. The 1σ preferred region to explain the NuTeV anomaly is shown by the blue target region. For comparison, DUNE is expected to constrain $|\langle r^2_{\nu_\mu} \rangle| < 2 \times 10^{-33}$ cm^2 and $|\langle r^2_{\nu_e} \rangle| < 1 \times 10^{-31}$ cm^2, which is an order of magnitude weaker than the FLArE bound for the electron neutrino. The DUNE projection considered the electron scattering signature, which suffers from lower event rates. A measurement using nuclear scattering at DUNE does not seem promising due to the large nuclear uncertainties in the cross section for GeV energy neutrinos.

6.6 Measurement of the Weak Mixing Angle and the NuTeV Anomaly

The measurement of neutrino interactions at the energies accessible at the FPF provides an opportunity to measure precisely the electroweak parameters. The weak mixing angle, $\sin^2\theta_W$, is one key parameter that parameterizes several measurable observables in the electroweak sector of the SM. The value of $\sin^2\theta_W$ gets radiative corrections and depends on the renormalization prescription [440], where $\overline{\text{MS}}$ (modified minimal subtraction) scheme is conventionally employed. One of the best measurements of the weak mixing angle comes from Z-pole observables [441, 420] (Tevatron, LEP1, SLC, LHC) with an average value of $\sin^2\theta_W(m_Z)_{\overline{\text{MS}}} = 0.23125(16)$, comparable to the SM value of $\sin^2\theta_W(m_Z)_{\overline{\text{MS}}} = 0.23122(4)$ [420]. At relatively low energy scales, several experimental measurements of weak mixing angle exist (for a review, see Ref. [442]) including the electron-deep inelastic scattering [443] (eDIS), neutrino-nucleus scattering [53] (NuTeV), atomic parity violation [444, 445, 446, 447] (APV on cesium), Moller scattering [448] (SLAC E158), elastic electron-proton scattering [449] (Q_{weak}), and coherent elastic neutrino-nucleus scattering at COHERENT [450] and Dresden-II [451]. The precise measurement of the weak mixing angle at different

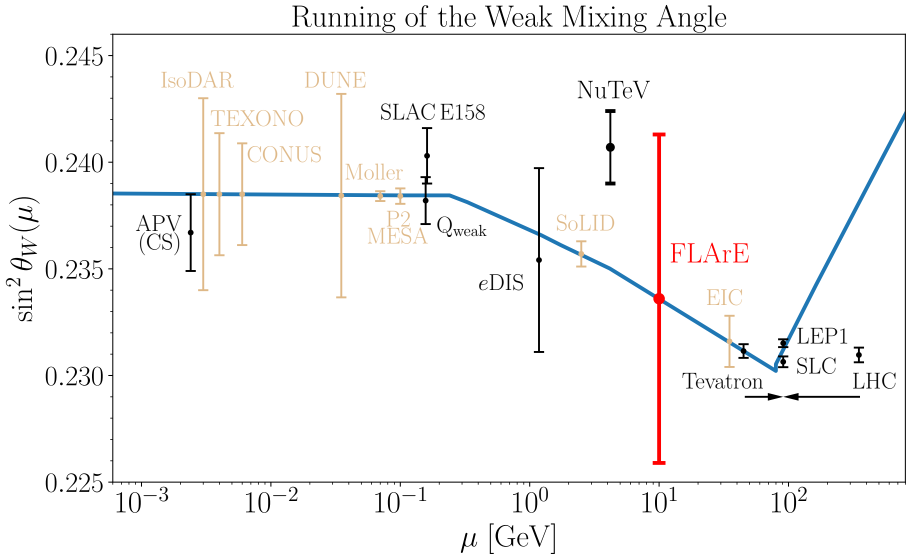

Figure 6.3: Scale dependence of the weak mixing angle in the $\overline{\rm MS}$ scheme, $\sin^2\theta_W(\mu)$, shown with the existing measurements (black), the expected sensitivity of experiments at FPF (red), and other future experiments (beige). The blue line corresponds to the SM prediction for the running of $\sin^2\theta_W$ with scale μ. For clarity, the Tevatron and LHC points are shifted horizontally on either side.

energy scales provides a direct probe of new physics beyond the SM [442, 452, 453]. In particular, it will allow one to test the NuTeV anomaly [53]. Using neutrino scattering, the collaboration measured a value of $\sin^2\theta_W$ that was 3σ above the SM prediction at a scale of ~ 4 GeV. A measurement at FPF will shed more light on the running of the weak mixing angle at a similar energy scale. Any change in the weak mixing angle from the SM value, $\sin^2\theta_W \to \sin^2\theta_W + \Delta\sin^2\theta_W$, will result in a shift in the vector coupling constant,

$$g_V^q \to g_V^q - 2Q_q \Delta\sin^2\theta_W. \tag{6.19}$$

The phenomenological consequences of this shift are therefore very similar to the study of neutrino charge radius presented in the previous section. We perform a similar analysis to obtain the FLArE expected sensitivity to the weak mixing angle and constrain $\Delta\sin^2\theta_W < 0.0077$ at 68% C.L. The estimate for sensitivity to $\sin^2\theta_W$ in the $\overline{\rm MS}$ scheme at the scale $\mu \sim Q \sim 10$ GeV, which is the typical momentum transfer for a TeV scale energy neutrino at FLArE, is shown in Fig. 6.3, along with the existing constraints and the running of the coupling predicted by the SM [440, 454, 420]. For comparison, we also show the projected sensitivities to the weak mixing angle from future experiments including DUNE [455], EIC [456], Moller at JLAB [448, 457], MESA-P2 [458], SoLID at JLAB [459], IsoDAR at Yemilab [460], and reactors [461, 462, 463, 464] (TEXONO, CONUS).

A precise measurement of the weak mixing angle requires good control over various systematic uncertainties. These are analogous to the measurement of the neutrino charge radius through nuclear scattering, and we refer the reader to the previous section for a more detailed discussion. As before, we have considered statistical uncertainties as well as uncertainties associated with flux normalization as constrained by charged current measurements in our sensitivity estimate. It is worth noting that the measurement of the weak mixing angle provides a well-motivated benchmark for detector performance requirements that should be considered during detector design.

6.7 Concluding remarks

The immense flux of neutrinos in the forward region of the LHC provides an excellent opportunity for neutrino physics. This neutrino beam is a powerful source of the most energetic human-made neutrinos for all three flavors. The proposed neutrino detectors at the FPF, FASERν2 and FLArE, can use this neutrino beam to set stringent constraints on neutrino electromagnetic properties and measure the weak mixing angle to percent level precision.

In this work, we have presented a detailed phenomenological study on the potential of the FPF experiments to probe the neutrino electromagnetic properties: magnetic moment, millicharge and charge radius. All these scenarios result in an excess of neutral current events that can be observed at these detectors. We first look at neutrino-electron elastic scattering, where in the presence of neutrino magnetic moment and millicharge the excess events are at low electron recoil energies. Focusing on this kinematic region and taking advantage of the huge tau neutrino flux, FPF can set the strongest laboratory-based limits on neutrino magnetic moment and millicharge for tau neutrinos. For neutrino charge radius, better constraints are obtained by looking at the neutral current neutrino DIS process, where the heavier target results in an increased event rate over neutrino-electron elastic scattering. By looking for excess events across the entire spectrum, FPF can set the world's leading limits on the neutrino charge radius for electron neutrinos and, for muon neutrinos, FPF can come within a factor of a few from the SM prediction. We have summarized our results in Table 6.1 and Fig. 6.2.

An important test of the SM is the measurement of electroweak parameters at different energy scales. FPF has the potential to measure the weak mixing angle with a precision of about 3% at an energy scale of $\mu \sim 10$ GeV. In Fig. 6.3, we show the scale dependence of the weak mixing angle along with the FPF measurement, which considers both statistical and flux uncertainties. This is an important test of the SM, especially in light of the NuTeV anomaly. The ability to measure the weak mixing angle with high precision sets an important benchmark for the design of the FPF neutrino detectors.

Chapter 7

Conclusions

The research program presented in this dissertation has carried out the analysis of exploring the sensitivity of fixed target proton colliders to dark sectors. Our investigations focused on utilizing accelerator probes to study dark matter and other Beyond the Standard Model particles, including dark photons, dark Higgs, and millicharged particles. We began by revisiting the case of a minimal dark scalar coupled to the Standard Model through the Higgs portal, decaying visibly to leptons. By carefully interpreting the dataset from the LSND experiment, we were able to establish leading constraints within two mass windows between 150 and 350 MeV. At LSND energies, heavy kaons and mesons with significant scalar branching rates are kinematically inaccessible. We also examined various other pertinent production mechanisms within the target, such as proton bremsstrahlung, Delta decays, and Primakov conversion, with the former being identified as the dominant process at LSND beam energies.

Motivated by proposals for new searches at Fermilab and the LHC, we revisited the rate of bremsstrahlung of light dark vectors and scalars, which emerged as a primary production mode in the forward direction for higher energy beams. The importance of this channel is particularly prominent within the mass range of 0.5 to 1.0 GeV, as it is enhanced by resonant hadronic mixing. Considering the modelling of forward elastic and diffractive scattering via pomeron exchange, we found that the combination of initial- and final-state radiation for quasi-elastic pomeron-mediated scattering is suppressed via interference. Consequently, we developed a model that approximated the bremsstrahlung rate solely from the initial state radiation in non-single diffraction inelastic scattering and analyzed the precision in comparison with other approximation methods.

The newly proposed LHC Forward Physics Facility emerged as a highly promising site for searching for long-lived particles, millicharged particles, and especially for studying high-energy colliding neutrinos. In this context, we proposed the FORMOSA experiment, strategically positioned within the LHC forward region, which can provide an exceptional sensitivity to search for millicharged particles in the 10 MeV to 100 GeV mass window by exploiting their scintillation signature. A large region of parameter space for millicharged dark matter models can be constrained by this scintillation-based experiment during HL-LHC operation. Additionally, the LHC forward region provides a unique opportunity for investigating neutrino interactions at TeV energies, given its high flux of neutrinos. Exploiting this advantage, we demonstrated the potential of proposed experiments in this location to study neutrino electromagnetic properties. In particular, our study highlights the potential for setting the strongest laboratory-based limits on neutrino magnetic moment and millicharge for tau neutrinos. Considering the neutral current deep inelastic scattering, we found that a liquid argon experiment has the potential to test the SM prediction for the neutrino charge radius and to determine the weak mixing angle with sub-percent accuracy. Investigating new interactions in the neutrino sector can help to better understand the broader scope of dark matter and neutrino physics with possible connections between the two sectors.

As an outlook, there are extensions of fixed targets' sensitivity to dark sectors worth exploring. The application of proton bremsstrahlung can be expanded to encompass other long-lived dark sectors such as axion-like particles (ALPs) [465, 466] with gluon coupling and millicharged particles. In the low mass limit, the bremsstrahlung production channel may dominate the ALP production through mixing with pseudo-scalar mesons. For light millicharged particle χ ($m_\chi \lesssim 100$ MeV), we expect the forward production cross-section via proton bremsstrahlung to have the same order of magnitude as the dominant $\pi \to \gamma\bar{\chi}\chi$ production channel.

Bibliography

[1] G. Bertone, D. Hooper, and J. Silk, "Particle dark matter: Evidence, candidates and constraints," *Phys. Rept.* **405** (2005) 279–390, `arXiv:hep-ph/0404175`.

[2] J. Billard *et al.*, "Direct detection of dark matter—APPEC committee report*," *Rept. Prog. Phys.* **85** (2022) no. 5, 056201, `arXiv:2104.07634 [hep-ex]`.

[3] B. W. Lee and S. Weinberg, "Cosmological Lower Bound on Heavy Neutrino Masses," *Phys. Rev. Lett.* **39** (1977) 165–168. [,183(1977)].

[4] C. Boehm, D. Hooper, J. Silk, M. Casse, and J. Paul, "MeV dark matter: Has it been detected?," *Phys. Rev. Lett.* **92** (2004) 101301, `arXiv:astro-ph/0309686 [astro-ph]`.

[5] M. Pospelov, A. Ritz, and M. B. Voloshin, "Secluded WIMP Dark Matter," *Phys.Lett.* **B662** (2008) 53–61, `arXiv:0711.4866 [hep-ph]`.

[6] M. Pospelov, "Secluded U(1) below the weak scale," *Phys. Rev.* **D80** (2009) 095002, `arXiv:0811.1030 [hep-ph]`.

[7] B. Batell, M. Pospelov, and A. Ritz, "Probing a Secluded U(1) at B-factories," *Phys.Rev.* **D79** (2009) 115008, `arXiv:0903.0363 [hep-ph]`.

[8] R. Essig, P. Schuster, and N. Toro, "Probing Dark Forces and Light Hidden Sectors at Low-Energy e+e- Colliders," *Phys.Rev.* **D80** (2009) 015003, `arXiv:0903.3941 [hep-ph]`.

[9] M. Reece and L.-T. Wang, "Searching for the light dark gauge boson in GeV-scale experiments," *JHEP* **0907** (2009) 051, `arXiv:0904.1743 [hep-ph]`.

[10] M. Freytsis, G. Ovanesyan, and J. Thaler, "Dark force detection in low energy *ep* collisions," *JHEP* **01** (2010) 111, `arXiv:0909.2862 [hep-ph]`.

[11] B. Batell, M. Pospelov, and A. Ritz, "Multi-lepton Signatures of a Hidden Sector in Rare B Decays," *Phys.Rev.* **D83** (2011) 054005, `arXiv:0911.4938 [hep-ph]`.

[12] M. Freytsis, Z. Ligeti, and J. Thaler, "Constraining the Axion Portal with $B \to K l^+ l^-$," *Phys. Rev. D* **81** (2010) 034001, `arXiv:0911.5355 [hep-ph]`.

[13] R. Essig, P. Schuster, N. Toro, and B. Wojtsekhowski, "An Electron Fixed Target Experiment to Search for a New Vector Boson A' Decaying to e+e-," *JHEP* **1102** (2011) 009, `arXiv:1001.2557 [hep-ph]`.

[14] R. Essig, R. Harnik, J. Kaplan, and N. Toro, "Discovering New Light States at Neutrino Experiments," *Phys.Rev.* **D82** (2010) 113008, `arXiv:1008.0636 [hep-ph]`.

[15] K. L. McDonald and D. E. Morrissey, "Low-Energy Signals from Kinetic Mixing with a Warped Abelian Hidden Sector," *JHEP* **1102** (2011) 087, `arXiv:1010.5999 [hep-ph]`.

[16] M. Williams, C. Burgess, A. Maharana, and F. Quevedo, "New Constraints (and Motivations) for Abelian Gauge Bosons in the MeV-TeV Mass Range," *JHEP* **1108** (2011) 106, `arXiv:1103.4556 [hep-ph]`.

[17] **APEX Collaboration** Collaboration, S. Abrahamyan *et al.*, "Search for a New Gauge Boson in Electron-Nucleus Fixed-Target Scattering by the APEX Experiment," *Phys.Rev.Lett.* **107** (2011) 191804, `arXiv:1108.2750 [hep-ex]`.

[18] **KLOE-2** Collaboration, F. Archilli, D. Babusci, D. Badoni, I. Balwierz, G. Bencivenni, *et al.*, "Search for a vector gauge boson in phi meson decays with the KLOE detector," *Phys.Lett.* **B706** (2012) 251–255, `arXiv:1110.0411 [hep-ex]`.

[19] **BaBar Collaboration** Collaboration, J. Lees *et al.*, "Search for Low-Mass Dark-Sector Higgs Bosons," *Phys.Rev.Lett.* **108** (2012) 211801, `arXiv:1202.1313 [hep-ex]`.

[20] H. Davoudiasl, H.-S. Lee, and W. J. Marciano, "'Dark' Z implications for Parity Violation, Rare Meson Decays, and Higgs Physics," *Phys.Rev.* **D85** (2012) 115019, `arXiv:1203.2947 [hep-ph]`.

[21] Y. Kahn and J. Thaler, "Searching for an invisible A' vector boson with DarkLight," *Phys.Rev.* **D86** (2012) 115012, `arXiv:1209.0777 [hep-ph]`.

[22] S. Andreas, C. Niebuhr, and A. Ringwald, "New Limits on Hidden Photons from Past Electron Beam Dumps," *Phys.Rev.* **D86** (2012) 095019, `arXiv:1209.6083 [hep-ph]`.

[23] J. Alexander *et al.*, "Dark Sectors 2016 Workshop: Community Report," 8, 2016. `arXiv:1608.08632 [hep-ph]`.

[24] M. Battaglieri *et al.*, "US Cosmic Visions: New Ideas in Dark Matter 2017: Community Report," `arXiv:1707.04591 [hep-ph]`. `https://www.osti.gov/biblio/1409838`.

[25] J. Beacham *et al.*, "Physics Beyond Colliders at CERN: Beyond the Standard Model Working Group Report," `arXiv:1901.09966 [hep-ex]`.

[26] B. Batell, M. Pospelov, and A. Ritz, "Exploring Portals to a Hidden Sector Through Fixed Targets," *Phys.Rev.* **D80** (2009) 095024, `arXiv:0906.5614 [hep-ph]`.

[27] P. deNiverville, M. Pospelov, and A. Ritz, "Observing a light dark matter beam with neutrino experiments," *Phys.Rev.* **D84** (2011) 075020, `arXiv:1107.4580 [hep-ph]`.

[28] P. deNiverville, D. McKeen, and A. Ritz, "Signatures of sub-GeV dark matter beams at neutrino experiments," *Phys.Rev.* **D86** (2012) 035022, `arXiv:1205.3499 [hep-ph]`.

[29] Y. Kahn, G. Krnjaic, J. Thaler, and M. Toups, "DAEdALUS and Dark Matter," *Phys. Rev.* **D91** (2014) no. 5, 055006, `arXiv:1411.1055 [hep-ph]`.

[30] **LBNE** Collaboration, C. Adams *et al.*, "The Long-Baseline Neutrino Experiment: Exploring Fundamental Symmetries of the Universe," 2013. `arXiv:1307.7335 [hep-ex]`. `http://www.osti.gov/scitech/biblio/1128102`.

[31] D. E. Soper, M. Spannowsky, C. J. Wallace, and T. M. P. Tait, "Scattering of Dark Particles with Light Mediators," *Phys. Rev.* **D90** (2014) no. 11, 115005, `arXiv:1407.2623 [hep-ph]`.

[32] B. A. Dobrescu and C. Frugiuele, "GeV-Scale Dark Matter: Production at the Main Injector," *JHEP* **02** (2015) 019, `arXiv:1410.1566 [hep-ph]`.

[33] P. Coloma, B. A. Dobrescu, C. Frugiuele, and R. Harnik, "Dark matter beams at LBNF," *JHEP* **04** (2016) 047, `arXiv:1512.03852 [hep-ph]`.

[34] P. deNiverville, C.-Y. Chen, M. Pospelov, and A. Ritz, "Light dark matter in neutrino beams: production modelling and scattering signatures at MiniBooNE, T2K and SHiP," *Phys. Rev.* **D95** (2017) no. 3, 035006, `arXiv:1609.01770 [hep-ph]`.

[35] **MiniBooNE** Collaboration, A. A. Aguilar-Arevalo *et al.*, "Dark Matter Search in a Proton Beam Dump with MiniBooNE," *Phys. Rev. Lett.* **118** (2017) no. 22, 221803, `arXiv:1702.02688 [hep-ex]`.

[36] **MiniBooNE DM** Collaboration, A. A. Aguilar-Arevalo *et al.*, "Dark Matter Search in Nucleon, Pion, and Electron Channels from a Proton Beam Dump with MiniBooNE," `arXiv:1807.06137 [hep-ex]`.

[37] J. L. Feng, I. Galon, F. Kling, and S. Trojanowski, "ForwArd Search ExpeRiment at the LHC," *Phys. Rev. D* **97** (2018) no. 3, 035001, `arXiv:1708.09389 [hep-ph]`.

[38] **MATHUSLA** Collaboration, C. Alpigiani *et al.*, "A Letter of Intent for MATHUSLA: A Dedicated Displaced Vertex Detector above ATLAS or CMS.," `arXiv:1811.00927 [physics.ins-det]`.

[39] **FASER** Collaboration, A. Ariga *et al.*, "Technical Proposal for FASER: ForwArd Search ExpeRiment at the LHC," `arXiv:1812.09139 [physics.ins-det]`.

[40] B. Dutta, D. Kim, S. Liao, J.-C. Park, S. Shin, L. E. Strigari, and A. Thompson, "Searching for Dark Matter Signals in Timing Spectra at Neutrino Experiments," `arXiv:2006.09386 [hep-ph]`.

[41] B. Batell, J. L. Feng, and S. Trojanowski, "Detecting Dark Matter with Far-Forward Emulsion and Liquid Argon Detectors at the LHC," *Phys. Rev. D* **103** (2021) no. 7, 075023, `arXiv:2101.10338 [hep-ph]`.

[42] B. Batell, J. L. Feng, A. Ismail, F. Kling, R. M. Abraham, and S. Trojanowski, "Discovering dark matter at the LHC through its nuclear scattering in far-forward emulsion and liquid argon detectors," *Phys. Rev. D* **104** (2021) no. 3, 035036, `arXiv:2107.00666 [hep-ph]`.

[43] J. D. Bjorken, R. Essig, P. Schuster, and N. Toro, "New Fixed-Target Experiments to Search for Dark Gauge Forces," *Phys.Rev.* **D80** (2009) 075018, `arXiv:0906.0580 [hep-ph]`.

[44] E. Izaguirre, G. Krnjaic, P. Schuster, and N. Toro, "New Electron Beam-Dump Experiments to Search for MeV to few-GeV Dark Matter," *Phys.Rev.* **D88** (2013) 114015, `arXiv:1307.6554 [hep-ph]`.

[45] M. D. Diamond and P. Schuster, "Searching for Light Dark Matter with the SLAC Millicharge Experiment," *Phys.Rev.Lett.* **111** (2013) no. 22, 221803, `arXiv:1307.6861 [hep-ph]`.

[46] E. Izaguirre, G. Krnjaic, P. Schuster, and N. Toro, "Physics Motivation for a Pilot Dark Matter Search at Jefferson Laboratory," `arXiv:1403.6826 [hep-ph]`.

[47] B. Batell, R. Essig, and Z. Surujon, "Strong Constraints on Sub-GeV Dark Sectors from SLAC Beam Dump E137," *Phys. Rev. Lett.* **113** (2014) no. 17, 171802, `arXiv:1406.2698 [hep-ph]`.

[48] **BaBar** Collaboration, J. P. Lees *et al.*, "Search for Invisible Decays of a Dark Photon Produced in e^+e^- Collisions at BaBar," *Phys. Rev. Lett.* **119** (2017) no. 13, 131804, `arXiv:1702.03327 [hep-ex]`.

[49] A. Berlin, N. Blinov, G. Krnjaic, P. Schuster, and N. Toro, "Dark Matter, Millicharges, Axion and Scalar Particles, Gauge Bosons, and Other New Physics with LDMX," *Phys. Rev.* **D99** (2019) no. 7, 075001, `arXiv:1807.01730 [hep-ph]`.

[50] D. Banerjee *et al.*, "Dark matter search in missing energy events with NA64," *Phys. Rev. Lett.* **123** (2019) no. 12, 121801, `arXiv:1906.00176 [hep-ex]`.

[51] A. Berlin, P. deNiverville, A. Ritz, P. Schuster, and N. Toro, “Sub-GeV dark matter production at fixed-target experiments,” *Phys. Rev. D* **102** (2020) no. 9, 095011, `arXiv:2003.03379 [hep-ph]`.

[52] C. Giunti and A. Studenikin, “Neutrino electromagnetic interactions: a window to new physics,” *Rev. Mod. Phys.* **87** (2015) 531, `arXiv:1403.6344 [hep-ph]`.

[53] **NuTeV** Collaboration, G. P. Zeller *et al.*, “A Precise Determination of Electroweak Parameters in Neutrino Nucleon Scattering,” *Phys. Rev. Lett.* **88** (2002) 091802, `arXiv:hep-ex/0110059`. [Erratum: Phys.Rev.Lett. 90, 239902 (2003)].

[54] T. R. Slatyer and C.-L. Wu, “Early-Universe constraints on dark matter-baryon scattering and their implications for a global 21 cm signal,” *Phys. Rev.* **D98** (2018) no. 2, 023013, `arXiv:1803.09734 [astro-ph.CO]`.

[55] J. L. Feng, F. Kling, *et al.*, “Forward physics facility,”. `https://doi.org/10.5281/zenodo.4009641`.

[56] **ATLAS** Collaboration, G. Aad *et al.*, “Observation of a new particle in the search for the Standard Model Higgs boson with the ATLAS detector at the LHC,” *Phys. Lett. B* **716** (2012) 1–29, `arXiv:1207.7214 [hep-ex]`.

[57] **Particle Data Group** Collaboration, M. Tanabashi *et al.*, “Review of Particle Physics,” *Phys. Rev. D* **98** (2018) no. 3, 030001.

[58] **LBNE** Collaboration, C. Adams *et al.*, “The Long-Baseline Neutrino Experiment: Exploring Fundamental Symmetries of the Universe,” `arXiv:1307.7335 [hep-ex]`.

[59] **WMAP** Collaboration, E. Komatsu *et al.*, “Seven-Year Wilkinson Microwave Anisotropy Probe (WMAP) Observations: Cosmological Interpretation,” *Astrophys. J. Suppl.* **192** (2011) 18, `arXiv:1001.4538 [astro-ph.CO]`.

[60] **SDSS** Collaboration, D. J. Eisenstein *et al.*, “Detection of the Baryon Acoustic Peak in the Large-Scale Correlation Function of SDSS Luminous Red Galaxies,” *Astrophys. J.* **633** (2005) 560–574, `arXiv:astro-ph/0501171`.

[61] V. C. Rubin and W. K. Ford, Jr., “Rotation of the Andromeda Nebula from a Spectroscopic Survey of Emission Regions,” *Astrophys. J.* **159** (1970) 379–403.

[62] E. van Uitert, H. Hoekstra, T. Schrabback, D. G. Gilbank, M. D. Gladders, and H. K. C. Yee, “Constraints on the shapes of galaxy dark matter haloes from weak gravitational lensing,” *Astron. Astrophys.* **545** (2012) A71, `arXiv:1206.4304 [astro-ph.CO]`.

[63] D. Clowe, A. Gonzalez, and M. Markevitch, “Weak lensing mass reconstruction of the interacting cluster 1E0657-558: Direct evidence for the existence of dark matter,” *Astrophys. J.* **604** (2004) 596–603, `arXiv:astro-ph/0312273`.

[64] H. Hoekstra, H. Yee, and M. Gladders, “Current status of weak gravitational lensing,” *New Astron. Rev.* **46** (2002) 767–781, `arXiv:astro-ph/0205205`.

[65] L. A. Moustakas and R. B. Metcalf, “Detecting dark matter substructure spectroscopically in strong gravitational lenses,” *Mon. Not. Roy. Astron. Soc.* **339** (2003) 607, `arXiv:astro-ph/0206176 [astro-ph]`.

[66] E. W. Kolb and M. S. Turner, *The Early Universe*, vol. 69. 1990.

[67] S. Weinberg, *Cosmology*. 2008.

[68] **Planck** Collaboration, N. Aghanim *et al.*, “Planck 2018 results. I. Overview and the cosmological legacy of Planck,” *Astron. Astrophys.* **641** (2020) A1, `arXiv:1807.06205 [astro-ph.CO]`.

[69] O. F. Piattella, *Lecture Notes in Cosmology*. UNITEXT for Physics. Springer, Cham, 2018. `arXiv:1803.00070 [astro-ph.CO]`.

[70] **2dFGRS** Collaboration, S. Cole *et al.*, “The 2dF Galaxy Redshift Survey: Power-spectrum analysis of the final dataset and cosmological implications,” *Mon. Not. Roy. Astron. Soc.* **362** (2005) 505–534, `arXiv:astro-ph/0501174`.

[71] J. E. Bautista *et al.*, “Measurement of baryon acoustic oscillation correlations at $z = 2.3$ with SDSS DR12 Lyα-Forests,” *Astron. Astrophys.* **603** (2017) A12, `arXiv:1702.00176 [astro-ph.CO]`.

[72] M. Blomqvist *et al.*, "Baryon acoustic oscillations from the cross-correlation of Lyα absorption and quasars in eBOSS DR14," *Astron. Astrophys.* **629** (2019) A86, `arXiv:1904.03430 [astro-ph.CO]`.

[73] **Supernova Cosmology Project** Collaboration, N. Suzuki *et al.*, "The Hubble Space Telescope Cluster Supernova Survey: V. Improving the Dark Energy Constraints Above z>1 and Building an Early-Type-Hosted Supernova Sample," *Astrophys. J.* **746** (2012) 85, `arXiv:1105.3470 [astro-ph.CO]`.

[74] **Pan-STARRS1** Collaboration, D. M. Scolnic *et al.*, "The Complete Light-curve Sample of Spectroscopically Confirmed SNe Ia from Pan-STARRS1 and Cosmological Constraints from the Combined Pantheon Sample," *Astrophys. J.* **859** (2018) no. 2, 101, `arXiv:1710.00845 [astro-ph.CO]`.

[75] E. Aubourg *et al.*, "Cosmological implications of baryon acoustic oscillation measurements," *Phys. Rev. D* **92** (2015) no. 12, 123516, `arXiv:1411.1074 [astro-ph.CO]`.

[76] **Planck** Collaboration, N. Aghanim *et al.*, "Planck 2018 results. VI. Cosmological parameters," *Astron. Astrophys.* **641** (2020) A6, `arXiv:1807.06209 [astro-ph.CO]`. [Erratum: Astron.Astrophys. 652, C4 (2021)].

[77] **Planck** Collaboration, P. A. R. Ade *et al.*, "Planck 2013 results. I. Overview of products and scientific results," *Astron. Astrophys.* **571** (2014) A1, `arXiv:1303.5062 [astro-ph.CO]`.

[78] J. Schaye *et al.*, "The EAGLE project: Simulating the evolution and assembly of galaxies and their environments," *Mon. Not. Roy. Astron. Soc.* **446** (2015) 521–554, `arXiv:1407.7040 [astro-ph.GA]`.

[79] V. Springel *et al.*, "First results from the IllustrisTNG simulations: matter and galaxy clustering," *Mon. Not. Roy. Astron. Soc.* **475** (2018) no. 1, 676–698, `arXiv:1707.03397 [astro-ph.GA]`.

[80] **DES** Collaboration, E. O. Nadler *et al.*, "Milky Way Satellite Census. III. Constraints on Dark Matter Properties from Observations of Milky Way

Satellite Galaxies," *Phys. Rev. Lett.* **126** (2021) 091101, `arXiv:2008.00022 [astro-ph.CO]`.

[81] S. Tulin and H.-B. Yu, "Dark Matter Self-interactions and Small Scale Structure," *Phys. Rept.* **730** (2018) 1–57, `arXiv:1705.02358 [hep-ph]`.

[82] V. C. Rubin, W. K. Ford, Jr., and N. Thonnard, "Extended rotation curves of high-luminosity spiral galaxies. IV. Systematic dynamical properties, Sa through Sc," *Astrophys. J. Lett.* **225** (1978) L107–L111.

[83] V. C. Rubin, N. Thonnard, and W. K. Ford, Jr., "Rotational properties of 21 SC galaxies with a large range of luminosities and radii, from NGC 4605 /R = 4kpc/ to UGC 2885 /R = 122 kpc/," *Astrophys. J.* **238** (1980) 471.

[84] J. P. Ostriker and P. J. E. Peebles, "A Numerical Study of the Stability of Flattened Galaxies: or, can Cold Galaxies Survive?," *Astrophys. J.* **186** (1973) 467–480.

[85] M. Kuhlen, M. Vogelsberger, and R. Angulo, "Numerical Simulations of the Dark Universe: State of the Art and the Next Decade," *Phys. Dark Univ.* **1** (2012) 50–93, `arXiv:1209.5745 [astro-ph.CO]`.

[86] J. F. Navarro, C. S. Frenk, and S. D. M. White, "The Structure of cold dark matter halos," *Astrophys. J.* **462** (1996) 563–575, `arXiv:astro-ph/9508025`.

[87] M. Markevitch, A. H. Gonzalez, D. Clowe, A. Vikhlinin, L. David, W. Forman, C. Jones, S. Murray, and W. Tucker, "Direct constraints on the dark matter self-interaction cross-section from the merging galaxy cluster 1E0657-56," *Astrophys. J.* **606** (2004) 819–824, `arXiv:astro-ph/0309303`.

[88] G. Bertone and D. Hooper, "History of dark matter," *Rev. Mod. Phys.* **90** (2018) no. 4, 045002, `arXiv:1605.04909 [astro-ph.CO]`.

[89] B. R. Safdi, "TASI Lectures on the Particle Physics and Astrophysics of Dark Matter," `arXiv:2303.02169 [hep-ph]`.

[90] T. Lin, "Dark matter models and direct detection," *PoS* **333** (2019) 009, `arXiv:1904.07915 [hep-ph]`.

[91] B. Carr, F. Kuhnel, and M. Sandstad, "Primordial Black Holes as Dark Matter," *Phys. Rev. D* **94** (2016) no. 8, 083504, `arXiv:1607.06077 [astro-ph.CO]`.

[92] J. Preskill, M. B. Wise, and F. Wilczek, "Cosmology of the Invisible Axion," *Phys. Lett. B* **120** (1983) 127–132.

[93] W. Hu, R. Barkana, and A. Gruzinov, "Cold and fuzzy dark matter," *Phys. Rev. Lett.* **85** (2000) 1158–1161, `arXiv:astro-ph/0003365`.

[94] A. Arvanitaki, S. Dimopoulos, M. Galanis, L. Lehner, J. O. Thompson, and K. Van Tilburg, "Large-misalignment mechanism for the formation of compact axion structures: Signatures from the QCD axion to fuzzy dark matter," *Phys. Rev. D* **101** (2020) no. 8, 083014, `arXiv:1909.11665 [astro-ph.CO]`.

[95] G. Gelmini and P. Gondolo, *DM production mechanisms*, p. 121–141. Cambridge University Press, 2010.

[96] V. Iršič *et al.*, "New Constraints on the free-streaming of warm dark matter from intermediate and small scale Lyman-α forest data," *Phys. Rev. D* **96** (2017) no. 2, 023522, `arXiv:1702.01764 [astro-ph.CO]`.

[97] K. Griest and M. Kamionkowski, "Unitarity Limits on the Mass and Radius of Dark Matter Particles," *Phys. Rev. Lett.* **64** (1990) 615.

[98] P. Gondolo and G. Gelmini, "Cosmic abundances of stable particles: Improved analysis," *Nucl. Phys.* **B360** (1991) 145–179.

[99] L. J. Hall, K. Jedamzik, J. March-Russell, and S. M. West, "Freeze-In Production of FIMP Dark Matter," *JHEP* **03** (2010) 080, `arXiv:0911.1120 [hep-ph]`.

[100] N. Bernal, M. Heikinheimo, T. Tenkanen, K. Tuominen, and V. Vaskonen, "The Dawn of FIMP Dark Matter: A Review of Models and Constraints," *Int. J. Mod. Phys. A* **32** (2017) no. 27, 1730023, `arXiv:1706.07442 [hep-ph]`.

[101] D. E. Kaplan, M. A. Luty, and K. M. Zurek, "Asymmetric Dark Matter," *Phys. Rev.* **D79** (2009) 115016, `arXiv:0901.4117 [hep-ph]`.

[102] K. Griest and D. Seckel, “Three exceptions in the calculation of relic abundances,” *Phys. Rev. D* **43** (1991) 3191–3203.

[103] R. T. D’Agnolo, D. Pappadopulo, and J. T. Ruderman, “Fourth Exception in the Calculation of Relic Abundances,” *Phys. Rev. Lett.* **119** (2017) no. 6, 061102, `arXiv:1705.08450 [hep-ph]`.

[104] Y. Hochberg, E. Kuflik, T. Volansky, and J. G. Wacker, “Mechanism for Thermal Relic Dark Matter of Strongly Interacting Massive Particles,” *Phys. Rev. Lett.* **113** (2014) 171301, `arXiv:1402.5143 [hep-ph]`.

[105] D. Pappadopulo, J. T. Ruderman, and G. Trevisan, “Dark matter freeze-out in a nonrelativistic sector,” *Phys. Rev. D* **94** (2016) no. 3, 035005, `arXiv:1602.04219 [hep-ph]`.

[106] E. Kuflik, M. Perelstein, N. R.-L. Lorier, and Y.-D. Tsai, “Elastically Decoupling Dark Matter,” *Phys. Rev. Lett.* **116** (2016) no. 22, 221302, `arXiv:1512.04545 [hep-ph]`.

[107] T. Marrodán Undagoitia and L. Rauch, “Dark matter direct-detection experiments,” *J. Phys. G* **43** (2016) no. 1, 013001, `arXiv:1509.08767 [physics.ins-det]`.

[108] M. Schumann, “Direct Detection of WIMP Dark Matter: Concepts and Status,” *J. Phys. G* **46** (2019) no. 10, 103003, `arXiv:1903.03026 [astro-ph.CO]`.

[109] R. Essig, M. Fernandez-Serra, J. Mardon, A. Soto, T. Volansky, and T.-T. Yu, “Direct Detection of sub-GeV Dark Matter with Semiconductor Targets,” *JHEP* **05** (2016) 046, `arXiv:1509.01598 [hep-ph]`.

[110] R. Essig, T. Volansky, and T.-T. Yu, “New Constraints and Prospects for sub-GeV Dark Matter Scattering off Electrons in Xenon,” *Phys. Rev. D* **96** (2017) no. 4, 043017, `arXiv:1703.00910 [hep-ph]`.

[111] R. Essig *et al.*, “Snowmass2021 Cosmic Frontier: The landscape of low-threshold dark matter direct detection in the next decade,” in *Snowmass 2021*. 3, 2022. `arXiv:2203.08297 [hep-ph]`.

[112] **LZ** Collaboration, J. Aalbers *et al.*, "First Dark Matter Search Results from the LUX-ZEPLIN (LZ) Experiment," `arXiv:2207.03764 [hep-ex]`.

[113] T. R. Slatyer, "Indirect Detection of Dark Matter," in *Theoretical Advanced Study Institute in Elementary Particle Physics: Anticipating the Next Discoveries in Particle Physics*, pp. 297–353. 2018. `arXiv:1710.05137 [hep-ph]`.

[114] **Fermi-LAT** Collaboration, M. Ackermann *et al.*, "Searching for Dark Matter Annihilation from Milky Way Dwarf Spheroidal Galaxies with Six Years of Fermi Large Area Telescope Data," *Phys. Rev. Lett.* **115** (2015) no. 23, 231301, `arXiv:1503.02641 [astro-ph.HE]`.

[115] **Fermi-LAT, DES** Collaboration, A. Albert *et al.*, "Searching for Dark Matter Annihilation in Recently Discovered Milky Way Satellites with Fermi-LAT," *Astrophys. J.* **834** (2017) no. 2, 110, `arXiv:1611.03184 [astro-ph.HE]`.

[116] **Fermi-LAT** Collaboration, M. Ackermann *et al.*, "The Fermi Galactic Center GeV Excess and Implications for Dark Matter," *Astrophys. J.* **840** (2017) no. 1, 43, `arXiv:1704.03910 [astro-ph.HE]`.

[117] **H.E.S.S.** Collaboration, H. Abdallah *et al.*, "Search for dark matter annihilations towards the inner Galactic halo from 10 years of observations with H.E.S.S," *Phys. Rev. Lett.* **117** (2016) no. 11, 111301, `arXiv:1607.08142 [astro-ph.HE]`.

[118] **H.E.S.S.** Collaboration, H. Abdallah *et al.*, "Search for dark matter signals towards a selection of recently detected DES dwarf galaxy satellites of the Milky Way with H.E.S.S.," *Phys. Rev. D* **102** (2020) no. 6, 062001, `arXiv:2008.00688 [astro-ph.HE]`.

[119] **MAGIC** Collaboration, M. L. Ahnen *et al.*, "Indirect dark matter searches in the dwarf satellite galaxy Ursa Major II with the MAGIC Telescopes," *JCAP* **03** (2018) 009, `arXiv:1712.03095 [astro-ph.HE]`.

[120] **MAGIC, Fermi-LAT** Collaboration, M. L. Ahnen *et al.*, "Limits to Dark Matter Annihilation Cross-Section from a Combined Analysis of MAGIC and

Fermi-LAT Observations of Dwarf Satellite Galaxies," *JCAP* **02** (2016) 039, `arXiv:1601.06590 [astro-ph.HE]`.

[121] D. Hooper, T. Linden, and P. Mertsch, "What Does The PAMELA Antiproton Spectrum Tell Us About Dark Matter?," *JCAP* **03** (2015) 021, `arXiv:1410.1527 [astro-ph.HE]`.

[122] G. Giesen, M. Boudaud, Y. Génolini, V. Poulin, M. Cirelli, P. Salati, and P. D. Serpico, "AMS-02 antiprotons, at last! Secondary astrophysical component and immediate implications for Dark Matter," *JCAP* **09** (2015) 023, `arXiv:1504.04276 [astro-ph.HE]`.

[123] M. Kamionkowski and M. S. Turner, "A Distinctive positron feature from heavy WIMP annihilations in the galactic halo," *Phys. Rev. D* **43** (1991) 1774–1780.

[124] **PAMELA** Collaboration, O. Adriani *et al.*, "An anomalous positron abundance in cosmic rays with energies 1.5-100 GeV," *Nature* **458** (2009) 607–609, `arXiv:0810.4995 [astro-ph]`.

[125] **AMS** Collaboration, M. Aguilar *et al.*, "First Result from the Alpha Magnetic Spectrometer on the International Space Station: Precision Measurement of the Positron Fraction in Primary Cosmic Rays of 0.5–350 GeV," *Phys. Rev. Lett.* **110** (2013) 141102.

[126] **AMS** Collaboration, M. Aguilar *et al.*, "Antiproton Flux, Antiproton-to-Proton Flux Ratio, and Properties of Elementary Particle Fluxes in Primary Cosmic Rays Measured with the Alpha Magnetic Spectrometer on the International Space Station," *Phys. Rev. Lett.* **117** (2016) no. 9, 091103.

[127] **IceCube** Collaboration, M. G. Aartsen *et al.*, "Search for dark matter annihilations in the Sun with the 79-string IceCube detector," *Phys. Rev. Lett.* **110** (2013) no. 13, 131302, `arXiv:1212.4097 [astro-ph.HE]`.

[128] **ANTARES** Collaboration, S. Adrian-Martinez *et al.*, "Limits on Dark Matter Annihilation in the Sun using the ANTARES Neutrino Telescope," *Phys. Lett. B* **759** (2016) 69–74, `arXiv:1603.02228 [astro-ph.HE]`.

[129] C. A. Argüelles, A. Diaz, A. Kheirandish, A. Olivares-Del-Campo, I. Safa, and A. C. Vincent, "Dark matter annihilation to neutrinos," *Rev. Mod. Phys.* **93** (2021) no. 3, 035007, `arXiv:1912.09486 [hep-ph]`.

[130] **IceCube** Collaboration, M. G. Aartsen *et al.*, "Search for annihilating dark matter in the Sun with 3 years of IceCube data," *Eur. Phys. J. C* **77** (2017) no. 3, 146, `arXiv:1612.05949 [astro-ph.HE]`. [Erratum: Eur.Phys.J.C 79, 214 (2019)].

[131] T. R. Slatyer, N. Padmanabhan, and D. P. Finkbeiner, "CMB Constraints on WIMP Annihilation: Energy Absorption During the Recombination Epoch," *Phys. Rev. D* **80** (2009) 043526, `arXiv:0906.1197 [astro-ph.CO]`.

[132] T. R. Slatyer, "Indirect dark matter signatures in the cosmic dark ages. I. Generalizing the bound on s-wave dark matter annihilation from Planck results," *Phys. Rev.* **D93** (2016) no. 2, 023527, `arXiv:1506.03811 [hep-ph]`.

[133] S. Galli, F. Iocco, G. Bertone, and A. Melchiorri, "CMB constraints on Dark Matter models with large annihilation cross-section," *Phys. Rev. D* **80** (2009) 023505, `arXiv:0905.0003 [astro-ph.CO]`.

[134] L. Bergstrom, T. Bringmann, I. Cholis, D. Hooper, and C. Weniger, "New Limits on Dark Matter Annihilation from AMS Cosmic Ray Positron Data," *Phys. Rev. Lett.* **111** (2013) 171101, `arXiv:1306.3983 [astro-ph.HE]`.

[135] F. Kahlhoefer, "Review of LHC Dark Matter Searches," *Int. J. Mod. Phys. A* **32** (2017) no. 13, 1730006, `arXiv:1702.02430 [hep-ph]`.

[136] **CMS** Collaboration, A. M. Sirunyan *et al.*, "Search for new physics in events with a leptonically decaying Z boson and a large transverse momentum imbalance in proton–proton collisions at $\sqrt{s} = 13$ TeV," *Eur. Phys. J. C* **78** (2018) no. 4, 291, `arXiv:1711.00431 [hep-ex]`.

[137] **CMS** Collaboration, A. M. Sirunyan *et al.*, "Search for new physics in the monophoton final state in proton-proton collisions at $\sqrt{s} = 13$ TeV," *JHEP* **10** (2017) 073, `arXiv:1706.03794 [hep-ex]`.

[138] **CMS** Collaboration, A. M. Sirunyan *et al.*, "Search for new physics in final states with an energetic jet or a hadronically decaying W or Z boson and

transverse momentum imbalance at $\sqrt{s} = 13$ TeV," *Phys. Rev. D* **97** (2018) no. 9, 092005, `arXiv:1712.02345 [hep-ex]`.

[139] **ATLAS** Collaboration, M. Aaboud *et al.*, "Search for dark matter and other new phenomena in events with an energetic jet and large missing transverse momentum using the ATLAS detector," *JHEP* **01** (2018) 126, `arXiv:1711.03301 [hep-ex]`.

[140] **ATLAS** Collaboration, M. Aaboud *et al.*, "Search for dark matter at $\sqrt{s} = 13$ TeV in final states containing an energetic photon and large missing transverse momentum with the ATLAS detector," *Eur. Phys. J. C* **77** (2017) no. 6, 393, `arXiv:1704.03848 [hep-ex]`.

[141] **ATLAS** Collaboration, M. Aaboud *et al.*, "Search for an invisibly decaying Higgs boson or dark matter candidates produced in association with a Z boson in pp collisions at $\sqrt{s} = 13$ TeV with the ATLAS detector," *Phys. Lett. B* **776** (2018) 318–337, `arXiv:1708.09624 [hep-ex]`.

[142] P. J. Fox, R. Harnik, R. Primulando, and C.-T. Yu, "Taking a Razor to Dark Matter Parameter Space at the LHC," *Phys. Rev. D* **86** (2012) 015010, `arXiv:1203.1662 [hep-ph]`.

[143] A. Rajaraman, W. Shepherd, T. M. P. Tait, and A. M. Wijangco, "LHC Bounds on Interactions of Dark Matter," *Phys. Rev. D* **84** (2011) 095013, `arXiv:1108.1196 [hep-ph]`.

[144] P. J. Fox, R. Harnik, J. Kopp, and Y. Tsai, "Missing Energy Signatures of Dark Matter at the LHC," *Phys. Rev. D* **85** (2012) 056011, `arXiv:1109.4398 [hep-ph]`.

[145] P. J. Fox, R. Harnik, J. Kopp, and Y. Tsai, "LEP Shines Light on Dark Matter," *Phys. Rev.* **D84** (2011) 014028, `arXiv:1103.0240 [hep-ph]`.

[146] Y. Bai, P. J. Fox, and R. Harnik, "The Tevatron at the Frontier of Dark Matter Direct Detection," *JHEP* **12** (2010) 048, `arXiv:1005.3797 [hep-ph]`.

[147] M. Beltran, D. Hooper, E. W. Kolb, Z. A. C. Krusberg, and T. M. P. Tait, "Maverick dark matter at colliders," *JHEP* **09** (2010) 037, `arXiv:1002.4137 [hep-ph]`.

[148] J. Abdallah *et al.*, "Simplified Models for Dark Matter Searches at the LHC," *Phys. Dark Univ.* **9-10** (2015) 8–23, `arXiv:1506.03116 [hep-ph]`.

[149] B. Batell *et al.*, "Dark Sector Studies with Neutrino Beams," in *Snowmass 2021*. 7, 2022. `arXiv:2207.06898 [hep-ph]`.

[150] J. L. Feng and J. Kumar, "The WIMPless Miracle: Dark-Matter Particles without Weak-Scale Masses or Weak Interactions," *Phys. Rev. Lett.* **101** (2008) 231301, `arXiv:0803.4196 [hep-ph]`.

[151] J. L. Feng, H. Tu, and H.-B. Yu, "Thermal Relics in Hidden Sectors," *JCAP* **10** (2008) 043, `arXiv:0808.2318 [hep-ph]`.

[152] G. Krnjaic and S. D. McDermott, "Implications of BBN Bounds for Cosmic Ray Upscattered Dark Matter," *Phys. Rev. D* **101** (2020) no. 12, 123022, `arXiv:1908.00007 [hep-ph]`.

[153] C. Boehm, M. J. Dolan, and C. McCabe, "A Lower Bound on the Mass of Cold Thermal Dark Matter from Planck," *JCAP* **1308** (2013) 041, `arXiv:1303.6270 [hep-ph]`.

[154] K. M. Nollett and G. Steigman, "BBN And The CMB Constrain Neutrino Coupled Light WIMPs," *Phys. Rev. D* **91** (2015) no. 8, 083505, `arXiv:1411.6005 [astro-ph.CO]`.

[155] D. Green and S. Rajendran, "The Cosmology of Sub-MeV Dark Matter," *JHEP* **10** (2017) 013, `arXiv:1701.08750 [hep-ph]`.

[156] C. M. Ho and R. J. Scherrer, "Limits on MeV Dark Matter from the Effective Number of Neutrinos," *Phys. Rev. D* **87** (2013) no. 2, 023505, `arXiv:1208.4347 [astro-ph.CO]`.

[157] R. H. Cyburt, B. D. Fields, K. A. Olive, and T.-H. Yeh, "Big Bang Nucleosynthesis: 2015," *Rev. Mod. Phys.* **88** (2016) 015004, `arXiv:1505.01076 [astro-ph.CO]`.

[158] **Muon g-2** Collaboration, B. Abi *et al.*, "Measurement of the Positive Muon Anomalous Magnetic Moment to 0.46 ppm," *Phys. Rev. Lett.* **126** (2021) no. 14, 141801, `arXiv:2104.03281 [hep-ex]`.

[159] B. Batell, N. Lange, D. McKeen, M. Pospelov, and A. Ritz, "Muon anomalous magnetic moment through the leptonic Higgs portal," *Phys. Rev. D* **95** (2017) no. 7, 075003, `arXiv:1606.04943 [hep-ph]`.

[160] D. E. Morrissey, D. Poland, and K. M. Zurek, "Abelian Hidden Sectors at a GeV," *JHEP* **07** (2009) 050, `arXiv:0904.2567 [hep-ph]`.

[161] J. Liu, N. Weiner, and W. Xue, "Signals of a Light Dark Force in the Galactic Center," *JHEP* **08** (2015) 050, `arXiv:1412.1485 [hep-ph]`.

[162] J. D. Bowman, A. E. E. Rogers, R. A. Monsalve, T. J. Mozdzen, and N. Mahesh, "An absorption profile centred at 78 megahertz in the sky-averaged spectrum," *Nature* **555** (2018) no. 7694, 67–70, `arXiv:1810.05912 [astro-ph.CO]`.

[163] R. Barkana, "Possible interaction between baryons and dark-matter particles revealed by the first stars," *Nature* **555** (2018) no. 7694, 71–74, `arXiv:1803.06698 [astro-ph.CO]`.

[164] H. Liu, N. J. Outmezguine, D. Redigolo, and T. Volansky, "Reviving Millicharged Dark Matter for 21-cm Cosmology," *Phys. Rev.* **D100** (2019) no. 12, 123011, `arXiv:1908.06986 [hep-ph]`.

[165] M. C. Gonzalez-Garcia and Y. Nir, "Neutrino Masses and Mixing: Evidence and Implications," *Rev. Mod. Phys.* **75** (2003) 345–402, `arXiv:hep-ph/0202058 [hep-ph]`.

[166] R. N. Mohapatra *et al.*, "Theory of neutrinos: A White paper," *Rept. Prog. Phys.* **70** (2007) 1757–1867, `arXiv:hep-ph/0510213 [hep-ph]`.

[167] A. Strumia and F. Vissani, "Neutrino masses and mixings and...," `arXiv:hep-ph/0606054 [hep-ph]`.

[168] M. C. Gonzalez-Garcia and M. Maltoni, "Phenomenology with Massive Neutrinos," *Phys. Rept.* **460** (2008) 1–129, `arXiv:0704.1800 [hep-ph]`.

[169] K. N. Abazajian *et al.*, "Light Sterile Neutrinos: A White Paper," `arXiv:1204.5379 [hep-ph]`.

[170] **MiniBooNE** Collaboration, A. A. Aguilar-Arevalo *et al.*, "A Search for Electron Neutrino Appearance at the $\Delta m^2 \sim 1 eV^2$ Scale," *Phys. Rev. Lett.* **98** (2007) 231801, `arXiv:0704.1500 [hep-ex]`.

[171] **LSND** Collaboration, C. Athanassopoulos *et al.*, "Evidence for anti-muon-neutrino —> anti-electron-neutrino oscillations from the LSND experiment at LAMPF," *Phys. Rev. Lett.* **77** (1996) 3082–3085, `arXiv:nucl-ex/9605003`.

[172] B. Dasgupta and J. Kopp, "Cosmologically Safe eV-Scale Sterile Neutrinos and Improved Dark Matter Structure," *Phys. Rev. Lett.* **112** (2014) no. 3, 031803, `arXiv:1310.6337 [hep-ph]`.

[173] N. Arkani-Hamed, S. Dimopoulos, and G. R. Dvali, "The Hierarchy problem and new dimensions at a millimeter," *Phys. Lett.* **B429** (1998) 263–272, `arXiv:hep-ph/9803315 [hep-ph]`.

[174] M. D. Schwartz, *Quantum Field Theory and the Standard Model*. Cambridge University Press, 3, 2014.

[175] A. E. Nelson and J. Scholtz, "Dark Light, Dark Matter and the Misalignment Mechanism," *Phys. Rev. D* **84** (2011) 103501, `arXiv:1105.2812 [hep-ph]`.

[176] P. W. Graham, J. Mardon, and S. Rajendran, "Vector Dark Matter from Inflationary Fluctuations," *Phys. Rev. D* **93** (2016) no. 10, 103520, `arXiv:1504.02102 [hep-ph]`.

[177] H. An, M. Pospelov, J. Pradler, and A. Ritz, "Direct Detection Constraints on Dark Photon Dark Matter," *Phys. Lett. B* **747** (2015) 331–338, `arXiv:1412.8378 [hep-ph]`.

[178] H. Ruegg and M. Ruiz-Altaba, "The Stueckelberg field," *Int. J. Mod. Phys. A* **19** (2004) 3265–3348, `arXiv:hep-th/0304245`.

[179] B. Kors and P. Nath, "A Stueckelberg extension of the standard model," *Phys. Lett. B* **586** (2004) 366–372, `arXiv:hep-ph/0402047`.

[180] D. Feldman, Z. Liu, and P. Nath, "The Stueckelberg Z-prime Extension with Kinetic Mixing and Milli-Charged Dark Matter From the Hidden Sector," *Phys. Rev. D* **75** (2007) 115001, `arXiv:hep-ph/0702123`.

[181] B. Holdom, "Two $U(1)$'s and ϵ charge shifts," *Phys. Lett.* **B166** (1986) 196.

[182] P. A. M. Dirac, "Quantized Singularities in the Electromagnetic Field," *Proc. Roy. Soc. Lond.* **A133** (1931) 60–72. [,278(1931)].

[183] J. C. Pati and A. Salam, "Unified Lepton-Hadron Symmetry and a Gauge Theory of the Basic Interactions," *Phys. Rev.* **D8** (1973) 1240–1251.

[184] H. Georgi, "The State of the Art?Gauge Theories," *AIP Conf. Proc.* **23** (1975) 575–582.

[185] D. E. Brahm and L. J. Hall, "U(1)-prime DARK MATTER," *Phys. Rev.* **D41** (1990) 1067.

[186] J. L. Feng, M. Kaplinghat, H. Tu, and H.-B. Yu, "Hidden Charged Dark Matter," *JCAP* **07** (2009) 004, `arXiv:0905.3039 [hep-ph]`.

[187] J. M. Cline, Z. Liu, and W. Xue, "Millicharged Atomic Dark Matter," *Phys. Rev. D* **85** (2012) 101302(R), `arXiv:1201.4858 [hep-ph]`.

[188] T. Emken, R. Essig, C. Kouvaris, and M. Sholapurkar, "Direct Detection of Strongly Interacting Sub-GeV Dark Matter via Electron Recoils," *JCAP* **1909** (2019) no. 09, 070, `arXiv:1905.06348 [hep-ph]`.

[189] M. S. Mahdawi and G. R. Farrar, "Constraints on Dark Matter with a moderately large and velocity-dependent DM-nucleon cross-section," *JCAP* **1810** (2018) no. 10, 007, `arXiv:1804.03073 [hep-ph]`.

[190] R. Plestid, V. Takhistov, Y.-D. Tsai, T. Bringmann, A. Kusenko, and M. Pospelov, "New Constraints on Millicharged Particles from Cosmic-ray Production," `arXiv:2002.11732 [hep-ph]`.

[191] B. Patt and F. Wilczek, "Higgs-field portal into hidden sectors," `arXiv:hep-ph/0605188 [hep-ph]`.

[192] G. Krnjaic, "Probing Light Thermal Dark-Matter With a Higgs Portal Mediator," *Phys. Rev.* **D94** (2016) no. 7, 073009, `arXiv:1512.04119 [hep-ph]`.

[193] M. Bauer, M. Neubert, and A. Thamm, "Collider Probes of Axion-Like Particles," *JHEP* **12** (2017) 044, `arXiv:1708.00443 [hep-ph]`.

[194] G. Magill, R. Plestid, M. Pospelov, and Y.-D. Tsai, "Dipole Portal to Heavy Neutral Leptons," *Phys. Rev.* **D98** (2018) no. 11, 115015, `arXiv:1803.03262 [hep-ph]`.

[195] L. A. Anchordoqui *et al.*, "The Forward Physics Facility: Sites, Experiments, and Physics Potential," `arXiv:2109.10905 [hep-ph]`.

[196] **FASERcollaboration** Collaboration, "First Results from the Search for Dark Photons with the FASER Detector at the LHC," tech. rep., CERN, Geneva, 2023. `https://cds.cern.ch/record/2853210`.

[197] A. Celentano, L. Darmé, L. Marsicano, and E. Nardi, "New production channels for light dark matter in hadronic showers," *Phys. Rev. D* **102** (2020) no. 7, 075026, `arXiv:2006.09419 [hep-ph]`.

[198] I. Boiarska, K. Bondarenko, A. Boyarsky, V. Gorkavenko, M. Ovchynnikov, and A. Sokolenko, "Phenomenology of GeV-scale scalar portal," *JHEP* **11** (2019) 162, `arXiv:1904.10447 [hep-ph]`.

[199] J. Alarcon, J. Martin Camalich, and J. Oller, "The chiral representation of the πN scattering amplitude and the pion-nucleon sigma term," *Phys. Rev. D* **85** (2012) 051503, `arXiv:1110.3797 [hep-ph]`.

[200] J. Alarcon, L. Geng, J. Martin Camalich, and J. Oller, "The strangeness content of the nucleon from effective field theory and phenomenology," *Phys. Lett. B* **730** (2014) 342–346, `arXiv:1209.2870 [hep-ph]`.

[201] A. Fradette and M. Pospelov, "BBN for the LHC: constraints on lifetimes of the Higgs portal scalars," *Phys. Rev.* **D96** (2017) no. 7, 075033, `arXiv:1706.01920 [hep-ph]`.

[202] C. Patrignani et al. (Particle Data Group), "Particle Data Group," *Chin. Phys. C* **40** (2016) 100001. `http://pdg.lbl.gov`.

[203] S. Foroughi-Abari and A. Ritz, "LSND Constraints on the Higgs Portal," *Phys. Rev. D* **102** (2020) no. 3, 035015, `arXiv:2004.14515 [hep-ph]`.

[204] **CHARM** Collaboration, F. Bergsma *et al.*, "Search for Axion Like Particle Production in 400-GeV Proton - Copper Interactions," *Phys. Lett.* **157B** (1985) 458–462.

[205] J. D. Clarke, R. Foot, and R. R. Volkas, "Phenomenology of a very light scalar (100 MeV ¡ m_h ¡ 10 GeV) mixing with the SM Higgs," *JHEP* **02** (2014) 123, `arXiv:1310.8042 [hep-ph]`.

[206] M. W. Winkler, "Decay and detection of a light scalar boson mixing with the Higgs boson," *Phys. Rev.* **D99** (2019) no. 1, 015018, `arXiv:1809.01876 [hep-ph]`.

[207] **BNL-E949** Collaboration, A. V. Artamonov *et al.*, "Study of the decay $K^+ \to \pi^+ \nu \bar{\nu}$ in the momentum region $140 < P_\pi < 199$ MeV/c," *Phys. Rev.* **D79** (2009) 092004, `arXiv:0903.0030 [hep-ex]`.

[208] **LHCb** Collaboration, R. Aaij *et al.*, "Search for long-lived scalar particles in $B^+ \to K^+ \chi(\mu^+\mu^-)$ decays," *Phys. Rev.* **D95** (2017) no. 7, 071101, `arXiv:1612.07818 [hep-ex]`.

[209] M. Pospelov and Y.-D. Tsai, "Light scalars and dark photons in Borexino and LSND experiments," *Phys. Lett.* **B785** (2018) 288–295, `arXiv:1706.00424 [hep-ph]`.

[210] K. Bondarenko, A. Boyarsky, M. Ovchynnikov, and O. Ruchayskiy, "Sensitivity of the intensity frontier experiments for neutrino and scalar portals: analytic estimates," *JHEP* **08** (2019) 061, `arXiv:1902.06240 [hep-ph]`.

[211] K. Bondarenko, A. Boyarsky, T. Bringmann, M. Hufnagel, K. Schmidt-Hoberg, and A. Sokolenko, "Direct detection and complementary constraints for sub-GeV dark matter," *JHEP* **03** (2020) 118, `arXiv:1909.08632 [hep-ph]`.

[212] P. B. Dev, R. N. Mohapatra, and Y. Zhang, "Revisiting supernova constraints on a light CP-even scalar," `arXiv:2005.00490 [hep-ph]`.

[213] B. Batell, J. Berger, and A. Ismail, "Probing the Higgs Portal at the Fermilab Short-Baseline Neutrino Experiments," *Phys. Rev. D* **100** (2019) no. 11, 115039, `arXiv:1909.11670 [hep-ph]`.

[214] **KOTO** Collaboration, J. Ahn *et al.*, "Search for the $K_L \to \pi^0 \nu \bar{\nu}$ and $K_L \to \pi^0 X^0$ decays at the J-PARC KOTO experiment," *Phys. Rev. Lett.* **122** (2019) no. 2, 021802, `arXiv:1810.09655 [hep-ex]`.

[215] **KOTO** Collaboration, S. Shinohara, “Search for the rare decay $K_L \to \pi^0 \nu \bar{\nu}$ at J-PARC KOTO experiment,” *J. Phys. Conf. Ser.* **1526** (2020) no. 1, 012002.

[216] D. Egana-Ugrinovic, S. Homiller, and P. Meade, “Light Scalars and the KOTO Anomaly,” *Phys. Rev. Lett.* **124** (2020) no. 19, 191801, `arXiv:1911.10203 [hep-ph]`.

[217] P. B. Dev, R. N. Mohapatra, and Y. Zhang, “Constraints on long-lived light scalars with flavor-changing couplings and the KOTO anomaly,” *Phys. Rev. D* **101** (2020) no. 7, 075014, `arXiv:1911.12334 [hep-ph]`.

[218] J. Liu, N. McGinnis, C. E. Wagner, and X.-P. Wang, “A light scalar explanation of $(g-2)_\mu$ and the KOTO anomaly,” *JHEP* **04** (2020) 197, `arXiv:2001.06522 [hep-ph]`.

[219] A. Djouadi, “The Anatomy of electro-weak symmetry breaking. I: The Higgs boson in the standard model,” *Phys. Rept.* **457** (2008) 1–216, `arXiv:hep-ph/0503172 [hep-ph]`.

[220] A. Fradette, M. Pospelov, J. Pradler, and A. Ritz, “Cosmological beam dump: constraints on dark scalars mixed with the Higgs boson,” *Phys. Rev.* **D99** (2019) no. 7, 075004, `arXiv:1812.07585 [hep-ph]`.

[221] M. Hoferichter, P. Klos, J. Menéndez, and A. Schwenk, “Improved limits for Higgs-portal dark matter from LHC searches,” *Phys. Rev. Lett.* **119** (2017) no. 18, 181803, `arXiv:1708.02245 [hep-ph]`.

[222] **LSND** Collaboration, C. Athanassopoulos *et al.*, “Evidence for $\nu_\mu \to \nu_e$ oscillations from pion decay in flight neutrinos,” *Phys. Rev.* **C58** (1998) 2489–2511, `arXiv:nucl-ex/9706006 [nucl-ex]`.

[223] **LSND** Collaboration, A. Aguilar-Arevalo *et al.*, “Evidence for neutrino oscillations from the observation of anti-neutrino(electron) appearance in a anti-neutrino(muon) beam,” *Phys. Rev.* **D64** (2001) 112007, `arXiv:hep-ex/0104049 [hep-ex]`.

[224] M.-S. Chen and P. M. Zerwas, “Equivalent-Particle Approximations in electron and Photon Processes of Higher Order QED,” *Phys. Rev. D* **12** (1975) 187.

[225] G. Altarelli and G. Parisi, "Asymptotic Freedom in Parton Language," *Nucl. Phys.* **B126** (1977) 298–318.

[226] Y.-S. Liu, D. McKeen, and G. A. Miller, "Validity of the Weizsacker-Williams approximation and the analysis of beam dump experiments: Production of a new scalar boson," *Phys. Rev. D* **95** (2017) no. 3, 036010, `arXiv:1609.06781 [hep-ph]`.

[227] R. Burman and E. Smith, "PARAMETRIZATION OF PION PRODUCTION AND REACTION CROSS-SECTIONS AT LAMPF ENERGIES," *LA-11502-MS, DE-98-011120, UC-414, Los Alamos* (1989) .

[228] B. Döbrich, J. Jaeckel, and T. Spadaro, "Light in the beam dump. Axion-Like Particle production from decay photons in proton beam-dumps," *JHEP* **05** (2019) 213, `arXiv:1904.02091 [hep-ph]`.

[229] D. Aloni, C. Fanelli, Y. Soreq, and M. Williams, "Photoproduction of Axionlike Particles," *Phys. Rev. Lett.* **123** (2019) no. 7, 071801, `arXiv:1903.03586 [hep-ph]`.

[230] R. D. Woods and D. S. Saxon, "Diffuse Surface Optical Model for Nucleon-Nuclei Scattering," *Phys. Rev.* **95** (1954) 577–578.

[231] B. Dobrich, J. Jaeckel, F. Kahlhoefer, A. Ringwald, and K. Schmidt-Hoberg, "ALPtraum: ALP production in proton beam dump experiments," *JHEP* **02** (2016) 018, `arXiv:1512.03069 [hep-ph]`. [JHEP02,018(2016)].

[232] E. Izaguirre, Y. Kahn, G. Krnjaic, and M. Moschella, "Testing Light Dark Matter Coannihilation With Fixed-Target Experiments," *Phys. Rev.* **D96** (2017) no. 5, 055007, `arXiv:1703.06881 [hep-ph]`.

[233] **LSND** Collaboration, L. B. Auerbach *et al.*, "Search for pi0 —¿ nu(mu) anti-nu(mu) decay in LSND," *Phys. Rev. Lett.* **92** (2004) 091801, `arXiv:hep-ex/0310060 [hep-ex]`.

[234] A. Filimonova, R. Schäfer, and S. Westhoff, "Probing dark sectors with long-lived particles at BELLE II," *Phys. Rev. D* **101** (2020) no. 9, 095006, `arXiv:1911.03490 [hep-ph]`.

[235] S. Foroughi-Abari and A. Ritz, "Dark sector production via proton bremsstrahlung," *Phys. Rev. D* **105** (2022) no. 9, 095045, `arXiv:2108.05900 [hep-ph]`.

[236] J. Blümlein and J. Brunner, "New Exclusion Limits on Dark Gauge Forces from Proton Bremsstrahlung in Beam-Dump Data," *Phys. Lett. B* **731** (2014) 320–326, `arXiv:1311.3870 [hep-ph]`.

[237] F. Kling and S. Trojanowski, "Forward experiment sensitivity estimator for the LHC and future hadron colliders," *Phys. Rev. D* **104** (2021) no. 3, 035012, `arXiv:2105.07077 [hep-ph]`.

[238] V. BERESTETSKII, E. LIFSHITZ, and L. PITAEVSKII, "Chapter x - interaction of electrons with photons," in *Quantum Electrodynamics (Second Edition)*, V. BERESTETSKII, E. LIFSHITZ, and L. PITAEVSKII, eds., pp. 354–455. Butterworth-Heinemann, Oxford, second edition ed., 1982. `https://www.sciencedirect.com/science/article/pii/B9780080503462500167`.

[239] A. Donnachie and P. V. Landshoff, "Multi - Gluon Exchange in pp Elastic Scattering," *Phys. Lett. B* **123** (1983) 345–348.

[240] A. Donnachie and P. V. Landshoff, "Elastic Scattering and Diffraction Dissociation," *Nucl. Phys. B* **244** (1984) 322.

[241] A. Donnachie and P. V. Landshoff, "Elastic Scattering at the LHC," `arXiv:1112.2485 [hep-ph]`.

[242] A. Donnachie and P. V. Landshoff, "pp and $\bar{p}p$ total cross sections and elastic scattering," *Phys. Lett. B* **727** (2013) 500–505, `arXiv:1309.1292 [hep-ph]`. [Erratum: Phys.Lett.B 750, 669–669 (2015)].

[243] V. A. Khoze, A. D. Martin, and M. G. Ryskin, "Soft diffraction and the elastic slope at Tevatron and LHC energies: A MultiPomeron approach," *Eur. Phys. J. C* **18** (2000) 167–179, `arXiv:hep-ph/0007359`.

[244] V. S. Fadin, E. A. Kuraev, and L. N. Lipatov, "On the Pomeranchuk Singularity in Asymptotically Free Theories," *Phys. Lett. B* **60** (1975) 50–52.

[245] V. S. Fadin and L. N. Lipatov, "BFKL pomeron in the next-to-leading approximation," *Phys. Lett. B* **429** (1998) 127–134, `arXiv:hep-ph/9802290`.

[246] A. Donnachie and P. V. Landshoff, "Total cross-sections," *Phys. Lett. B* **296** (1992) 227–232, `arXiv:hep-ph/9209205`.

[247] G. Pancheri and Y. N. Srivastava, "Introduction to the physics of the total cross-section at LHC: A Review of Data and Models," *Eur. Phys. J. C* **77** (2017) no. 3, 150, `arXiv:1610.10038 [hep-ph]`.

[248] P. Lebiedowicz and A. Szczurek, "Exclusive diffractive photon bremsstrahlung at the LHC," *Phys. Rev. D* **87** (2013) no. 11, 114013, `arXiv:1302.4346 [hep-ph]`.

[249] V. A. Khoze, J. W. Lamsa, R. Orava, and M. G. Ryskin, "Forward Physics at the LHC, Detecting Elastic pp Scattering by Radiative Photons," *JINST* **6** (2011) P01005, `arXiv:1007.3721 [hep-ph]`.

[250] P. Kessler, "Sur une méthode simplifiée de calcul pour les processus relativistes en électrodynamique quantique," *Il Nuovo Cimento (1955-1965)* **17** (1960) 809–829.

[251] V. N. Baier, V. S. Fadin, and V. A. Khoze, "Quasireal electron method in high-energy quantum electrodynamics," *Nucl. Phys. B* **65** (1973) 381–396.

[252] V. N. Baier, E. A. Kuraev, V. S. Fadin, and V. A. Khoze, "Inelastic Processes in Quantum Electrodynamics at High-Energies," *Phys. Rept.* **78** (1981) 293–393.

[253] O. Nicrosini and L. Trentadue, "Structure Function Approach to the Neutrino Counting Problem," *Nucl. Phys. B* **318** (1989) 1–21.

[254] A. Denig and G. Salme, "Nucleon Electromagnetic Form Factors in the Timelike Region," *Prog. Part. Nucl. Phys.* **68** (2013) 113–157, `arXiv:1210.4689 [hep-ex]`.

[255] C. Adamuscin, E. A. Kuraev, E. Tomasi-Gustafsson, and F. E. Maas, "Testing axial and electromagnetic nucleon form factors in time-like regions in the processes anti-p + n —> pi- + l- + l+ and anti-p + p —> pi0 + l- + l+, l=e, mu," *Phys. Rev. C* **75** (2007) 045205, `arXiv:hep-ph/0610429`.

[256] H. Fonvieille and V. A. Karmanov, "Antiproton-nucleus electromagnetic annihilation as a way to access the proton timelike form factors," *Eur. Phys. J. A* **42** (2009) 287–298, `arXiv:0909.0186 [nucl-th]`.

[257] C. Adamuscin, E. Bartos, S. Dubnicka, and A. Z. Dubnickova, "Numerical values of f^F, f^D, f^S coupling constants in $SU(3)$ invariant interaction Lagrangian of vector-meson nonet with $1/2^+$ octet baryons," *Phys. Rev. C* **93** (2016) no. 5, 055208, `arXiv:1601.06190 [hep-ph]`.

[258] A. Faessler, M. I. Krivoruchenko, and B. V. Martemyanov, "Once more on electromagnetic form factors of nucleons in extended vector meson dominance model," *Phys. Rev. C* **82** (2010) 038201, `arXiv:0910.5589 [hep-ph]`.

[259] E. Tomasi-Gustafsson, F. Lacroix, C. Duterte, and G. I. Gakh, "Nucleon electromagnetic form-factors and polarization observables in space-like and time-like regions," *Eur. Phys. J. A* **24** (2005) 419–430, `arXiv:nucl-th/0503001`.

[260] B. Batell, J. A. Evans, S. Gori, and M. Rai, "Dark Scalars and Heavy Neutral Leptons at DarkQuest," *JHEP* **05** (2021) 049, `arXiv:2008.08108 [hep-ph]`.

[261] T. Feuster and U. Mosel, "Photon and meson induced reactions on the nucleon," *Phys. Rev. C* **59** (1999) 460–491, `arXiv:nucl-th/9803057`.

[262] D. Ronchen, M. Doring, F. Huang, H. Haberzettl, J. Haidenbauer, C. Hanhart, S. Krewald, U. G. Meissner, and K. Nakayama, "Coupled-channel dynamics in the reactions piN –> piN, etaN, KLambda, KSigma," *Eur. Phys. J. A* **49** (2013) 44, `arXiv:1211.6998 [nucl-th]`.

[263] H. Kamano, S. X. Nakamura, T. S. H. Lee, and T. Sato, "Nucleon resonances within a dynamical coupled-channels model of πN and γN reactions," *Phys. Rev. C* **88** (2013) no. 3, 035209, `arXiv:1305.4351 [nucl-th]`.

[264] S. Janssen, J. Ryckebusch, D. Debruyne, and T. Van Cauteren, "Kaon photoproduction: Background contributions, form-factors and missing resonances," *Phys. Rev. C* **65** (2002) 015201, `arXiv:nucl-th/0107028`.

[265] Y.-s. Oh, A. I. Titov, and T. S. H. Lee, "Nucleon resonances in omega photoproduction," *Phys. Rev. C* **63** (2001) 025201, `arXiv:nucl-th/0006057`.

[266] G. Penner and U. Mosel, "Vector meson production and nucleon resonance analysis in a coupled channel approach for energies m(N) less than s**(1/2) less than 2-GeV. 1. Pion induced results and hadronic parameters," *Phys. Rev. C* **66** (2002) 055211, `arXiv:nucl-th/0207066`.

[267] G. Penner and U. Mosel, "Vector meson production and nucleon resonance analysis in a coupled channel approach for energies m(N) less than S**(1/2) less than 2-GeV. 2. Photon induced results," *Phys. Rev. C* **66** (2002) 055212, `arXiv:nucl-th/0207069`.

[268] H. Haberzettl, C. Bennhold, T. Mart, and T. Feuster, "Gauge-invariant tree-level photoproduction amplitudes with form factors," *Phys. Rev. C* **58** (1998) no. 1, R40–R44, `arXiv:nucl-th/9804051`.

[269] K. J. Kim and Y.-S. Tsai, "IMPROVED WEIZSACKER-WILLIAMS METHOD AND ITS APPLICATION TO LEPTON AND W BOSON PAIR PRODUCTION," *Phys. Rev. D* **8** (1973) 3109.

[270] A. Berlin and F. Kling, "Inelastic Dark Matter at the LHC Lifetime Frontier: ATLAS, CMS, LHCb, CODEX-b, FASER, and MATHUSLA," *Phys. Rev. D* **99** (2019) no. 1, 015021, `arXiv:1810.01879 [hep-ph]`.

[271] A. Berlin, S. Gori, P. Schuster, and N. Toro, "Dark Sectors at the Fermilab SeaQuest Experiment," *Phys. Rev. D* **98** (2018) no. 3, 035011, `arXiv:1804.00661 [hep-ph]`.

[272] S. Foroughi-Abari and A. Ritz, "Benchmarking Dark Sector Production via Proton Bremsstrahlung." Work in progress, 2023.

[273] V. Del Duca, "High-energy Bremsstrahlung Theorems for Soft Photons," *Nucl. Phys. B* **345** (1990) 369–388.

[274] P. Lebiedowicz, O. Nachtmann, and A. Szczurek, "Exclusive diffractive bremsstrahlung of one and two photons at forward rapidities: possibilities for experimental studies in *pp* collisions at the LHC," `arXiv:2303.13979 [hep-ph]`.

[275] S. Foroughi-Abari, F. Kling, and Y.-D. Tsai, "Looking forward to millicharged dark sectors at the LHC," *Phys. Rev. D* **104** (2021) no. 3, 035014, `arXiv:2010.07941 [hep-ph]`.

[276] X.-G. Wen and E. Witten, "Electric and Magnetic Charges in Superstring Models," *Nucl. Phys. B* **261** (1985) 651–677.

[277] G. Shiu, P. Soler, and F. Ye, "Milli-Charged Dark Matter in Quantum Gravity and String Theory," *Phys. Rev. Lett.* **110** (2013) no. 24, 241304, `arXiv:1302.5471 [hep-th]`.

[278] M. I. Dobroliubov and A. Yu. Ignatiev, "MILLICHARGED PARTICLES," *Phys. Rev. Lett.* **65** (1990) 679–682.

[279] A. A. Prinz *et al.*, "Search for millicharged particles at SLAC," *Phys. Rev. Lett.* **81** (1998) 1175–1178, `arXiv:hep-ex/9804008 [hep-ex]`.

[280] S. Davidson, S. Hannestad, and G. Raffelt, "Updated bounds on millicharged particles," *JHEP* **05** (2000) 003, `arXiv:hep-ph/0001179 [hep-ph]`.

[281] E. Golowich and R. W. Robinett, "Limits on Millicharged Matter From Beam Dump Experiments," *Phys. Rev.* **D35** (1987) 391.

[282] K. S. Babu, T. M. Gould, and I. Z. Rothstein, "Closing the windows on MeV Tau neutrinos," *Phys. Lett.* **B321** (1994) 140–144, `arXiv:hep-ph/9310349 [hep-ph]`.

[283] S. N. Gninenko, N. V. Krasnikov, and A. Rubbia, "Search for millicharged particles in reactor neutrino experiments: A Probe of the PVLAS anomaly," *Phys. Rev.* **D75** (2007) 075014, `arXiv:hep-ph/0612203 [hep-ph]`.

[284] **CDMS** Collaboration, R. Agnese *et al.*, "First Direct Limits on Lightly Ionizing Particles with Electric Charge Less Than $e/6$," *Phys. Rev. Lett.* **114** (2015) no. 11, 111302, `arXiv:1409.3270 [hep-ex]`.

[285] A. Haas, C. S. Hill, E. Izaguirre, and I. Yavin, "Looking for milli-charged particles with a new experiment at the LHC," *Phys. Lett.* **B746** (2015) 117–120, `arXiv:1410.6816 [hep-ph]`.

[286] A. Ball *et al.*, "A Letter of Intent to Install a milli-charged Particle Detector at LHC P5," `arXiv:1607.04669 [physics.ins-det]`.

[287] **Majorana** Collaboration, S. I. Alvis *et al.*, "First Limit on the Direct Detection of Lightly Ionizing Particles for Electric Charge as Low as e/1000

with the Majorana Demonstrator," *Phys. Rev. Lett.* **120** (2018) no. 21, 211804, `arXiv:1801.10145 [hep-ex]`.

[288] G. Magill, R. Plestid, M. Pospelov, and Y.-D. Tsai, "Millicharged particles in neutrino experiments," *Phys. Rev. Lett.* **122** (2019) no. 7, 071801, `arXiv:1806.03310 [hep-ph]`.

[289] K. J. Kelly and Y.-D. Tsai, "Proton fixed-target scintillation experiment to search for millicharged dark matter," *Phys. Rev.* **D100** (2019) no. 1, 015043, `arXiv:1812.03998 [hep-ph]`.

[290] S. Choi *et al.*, "Letter of Intent: Search for sub-millicharged particles at J-PARC," `arXiv:2007.06329 [physics.ins-det]`.

[291] P. deNiverville, M. Pospelov, and A. Ritz, "Light new physics in coherent neutrino-nucleus scattering experiments," *Phys. Rev. D* **92** (2015) no. 9, 095005, `arXiv:1505.07805 [hep-ph]`.

[292] S. Gardner, R. J. Holt, and A. S. Tadepalli, "New prospects in fixed target searches for dark forces with the SeaQuest experiment at Fermilab," *Phys. Rev.* **D93** (2016) 115015, `arXiv:1509.00050 [hep-ph]`.

[293] E. Izaguirre, G. Krnjaic, and M. Pospelov, "MeV-Scale Dark Matter Deep Underground," *Phys. Rev.* **D92** (2015) no. 9, 095014, `arXiv:1507.02681 [hep-ph]`.

[294] L. Darmé, S. Rao, and L. Roszkowski, "Light dark Higgs boson in minimal sub-GeV dark matter scenarios," *JHEP* **03** (2018) 084, `arXiv:1710.08430 [hep-ph]`.

[295] J. R. Jordan, Y. Kahn, G. Krnjaic, M. Moschella, and J. Spitz, "Signatures of Pseudo-Dirac Dark Matter at High-Intensity Neutrino Experiments," *Phys. Rev. D* **98** (2018) no. 7, 075020, `arXiv:1806.05185 [hep-ph]`.

[296] P. deNiverville and C. Frugiuele, "Hunting sub-GeV dark matter with the NOνA near detector," *Phys. Rev. D* **99** (2019) no. 5, 051701(R), `arXiv:1807.06501 [hep-ph]`.

[297] E. Bertuzzo, S. Jana, P. A. N. Machado, and R. Zukanovich Funchal, "Dark Neutrino Portal to Explain MiniBooNE excess," *Phys. Rev. Lett.* **121** (2018) no. 24, 241801, `arXiv:1807.09877 [hep-ph]`.

[298] E. Bertuzzo, S. Jana, P. A. N. Machado, and R. Zukanovich Funchal, "Neutrino Masses and Mixings Dynamically Generated by a Light Dark Sector," `arXiv:1808.02500 [hep-ph]`.

[299] P. Ballett, S. Pascoli, and M. Ross-Lonergan, "U(1)' mediated decays of heavy sterile neutrinos in MiniBooNE," *Phys. Rev.* **D99** (2019) 071701(R), `arXiv:1808.02915 [hep-ph]`.

[300] C. A. Argüelles, M. Hostert, and Y.-D. Tsai, "Testing New Physics Explanations of MiniBooNE Anomaly at Neutrino Scattering Experiments," *Phys. Rev. Lett.* **123** (2019) no. 26, 261801, `arXiv:1812.08768 [hep-ph]`.

[301] B. Batell, A. Freitas, A. Ismail, and D. McKeen, "Probing Light Dark Matter with a Hadrophilic Scalar Mediator," *Phys. Rev. D* **100** (2019) no. 9, 095020, `arXiv:1812.05103 [hep-ph]`.

[302] C. A. Argüelles *et al.*, "White Paper on New Opportunities at the Next-Generation Neutrino Experiments (Part 1: BSM Neutrino Physics and Dark Matter)," `arXiv:1907.08311 [hep-ph]`.

[303] Y.-D. Tsai, P. deNiverville, and M. X. Liu, "The High-Energy Frontier of the Intensity Frontier: Closing the Dark Photon, Inelastic Dark Matter, and Muon g-2 Windows," `arXiv:1908.07525 [hep-ph]`.

[304] V. De Romeri, K. J. Kelly, and P. A. Machado, "DUNE-PRISM Sensitivity to Light Dark Matter," *Phys. Rev. D* **100** (2019) no. 9, 095010, `arXiv:1903.10505 [hep-ph]`.

[305] L. Buonocore, C. Frugiuele, and P. deNiverville, "Hunt for sub-GeV dark matter at neutrino facilities: A survey of past and present experiments," *Phys. Rev. D* **102** (2020) no. 3, 035006, `arXiv:1912.09346 [hep-ph]`.

[306] **FASER** Collaboration, A. Ariga *et al.*, "FASER's physics reach for long-lived particles," *Phys. Rev. D* **99** (2019) no. 9, 095011, `arXiv:1811.12522 [hep-ph]`.

[307] A. Ball *et al.*, "Search for millicharged particles in proton-proton collisions at $\sqrt{s} = 13$ TeV," *Phys. Rev. D* **102** (2020) no. 3, 032002, `arXiv:2005.06518 [hep-ex]`.

[308] **OPAL** Collaboration, R. Akers *et al.*, "Search for heavy charged particles and for particles with anomalous charge in e^+e^- collisions at LEP," *Z. Phys. C* **67** (1995) 203–212.

[309] **CMS** Collaboration, S. Chatrchyan *et al.*, "Search for Fractionally Charged Particles in pp Collisions at $\sqrt{s} = 7$ TeV," *Phys. Rev.* **D87** (2013) no. 9, 092008, `arXiv:1210.2311 [hep-ex]`.

[310] J. Jaeckel, M. Jankowiak, and M. Spannowsky, "LHC probes the hidden sector," *Phys. Dark Univ.* **2** (2013) 111–117, `arXiv:1212.3620 [hep-ph]`.

[311] **ArgoNeuT** Collaboration, R. Acciarri *et al.*, "Improved Limits on Millicharged Particles Using the ArgoNeuT Experiment at Fermilab," *Phys. Rev. Lett.* **124** (2020) no. 13, 131801, `arXiv:1911.07996 [hep-ex]`.

[312] **milliQan** Collaboration, A. Ball *et al.*, "Sensitivity to millicharged particles in future proton-proton collisions at the LHC," `arXiv:2104.07151 [hep-ex]`.

[313] A. L. Erickcek, P. J. Steinhardt, D. McCammon, and P. C. McGuire, "Constraints on the Interactions between Dark Matter and Baryons from the X-ray Quantum Calorimetry Experiment," *Phys. Rev.* **D76** (2007) 042007, `arXiv:0704.0794 [astro-ph]`.

[314] J. Rich, R. Rocchia, and M. Spiro, "A Search for Strongly Interacting Dark Matter," *Phys. Lett.* **B194** (1987) 173. [,221(1987)].

[315] J. L. Feng, I. Galon, F. Kling, and S. Trojanowski, "Dark Higgs bosons at the ForwArd Search ExpeRiment," *Phys. Rev.* **D97** (2018) no. 5, 055034, `arXiv:1710.09387 [hep-ph]`.

[316] F. Kling and S. Trojanowski, "Heavy Neutral Leptons at FASER," *Phys. Rev.* **D97** (2018) no. 9, 095016, `arXiv:1801.08947 [hep-ph]`.

[317] J. L. Feng, I. Galon, F. Kling, and S. Trojanowski, "Axionlike particles at FASER: The LHC as a photon beam dump," *Phys. Rev. D* **98** (2018) no. 5, 055021, `arXiv:1806.02348 [hep-ph]`.

[318] **FASER** Collaboration, A. Ariga *et al.*, "Letter of Intent for FASER: ForwArd Search ExpeRiment at the LHC," `arXiv:1811.10243 [physics.ins-det]`.

[319] F. Kling and S. Trojanowski, "Looking forward to test the KOTO anomaly with FASER," *Phys. Rev. D* **102** (2020) no. 1, 015032, `arXiv:2006.10630 [hep-ph]`.

[320] **FASER** Collaboration, H. Abreu *et al.*, "Detecting and Studying High-Energy Collider Neutrinos with FASER at the LHC," *Eur. Phys. J. C* **80** (2020) no. 1, 61, `arXiv:1908.02310 [hep-ex]`.

[321] **FASER** Collaboration, H. Abreu *et al.*, "Technical Proposal: FASERnu," `arXiv:2001.03073 [physics.ins-det]`.

[322] **FASER** Collaboration, "FASER 2: Forward Search Experiment at the HL LHC." `https://www.snowmass21.org/docs/files/summaries/EF/SNOWMASS21-EF9_EF6-NF3_NF6-RF6_RF0-CF7_CF0-AF5_AF0_FASER2-038.pdf`.

[323] **FASER** Collaboration, "FASERν 2: A Forward Neutrino Experiment at the HL LHC." `https://www.snowmass21.org/docs/files/summaries/NF/SNOWMASS21-NF10_NF6-EF6_EF9-IF0_FASERnu2-006.pdf`.

[324] CERN Sources, Targets, and Interactions Group, M. Sabate-Gilarte, F. Cerutti, and A. Tsinganis, "Characterization of the radiation field for the FASER experiment," tech. rep., CERN, 2018.

[325] L. B. Okun, "Limits of electrodynamcis: Paraphotons?," *Sov. Phys. JETP* **56** (1982) 502. [Zh. Eksp. Teor. Fiz. **83** (1982) 892].

[326] T. Pierog, I. Karpenko, J. M. Katzy, E. Yatsenko, and K. Werner, "EPOS LHC: Test of collective hadronization with data measured at the CERN Large Hadron Collider," *Phys. Rev.* **C92** (2015) no. 3, 034906, `arXiv:1306.0121 [hep-ph]`.

[327] T. Sjöstrand, S. Ask, J. R. Christiansen, R. Corke, N. Desai, P. Ilten, S. Mrenna, S. Prestel, C. O. Rasmussen, and P. Z. Skands, "An Introduction to PYTHIA 8.2," *Comput. Phys. Commun.* **191** (2015) 159–177, `arXiv:1410.3012 [hep-ph]`.

[328] **LHCb** Collaboration, R. Aaij *et al.*, "Measurement of forward J/ψ production cross-sections in pp collisions at $\sqrt{s} = 13$ TeV," *JHEP* **10** (2015) 172, `arXiv:1509.00771 [hep-ex]`. [Erratum: JHEP 05, 063 (2017)].

[329] **LHCb** Collaboration, R. Aaij *et al.*, "Measurement of Υ production in pp collisions at $\sqrt{s}$= 13 TeV," *JHEP* **07** (2018) 134, `arXiv:1804.09214 [hep-ex]`. [Erratum: JHEP 05, 076 (2019)].

[330] **LHCb** Collaboration, R. Aaij *et al.*, "Measurement of $\psi(2S)$ production cross-sections in proton-proton collisions at $\sqrt{s} = 7$ and 13 TeV," *Eur. Phys. J. C* **80** (2020) no. 3, 185, `arXiv:1908.03099 [hep-ex]`.

[331] J. Alwall, R. Frederix, S. Frixione, V. Hirschi, F. Maltoni, O. Mattelaer, H. S. Shao, T. Stelzer, P. Torrielli, and M. Zaro, "The automated computation of tree-level and next-to-leading order differential cross sections, and their matching to parton shower simulations," *JHEP* **07** (2014) 079, `arXiv:1405.0301 [hep-ph]`.

[332] J. F. Grosse-Oetringhaus and K. Reygers, "Charged-Particle Multiplicity in Proton-Proton Collisions," *J. Phys. G* **37** (2010) 083001, `arXiv:0912.0023 [hep-ex]`.

[333] **LHCf** Collaboration, O. Adriani *et al.*, "Measurement of forward photon production cross-section in proton–proton collisions at $\sqrt{s} = 13$ TeV with the LHCf detector," *Phys. Lett. B* **780** (2018) 233–239, `arXiv:1703.07678 [hep-ex]`.

[334] R. Ulrich, T. Pierog, and C. Baus, "Cosmic ray monte carlo package, crmc." `https://doi.org/10.5281/zenodo.5270381`, Aug., 2021.

[335] K. Jodlowski, F. Kling, L. Roszkowski, and S. Trojanowski, "Extending the reach of FASER, MATHUSLA, and SHiP towards smaller lifetimes using secondary particle production," *Phys. Rev. D* **101** (2020) no. 9, 095020, `arXiv:1911.11346 [hep-ph]`.

[336] Saint-Gobain, "Plastic scintillators." `https://www.crystals.saint-gobain.com/products/organic-scintillation-materials`. Accessed: 2016-02-12.

[337] **KM3NeT** Collaboration, S. Aiello *et al.*, "Characterisation of the Hamamatsu photomultipliers for the KM3NeT Neutrino Telescope," *JINST* **13** (2018) no. 05, P05035.

[338] **DEAP** Collaboration, P.-A. Amaudruz *et al.*, "In-situ characterization of the Hamamatsu R5912-HQE photomultiplier tubes used in the DEAP-3600 experiment," *Nucl. Instrum. Meth. A* **922** (2019) 373–384, `arXiv:1705.10183 [physics.ins-det]`.

[339] J. Bovy and S. Tremaine, "On the local dark matter density," *Astrophys. J.* **756** (2012) 89, `arXiv:1205.4033 [astro-ph.GA]`.

[340] G. D. Starkman, A. Gould, R. Esmailzadeh, and S. Dimopoulos, "Opening the Window on Strongly Interacting Dark Matter," *Phys. Rev.* **D41** (1990) 3594.

[341] P.-K. Hu, A. Kusenko, and V. Takhistov, "Dark Cosmic Rays," *Phys. Lett.* **B768** (2017) 18–22, `arXiv:1611.04599 [hep-ph]`.

[342] D. Dunsky, L. J. Hall, and K. Harigaya, "CHAMP Cosmic Rays," *JCAP* **1907** (2019) no. 07, 015, `arXiv:1812.11116 [astro-ph.HE]`.

[343] J.-T. Li and T. Lin, "Dynamics of millicharged dark matter in supernova remnants," `arXiv:2002.04625 [astro-ph.CO]`.

[344] L. Chuzhoy and E. W. Kolb, "Reopening the window on charged dark matter," *JCAP* **0907** (2009) 014, `arXiv:0809.0436 [astro-ph]`.

[345] S. L. Dubovsky, D. S. Gorbunov, and G. I. Rubtsov, "Narrowing the window for millicharged particles by CMB anisotropy," *JETP Lett.* **79** (2004) 1–5, `arXiv:hep-ph/0311189 [hep-ph]`. [Pisma Zh. Eksp. Teor. Fiz.79,3(2004)].

[346] A. D. Dolgov, S. L. Dubovsky, G. I. Rubtsov, and I. I. Tkachev, "Constraints on millicharged particles from Planck data," *Phys. Rev.* **D88** (2013) no. 11, 117701, `arXiv:1310.2376 [hep-ph]`.

[347] E. D. Kovetz, V. Poulin, V. Gluscevic, K. K. Boddy, R. Barkana, and M. Kamionkowski, "Tighter limits on dark matter explanations of the anomalous EDGES 21 cm signal," *Phys. Rev.* **D98** (2018) no. 10, 103529, `arXiv:1807.11482 [astro-ph.CO]`.

[348] A. Berlin, D. Hooper, G. Krnjaic, and S. D. McDermott, "Severely Constraining Dark Matter Interpretations of the 21-cm Anomaly," `arXiv:1803.02804 [hep-ph]`.

[349] M. Sher and J. Stevens, "Detecting a heavy neutrino electric dipole moment at the LHC," *Phys. Lett.* **B777** (2018) 246–249, `arXiv:1710.06894 [hep-ph]`.

[350] X. Chu, J. Pradler, and L. Semmelrock, "Light dark states with electromagnetic form factors," *Phys. Rev. D* **99** (2019) no. 1, 015040, `arXiv:1811.04095 [hep-ph]`.

[351] M. Frank, M. de Montigny, P.-P. A. Ouimet, J. Pinfold, A. Shaa, and M. Staelens, "Searching for Heavy Neutrinos with the MoEDAL-MAPP Detector at the LHC," *Phys. Lett. B* **802** (2020) 135204, `arXiv:1909.05216 [hep-ph]`.

[352] X. Chu, J.-L. Kuo, and J. Pradler, "Dark sector-photon interactions in proton-beam experiments," *Phys. Rev. D* **101** (2020) no. 7, 075035, `arXiv:2001.06042 [hep-ph]`.

[353] W. Bai, M. Diwan, M. V. Garzelli, Y. S. Jeong, and M. H. Reno, "Far-forward neutrinos at the Large Hadron Collider," *JHEP* **06** (2020) 032, `arXiv:2002.03012 [hep-ph]`.

[354] R. Mammen Abraham, S. Foroughi-Abari, F. Kling, and Y.-D. Tsai, "Neutrino Electromagnetic Properties and the Weak Mixing Angle at the LHC Forward Physics Facility," `arXiv:2301.10254 [hep-ph]`.

[355] R. E. Shrock, "Electromagnetic properties and decays of dirac and majorana neutrinos in a general class of gauge theories," *Nuclear Physics B* **206** (1982) no. 3, 359 – 379. `http://www.sciencedirect.com/science/article/pii/0550321382902735`.

[356] J.-M. Frère, J. Heeck, and S. Mollet, "Triangle Inequalities for Majorana-Neutrino Magnetic Moments," *Phys. Rev. D* **92** (2015) no. 5, 053002, `arXiv:1506.02964 [hep-ph]`.

[357] **XENON** Collaboration, E. Aprile *et al.*, "Excess electronic recoil events in XENON1T," *Phys. Rev. D* **102** (2020) no. 7, 072004, `arXiv:2006.09721 [hep-ex]`.

[358] **XENON** Collaboration, E. Aprile *et al.*, “Search for New Physics in Electronic Recoil Data from XENONnT,” `arXiv:2207.11330 [hep-ex]`.

[359] D. Croon, S. D. McDermott, and J. Sakstein, “Missing in axion: Where are XENON1T’s big black holes?,” *Phys. Dark Univ.* **32** (2021) 100801, `arXiv:2007.00650 [hep-ph]`.

[360] J. Sakstein, D. Croon, S. D. McDermott, M. C. Straight, and E. J. Baxter, “Beyond the Standard Model Explanations of GW190521,” *Phys. Rev. Lett.* **125** (2020) no. 26, 261105, `arXiv:2009.01213 [gr-qc]`.

[361] M. B. Voloshin, “On Compatibility of Small Mass with Large Magnetic Moment of Neutrino,” *Sov. J. Nucl. Phys.* **48** (1988) 512.

[362] R. Barbieri and R. N. Mohapatra, “A Neutrino With a Large Magnetic Moment and a Naturally Small Mass,” *Phys. Lett. B* **218** (1989) 225–229.

[363] S. Rajpoot, “DIRAC NEUTRINO MAGNETIC MOMENTS IN THE LEFT-RIGHT SYMMETRIC MODEL,” *Phys. Lett. B* **237** (1990) 77–80.

[364] A. Aboubrahim, T. Ibrahim, A. Itani, and P. Nath, “Large Neutrino Magnetic Dipole Moments in MSSM Extensions,” *Phys. Rev. D* **89** (2014) no. 5, 055009, `arXiv:1312.2505 [hep-ph]`.

[365] M. Lindner, B. Radovčić, and J. Welter, “Revisiting Large Neutrino Magnetic Moments,” *JHEP* **07** (2017) 139, `arXiv:1706.02555 [hep-ph]`.

[366] K. S. Babu, S. Jana, and M. Lindner, “Large Neutrino Magnetic Moments in the Light of Recent Experiments,” *JHEP* **10** (2020) 040, `arXiv:2007.04291 [hep-ph]`.

[367] K. S. Babu, S. Jana, M. Lindner, and V. P. K, “Muon $g-2$ Anomaly and Neutrino Magnetic Moments,” `arXiv:2104.03291 [hep-ph]`.

[368] A. G. Beda, V. B. Brudanin, V. G. Egorov, D. V. Medvedev, V. S. Pogosov, M. V. Shirchenko, and A. S. Starostin, “The results of search for the neutrino magnetic moment in GEMMA experiment,” *Adv. High Energy Phys.* **2012** (2012) 350150.

[369] **TEXONO** Collaboration, H. T. Wong *et al.*, "A Search of Neutrino Magnetic Moments with a High-Purity Germanium Detector at the Kuo-Sheng Nuclear Power Station," *Phys. Rev. D* **75** (2007) 012001, `arXiv:hep-ex/0605006`.

[370] **LSND Collaboration** Collaboration, L. Auerbach *et al.*, "Measurement of electron - neutrino - electron elastic scattering," *Phys.Rev.* **D63** (2001) 112001, `arXiv:hep-ex/0101039 [hep-ex]`.

[371] **DONUT** Collaboration, R. Schwienhorst *et al.*, "A New upper limit for the tau - neutrino magnetic moment," *Phys. Lett. B* **513** (2001) 23–29, `arXiv:hep-ex/0102026`.

[372] R. C. Allen *et al.*, "Study of electron-neutrino electron elastic scattering at LAMPF," *Phys. Rev. D* **47** (1993) 11–28.

[373] **Borexino** Collaboration, C. Arpesella *et al.*, "Direct Measurement of the Be-7 Solar Neutrino Flux with 192 Days of Borexino Data," *Phys. Rev. Lett.* **101** (2008) 091302, `arXiv:0805.3843 [astro-ph]`.

[374] **Borexino** Collaboration, M. Agostini *et al.*, "Limiting neutrino magnetic moments with Borexino Phase-II solar neutrino data," *Phys. Rev. D* **96** (2017) no. 9, 091103, `arXiv:1707.09355 [hep-ex]`.

[375] P. Coloma, M. C. Gonzalez-Garcia, M. Maltoni, J. a. P. Pinheiro, and S. Urrea, "Constraining New Physics with Borexino Phase-II spectral data," `arXiv:2204.03011 [hep-ph]`.

[376] S. K. A., A. Majumdar, D. K. Papoulias, H. Prajapati, and R. Srivastava, "First results of LZ and XENONnT: A comparative study of neutrino properties and light mediators," `arXiv:2208.06415 [hep-ph]`.

[377] D. Aristizabal Sierra, O. G. Miranda, D. K. Papoulias, and G. S. Garcia, "Neutrino magnetic and electric dipole moments: From measurements to parameter space," *Phys. Rev. D* **105** (2022) no. 3, 035027, `arXiv:2112.12817 [hep-ph]`.

[378] I. M. Shoemaker, Y.-D. Tsai, and J. Wyenberg, "Active-to-sterile neutrino dipole portal and the XENON1T excess," *Phys. Rev. D* **104** (2021) no. 11, 115026, `arXiv:2007.05513 [hep-ph]`.

[379] A. Ismail, S. Jana, and R. M. Abraham, "Neutrino up-scattering via the dipole portal at forward LHC detectors," *Phys. Rev. D* **105** (2022) no. 5, 055008, `arXiv:2109.05032 [hep-ph]`.

[380] K. Jodłowski and S. Trojanowski, "Neutrino beam-dump experiment with FASER at the LHC," *JHEP* **05** (2021) 191, `arXiv:2011.04751 [hep-ph]`.

[381] B. Kayser, "Majorana Neutrinos and their Electromagnetic Properties," *Phys. Rev. D* **26** (1982) 1662.

[382] J. F. Nieves, "Electromagnetic Properties of Majorana Neutrinos," *Phys. Rev. D* **26** (1982) 3152.

[383] K. A. Kouzakov and A. I. Studenikin, "Electromagnetic properties of massive neutrinos in low-energy elastic neutrino-electron scattering," *Phys. Rev. D* **95** (2017) no. 5, 055013, `arXiv:1703.00401 [hep-ph]`. [Erratum: Phys.Rev.D 96, 099904 (2017)].

[384] C. Giunti, J. Gruszko, B. Jones, L. Kaufman, D. Parno, and A. Pocar, "Report of the Topical Group on Neutrino Properties for Snowmass 2021," `arXiv:2209.03340 [hep-ph]`.

[385] W. Grimus and T. Schwetz, "Elastic neutrino electron scattering of solar neutrinos and potential effects of magnetic and electric dipole moments," *Nucl. Phys. B* **587** (2000) 45–66, `arXiv:hep-ph/0006028`.

[386] J. F. Beacom and P. Vogel, "Neutrino magnetic moments, flavor mixing, and the Super-Kamiokande solar data," *Phys. Rev. Lett.* **83** (1999) 5222–5225, `arXiv:hep-ph/9907383`.

[387] C. Q. Geng and R. E. Marshak, "Uniqueness of Quark and Lepton Representations in the Standard Model From the Anomalies Viewpoint," *Phys. Rev. D* **39** (1989) 693.

[388] K. S. Babu and R. N. Mohapatra, "Quantization of Electric Charge From Anomaly Constraints and a Majorana Neutrino," *Phys. Rev. D* **41** (1990) 271.

[389] A. Das, D. Ghosh, C. Giunti, and A. Thalapillil, "Neutrino charge constraints from scattering to the weak gravity conjecture to neutron stars," *Phys. Rev. D* **102** (2020) no. 11, 115009, `arXiv:2005.12304 [hep-ph]`.

[390] K. Fujikawa and R. Shrock, “The Magnetic Moment of a Massive Neutrino and Neutrino Spin Rotation,” *Phys. Rev. Lett.* **45** (1980) 963.

[391] P. Vogel and J. Engel, “Neutrino Electromagnetic Form-Factors,” *Phys. Rev. D* **39** (1989) 3378.

[392] P. B. Pal and L. Wolfenstein, “Radiative Decays of Massive Neutrinos,” *Phys. Rev. D* **25** (1982) 766.

[393] R. N. Mohapatra, S.-P. Ng, and H.-b. Yu, “Reactor searches for neutrino magnetic moment as a probe of extra dimensions,” *Phys. Rev. D* **70** (2004) 057301, `arXiv:hep-ph/0404274`.

[394] K. S. Babu and R. N. Mohapatra, “Model for Large Transition Magnetic Moment of the ν_e,” *Phys. Rev. Lett.* **63** (1989) 228.

[395] S. M. Barr, E. M. Freire, and A. Zee, “A Mechanism for large neutrino magnetic moments,” *Phys. Rev. Lett.* **65** (1990) 2626–2629.

[396] J. Bernabeu, J. Papavassiliou, and J. Vidal, “The Neutrino charge radius is a physical observable,” *Nucl. Phys. B* **680** (2004) 450–478, `arXiv:hep-ph/0210055`.

[397] J. Bernabeu, L. G. Cabral-Rosetti, J. Papavassiliou, and J. Vidal, “On the charge radius of the neutrino,” *Phys. Rev. D* **62** (2000) 113012, `arXiv:hep-ph/0008114`.

[398] C. Ahdida *et al.*, “SND@LHC - Scattering and Neutrino Detector at the LHC,” tech. rep., CERN, Geneva, Jan, 2021. `https://cds.cern.ch/record/2750060`.

[399] **SHiP** Collaboration, C. Ahdida *et al.*, “SND@LHC,” `arXiv:2002.08722 [physics.ins-det]`.

[400] **DONuT** Collaboration, K. Kodama *et al.*, “Final tau-neutrino results from the DONuT experiment,” *Phys. Rev. D* **78** (2008) 052002, `arXiv:0711.0728 [hep-ex]`.

[401] **OPERA** Collaboration, N. Agafonova *et al.*, “Final Results of the OPERA Experiment on ν_τ Appearance in the CNGS Neutrino Beam,” *Phys. Rev. Lett.*

120 (2018) no. 21, 211801, arXiv:1804.04912 [hep-ex]. [Erratum: Phys.Rev.Lett. 121, 139901 (2018)].

[402] J. L. Feng *et al.*, "The Forward Physics Facility at the High-Luminosity LHC," arXiv:2203.05090 [hep-ex].

[403] **LAr1-ND, ICARUS-WA104, MicroBooNE** Collaboration, M. Antonello *et al.*, "A Proposal for a Three Detector Short-Baseline Neutrino Oscillation Program in the Fermilab Booster Neutrino Beam," arXiv:1503.01520 [physics.ins-det].

[404] **DUNE** Collaboration, B. Abi *et al.*, "Deep Underground Neutrino Experiment (DUNE), Far Detector Technical Design Report, Volume II DUNE Physics," arXiv:2002.03005 [hep-ex].

[405] B. Batell, J. L. Feng, M. Fieg, A. Ismail, F. Kling, R. M. Abraham, and S. Trojanowski, "Hadrophilic dark sectors at the Forward Physics Facility," *Phys. Rev. D* **105** (2022) no. 7, 075001, arXiv:2111.10343 [hep-ph].

[406] A. Ismail, R. Mammen Abraham, and F. Kling, "Neutral current neutrino interactions at FASERν," *Phys. Rev. D* **103** (2021) no. 5, 056014, arXiv:2012.10500 [hep-ph].

[407] **FASER** Collaboration, H. Abreu *et al.*, "The FASER Detector," arXiv:2207.11427 [physics.ins-det].

[408] E.-J. Ahn, R. Engel, T. K. Gaisser, P. Lipari, and T. Stanev, "Cosmic ray interaction event generator SIBYLL 2.1," *Phys. Rev.* **D80** (2009) 094003, arXiv:0906.4113 [hep-ph].

[409] F. Riehn, R. Engel, A. Fedynitch, T. K. Gaisser, and T. Stanev, "A new version of the event generator Sibyll," *PoS* **ICRC2015** (2016) 558, arXiv:1510.00568 [hep-ph].

[410] F. Riehn, H. P. Dembinski, R. Engel, A. Fedynitch, T. K. Gaisser, and T. Stanev, "The hadronic interaction model SIBYLL 2.3c and Feynman scaling," *PoS* **ICRC2017** (2018) 301, arXiv:1709.07227 [hep-ph].

[411] F. Riehn, R. Engel, A. Fedynitch, T. K. Gaisser, and T. Stanev, "Hadronic interaction model Sibyll 2.3d and extensive air showers," *Phys. Rev. D* **102** (2020) no. 6, 063002, `arXiv:1912.03300 [hep-ph]`.

[412] F. Kling and L. J. Nevay, "Forward neutrino fluxes at the LHC," *Phys. Rev. D* **104** (2021) no. 11, 113008, `arXiv:2105.08270 [hep-ph]`.

[413] J. A. Formaggio and G. P. Zeller, "From eV to EeV: Neutrino Cross Sections Across Energy Scales," *Rev. Mod. Phys.* **84** (2012) 1307–1341, `arXiv:1305.7513 [hep-ex]`.

[414] K. S. McFarland, "Neutrino Interactions," in *61st Scottish Universities Summer School in Physics: Neutrinos in Particle Physics, Astrophysics and Cosmology (SUSSP61)*, pp. 65–90. 4, 2008. `arXiv:0804.3899 [hep-ex]`.

[415] K. Kovarik *et al.*, "nCTEQ15 - Global analysis of nuclear parton distributions with uncertainties in the CTEQ framework," *Phys. Rev. D* **93** (2016) no. 8, 085037, `arXiv:1509.00792 [hep-ph]`.

[416] A. de Gouvea and J. Jenkins, "What can we learn from neutrino electron scattering?," *Phys. Rev.* **D74** (2006) 033004, `arXiv:hep-ph/0603036 [hep-ph]`.

[417] W. Grimus and P. Stockinger, "Effects of neutrino oscillations and neutrino magnetic moments on elastic neutrino - electron scattering," *Phys. Rev. D* **57** (1998) 1762–1768, `arXiv:hep-ph/9708279`.

[418] F. Kling, J.-L. Kuo, S. Trojanowski, and Y.-D. Tsai, "FLArE up dark sectors with EM form factors at the LHC Forward Physics Facility," `arXiv:2205.09137 [hep-ph]`.

[419] V. Mathur, I. M. Shoemaker, and Z. Tabrizi, "Using DUNE to Shed Light on the Electromagnetic Properties of Neutrinos," `arXiv:2111.14884 [hep-ph]`.

[420] **Particle Data Group** Collaboration, R. L. Workman and Others, "Review of Particle Physics," *PTEP* **2022** (2022) 083C01.

[421] M. Cadeddu, F. Dordei, C. Giunti, Y. F. Li, E. Picciau, and Y. Y. Zhang, "Physics results from the first COHERENT observation of coherent elastic

neutrino-nucleus scattering in argon and their combination with cesium-iodide data," *Phys. Rev. D* **102** (2020) no. 1, 015030, `arXiv:2005.01645 [hep-ph]`.

[422] J. Bernstein and T. D. Lee, "Electromagnetic Form-factor of the Neutrinos," *Phys. Rev. Lett.* **11** (1963) 512–516.

[423] A. Grau and J. A. Grifols, "Neutrino Charge Radius and Substructure," *Phys. Lett. B* **166** (1986) 233–237.

[424] Y. S. Jeong, W. Bai, M. Diwan, M. V. Garzelli, F. K. Kumar, and M. H. Reno, "Neutrinos from charm: forward production at the LHC and in the atmosphere," *PoS* **ICRC2021** (2021) 1218, `arXiv:2107.01178 [hep-ph]`.

[425] R. Maciula and A. Szczurek, "Far-forward production of charm mesons and neutrinos at Forward Physics Facilities at the LHC and the intrinsic charm in the proton," `arXiv:2210.08890 [hep-ph]`.

[426] A. N. Khan, "New limits on neutrino electromagnetic interactions and light new physics with XENONnT," `arXiv:2208.02144 [hep-ph]`.

[427] M. Atzori Corona, M. Cadeddu, N. Cargioli, F. Dordei, C. Giunti, Y. F. Li, C. A. Ternes, and Y. Y. Zhang, "Impact of the Dresden-II and COHERENT neutrino scattering data on neutrino electromagnetic properties and electroweak physics," *JHEP* **09** (2022) 164, `arXiv:2205.09484 [hep-ph]`.

[428] **CONUS** Collaboration, H. Bonet *et al.*, "First upper limits on neutrino electromagnetic properties from the CONUS experiment," *Eur. Phys. J. C* **82** (2022) no. 9, 813, `arXiv:2201.12257 [hep-ex]`.

[429] J.-W. Chen, H.-C. Chi, H.-B. Li, C. P. Liu, L. Singh, H. T. Wong, C.-L. Wu, and C.-P. Wu, "Constraints on millicharged neutrinos via analysis of data from atomic ionizations with germanium detectors at sub-keV sensitivities," *Phys. Rev. D* **90** (2014) no. 1, 011301, `arXiv:1405.7168 [hep-ph]`.

[430] A. Studenikin, "New bounds on neutrino electric millicharge from limits on neutrino magnetic moment," *EPL* **107** (2014) no. 2, 21001, `arXiv:1302.1168 [hep-ph]`. [Erratum: EPL 107, 39901 (2014), Erratum: Europhys.Lett. 107, 39901 (2014)].

[431] **XMASS** Collaboration, K. Abe *et al.*, "Search for exotic neutrino-electron interactions using solar neutrinos in XMASS-I," *Phys. Lett. B* **809** (2020) 135741, `arXiv:2005.11891 [hep-ex]`.

[432] G. G. Raffelt, "Limits on neutrino electromagnetic properties: An update," *Phys. Rept.* **320** (1999) 319–327.

[433] A. I. Studenikin and I. Tokarev, "Millicharged neutrino with anomalous magnetic moment in rotating magnetized matter," *Nucl. Phys. B* **884** (2014) 396–407, `arXiv:1209.3245 [hep-ph]`.

[434] G. Barbiellini and G. Cocconi, "Electric Charge of the Neutrinos from SN1987A," *Nature* **329** (1987) 21–22.

[435] A. N. Khan, "Electric charge dequantization with Dirac neutrinos in CEνNS," `arXiv:2201.10578 [hep-ph]`.

[436] **CHARM-II** Collaboration, P. Vilain *et al.*, "Experimental study of electromagnetic properties of the muon-neutrino in neutrino - electron scattering," *Phys. Lett. B* **345** (1995) 115–118.

[437] **CCFR, E744, E770** Collaboration, K. S. McFarland *et al.*, "A Precision measurement of electroweak parameters in neutrino - nucleon scattering," *Eur. Phys. J. C* **1** (1998) 509–513, `arXiv:hep-ex/9701010`.

[438] M. Hirsch, E. Nardi, and D. Restrepo, "Bounds on the tau and muon neutrino vector and axial vector charge radius," *Phys. Rev. D* **67** (2003) 033005, `arXiv:hep-ph/0210137`.

[439] **TEXONO** Collaboration, M. Deniz *et al.*, "Measurement of Nu(e)-bar -Electron Scattering Cross-Section with a CsI(Tl) Scintillating Crystal Array at the Kuo-Sheng Nuclear Power Reactor," *Phys. Rev.* **D81** (2010) 072001, `arXiv:0911.1597 [hep-ex]`.

[440] J. Erler and M. J. Ramsey-Musolf, "The Weak mixing angle at low energies," *Phys. Rev. D* **72** (2005) 073003, `arXiv:hep-ph/0409169`.

[441] **ALEPH, CDF, D0, DELPHI, L3, OPAL, SLD, LEP Electroweak Working Group, Tevatron Electroweak Working Group, SLD Electroweak and Heavy Flavour Groups** Collaboration, L. E. W. Group,

"Precision Electroweak Measurements and Constraints on the Standard Model," `arXiv:1012.2367 [hep-ex]`.

[442] K. S. Kumar, S. Mantry, W. J. Marciano, and P. A. Souder, "Low Energy Measurements of the Weak Mixing Angle," *Ann. Rev. Nucl. Part. Sci.* **63** (2013) 237–267, `arXiv:1302.6263 [hep-ex]`.

[443] **PVDIS** Collaboration, D. Wang *et al.*, "Measurement of parity violation in electron–quark scattering," *Nature* **506** (2014) no. 7486, 67–70.

[444] C. S. Wood, S. C. Bennett, D. Cho, B. P. Masterson, J. L. Roberts, C. E. Tanner, and C. E. Wieman, "Measurement of parity nonconservation and an anapole moment in cesium," *Science* **275** (1997) 1759–1763.

[445] J. Guena, M. Lintz, and M. A. Bouchiat, "Measurement of the parity violating 6S-7S transition amplitude in cesium achieved within 2 x 10(-13) atomic-unit accuracy by stimulated-emission detection," *Phys. Rev. A* **71** (2005) 042108, `arXiv:physics/0412017`.

[446] V. A. Dzuba, J. C. Berengut, V. V. Flambaum, and B. Roberts, "Revisiting parity non-conservation in cesium," *Phys. Rev. Lett.* **109** (2012) 203003, `arXiv:1207.5864 [hep-ph]`.

[447] M. S. Safronova, D. Budker, D. DeMille, D. F. J. Kimball, A. Derevianko, and C. W. Clark, "Search for New Physics with Atoms and Molecules," *Rev. Mod. Phys.* **90** (2018) no. 2, 025008, `arXiv:1710.01833 [physics.atom-ph]`.

[448] **SLAC E158** Collaboration, P. L. Anthony *et al.*, "Precision measurement of the weak mixing angle in Moller scattering," *Phys. Rev. Lett.* **95** (2005) 081601, `arXiv:hep-ex/0504049`.

[449] **Qweak** Collaboration, D. Androić *et al.*, "Precision measurement of the weak charge of the proton," *Nature* **557** (2018) no. 7704, 207–211, `arXiv:1905.08283 [nucl-ex]`.

[450] **COHERENT** Collaboration, D. Akimov *et al.*, "Measurement of the Coherent Elastic Neutrino-Nucleus Scattering Cross Section on CsI by COHERENT," *Phys. Rev. Lett.* **129** (2022) no. 8, 081801, `arXiv:2110.07730 [hep-ex]`.

[451] A. Majumdar, D. K. Papoulias, R. Srivastava, and J. W. F. Valle, "Physics implications of recent Dresden-II reactor data," *Phys. Rev. D* **106** (2022) no. 9, 093010, `arXiv:2208.13262 [hep-ph]`.

[452] H. Davoudiasl, H.-S. Lee, and W. J. Marciano, "Muon Anomaly and Dark Parity Violation," *Phys. Rev. Lett.* **109** (2012) 031802, `arXiv:1205.2709 [hep-ph]`.

[453] H. Davoudiasl, H.-S. Lee, and W. J. Marciano, "Low Q^2 weak mixing angle measurements and rare Higgs decays," *Phys. Rev. D* **92** (2015) no. 5, 055005, `arXiv:1507.00352 [hep-ph]`.

[454] J. Erler and R. Ferro-Hernández, "Weak Mixing Angle in the Thomson Limit," *JHEP* **03** (2018) 196, `arXiv:1712.09146 [hep-ph]`.

[455] A. de Gouvea, P. A. N. Machado, Y. F. Perez-Gonzalez, and Z. Tabrizi, "Measuring the Weak Mixing Angle in the DUNE Near Detector Complex," *Phys. Rev. Lett.* **125** (2020) no. 5, 051803, `arXiv:1912.06658 [hep-ph]`.

[456] R. Boughezal, A. Emmert, T. Kutz, S. Mantry, M. Nycz, F. Petriello, K. Şimşek, D. Wiegand, and X. Zheng, "Neutral-current electroweak physics and SMEFT studies at the EIC," *Phys. Rev. D* **106** (2022) no. 1, 016006, `arXiv:2204.07557 [hep-ph]`.

[457] **MOLLER** Collaboration, J. Mammei, "The MOLLER Experiment," *Nuovo Cim. C* **035N04** (2012) 203–208, `arXiv:1208.1260 [hep-ex]`.

[458] N. Berger *et al.*, "Measuring the weak mixing angle with the P2 experiment at MESA," *J. Univ. Sci. Tech. China* **46** (2016) no. 6, 481–487, `arXiv:1511.03934 [physics.ins-det]`.

[459] **H1, ZEUS** Collaboration, P. A. Souder, "Parity-violating PVDIS with SoLID," *AIP Conf. Proc.* **1441** (2012) no. 1, 123–125.

[460] J. Alonso *et al.*, "Neutrino physics opportunities with the IsoDAR source at Yemilab," *Phys. Rev. D* **105** (2022) no. 5, 052009, `arXiv:2111.09480 [hep-ex]`.

[461] T. S. Kosmas, O. G. Miranda, D. K. Papoulias, M. Tortola, and J. W. F. Valle, "Sensitivities to neutrino electromagnetic properties at the TEXONO

experiment," *Phys. Lett. B* **750** (2015) 459–465, `arXiv:1506.08377 [hep-ph]`.

[462] B. C. Canas, E. A. Garces, O. G. Miranda, M. Tortola, and J. W. F. Valle, "The weak mixing angle from low energy neutrino measurements: a global update," *Phys. Lett. B* **761** (2016) 450–455, `arXiv:1608.02671 [hep-ph]`.

[463] B. C. Cañas, E. A. Garcés, O. G. Miranda, and A. Parada, "Future perspectives for a weak mixing angle measurement in coherent elastic neutrino nucleus scattering experiments," *Phys. Lett. B* **784** (2018) 159–162, `arXiv:1806.01310 [hep-ph]`.

[464] M. Lindner, W. Rodejohann, and X.-J. Xu, "Coherent Neutrino-Nucleus Scattering and new Neutrino Interactions," *JHEP* **03** (2017) 097, `arXiv:1612.04150 [hep-ph]`.

[465] N. Blinov, E. Kowalczyk, and M. Wynne, "Axion-like particle searches at DarkQuest," *JHEP* **02** (2022) 036, `arXiv:2112.09814 [hep-ph]`.

[466] R. T. Co, S. Kumar, and Z. Liu, "Searches for heavy QCD axions via dimuon final states," *JHEP* **02** (2023) 111, `arXiv:2210.02462 [hep-ph]`.

[467] **Particle Data Group** Collaboration, P. Zyla *et al.*, "Review of Particle Physics," *PTEP* **2020** (2020) no. 8, 083C01.

[468] L. Frankfurt and M. Strikman, *Diffractive phenomena in high energy processes*, pp. 363–423. 2013. `arXiv:1304.4308 [hep-ph]`.

[469] **ALICE** Collaboration, B. Abelev *et al.*, "Measurement of inelastic, single- and double-diffraction cross sections in proton–proton collisions at the LHC with ALICE," *Eur. Phys. J. C* **73** (2013) no. 6, 2456, `arXiv:1208.4968 [hep-ex]`.

[470] **TOTEM** Collaboration, G. Antchev *et al.*, "First measurement of elastic, inelastic and total cross-section at $\sqrt{s} = 13$ TeV by TOTEM and overview of cross-section data at LHC energies," *Eur. Phys. J. C* **79** (2019) no. 2, 103, `arXiv:1712.06153 [hep-ex]`.

[471] **COMPETE** Collaboration, J. R. Cudell, V. V. Ezhela, P. Gauron, K. Kang, Y. V. Kuyanov, S. B. Lugovsky, E. Martynov, B. Nicolescu, E. A. Razuvaev, and N. P. Tkachenko, "Benchmarks for the forward observables at RHIC, the

Tevatron Run II and the LHC," *Phys. Rev. Lett.* **89** (2002) 201801, `arXiv:hep-ph/0206172`.

[472] A. Donnachie and P. V. Landshoff, "The Interest of large - t elastic scattering," *Phys. Lett. B* **387** (1996) 637–641, `arXiv:hep-ph/9607377`.

[473] **TOTEM** Collaboration, G. Antchev *et al.*, "First measurement of elastic, inelastic and total cross-section at $\sqrt{s} = 13$ TeV by TOTEM and overview of cross-section data at LHC energies," *Eur. Phys. J. C* **79** (2019) no. 2, 103, `arXiv:1712.06153 [hep-ex]`.

[474] **TOTEM** Collaboration, G. Antchev *et al.*, "Measurement of proton-proton elastic scattering and total cross-section at S**(1/2) = 7-TeV," *EPL* **101** (2013) no. 2, 21002.

[475] **ATLAS** Collaboration, G. Aad *et al.*, "Measurement of the total cross section from elastic scattering in pp collisions at $\sqrt{s} = 7$ TeV with the ATLAS detector," *Nucl. Phys. B* **889** (2014) 486–548, `arXiv:1408.5778 [hep-ex]`.

[476] A. Breakstone *et al.*, "A Measurement of $\bar{p}p$ and pp Elastic Scattering in the Dip Region at $\sqrt{s} = 53$-GeV," *Phys. Rev. Lett.* **54** (1985) 2180.

[477] G. Antchev *et al.*, "First measurement of the total proton-proton cross section at the LHC energy of $\sqrt{s}$ =7 TeV," *EPL* **96** (2011) no. 2, 21002, `arXiv:1110.1395 [hep-ex]`.

[478] **TOTEM** Collaboration, G. Antchev *et al.*, "Proton-proton elastic scattering at the LHC energy of s** (1/2) = 7-TeV," *EPL* **95** (2011) no. 4, 41001, `arXiv:1110.1385 [hep-ex]`.

[479] A. Donnachie and P. V. Landshoff, "Small t elastic scattering and the ρ parameter," *Phys. Lett. B* **798** (2019) 135008, `arXiv:1904.11218 [hep-ph]`.

[480] V. A. Khoze, A. D. Martin, and M. G. Ryskin, "Elastic scattering and Diffractive dissociation in the light of LHC data," *Int. J. Mod. Phys. A* **30** (2015) no. 08, 1542004, `arXiv:1402.2778 [hep-ph]`.

[481] R. B. Appleby, R. J. Barlow, J. G. Molson, M. Serluca, and A. Toader, "The Practical Pomeron for High Energy Proton Collimation," *Eur. Phys. J. C* **76** (2016) no. 10, 520, `arXiv:1604.07327 [hep-ph]`.

[482] C. O. Rasmussen and T. Sjöstrand, “Models for total, elastic and diffractive cross sections,” *Eur. Phys. J. C* **78** (2018) no. 6, 461, `arXiv:1804.10373 [hep-ph]`.

[483] A. B. Kaidalov and M. G. Poghosyan, “Description of soft diffraction in the framework of reggeon calculus: Predictions for LHC,” in *13th International Conference on Elastic and Diffractive Scattering (Blois Workshop): Moving Forward into the LHC Era*. 9, 2009. `arXiv:0909.5156 [hep-ph]`.

[484] E. Gotsman, E. Levin, and U. Maor, “Description of LHC data in a soft interaction model,” *Phys. Lett. B* **716** (2012) 425–429, `arXiv:1208.0898 [hep-ph]`.

[485] A. K. Likhoded, A. V. Luchinsky, and A. A. Novoselov, “Light hadron production in inclusive pp-scattering at LHC,” *Phys. Rev. D* **82** (2010) 114006, `arXiv:1005.1827 [hep-ph]`.

[486] M. Schindler, T. Fuchs, J. Gegelia, and S. Scherer, “Axial, induced pseudoscalar, and pion-nucleon form-factors in manifestly Lorentz-invariant chiral perturbation theory,” *Phys. Rev. C* **75** (2007) 025202, `arXiv:nucl-th/0611083`.

[487] G. Megias, S. Bolognesi, M. Barbaro, and E. Tomasi-Gustafsson, “New evaluation of axial nucleon form factor from electron- and neutrino-scattering data and impact on neutrino-nucleus cross-section,” *Phys. Rev. C* **101** (2020) no. 2, 025501, `arXiv:1910.13263 [hep-ph]`.

[488] W. R. Gibbs and B. Loiseau, “Two-pion exchange contribution to proton-proton scattering at medium energies,” *Phys. Rev. C* **77** (2008) 014003, `arXiv:nucl-th/0606045`.

[489] W. R. Wortman, “Two-pion-exchange contributions to nucleon-nucleon scattering,” *Phys. Rev.* **176** (1968) 1762–1768.

[490] W.-M. e. a. Yao, “Review of Particle Physics,” *Journal of Physics G* **33** (2006) 1+. `http://pdg.lbl.gov`.

[491] M. Bonesini, A. Marchionni, F. Pietropaolo, and T. Tabarelli de Fatis, “On Particle production for high-energy neutrino beams,” *Eur. Phys. J.* **C20** (2001) 13–27, `arXiv:hep-ph/0101163 [hep-ph]`.

[492] M. Aguilar-Benitez *et al.*, “Inclusive particle production in 400-GeV/c p p interactions,” *Z. Phys. C* **50** (1991) 405–426.

[493] A. Suzuki *et al.*, “High Mass Meson Resonance Production in pp Interactions at 405-GeV/c,” *Nucl. Phys. B* **172** (1980) 327–334.

Appendix A

Proton-Proton Scattering and Diffraction

A.1 Introduction

This appendix discusses the modelling of pp scattering processes characterized by small-momentum transfer, particularly in the forward direction, across two distinct low- and high-energy regimes. We present a comprehensive parameterization for the elastic scattering process in high energy pp collisions with the centre of mass energy $\sqrt{s} \gtrsim 10\,\mathrm{GeV}$. This parameterization employs a model that effectively captures the diffractive pp scattering phenomena through pomeron exchange. On the other hand, focusing on low beam energies around GeV, which are particularly relevant to the LSND experiment, we provide a description of modelling pp elastic scattering via one pion exchange. Lastly, we briefly discuss the parametrization concerning the production rate of vector mesons in inclusive reactions.

A.2 Modeling forward pp scattering

We start by reviewing the high-energy behaviour of hadronic scattering processes with small momentum transfer that cannot be described in terms of perturbative QCD. In high energy pp collisions, where soft interactions play a dominant role, the total cross-section can be divided into diffractive and non-diffractive scattering processes [467, 468]. In elastic diffractive scattering both protons stay intact after the collision while in inelastic diffractive scattering, one of the incoming protons or both dissociate into multi-particle final states with the invariant mass $M \ll \sqrt{s}$, preserving the quantum number(s) of the associated initial proton(s). Non-diffractive scattering denotes more generic inelastic processes and is the characteristic process used at the LHC to observe new physics events with large transverse momentum. Our

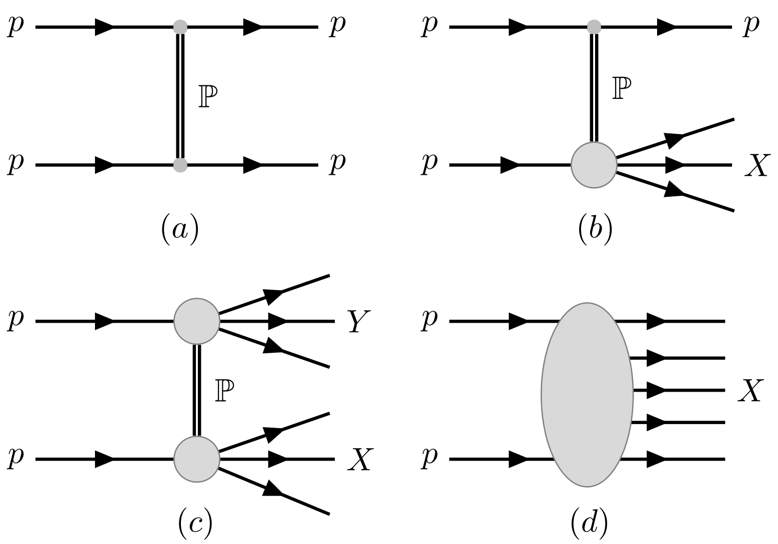

Figure A.1: Schematic diagrams for the lowest order Pomeron exchange processes contributing to (a) elastic scattering, (b) single dissociation, (c) double dissociation and (d) non-diffractive interactions. The double line $\mathbb{P}$ corresponds to the Pomeron exchange and p for the proton.

focus here is instead on the forward region, and processes with GeV-scale or sub-GeV momentum transfer.

Within the category of diffractive scattering, single dissociation (SD), corresponding to $pp{\to}p{+}X$, and double dissociation (DD), corresponding to $pp{\to}X{+}Y$, have the following characteristics: *i*) the diffracted state is separated from the scattered proton by a large rapidity gap devoid of any hadronic activity; *ii*) the energy transfer between the two interacting protons remains small; and *iii*) the coherence condition implies $\xi{=}\,M_X^2/s \lesssim 0.15$ which separates dissociation from the inelastic process. Such processes have traditionally been modeled phenomenologically with Regge exchanges, along with single or multi-pomeron exchange. Feynman diagrams corresponding to one pomeron exchange in elastic, single- and double-diffraction processes are shown in Fig. A.1, where the remaining configurations correspond to non-diffractive interactions. Experimental data indicates that the high-energy total and elastic pp cross sections grow slowly with centre of mass energy as shown in Fig. A.2, and have the asymptotic behavior $\sigma_{\text{tot}} \sim \ln(s)^2$ [246]. At LHC energies, diffractive processes constitute up to 40% of the total pp cross section [469].

The Donnachie-Landshoff (DL) model of diffractive pp scattering incorporates the Regge theory approach which sums the exchanges of many particles and provides a

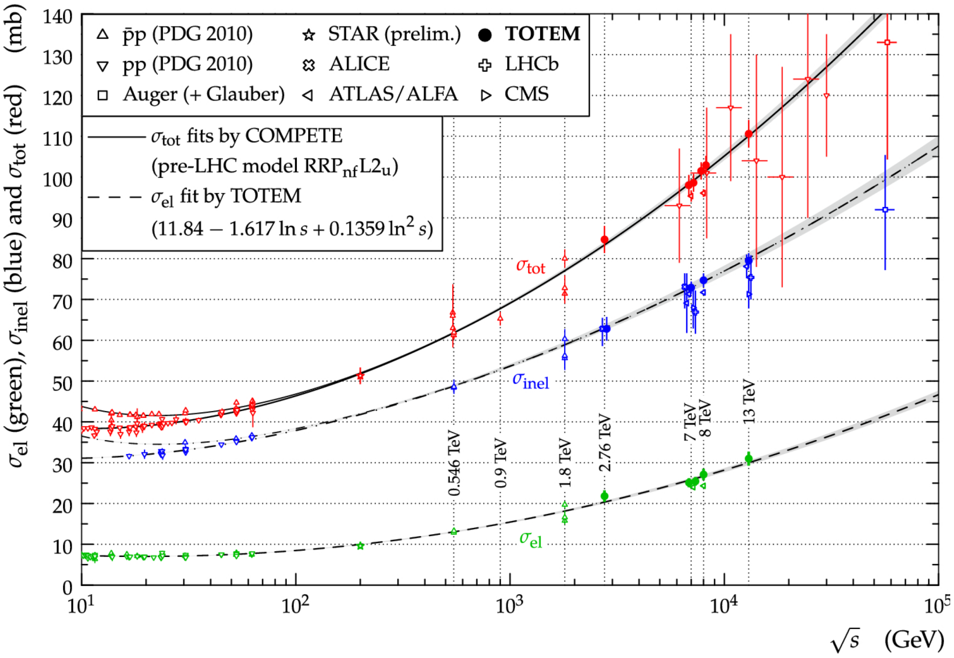

Figure A.2: The figure, adapted from Ref. [470], presents an overview of the elastic, inelastic, and total cross-section data for pp and $\bar{p}p$ collisions and illustrates the dependence on the center-of-mass energy ($\sqrt{s}$). The solid black line corresponds to the best fit of the total cross-section data obtained by the COMPETE collaboration [471].

good description of the existing elastic differential cross section data, including the exponential fall at low Mandelstam t, the dip region at mid t, and the rapid fall in cross section at high t. The DL parameterization utilizes single Regge (with ρ, ω and f, a_2 trajectories) and Pomeron exchange [239], along with multiple Regge and Pomeron exchanges [240, 241, 242], plus triple-gluon exchange for $|t| \gtrsim 3.5$ GeV^2 [472]. This parametrization will form the basis of our bremsstrahlung model, and we review the components in more detail below.

Elastic scattering:- We first review the elastic cross-section. DL parameterization for the pp elastic scattering interaction at high energies includes Regge, single Pomeron exchange, and multiple Regge and Pomeron exchanges. It is notable that just including single-pomeron exchange describes the measured pp elastic cross section at high-energies remarkably well for sufficiently small t. For later purposes, we find it convenient to present this parametrization in terms of a phenomenological soft pomeron propagator $G_{\mathbb{P}}(s,t)g^{\mu\nu}$ and an effective proton-pomeron vertex $\Gamma^{\mu}_{\mathbb{P}}(t)$,

$$G_{\mathbb{P}}(s,t) = \frac{(2\nu\alpha'_{\mathbb{P}})^{\alpha_{\mathbb{P}}(t)}}{2\nu}\eta_{\mathbb{P}}(t), \tag{A.1}$$

$$\Gamma^{\mu}_{\mathbb{P}}(t) = -iY_{\mathbb{P}}F_{\mathbb{P}}(t)\gamma^{\mu}, \tag{A.2}$$

where $2\nu = (s-u)/2$. The effective soft pomeron trajectory is linear in t,

$$\alpha_{\mathbb{P}}(t) = 1 + \epsilon_{\mathbb{P}} + \alpha'_{\mathbb{P}}t, \tag{A.3}$$

where the intercept $\alpha_{\mathbb{P}}(0) > 1$, and $Y_{\mathbb{P}}$ is the coupling strength of the pomeron to the proton. The relevant parameters are listed in Table A.1. The pomeron form factor was traditionally assumed to have a dipole form [239], $F_{\mathbb{P}}(t) \sim 1/(1-t/0.71\,\text{GeV}^2)^2$, as for the proton electromagnetic form factor. However, more recent studies [242] utilize an exponential form factor, $F^2_{\mathbb{P}}(t) = A\exp(at)+(1-A)\exp(bt)$. Finally, $\eta_{\mathbb{P}}(t) = -\exp\big\{(-\frac{1}{2}i\pi\alpha_{\mathbb{P}}(t))\big\}$ is the signature factor.

As is apparent in Fig. A.3, the cross-section modeled with soft pomeron exchange in the region where the squared momentum transfer t is not too large can be approximated by a simple exponential fall-off

$$\frac{d\sigma^{\text{el}}}{dt} \simeq B(s)\sigma_{\text{el}}(s)\exp(-B|t|). \tag{A.4}$$

Note that with increasing energy the differential cross section becomes steeper and the diffractive slope B which grows linearly in $\log(s)$ (the so-called shrinkage of the diffractive peak) has been measured by several experiments [473] and is $\sim 20\,\text{GeV}^{-2}$ at LHC energies. Measurements of the diffractive elastic scattering allow us to extract information on the total cross-section using *optical theorem* stating that

$$\pi\left(\frac{\sigma_{\text{tot}}(s)}{4\pi}\right)^2 \approx \left.\frac{d\sigma^{\text{el}}(s,t)}{dt}\right|_{t=0} = B(s)\sigma_{\text{el}}(s). \tag{A.5}$$

While single pomeron exchange is sufficient to model the elastic cross section for small t, the inclusion of higher exchanges, including double pomeron exchange, becomes important for fitting the diffractive dip apparent in Fig. A.3 for $|t| \gtrsim 1$ GeV. Considering all the contributions from single-pomeron ($\mathbb{P}$) and double-pomeron ($\mathbb{PP}$) exchange, and triple-gluon ($3g$) exchange, the elastic pp-scattering at high energies takes the form

$$\frac{d\sigma^{\text{el}}}{dt} \simeq \frac{1}{4\pi}|\mathcal{A}_{\text{el}}|^2, \tag{A.6}$$

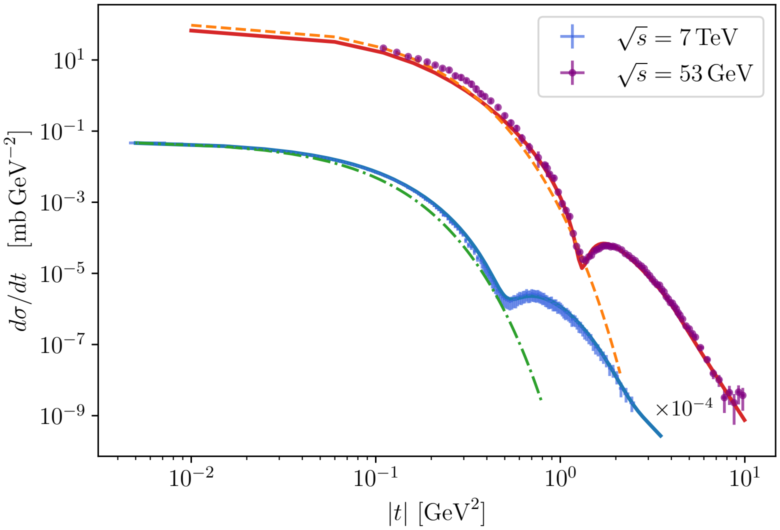

Figure A.3: The DL model fit for the elastic differential cross-section compared with pp data at $\sqrt{s} = 7\,\mathrm{TeV}$ [474, 475] (in blue) and $\sqrt{s} = 53\,\mathrm{GeV}$ [476] (in purple). A single soft pomeron exchange fit is also shown in each case for small t-values with dashed lines. The diffractive dip requires the addition of double pomeron exchange and other components of the full model.

where

$$\mathcal{A}_{\mathrm{el}}(s,t) = \sum_{\mathbb{P},\mathbb{PP}} (Y_i F_i(t))^2 G_i(s,t) + Y_{3g}^2 G_{3g}(t). \tag{A.7}$$

The full parametrization involves adding these contributions, and the values of the best fit parameters of the DL model are given in Table A.1. A brief overview of these additional components of the model follows.

Measured high energy pp elastic scattering at the LHC [477, 478] may also point toward an additional hard-pomeron contribution [241], although it is not strictly necessary to fit the data [242, 479]. Instead, multiple-pomeron exchange, which one has to take into account to avoid the breakdown of unitarity, effectively behaves as a simple power of s^{ϵ} over a very wide range of energies. Following Ref. [242], we model the double-pomeron effective propagator and vertex as

$$G_{\mathbb{PP}}(s,t) = \frac{(2\nu\alpha'_{\mathbb{P}})^{\alpha_{\mathbb{PP}}(t)}}{2\nu}\eta_{\mathbb{PP}}(t), \tag{A.8}$$

$$\Gamma^{\mu}_{\mathbb{PP}}(t) = -iY_{\mathbb{PP}}F_{\mathbb{PP}}(t)\gamma^{\mu}, \tag{A.9}$$

Parameter	Value
$\epsilon_{\mathbb{P}}$	0.110
$\alpha'_{\mathbb{P}}$	$0.165\ \mathrm{GeV}^{-2}$
$Y_{\mathbb{P}}$	13.019
Y_{3g}	0.142
t_0	$-4.230\ \mathrm{GeV}^2$
A	0.682
a	$7.854\ \mathrm{GeV}^{-2}$
b	$2.470\ \mathrm{GeV}^{-2}$

Table A.1: The best fit parameters for the elastic scattering DL model [242].

with the corresponding trajectory,

$$\alpha_{\mathbb{P}\mathbb{P}}(t) = 1 + 2\epsilon_{\mathbb{P}} + \frac{1}{2}\alpha'_{\mathbb{P}}t, \tag{A.10}$$

where the effective coupling strength of the double pomeron exchange takes the form $Y_{\mathbb{P}\mathbb{P}} = Y_{\mathbb{P}}^2/4\sqrt{\pi}$. The signature factor reads $\eta_{\mathbb{P}\mathbb{P}}(t){=}\exp\left\{(-\frac{1}{2}i\pi\alpha_{\mathbb{P}\mathbb{P}}(t))\right\}$, and the form factor squared takes the semi-eikonal form,

$$F_{\mathbb{P}\mathbb{P}}^2(t) = \frac{A^2}{a/\alpha'_{\mathbb{P}} + L}e^{\frac{1}{2}at} + \frac{(1-A)^2}{b/\alpha'_{\mathbb{P}} + L}e^{\frac{1}{2}bt}, \tag{A.11}$$

with additional logarithmic factors $L = \log(2\nu\alpha'_{\mathbb{P}}) - i\pi/2$ in the denominator.

The dominant contribution to the elastic cross section at larger values of $|t| \gtrsim 3.5\,\mathrm{GeV}^2$ exhibits an energy-independent behavior $\sim t^{-8}$, in agreement with triple-gluon exchange [472], with an amplitude of the from,

$$G_{3g}(t) = \begin{cases} \frac{|t_0|^3}{t^4}, & t < t_0 \\ \frac{1}{|t_0|}e^{2(1-t^2/t_0^2)}, & t_0 < t \end{cases} \tag{A.12}$$

$$\Gamma^{\mu}_{3g} = -iY_{3g}\gamma^{\mu}, \tag{A.13}$$

where for $|t| < |t_0|$, a smooth transition was adopted to avoid a divergence as $t \to 0$.

In principle one should also include the Reggeon f_2, a_2, ρ, and ω exchanges, but at large energies $\sqrt{s} \gg 10$ GeV these contributions with intercepts $\alpha_{\mathbb{R}} \simeq 0.5$ are suppressed, which allows us to focus on the Pomeron only [239]. Note that the electromagnetic contribution must also be included in order to fit elastic scattering data at very small t. However, this coulomb amplitude will be negligible for the parameters of interest here.

Dissociative scattering:- Scattering with single diffractive (SD) dissociation of one proton can be modeled with the triple-pomeron formalism using a generalized optical theorem [243, 480], in which the corresponding $pp \to p+X$ cross section is given by

$$\frac{d\sigma^{\rm SD}}{dt dM_X^2} = \frac{g_{3\mathbb{P}}(t)}{16\pi^2}\frac{g_{\mathbb{P}}(0)g_{\mathbb{P}}(t)^2}{M_X^2} \times \left(\frac{s}{M_X^2}\right)^{2\alpha_{\mathbb{P}}(t)-2}\left(\frac{M_X^2}{s_0}\right)^{\alpha_{\mathbb{P}}(0)-1}, \tag{A.14}$$

where the diffractive mass is $M_X^2 = \xi s$, with $\xi \lesssim 0.15$, $g_{\mathbb{P}}(t)$ is the *soft* pomeron-proton coupling strength with an exponential t-dependent form-factor, and $g_{3\mathbb{P}}(t)$ is the triple-pomeron coupling. The dimensionful coupling $g^2_{\mathbb{P}}(0) \approx 57$ mb specifies $\sigma_{\rm tot}$, and is distinct from the single pomeron-exchange value defined previously, while $g_{3\mathbb{P}}(0)/g_{\mathbb{P}}(0) \simeq 0.2$ is obtained from a triple-Regge analysis of lower energy data [480]. In the low-mass regime $M_X \lesssim t$, the system X is dominated by baryon resonances and low level excited states of the proton [481, 482].

In Section 4.2 we consider initial and final state radiation for these exchange processes and it will be useful to have parameterizations for the total pp cross-section (in mb) taken from experimental data [202, 471],

$$\sigma_{\rm tot}(s) = 34.4 + 0.3\log^2(s/s_0) + 13.1(\frac{s}{s_0})^{-\eta_1} + 7.4(\frac{s}{s_0})^{-\eta_2}, \tag{A.15}$$

where $s_0 = 15.98$ GeV^2, $\eta_1 = 0.45$, $\eta_2 = 0.55$ and similarly the elastic scattering cross section (in mb) [473] ,

$$\sigma_{\rm el}(s) = 11.8 - 1.6\log(s) + 0.14\log^2(s). \tag{A.16}$$

The single diffractive cross section can similarly be modeled [483, 484] and parametrized based on the experimental data [469]. However, larger systematic uncertainties in the diffractive cross sections of about 5−10% (depending on the energy) arise due to the fact that at high energies, defining (and selecting) purely diffractive events is problematic [469]. The $\sqrt{s} = 14$ TeV LHC cross-section for SD scattering is ~ 10 mb, while for DD scattering it is ~ 7 mb [469]. We also introduce the inelastic, non-single diffractive (NSD) cross-section, $\sigma_{\rm NSD} \equiv \sigma_{\rm tot} - \sigma_{\rm el} - \sigma_{\rm SD}$, which can be parametrized following Ref. [485] as

$$\sigma_{\rm NSD}(s) = 1.76 + 19.8\Big(\frac{s}{\rm GeV^2}\Big)^{0.057} \quad {\rm mb}. \tag{A.17}$$

A.3 Low Energy Beams: Pion Exchange

Thus far, our discussions have primarily focused on the modelling of high-energy proton-proton collisions. Here we will extend of discussion and consider a low-energy description of modelling proton-proton scattering via one pion exchange, which is expected to provide the dominant hadronic (as opposed to electromagnetic) contribution to bremsstrahlung at sub-relativistic beam energies. Using $\mathcal{L} = g_{\pi NN}\bar{N}\gamma_5\tau \cdot \pi N$, with $g^2_{\pi NN}/(4\pi) \approx 13.5$, we first verify that the tree-level one pion exchange contribution to pp elastic scattering does provide a relatively good fit, after accounting for the electromagnetic component, as shown in Fig. A.4. We utilize a dipole form for the pion-nucleon form factor $\sim 1/(1 + Q^2/m_A^2)^2$ where $m_A \sim 1\,\text{GeV}$ is the axial mass [486, 487], and similarly the proton electromagnetic form factor $F_1(Q^2) \sim 1/(1 + Q^2/(0.71\text{GeV})^2)^2$. The contribution from one pion exchange is significant in a narrow energy range, and it is known that additional processes, such as two pion exchange, become important for beam momenta above 600-700 MeV [488, 489]. Retaining just the one pion exchange contribution will nonetheless be sufficient in our case, as we are interested in the ratio of two- to three-body final states, in which the overall normalization of the pp cross section drops out as for the splitting function calculation above. Note that above a beam momentum of about a GeV, the inelastic channel via the Δ-resonance contributes at a comparable level to elastic scattering, but is not accounted for in this approximation.

A.4 Inclusive Reactions

In this section, we provide a concise overview of the kinematic distribution observed in inclusive reactions, with a specific focus on the production rate of vector mesons $\mathfrak{m} = \rho, \omega, \varphi$. The analysis of such data can serve as a benchmark for comparing against our approximate model of vector-particle radiation via proton bremsstrahlung, which will be further discussed in Chapter 4. The Feynman scaling variable $x_F \equiv p_\ell/p_{\rm max}$ is defined in the center of mass frame, where p_ℓ is the longitudinal momentum carried by the produced meson and $p_{\rm max} \approx \sqrt{s}/2$ at very large scattering energies. An

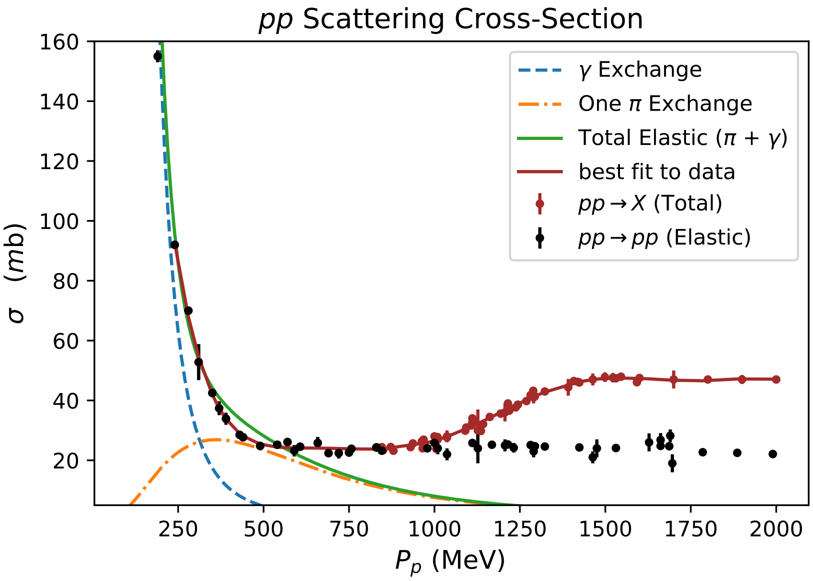

Figure A.4: The pp - scattering cross-section as a function of the proton beam 3-momentum (MeV). The curves denote the contributions from one pion exchange (dash-dotted line), photon exchange (dashed line), and the total cross section (solid line), compared with data for elastic and inelastic scattering from the Particle Data Group [490]. For the electromagnetic component, there is a cut on the forward/backward angle of the scattered proton in the lab frame of 2°.

alternative scaling variable $x_R \equiv E/E_{\max}$ in the center of mass frame is defined to greatly extend the range of validity of scaling at sub-asymptotic energies. Following [491], the parametrization of the invariant cross-section may be presented by a fit function

$$E\frac{d^3\sigma}{dp^3} = \frac{E}{\pi p_{\max}}\frac{d^2\sigma}{dx_F dp_T^2} \approx A\frac{(1-x_R)^\alpha}{x_R^\beta}\exp\left(-Bp_T^2\right), \tag{A.18}$$

where the exponents α and β are fit to the data (conventionally presented in terms of x_F variable [492]). At all energies, the p_T dependence out to $\sim$ 2 GeV is well presented by the exponential form, where the measured value of the exponent is $B = 2.6 \pm 0.1\,\mathrm{GeV}^{-2}$ at 400 GeV beam energy [492]. Alternatively, the parametrization can be expressed by a similar variable $x_0 \equiv p/p_{\max} = \sqrt{x_F^2 + p_T^2/p_{\max}^2}$ [493].

Appendix B

Numerical Computations

The codes used to carry out the analysis for the studies presented in the current dissertation were developed using Python. Here, we show part of the script utilized to derive sensitivity predictions for the FORMOSA experiment in the search for millicharged particles (mCPs). The production rates for mCPs are obtained from a Monte Carlo generator developed in the FORESEE software package [237]. These rates, stored in `mcpspectrum_{mass}.txt` format, are then incorporated into the code. The code defines the specific detector configurations. By assessing the interactions between mCPs and the detector material, the code calculates the number of photoelectrons generated and determines the total count of signal events. To obtain sensitivity contours for mCPs in the FORMOSA setup, the code utilizes a loop over different mass values, employing the previously introduced function `N_Event`. The resulting data is saved into a `.txt` file for later analysis and visualization purposes.

```python
import random
import matplotlib.pyplot as plt
import numpy as np
from skhep.math.vectors import LorentzVector, Vector3D
import math

def dEdx(m_chi, epsilon, E_chi, material):
# Energy loss (linear stopping power) function; MeV/cm

    gamma = E_chi/m_chi
    beta = np.sqrt(1-1/gamma**2)
    me = 0.511e-3   # GeV
    alpha_em = 1/137
    W_max = (2*me*beta**2*gamma**2)/(1 + 2*gamma*me/m_chi + (me/m_chi)**2)
```

```

    if material == "P-Scint":  # BC-408 Plastic scintillator
        density = 1.023  # g/cm^3
        # Ratio of Hydrogen to Carbon Atoms in the plastic Scintillator
        Ratio_HC = 1.104
        # Atomic number / Atomic mass
        ZoA = (Ratio_HC*(1) + 1*(6))/(Ratio_HC*(1) + 1*(12))
        Z = (Ratio_HC*(1) + 1*(6))/(Ratio_HC+1)
        omega_p = np.sqrt(density*ZoA)*28.816*1e-9  # Plasma Energy in GeV

    elif material == "LAr":  # Liquid-Argon only (could be a mixture of Ar and Kr)
        density = 1.3973  # g/cm^3
        ZoA = 18/40 # Atomic number / Atomic mass
        Z = 18
        omega_p = np.sqrt(density*ZoA)*28.816*1e-9  # Plasma Energy in GeV

    # Stopping Power
    K = 0.307075  # MeV*cm^2/g
    I = Z*15.6*1e-9  # Mean Excitation Energy in GeV
    # Density effect correction
    delta = np.log(omega_p/I) + np.log(beta*gamma) - 1/2

    # The mass stopping power; MeV*cm^2/g
    dEdx = K*ZoA*epsilon**2/beta**2*(0.5*np.log(2*me*beta**2*gamma**2*W_max/I**2)
    - beta**2 - delta/2)

    return density*dEdx

    def N_Event_Integrand(m_chi, epsilon, E_chi, dNdE, material, length_det,
    efficiency_det, n_layer):
    # Energy and mass of mCPs are in GeV; detector length is in cm.
    # dNdE is the mCPs differential energy spectra in GeV^-1
    (number per energy bin) for epsilon = 1

    if material == "P-Scint":  # BC-408 Plastic scintillator
        Light_Output = 0.64
        # The number of photons per MeV of energy deposited in the material
        photon_yield = 17.4e3*Light_Output # MeV^-1;

    elif material == "LAr":  # Liquid-Argon only (could be a mixture of Ar and Kr)
        Light_Output = 1.0
        photon_yield = 24.0e3*Light_Output # MeV^-1;

```

```
    # The average number of photoelectrons collected
    in a detector (scintillator bar or chamber)
    N_PhotoElectron = dEdx(m_chi, epsilon, E_chi, material)
    *efficiency_det * photon_yield * length_det

    # The probability of observing an mCP requires the detection of at least one
    # photoelectron which follows the Poisson distribution
    # In plastic scintillator: Multiple coincidence signature (reduces the PMT
    Dark Current background)

    Prob_det = (1 - np.exp(-abs(N_PhotoElectron)))**n_layer
    Signal = epsilon**2 * dNdE * Prob_det

    return Signal

def readfile(filename):
    list_of_lists = []
    with open(filename) as f:
        for line in f:
            if line[0]=="#":continue
            inner_list = [float(elt.strip()) for elt in line.split( )]
            list_of_lists.append(inner_list)
    return np.array(list_of_lists)

def N_Event(mass, eps, detector,n_layer):
    # The detector width and distance to the IP is in meter.
    # The detector length is in cm.

    luminosity_HL_LHC = 3.0e6 # pb^-1
    luminosity_LHC_R3 = 2.0e5 # pb^-1; This is 200/fb
    list_logth, list_logp, list_xs = readfile("mcpspectra/mcpspectrum_"
    + str(mass) + ".txt").T

    particles, weights = [], []
    for logth,logp,xs in zip(list_logth,list_logp, list_xs):

        p  = 10.**logp
        th = 10.**logth
        pt = p * np.sin(th)

        phi= random.uniform(-math.pi,math.pi)
        fth = 10**np.random.uniform(-0.025, 0.025, 1)[0]
        fp  = 10**np.random.uniform(-0.025, 0.025, 1)[0]
```

```

        th_sm=th*fth
        p_sm=p*fp

        en = math.sqrt(p_sm**2+mass**2)
        pz = p_sm*np.cos(th_sm)
        pt = p_sm*np.sin(th_sm)
        px = pt*np.cos(phi)
        py = pt*np.sin(phi)
        part=LorentzVector(px,py,pz,en)

        particles.append(part)
        weights.append(xs)

    if detector == "FORMOSA_Plastic":  # Plastic scintillator
        det_name = "FORMOSA"
        luminosity = luminosity_HL_LHC
        material, length_det, location_det, width_det = "P-Scint", 100, 500, 1
        efficiency_det = 0.1

    elif detector == "FLArE": # LArTPC
        det_name = "FLArE"
        luminosity = luminosity_HL_LHC
        material, length_det, location_det, width_det = "LAr", 700, 500, 1
        efficiency_det = 0.02
        e_threshold = 0.03  # in GeV

    list_weight = []
    list_Event = []

    for particle, weight in zip(particles,weights):
        angle_det = width_ratio * (width_det/2)/location_det
        N_Event_per_bin_inside = weight*luminosity if (particle.theta() <=
        angle_det) else 0.0
        list_Event.append(N_Event_Integrand(mass, eps, particle.e,
                                            N_Event_per_bin_inside,
                                            material, length_det,
                                            efficiency_det, n_layer))

    N_Event = sum(list_Event)

    return N_Event

```

```
def Sensitivity_Reach(detector,n_layer,Levels):

    # Evaluating the number of events on a grid of (mass, eps) points
    mass_array = np.array(list_mCP_mass())[::]
    epsilon_array = np.outer(np.logspace(-5,-1,5),np.arange(1,10,0.5)).flatten()
    Mass, Epsilon = np.meshgrid(mass_array, epsilon_array) # grid of point
    Event_rate = N_Event_vectorized(Mass, Epsilon, detector, n_layer)

    # Determining countor levels
    # Signal level for detecting at least 1 event
    (Poisson distribution); no background
    Level_90CL = Levels # (np.log(1/0.1),)
    CS = plt.contour(Mass, Epsilon, Event_rate, Level_90CL)
    plt.close()
    Projected_Sensitivity=[CS.collections[i].get_paths()[0].vertices for (i,level)
    in enumerate(Level_90CL)]
    [np.savetxt(detector + '_' + str(n_layer) + '_' + str(level) +'.csv',
                Projected_Sensitivity[i], delimiter=',') for (i, level)
                                                    in enumerate(Level_90CL)]
```